Universidad Politécnica de Cartagena

ESCUELA INTERNACIONAL DE DOCTORADO

PROGRAMA DE DOCTORADO EN ENERGÍAS RENOVABLES Y EFICIENCIA ENERGÉTICA

TESIS DOCTORAL

LARGE EDDY SIMULATIONS PARA MODELADO DE COMBUSTIÓN DE HIDRÓGENO. APLICACIONES A UNIDADES BALÍSTICAS DE REDUCCIÓN DE ARRASTRE DE BASE Y ANÁLISIS DE SECUENCIAS DE ACCIDENTES NUCLEARES

Presentada por Francisco Nicolás Pérez para optar al
grado de Doctor
por la Universidad Politécnica de Cartagena

Dirigida por:
Dr. Francisco Javier Sánchez Velasco

Codirigida por:
Dr. José Serna Serrano

Cartagena, 2022

Universidad Politécnica de Cartagena

ESCUELA INTERNACIONAL DE DOCTORADO

DOCTORAL PROGRAMME IN RENEWABLE ENERGIES AND ENERGY EFFICIENCY

PhD THESIS

LARGE EDDY SIMULATIONS FOR HYDROGEN COMBUSTION MODELLING. APPLICATIONS TO BALLISTIC BASE DRAG REDUCTION UNITS AND NUCLEAR ACCIDENT SEQUENCE ANALYSIS

Presented by Francisco Nicolás Pérez
to the Technical University of Cartagena in fulfilment of
the thesis requirement for the award of PhD

Supervisor:
Dr. Francisco Javier Sánchez Velasco

Co-supervisor:
Dr. José Serna Serrano

Cartagena, 2022

This PhD thesis is presented according to the Compendium of Publications mode, regulated under art. 20 of the Regulation of Official Doctoral Studies of the Technical University of Cartagena of March 24, 2021.

Publications:

Article 1.- F. Nicolás-Pérez, F.J.S. Velasco, J.R. García-Cascales, R.A. Otón-Martínez, A. López-Belchí, D. Moratilla, F. Rey, A. Laso, On the accuracy of RANS, DES and LES turbulence models for predicting drag reduction with Base Bleed technology, Aerospace Science and Technology, Volume 67, 2017, Pages 126-140, ISSN 1270-9638, https://doi.org/10.1016/j.ast.2017.03.031

Article 2.- F. Nicolás-Pérez, F.J.S. Velasco, José R. García-Cascales, Ramón A. Otón-Martínez, Ahmed Bentaib, Nabiha Chaumeix, Evaluation of different models for turbulent combustion of hydrogen-air mixtures. Large Eddy Simulation of a LOVA sequence with hydrogen deflagration in ITER Vacuum Vessel, Fusion Engineering and Design, Volume 161, 2020, 111901, ISSN 0920-3796, https://doi.org/10.1016/j.fusengdes.2020.111901

Article 3.- F. Nicolás-Pérez, F.J.S. Velasco, Ramón A. Otón-Martínez, José R. García-Cascales, Ahmed Bentaib and Nabiha Chaumeix, Capabilities and limitations of Large Eddy Simulation with perfectly stirred reactor assumption for engineering applications of unsteady, hydrogen combustion sequences, Engineering Applications of Computational Fluid Mechanics (TCFM) 2021 https://doi.org/10.1080/19942060.2021.1974092

Article 4.- F. Nicolás-Pérez, F.J.S. Velasco, Ramón A. Otón-Martínez, José R. García-Cascales, Ahmed Bentaib and Nabiha Chaumeix, Mathematical Modelling of Turbulent Combustion of Two-Phase Mixtures of Gas and Solid Particles with a Eulerian–Eulerian Approach: The Case of Hydrogen Combustion in the Presence of Graphite Particles, Mathematics 2021, 9(17), 2017; https://doi.org/10.3390/math9172017

INDEX OF CONTENTS

1 RESUMEN 1

2 ABSTRACT 4

3 ACKNOWLEDGEMENTS 6

4 OBJECTIVES 7

5 INTRODUCTION AND STATE OF THE ART 8

6 ARTICLES 11

6.1 On the accuracy of RANS, DES and LES turbulence models for predicting drag reduction with Base Bleed technology 11

6.2 Evaluation of different models for turbulent combustion of hydrogen-air mixtures. Large Eddy Simulation of a LOVA sequence with hydrogen deflagration in ITER Vacuum Vessel 49

6.3 Capabilities and limitations of Large Eddy Simulation with perfectly stirred reactor assumption for engineering applications of unsteady, hydrogen combustion sequences 89

6.4 Mathematical modelling of turbulent combustion of two-phase mixtures of gas and solid particles with a Eulerian-Eulerian approach 112

7 CONCLUSIONS 130

8 REFERENCES 134

APPENDIX 136

1 Resumen

En este trabajo se han desarrollado modelos de simulación mediante herramientas de mecánica de fluidos computacional (CFD) utilizando modelado de turbulencia *Large Eddy Simulation* (LES) para abordar el análisis de problemas en los que, tradicionalmente, se han utilizado de forma extendida simulaciones con modelado de turbulencia *Reynolds Averaged Navier Stokes Equations* (RANS), en las que los resultados alcanzados presentan ,en muchas ocasiones, diferencias significativas comparados con datos experimentales. En la actualidad, simulaciones CFD con modelado de turbulencia LES se están convirtiendo en una atractiva alternativa a simulaciones RANS, siendo abordable en términos de coste computacional y tiempo de simulación para muchas aplicaciones industriales, debido principalmente a la evolución y avances en materia de recursos y potencia computacional.

En ese contexto, el objetivo principal de este trabajo consiste en desarrollar y validar modelos y estrategias de simulación CFD para ser aplicados y extraer conclusiones relevantes en problemas donde tradicionalmente simulaciones con modelos RANS han sido ampliamente aplicadas, pero con limitaciones en su validación experimental. Estos problemas son el análisis de balística exterior incluyendo unidades de reducción de resistencia de base mediante tecnología *Base Bleed*, así como el estudio de problemas de combustión en secuencias de accidente nuclear. Ambas aplicaciones tienen en común que involucran procesos de combustión hidrógeno-aire en condiciones de flujo turbulento. Para cada una de estas aplicaciones, diferentes metodologías y estrategias numéricas han sido desarrolladas y validadas. Adicionalmente, junto al desarrollo de estos modelos, se proponen metodologías para optimizar el coste computacional con limitado impacto en la precisión de los resultados alcanzados.

La tecnología conocida como *Base Bleed* ha sido, y es, ampliamente utilizada con el objetivo de reducir la resistencia aerodinámica de cuerpos esbeltos mediante la destilación de gases (procedentes de una combustión) en su zona posterior. Los modelos desarrollados en este trabajo permiten estimar el coeficiente de resistencia aerodinámica (C_D) cuando el cuerpo, con unidad de *Base Bleed* (activa o no), posee rotación axial (*spin*) y se considera vuelo cuasi - estacionario en régimen transónico y supersónico (Mach 0.99-1.5). Se han comparado los resultados de varios modelos bidimensionales y tridimensionales con datos experimentales obtenidos mediante técnicas de trayectografía. Los resultados alcanzados evidencian que los modelos de turbulencia RANS y *Detached-Eddy Simulation* (DES) obtienen buenas predicciones de C_D en ausencia de unidades *Base Bleed*. Sin embargo, el efecto de reducción de resistencia provocado por estas no aparece reflejado en las predicciones de C_D calculados con estos modelos de turbulencia. En cambio, con modelos de turbulencia LES, se obtienen predicciones más realistas.

En relación al estudio de procesos de combustión en secuencias de accidente nuclear, estos precisan de simulaciones de combustión premezclada turbulenta en espacios confinados, simulaciones que presentan comúnmente la limitación del elevado coste computacional requerido, así como el reducido número de datos experimentales disponibles para la

validación. De forma general, ciertos modelos de combustión turbulenta basados en RANS han obtenido resultados satisfactorios para predecir parámetros globales de la combustión, pero presentan limitaciones para modelar correctamente algunos fenómenos transitorios, especialmente interacciones dinámicas de los frentes de llama en un medio turbulento y su influencia en la combustión. En este contexto, los modelos de combustión basados en LES se presentan como una alternativa eficiente en términos de coste computacional para analizar secuencias de accidente involucrando la combustión del hidrógeno.

En este trabajo, dos modelos diferentes han sido desarrollados y propuestos para analizar la evolución de la velocidad de combustión de deflagraciones y la interacción de estas en medios turbulentos. Estas estrategias han sido, un modelo de variable de progreso (*Flamelet Progress Variable*, LES-FPV) y otro con modelado de tasa de reacción química de gases multicomponente (*Finite-Rate chemistry model*) denominado *Thickened Flame Model* (LES-TFM) en el que se pretende modelar la interacción entre el mecanismo de cinética química con la turbulencia. Se ha llevado a cabo la validación de estos modelos para predecir fenómenos tales como la velocidad de combustión, aceleración turbulenta y evolución de la presión. Adicionalmente, se han propuesto técnicas para reducir el coste computacional y para hacer abordable su aplicación en problemas industriales, de mayor escala que los ensayos de laboratorio para validación. Estas técnicas incluyen: *Dynamic Adaptive Chemistry* (DAC), *in-situ Adaptive Tabulation* (ISAT) y mallados dinámicos adaptativos. Esta última técnica tiene el objetivo de aumentar la resolución espacial localmente en el frente de llama, manteniendo un coste computacional y tiempos de simulación abordables. Finalmente, se ha aplicado los modelos previamente validados para analizar dos secuencias de pérdidas de vacío en ITER (*Loss Of Vacuum Accident*, LOVA). Con ellos se han obtenido conclusiones relevantes sobre dichos accidentes.

Adicionalmente, otra aproximación basada en la hipótesis de "Reactor Perfectamente Agitado" (*Perfectly Stirred Reactor*, PSR) ha sido propuesta y validada para predicción de variables globales en secuencias de combustión de hidrógeno-aire premezclado. Esta aproximación tiene la ventaja de una menor complejidad desde el punto de vista de modelado, a expensas de requerir un mayor coste computacional, además de presentar una aplicabilidad limitada en determinados regímenes de combustión. Se ha llevado a cabo una validación y evaluación de estos modelos comparando con datos experimentales y con otros estudios numéricos de aceleración de llama en un canal con obstáculos. Los resultados permiten identificar las principales deficiencias a tener en cuenta al utilizar esta aproximación y evaluar las incertidumbres relacionadas con el uso de diferentes modelos de turbulencia *sub-grid scale*.

Por último, se ha desarrollado un modelo, para simular problemas de combustión bifásicos de flujos reactivos en presencia de partículas de grafito a partir de los modelos LES-TFM. La modelización numérica de la combustión turbulenta de mezclas de H_2-aire con partículas sólidas de grafito es un reto clave en muchos problemas industriales, incluyendo el ámbito de la seguridad nuclear. El modelo se basa en una aproximación Euler-Euler acoplada con diferentes cinéticas químicas detalladas para simular la combustión de mezclas de gases y partículas. El modelo se ha empleado para predecir la evolución transitoria de las secuencias de combustión turbulenta de mezclas de H_2, aire y partículas de grafito en condiciones de baja concentración de este último, obteniendo resultados que se ajustan a los experimentales

obtenidos en una bomba esférica. El modelo permite predecir ciertas tendencias experimentales, como la composición de productos de la combustión, mostrando que una baja concentración inicial de partículas de grafito (~96 g/m^3) influye en la dinámica de la combustión del H_2 para mezclas de 20% en volumen de H_2 en aire. En estas condiciones, se aumentaron los niveles de presión alcanzados en las paredes de la esfera y se redujo el tiempo de combustión respecto al caso sin presencia de partículas. Los resultados muestran la viabilidad de utilizar este tipo de modelado para caracterizar parámetros globales como la evolución temporal de la presión en las paredes.

2 Abstract

In this work, *Computational Fluid Dynamics* (CFD) simulations using *Large Eddy Simulation* (LES) turbulence modeling are proposed for analyzing problems where traditionally *Reynolds Averaged Navier Stokes Equations* (RANS) have been extensively used, but with results that did not find good agreement when compared with experimental data. Nowadays, as a consequence of the increase in computational efficiency and power during last years, LES models has become an affordable alternative for being applied on a lot of fluid-dynamics problems even from an industrial perspective.

This work is focused on two problems: external ballistics for slender bodies with drag reduction (*Base Bleed*) units, and nuclear accident sequences. Both problems have in common that involve hydrogen-air combustion processes under turbulent flow conditions. For each application, different approaches have been developed and tested, and methodologies for improving computational cost with low (or not) penalty on the results accuracy have been analyzed and proposed.

Base Bleed technology is a common strategy used for body drag reduction. This work studied analyzes CFD models to estimate the drag coefficient of slender bodies with spin *and Base Bleed* technology under transonic and supersonic (Mach number 0.99–1.5) quasi-steady conditions. 2-dimensional and 3-dimensional numerical models based on RANS, *Detached Eddy Simulation* (DES) and LES models were presented and benchmarked against *ad-hoc* experimental flight measurements performed with both active and inactive *Base Bleed* units. Results show that RANS and DES models predict well the drag coefficient in the absence of *Base Bleed* units. However, they have a very limited accuracy in drag prediction when facing a problem involving a high temperature jet mixing layer with a transonic wake as in the case of active *Base Bleed*. Notwithstanding, a reasonable agreement is found between numerical predictions of drag reduction and experimental data for the case of LES.

On the other hand, the modelling of premixed combustion in three-dimensional confined scenarios is also studied in this work. Accurate modelling of combustion sequences is difficult due to computational costs and the limited *ad-hoc* experiments available to validate the models. RANS based combustion models have shown to be successful in predicting gross features of combustion, nevertheless, they have serious deficiencies to predict transient phenomena, such as combustion instabilities, cycle-to-cycle variations, self-ignition, and pollutant emission. LES seems to be a cost-effective method to reach this goal when analyzing H_2 combustion dynamics in accident sequences. In this work, two different LES models have been proposed and assessed for predicting flame combustion acceleration and interaction in the presence of turbulence: a *Flamelet Progress Variable* (LES-FPV) and a *Thickened Flame Model* (LES-TFM). With the aim of reducing computational costs, *Dynamic Adaptive Chemistry* (DAC) and in-situ adaptive tabulation (ISAT) methods have been exploited when facing detailed kinetic mechanism for hydrogen combustion. Moreover, an adaptive meshing technique was used with the aim of tracking the flame front to ensure an adequate local spatial resolution, where the model requires such level discretization. Experimental validation was performed to assess the ability of the different studied approaches to predict the flame burning speed, flame

acceleration, and pressure evolution for lean H_2-Air volume percent mixtures from 16 to 28% propagating within a turbulent field. Results revealed that both approaches led to accurate predictions in terms of flame burning speed. When considering DAC and ISAT methods with detailed chemistry, LES-TFM model was found to be a cost-efficient solution, which relies less on experimental inputs than the LES-FPV alternative. Once this model has been validated, it is used to analyze two loss of vacuum accident (LOVA) sequences within the *International Thermonuclear Experimental Reactor* (ITER) Vacuum Vessel. Results permitted to get key insights into these accidents.

Additionally, LES turbulence with perfectly stirred reactor (PSR) assumption and detailed chemistry have been also assessed to predict global variables of unsteady, premixed, hydrogen combustion sequences. This approach requires less modeling efforts but increases the need of computational resources and it shows application limitations. The assessment is faced by benchmarking the model with hydrogen-air experimental tests and with numerical data of flame acceleration in an obstructed channel obtained with other models. Results permit to identify major shortcomings that should be addressed with this approach and to assess the uncertainties linked to the use of different sub-models.

Finally, LES-TFM approach have been proposed for modeling two-phase combustion problems to describe reacting flows in presence of graphite particles. The model proposed is benchmarked against experimental combustion data obtained in a spherical bomb. The numerical modelling of turbulent combustion of H_2-air mixtures with solid graphite particles is a challenging and key issue in many industrial problems including nuclear safety. The model relies in an Eulerian–Eulerian approach coupled with different detailed chemical kinetics to simulate the combustion of mixtures of gases and particles. The model is applied to predict the transient evolution of turbulent combustion sequences of mixtures of hydrogen, air, and a low concentration of graphite particles. Results show a good agreement between experimental and numerical data. Moreover, the model is able to predict some key experimental tendencies and reveals that the presence of a low concentration of graphite particles (~96 g/m^3) influences the hydrogen combustion dynamics for mixtures of 20% (in volume) of hydrogen in air. Under these conditions, pressure levels reached at the walls of the sphere are increased and the combustion time is shortened. The results also show the viability of using this kind of models for obtaining global combustion parameters such as the temporal evolution of the wall pressure.

3 Acknowledgements

Firstly, I would like to express my sincere gratitude to my supervisor Prof. Dr. Francisco Javier Sánchez Velasco and co-supervisor Dr. José Serna Serrano for the continuous support during my Ph.D study and related research, for their patience, motivation, and their immense knowledge that they transmitted to me. Besides, I would also like to thank to my mentor Prof. José Ramón García Cascales, who provided me the opportunity to join his team and thus performing this research. Their guidance helped me in all the time of working on this thesis.

In addition, I would like to thank the Prof. Ahmed Bentaib, Prof. Nabiha Chaumeix and Dr. Alexander Bleyer, for providing me the opportunity to perform my pre-doctoral research stay at the *Institute de Radioprotection et de Sûrete Nucléaire* (IRSN), and for their support, which made possible to carry out some of the main work included in this thesis.

My research would have been impossible without the support, patience and comprehension of my girlfriend María.

Particularly to my colleague Francisco Sánchez, who has been always helping and supporting me since we started our degree, encouraging me always to be a better engineer and person. I thank my research colleague Carmen López in for the support and help during our working period during our research.

Last but not the least, I would like to thank my family and friends: my parents and to my brother and sister for supporting me throughout writing this thesis and my life in general.

4 Objectives

The main objective of this thesis consists of developing and validating *Computational Fluid Dynamics* (CFD) models and strategies for being applied and extracting relevant conclusions in key problems where classical *Reynolds Averaged Navier Stokes Equations* (RANS) approaches have been extensively applied, but with several limitations in terms of accuracy when assessed with experimental data. These key problems are external ballistics with *Base Bleed* units and nuclear accident sequences. In both problems, simulations involving hydrogen-air combustion raise as modelling challenges that might help to get insights into the physics of these scenarios. Thus, four specific objectives have been addressed within the context of this main objective.

The first specific objective addressed is assessing the capacity of different RANS, *Detached Eddy Simulation* (DES) and *Large Eddy Simulation* (LES) turbulence models to estimate the drag coefficient of slender bodies with spin and *Base Bleed* technology under transonic and supersonic quasi-steady conditions. Accuracy of the results reached with each numerical strategy is assessed with experimental data.

As a second specific objective, the modelling of premixed combustion in the presence of a turbulent field in three-dimensional (3-D) confined scenarios is studied in this work. Experimental validation is performed to assess the ability of the different studied approaches to predict the flame burning speed, flame acceleration, and pressure evolution for lean H_2-Air volume percent mixtures from 16 to 28 % propagating within a turbulent field. Different numerical strategies to make these model computationally affordable for industrial-scale applications have been studied and implemented. This model is used to analyze two loss of vacuum accident (LOVA) sequences within ITER VV in order to assess the potential impact of the accidents

In third place, LES combustion modelling with perfectly stirred reactor (PSR) assumption and detailed chemistry models are developed to predict unsteady, premixed, hydrogen combustion sequences. This model is benchmarked with hydrogen-air experimental tests and with numerical data of flame acceleration in an obstructed channel, identifying the major shortcomings that should be addressed with this approach and to assess the uncertainties linked to the use of different closure models.

The last specific objective consists of extending the gas-monophase models previously developed to implement an Eulerian–Eulerian model approach based on the resolution of the Navier–Stokes equations via LES coupled with a system of ordinary differential equations (ODEs) of the detailed chemical kinetics to simulate the combustion of mixtures of gases and particles. The proposed model was applied to predict the transient evolution of lab-scale turbulent combustion sequences of mixtures of hydrogen, air and graphite particles under low concentration conditions, assessing thus the capabilities and level of agreement when compared to experimental data.

5 Introduction and state of the art

Turbulence modelling has been traditionally one of the most challenging problems in CFD. *Direct Numerical Simulation* (DNS) is currently far from being computationally affordable in most of the industrial problems due to the required computational cost. RANS modelling has been an extensively used approach, but the level of accuracy reached is often not good and some key aspect of the flow phenomena can neither be captured nor predicted by these models in some specific problems[1]. Modelling the effects that Base Drag reduction devices produce in the wake flow, as the *Base Bleed* units, is a common problem in which RANS simulations have not been providing accurate results[2-5].

In addition, post-combustion of the gases produced by the *Base Bleed* propellants also plays some role in this problem, adding even more complexity to the problem[6,7]. In this context, Premixed and Partially-Premixed combustion problems are also a common application where RANS approaches have been extensively applied, but presenting limitations that belong intrinsically to the formulation of this kind of turbulence approach[1]. The improvements in the computational resources in the last two decades have made LES a promising alternative to DNS and RANS, being placed between both approaches in terms of computational cost, but improving the accuracy and turbulent unsteadiness phenomena that it is captured by the simulated flow fields when compared with RANS computations.

In this thesis, this turbulence modelling is analyzed and applied for studying two different problems: external ballistics including base drag reduction units and hydrogen-air turbulent combustion modelling analysis. It is worth mentioning both problems have in common that RANS numerical simulations have been extensively employed, but with the problem or reporting not accurate enough results when assessed with experimental data. This context motivated the work carried out in this thesis.

Base Bleed is a widely used technology consisting of injecting a flow behind the base of a body with the aim or reducing the aerodynamic drag by means of increasing the base pressure. This injecting mass-flow is usually generated by the combustion of a propellant present in some device located close to the base of the body. In contrast to the effect produced by rocket devices, it does not generate thrust, but the net flight range of the body is considerably increased by reducing the net drag, since the pressure difference between the front and the base of the body is partially reduced.

Due to the limited amount of propellant available at the *Base Bleed* units, the base gas injection last only for a certain period of time which is expected to cover, at least, the supersonic regime of the flight. This regime is the first that the body affords during its flight. After that, the body suffers a transonic transition in which the wave drag results in a maximum drag coefficient at around Mach number Ma=1.05. At the end of the flight time, the body enters into the subsonic regime resulting in a reduction of the drag coefficient. At this last stage, the body may undergo a rich sequence of transitions during its deceleration. The accuracy of the aerodynamic model of the body is of outstanding importance for external ballistics, permitting for example, predicting the range and trajectory of artillery projectiles.

A wide variety of published works related to numerical modelling of the drag reduction using this technology demonstrated that turbulence modelling is a key aspect to predict properly wake flow, and thus the base pressures, needed for calculating the efficiency of these units in terms of flight range enhancement. A wide amount of studies focused on simulating the wake region of a slender body, pointing that turbulence modeling is one of the main focused topics when discussing the results accuracy [2-5], The predicted pressures dependency on the turbulence modelling has been demonstrated to be particularly true when the *Base Bleed* effects on the wake is included [8]. This is still an open issue to be faced for precisely predicting the *Base Bleed* reduction drag by means of computational simulations.

On the other hand, the modelling of unsteady premixed combustion in the presence of a turbulent field in three-dimensional scenarios under different conditions is also studied in this thesis. Whereas RANS based combustion models have been successful in predicting gross features of combustion, they have difficulties to predict transient phenomena, such as combustion instabilities, cycle-to-cycle variations, self-ignition, and pollutant emission[1]. In this manner, LES based combustion models are a promising alternative, demonstrating abilities that can be used to predict such flow unsteadiness, being a cost-effective method to reach this goal when analyzing hydrogen combustion dynamics in accident sequences.

Nowadays, accurate modeling of hydrogen combustion on accident sequences in confined scenarios is difficult due to computational costs and the limited ad-hoc experiments available to validate the models. When it comes to validation, turbulence and chemistry are key topics [9]. Modeling of these processes together is highly desirable in many high-Reynolds-number problems, to obtain realistic predictions from the numerical results. A realistic description of this type of combustion sequences requires the model to take into account several important flow mechanisms. Flow instability and wall interaction are key aspects of gas combustion dynamics playing an important role in flame acceleration or quenching.

The non-linearity of the advection process leads to instabilities making the flow unsteady and three dimensional (3D). These instabilities, linked with the vortex dynamics, are some of the dominant flow mechanisms leading the combustion dynamics. During acceleration, interactions between the flame front and the reflections of pressure perturbations in walls and obstacles might enhance heat release rate and vorticity generation due to Richtmyer-Meshkov instability [10-11]. Several investigations [11], showed that stretching of the flame front due to the interaction with a non-uniform velocity field is one of the main causes of the flame acceleration. Therefore, to obtain a proper prediction of a combustion sequence, correct modeling of turbulence is essential. For problems with high Reynolds number, DNS is still a prohibitive approach due to the required computational cost. On the contrary, LES is currently presented as an option that provides results with reasonable accuracy for turbulent combustion[12]. Some of the finite-rate combustion approaches to overcome this problem which can be found within the LES framework are: the Implicit LES (ILES)[13-18], the *Thickened Flame Models / Artificially Thickened Flame* models (TFM / ATF)[19], the *Partially Stirred Reactor* (PaSR) models[20] or the combustion modeling based on the *Eddy Dissipation Concept* (EDC) [21]. It is also worth citing other models such as the LES *Conditional Moment Closure* (CMC), that uses conditionally averaged species equations [22], the *Linear Eddy Model* (LEM) which is based on solving 1D problems with high resolution meshes to obtain data required to model the sub-

grid variables involved in LES of a 3D problem[23] or *Probability/Filtered Density Function* (PDF/FDF) models [12]. In the case of reacting flows, not only the small eddies have to be modelled, but also the filtered mixing and some chemical source terms require closure modelling since the reaction zone is often not well resolved on LES grids.

In this context, in this thesis it is analyzed, developed and validated some of the available combustion models for applications of hydrogen combustion sequences under different conditions, studying their performance, capabilities and model limitations. This way, a key tool has been developed and validated to be applied in future analysis of ITER or other nuclear safety scenarios.

In addition to turbulent monophase gas combustion problems, the numerical modelling of turbulent combustion of H_2–air mixtures with solid graphite particles is a challenging and key issue in many different fields, including industrial combustors, pollutant emissions, solid propellants or accident prediction and mitigation. In this last field, prediction of particle behavior with and without combustion is a key topic in nuclear power plants as well as in fusion reactors such as the ITER. In this case, the presence of particles might influence the combustion dynamics during a potential accident. Therefore, it is of outmost importance to properly predict the effects of this type of turbulent combustion sequences in presence of solid particles. Among the technological applications of this combustion scenario, it can be cited the ITER "old design" where graphite wall were considered, nuclear safety sequences in presence of H_2, CO and CO_2 and the design of energetic materials for rocket propulsion systems with drag reductions units. In order to be able to include in the computations the effects of this solid graphite particles, a two-phase model is developed, being derived from the LES-TFM previously validated. This model was proposed to describe this reacting flow with LES and detailed chemistry. The model proposed was benchmarked against experimental combustion data obtained in a spherical bomb.

6 Articles

6.1 On the accuracy of RANS, DES and LES turbulence models for predicting drag reduction with Base Bleed technology

In this work, a numerical study using the commercial software *ANSYS-Fluent® 14* focused on analyzing the different wake flow and accuracy of the predicted body drag coefficients is presented. Thus, it is assessed the capacity of different RANS, DES and LES models to estimate the drag coefficient of slender bodies with spin and *Base Bleed* technology under transonic and supersonic (Mach number 0.99-1.5) quasi-steady conditions.

An extensive state of the art is also included, where it has been found that a repeated and accepted conclusion: RANS and DES models, which is an hybrid approach between RANS and LES, have very limited accuracy in drag prediction when facing a problem involving a high temperature jet mixing layer with a transonic wake as in the case of active *Base Bleed*. Notwithstanding, LES has been proposed as an improvement for simulating these *Base Bleed* effects.

2-dimensional and 3-dimensional numerical models based on RANS and DES with *k-ε RNG*, *k-ω Standard* and *k-ω SST*, as well as LES *Smagorinsky-Lilly*, *Wall Adapting Local Eddy* (WALE) and *Dynamic sub-grid Kinetic Energy Equation* models were described and presented and benchmarked against ad-hoc experimental flight measurements performed with both active and inactive *Base Bleed* units.

Due to the coupling between the internal *Base Bleed* pressure and the external body airflow pressure, the numerical simulation of the space within the Base Bleed cavity is recommended in order to predict the drag coefficient under the flow regimes without chocked conditions at the nozzle of the *Base Bleed* unit. Results showed that RANS and DES models had good accuracy for predicting drag for the case of inactive *Base Bleed* simulations. On the contrary, these models had very limited accuracy in drag prediction when facing a problem involving a high temperature jet mixing layer with a transonic wake as in the case of active *Base Bleed*. Notwithstanding, a reasonable agreement was found between numerical predictions of drag reduction and experimental data for the case of LES WALE. Overall, LES was found to have a better prediction capacity than RANS and DES. WALE LES was found to be the best turbulence model to predict drag coefficient with an average absolute error of 4.4%. The use of DES models (*Real k-ε*, *SST k-ω*) is not recommended as they provide drag coefficient average prediction errors over 23%, but requiring more computational cost than RANS approaches.

On the accuracy of RANS, DES and LES turbulence models for predicting drag reduction with Base Bleed technology

Nicolás-Pérez F.*
Universidad Politécnica de Cartagena, Cartagena, Spain, 30202

Velasco F.J.S.
University Centre of Defence at the Spanish Air Force Academy, MDE-UPCT, San Javier, Spain, *30720*

García-Cascales J.R.
Universidad Politécnica de Cartagena, Cartagena, Spain, 30202

Otón-Martínez R.A.,
EXPAL Systems S.A., Madrid, Spain, 28042

López-Belchí A.
University Centre of Defence at the Spanish Air Force Academy, MDE-UPCT, San Javier, Spain, *30720*

Moratilla. D, Rey. F, Laso A.
EXPAL Systems S.A., Madrid, Spain, 28042

ABSTRACT

Base bleed technology is a common strategy used for body drag reduction. This work assessed the capacity of different RANS, DES and LES models to estimate the drag coefficient of slender bodies with spin and Base Bleed technology under transonic and supersonic (Mach number 0.99-1.5) quasi-steady conditions. 2-dimensional and 3-dimensional numerical models based on RANS and DES with k-ε RNG, k-ω Standard and k-ω SST, as well as LES Smagorinsky-Lilly, Wall Adapting Local Eddy (WALE) and Dynamic sub-grid Kinetic Energy Equation models were presented and benchmarked against ad-hoc experimental flight measurements performed with both active and inactive Base Bleed units. Results showed that RANS and DES models had very limited accuracy in drag prediction when facing a problem involving a high temperature jet mixing layer with a transonic wake as in the case of active Base Bleed. Notwithstanding, a reasonable agreement was found between numerical predictions of drag reduction and experimental data for the case of LES WALE.

*corresponding author: francisco.nperez@upct.es, Research engineer, *Universidad Politécnica de Cartagena, Dr. Fleming s/n, Cartagena, Spain, 30202*

1. INTRODUCTION

The injection of a low velocity fluid behind the base of a body is known as Base Bleed technology. It is a commonly used strategy to reduce the drag force in slender bodies. The objective is not the generation of an additional thrust, but the reduction of the actual drag by increasing the pressure at the base of the body through the injection of a gas mass flow rate generated by the combustion of a propellant located at the Base Bleed unit. By this injection, the average pressure in the wake of the body increases and therefore the net drag component due to the pressure difference between the front and the base of the body is partially reduced and the body range is considerably increased.

Due to the limited amount of propellant available at the Base Bleed unit, the base gas injection last only for a certain period of time which is expected to cover, at least, the supersonic regime of the flight. This regime is the first that the body affords during the flight time. After that, the body suffers a transonic transition in which the wave drag results in a maximum drag coefficient at around Mach number Ma=1.05. At the end of the flight time, the body enters into the subsonic regime resulting in a reduction of the drag coefficient. At this last stage, the body may undergo a rich sequence of transitions during its deceleration[1] .The accuracy of the aerodynamic model of the body is of outstanding importance for predicting, for example, the trajectory of artillery projectiles. Under these conditions, it is important to assess the ability of Reynolds Average Navier Stokes (RANS) based models and Detached Eddy Simulation (DES) and Large Eddy Simulation (LES) models to predict the behaviour of a body during its complete time of flight.

The coupling of RANS equations with the Boussinesq hypothesis is a usual approach when computing statistically averaged mean quantities of turbulent flows [1]. Among the turbulence models used in the Boussinesq approach, the k-ε and k-ω models are the most commonly used to deal with “industrial” problems. They are considered to be a suitable compromise between robustness, accuracy and, no less important, computational cost. In general terms, this approach is considered to give satisfactory results when dealing with flows in which turbulent fluctuation scales are small and the mean flow can be considered as steady. In this work it is analysed the ability of RANS and DES with k-ε RNG, k-ω Standard and k-ω SST, turbulence models, as well as LES Smagorinsky-Lilly, LES WALE and LES Dynamic ksgs-Equation to estimate drag coefficient in the case of bodies with Base Bleed unit under transonic and supersonic conditions. This evaluation is performed through the simulation of different body flights regimes and compared with experimental data. A compressible,

steady state configuration with zero angle of attack was chosen to simulate de flight conditions. Experimental data was obtained from firing tests performed with an artillery gun.

The paper is structured as follows: firstly it is described the state of the art in the drag prediction of bodies with Base Bleed with CFD (computational fluid dynamics) codes. Then, the numerical model used is presented. Later, the numerical simulations of the reference base case are validated against experimental data and the influence of the different numerical strategies is assessed. The parameters analysed include the solver (pressure based vs. density based solver), grid configuration, turbulence model, combustion gases molecular weight, propellant burning front temperature, and Base Bleed mass flow rate. Finally, the paper summarizes the main conclusions of the study.

2. STATE OF THE ART

In the scientific literature, there are several studies related to CFD drag prediction of bodies with Base Bleed units. They were initiated with the first works of Sahu [1]-[3]. Among the available works, it is worth citing Regodic et al. [4]. They presented a numerical study on the prediction of the drag reduction in projectiles with and without Base Bleed units. Their simulations accounted for the full projectile shape what ensures the estimation of the skin friction, pressure and base drag components for different flight conditions. In that case, the experimental data obtained in a supersonic wind tunnel for the case of boat tail configuration (i.e. no Base Bleed unit) was used for validation. They reported a maximum relative error between experimental and numerical data of about 23%. The numerical code used was not reported in the work. As for the study of the Base Bleed case, the Base Bleed cavity was not directly resolved in the simulations. On the contrary, its effect was simulated by the injection of a gas mass flow at the base of the projectile. This flow injection was performed with a uniform spatial velocity profile along the base of the projectile. The mass flow rate injected was obtained from a burning rate model of the pyrotechnic grain mixture used in the gas generator. Regarding the turbulence model, the Spallart-Allmaras viscous model was used. Numerical results show five different simulations with different projectile diameter, boat tail length, propellant grain diameter, and grain area. The numerical predictions reported assess an effective axial aerodynamic drag reduction that ranges between 13% and 38% depending on the projectile geometry and the Mach number regime.

Suliman et al. [5] studied the drag influence of the boat tail angle in a 155mm artillery projectile with Base Bleed unit using a commercial CFD software. As in the previous study, the Base Bleed cavity was not modelled. Its effect was simulated by the injection of a certain gas mass flow rate at the base of the projectile. The authors concluded that the optimal angle for drag reduction with Base Bleed unit was close to 9.5º. No validation of the Base Bleed simulations was provided in this work. Under these conditions, they predicted an effective drag reduction that rounds 13% when Base Bleed unit was active.

Kaurinkoski et al. [6],[7] performed a detailed study of the influence of the combustion modelling on the wake flow field. They developed an ad-hoc CFD code based on finite volumes to solve the flow field and the coupled combustion process within the Base Bleed unit. It accounted for an updated k-ε model for modelling turbulence. Their results showed that a simple reaction model is sufficient to reproduce the main effects of base combustion. They also studied the influence of the shape of the projectile's base in the predicted flow field. The results presented did not accounted for the resolution of the flow field within Base Bleed cavity. They simulated its effect through the injection of a gas mass flow at the base. No validation was provided for flight conditions.

Base pressure prediction is a key issue when facing drag estimation in supersonic regime of slender bodies with base bleed and CFDs. Simons et al. [8] highlighted the difficulties of RANS and DES turbulence models to predict base pressure due to the presence of a flow instability in the shear layer behind the base of the body. This instability generates 3D flow structures with additional numerical eddy dissipation in the simulations. In addition, RANS models are tuned to incompressible subsonic flows and need also to be tested in the case of compressible flows. To face these shortcomings they propose the use of hybrid methods such as MILES [9] or ZDES [10]. The computational domain studied by Simons et al. [8] was limited to the base of the projectile. Neither the projectile head, nor the combustion chamber of the base bleed unit were included in the domain. The results were validated against base pressure experimental data obtained in the case of non-reactive base flow and no body spin in a supersonic wind tunnel at Mach 2.47 by Mathur, Herrin and Dutton [11]-[14]. The benchmark of the simulations shows that RANS methods are not able to correctly predict base pressure due to the overestimation of the production of turbulent kinetic energy for these flow conditions. In the case of slender bodies with boat tail and without base bleed, Sivasubramanian et al. [15] conclude that hybrid DES methods are able to predict correctly base pressure under compressible conditions even in the case of 2D axisymmetric simulations. Shin et al. [16],[17] used DES and LES to study the effect of different filter parameters of the models on the prediction of Herrin and Dutton [14] data. They also assessed the effect of the mesh size on the prediction of wake vorticity. In opinion of the authors, further work is needed to extend the benchmark of

turbulence models to the case of experimental data under transonic conditions with reactive base flow and body spin.

Finally, it is worthwhile to cite the work of Yu et al. [18] who used commercial CFD software to estimate the influence of nozzle geometry at the base bleed unit on the base pressures. Simulations were performed with a 2D axisymmetric model and a k-ω turbulence model. The computational domain studied was limited to the base of the projectile. Neither the projectile head, nor the combustion chamber of the base bleed unit were included in the domain. They found that base pressure in the case of an annulus nozzle is higher than that of a circular nozzle. This effect is more important as the mass injected increases.

3. COMPUTATIONAL APPROACH

This section describes the physical and numerical models chosen for the present study. RANS under steady state, as well as the unsteady DES and LES formulations were used. Its fundamentals are briefly described in this section. Additionally, an "a-priori" analysis of the capabilities of the turbulence models based on the literature reviewed is also presented.

3.1. GOVERNING EQUATIONS AND TURBULENCE MODELS

The equations considered in this study for a compressible fluid flow were:

$$\text{Continuity:}\quad \frac{\partial \rho}{\partial t} + \frac{\partial (\rho u_i)}{\partial x_i} = 0 \tag{1}$$

$$\text{Momentum:}\ \frac{\partial (\rho u_i)}{\partial t} + \frac{\partial (\rho u_i u_j)}{\partial x_j} = -\frac{\partial p}{\partial x_i} + \frac{\partial}{\partial x_j}\tau_{ij} \tag{2}$$

$$\text{Energy:}\ \frac{\partial}{\partial t}\left[\rho\left(e + \frac{V^2}{2}\right)\right] + \frac{\partial}{\partial x_j}\left[\rho u_j\left(e + \frac{V^2}{2}\right) + p + q_j - u_i\tau_{ij}\right] = 0 \tag{3}$$

Note that, u denotes instantaneous, velocity, V velocity modulus, ρ gas density, p gas pressure, q_j heat flux and τ_{ij} viscous stress tensor. In addition, perfect gas equation of state was considered. As for the closure of the system, RANS-based, two equations, turbulence models as well as LES and DES turbulence models were considered. Regarding RANS-based, two equations, turbulence models, RNG k-ε, Realizable k-ε, Standard (Wilcox) k-ω and SST k-ω models were tested. Default constant values were employed for these models.

It is well known that, Standard k-ε model has some deficiencies when it is applied to shear flow problems such us, the prediction of the size of the recirculation bubble in a backward facing step or to the separation point in the simulation of flow impingement [19]. The RNG (re-normalization group) k-ε model [20]-[22] was a refinement of the Standard k-ε model which, according to its authors, was specially defined for enhancing accuracy in the case of rapidly strained and swirly flows. Monpean [23] compared the flow prediction of the RNG k-ε model to DNS and experimental measurements in the case of a straight square duct, involving secondary motion at Reynolds number 4400. He showed that mean velocity values obtained with the RNG k- ε model were predicted exactly at the same position when compared with DNS. However, the secondary flows were unpredicted for the case of the strongest velocities. As for drag coefficient prediction at high Reynolds numbers, Lee [24], compared RNG k- ε model with LES and experimental data at Reynolds number $2.2 \cdot 10^4$. He found that RNG k- ε model successfully reproduce the unsteady force coefficients for turbulent flows over a square cylinder. However, relatively high temporal accuracy, spatial accuracy and high-order convection scheme were required for a proper prediction as the results were quite sensitive to the spatial resolution and the choice of convection schemes. These results permitted to identify this model, and its extensions, as potentially suitable turbulence models for estimating drag coefficient in the present work.

Realizable k-ε model is one of the modifications of the previous model. According to its authors [25],[26], this model was tuned to predict flow conditions in problems involving rotating homogeneous shear flows, boundary-free shear flows such as mixing layers, planar and round jets, channel flows, flat plate boundary layers with and without a pressure gradient and backward facing step separated flows. They were tuned against, DNS, LES and experimental data at medium Reynolds numbers and low mach numbers. In the problem under study in the present work, body spin introduce an additional rotating shear flow which must be properly predicted by the turbulence model. Based on Shih et al. [26] indications, Realizable k-ε model seems to be able to predict this flow conditions. However, additional results from different authors [22],[27], concluded that these models are recommended for free-shear layer flows with low pressure gradients, reducing their accuracy when pressure gradient is increased.

Standard k–ω model [28] considers a transport equation for the specific dissipation ($\omega = k/\varepsilon$) which determines the scale of the turbulence. This model predicts the behaviour of attached boundary layers in adverse pressure gradients more accurately than k-ε models [27]. It also shows good behaviour in the prediction of round-jet or plane-jet flows [29] or the skin friction coefficient in a backward facing step at Reynolds number $Re=3.7 \cdot 10^4$

[30]. In the case of supersonic flows, Wilcox [31] showed using the perturbation methods, that the k–ω models can efficiently capture the compressible law of the wall. Actually, the main advantage of the k-ω models over the k-ε- model is the way in which ε and ω are specified on the boundary surface. For k-ε models, zero normal gradient to the wall for ε is specified on the boundary. This boundary condition is very robust but it seems not to have an experimental support. However, for the k- ω models, ω at the wall is prescribed in terms of the equivalent sand-grain roughness height. This formulation for ω on the rough boundary is based on experimental data of the sublayer flow obtained for incompressible flow over rough surfaces [32]. Its validity for compressible flow was also reviewed by Sharif and Guo [33]. They showed that for smooth surface, k–ω models perform very well in predicting the mean flow and turbulence quantities. For rough surfaces, these models matched the experimental data fairly well for lower roughness heights but performed unsatisfactorily for higher roughness conditions. The SST k–ω model [34]-[36] includes a cross-diffusion term in the ω equation which leads the blending of the standard k-ε and k-ω models. The SST model is characterized by an advanced near-wall treatment that automatically switches between the low and high Reynolds number formulation. In this case, Standard k–ω model is applied in the inner region of the boundary layer, and it is supplemented with the less demanding Standard k–ε modelling the outer part of the boundary layer. Bardina et al. [27] extensively tested and validated two-equation eddy viscosity models and showed a better performance of the SST k–ω model in complex flows with boundary layer separation. A major feature of the SST k–ω model is the consideration of the main turbulent shear stress transport, which enables to predict adverse pressure gradients. This was key point in the flow configuration that was expected in the present application. These results identified these turbulence models, as additional “a-priori” candidates with potential capabilities to properly simulate the base flow problem studied in this work. A more detailed descriptions of the expressions used in these models may be found in [27], [28],[35].

The previous models are, in general terms, not able to provide any information about the unsteadiness nature of turbulence of these flows. On the other hand, LES and DES turbulence models are well adapted to handle massive separated flows or free shear layers encountered on flows around the base of a body.

LES is a widely used technique where the large scale field is solved directly from the filtered local volume-averaged Navier Stokes equations (Favre averaged Navier Stokes equations), whereas the small scale stresses are solved through the subgrid-scale model. Small scales are less dependent on the geometry, and for this reason, it is easier to find a universal turbulence model for these scales. Thus, LES is between Direct Numerical

Simulation and RANS in terms of the fraction of the resolved scales. In addition to increasing the computational cost, LES requires substantially finer meshes than those used for RANS. Besides, LES has to be run for a sufficiently long flow-time to obtain stable statistics of the flow being modelled. As previously said, small scales have a dissipative effect, and it is assumed a Boussinesq approximation in addition to a Subgrid-Scale Model (SGS) [37] to compute the subgrid-scale turbulent stresses. Three different LES models were employed for the simulations.

The first one is the Smagorinsky-Lilly model, where the eddy-viscosity is modelled as: $\mu_t = \rho {L_S}^2 |\bar{S}|$. L_S is the mixing length for subgrid scales, computed as $L_S = \min(kd, C_S V^{1/3})$ where k is von Kàrman constant, d is te distance to the closest wall and $V^{1/3}$ is the local grid scale, calculated from the cell volume and. C_S is the Smagorinsky constant, which is set to 0.1. The second LES model used in this work was the Wall-Adapting Local Eddy-Viscosity (WALE) model [37]. It is also based on Eddy-viscosity models and it is designed to return the correct wall asymptotic (y^3) behaviour of wall bounded flows. In this case, the eddy-viscosity is calculated as:

$$\mu_t = \rho {L_S}^2 \frac{\left({S_{ij}}^d {S_{ij}}^d\right)^{3/2}}{\left(\bar{S}_{ij}\bar{S}_{ij}\right)^{5/2} + \left({S_{ij}}^d {S_{ij}}^d\right)^{5/4}} \tag{4}$$

Where now L_S in this case is calculated by $L_S = \min(kd, C_w V^{1/3})$ and ${S_{ij}}^d = \frac{1}{2}\left({\bar{g}_{ij}}^2 + {\bar{g}_{ji}}^2\right) - \frac{1}{3}\delta_{ij}{\bar{g}_{kk}}^2$

$\bar{g}_{ij} = \frac{\partial \bar{u}_i}{\partial x_j}$. The C_wWALE constant was set to a value of 0.325. The third model used is the dynamic sub-grid scale kinetic energy model (Dyn. k_{sgs}-Eqn.) [38][39]. In this case, turbulence is modelled by accounting for the transport equation of the subrgid-scale turbulence kinetic energy, k_{sgs}, defined as:

$$k_{sgs} = \frac{1}{2}(\overline{{u_k}^2} - {\bar{u}_k}^2) \tag{5}$$

The subrgid-scale turbulence kinetic energy is calculated by solving its transport equation:

$$\rho \frac{\partial \bar{k}_{sgs}}{\partial t} + \rho \frac{\partial \bar{u}_j \bar{k}_{sgs}}{\partial x_j} = -\tau_{ij} \frac{\partial \bar{u}_i}{\partial x_j} - C_\varepsilon \rho \frac{{k_{sgs}}^{3/2}}{\Delta_f} + \frac{\partial}{\partial x_j}\left(\frac{\mu_t}{\sigma_k}\frac{\partial k_{sgs}}{\partial x_j}\right) \tag{6}$$

This equation is known as SGS kinetic energy equation. Menon & Kim [40] showed that using the SGS kinetic energy equation yields better performance in large-eddy simulations of incompressible flows. In [39], this idea was extended to compressible flows. This is the final approach that was used in this work. For this model, the

subgrid-scale eddy viscosity, μ_t, is computed using k_{sgs} as $\mu_t = C_k \rho {k_{sgs}}^{1/2} V^{1/3}$. Thus, the subgrid-scale stress can be written as:

$$\tau_{ij} - \frac{2}{3}\rho k_{sgs}\delta_{ij} = -2C_k \rho {k_{sgs}}^{1/2} V^{1/3} \overline{S_{ij}} \quad (7)$$

In the three LES models used in this work, default values were set for the model constants. Again, it is worth to be noted that the dynamic k_{sgs}-Eqn turbulence model was developed to satisfy flow conditions with compressible flow conditions [39], in contrast with the Smagorinsky-Lilly and WALES LES model also used in this work.

DES approach, also known as the hybrid LES/RANS, was first proposed by Spalart et al. [41]. It combines the best features of RANS and LES models. The LES region is associated with the core turbulent region, where DES recovers LES subgrid models. In the near-wall region, the respective RANS models are recovered. According to their authors [41], DES is appropriate for high Reynolds number wall bounded flows, due to the computational cost of the LES models in the near-wall region. For the simulations carried out in this work, two different DES models were employed. Realizable k-ε based DES model and SST k-ω based DES models. The Realizable k-ε based DES model rely on the RANS Realizable k-ε model, with the exception of the dissipation term in the *k* equation. In the DES case, this term is calculated as $Y_k = \frac{\rho k^{3/2}}{l_{DES}}$, where $l_{DES} = \min(l_{RKE}, l_{LES})$, $l_{RKE} = \frac{k^{3/2}}{\varepsilon}$ and $l_{les} = C_{DES}\Delta_{MAX}$. In this last equation C_{DES} is a calibration constant, which was set in this work to the default value of 0.61 and Δ_{MAX} is the minimum local grid spacing. In SST k-ω based DES model [42][43], the dissipation term is defined as $Y_k = \rho\beta^* k\omega F_{DES}$, where $F_{DES} = \max\left(\frac{L_t}{C_{DES}\Delta_{MAX}}, 1\right)$. Menter et al. [44] showed that the SST k-ω model could fully resolve the viscous sublayer at a y+ value of approximately 1. This feature also made the SST k-ω model a popular option for DES. As previously indicated, DES methods are able to predict correctly base pressure under tunnel compressible conditions (Mach 2.47) with non-reactive base flow and without body spin [15]. Shin et al. [16],[17] used DES and LES to study the effect of different filter parameters of the models on the prediction of the same experimental conditions [14]. They also assessed the effect of the mesh size on the results prediction hence on the drag prediction. In light of these results, Realizable k-ε based DES model and SST k-ω based DES models were also identified in this study as potential suitable models for the transonic problem with body spin studied in this work.

3.2. HYPOTHESIS AND BOUNDARY CONDITIONS

A steady state problem was considered for the computations. Despite the body flight was a transient process, the characteristic time of variation of the boundary conditions was considered bigger than the characteristic residence time of the fluid particle within the domain. This means that the transient terms in the mass, momentum, and energy conservation equations were negligible compared to the convective terms (i.e. Strouhal number St <<1). Therefore, the simulations were performed considering steady state boundary conditions for different flight conditions: flight Mach number, Base Bleed propellant burning surface and the atmospheric pressure and the temperature at the flight altitude. These atmospheric conditions, considered as stagnation conditions, were corrected by International Standard Atmosphere models from the radar altitude atmospheric conditions. This way, different flight conditions cases were simulated to obtain the body drag coefficient at different Mach numbers. For turbulence variables, 2% of turbulent intensity and 0.001m of turbulent length scale were imposed at the far field regions. The fluid considered in the simulations was air and combustion gases. In both cases, the ideal gas assumption was used. Constant values were assumed for heat capacity and Sutherland law for variable dynamic viscosity was used due to the high temperature ranges encountered in the problem studied, especially in the Base Bleed on configuration.

As for the boundary conditions, the body was assumed to fly under zero angle of attack with a constant swirl velocity by considering rotating moving walls. All the walls were considered to be adiabatic. The flow field was considered compressible and the far field condition was imposed at the external boundary, where the flight Mach, pressure and temperature (stagnation values) were introduced. The entire domain was initialized with these far field conditions.

Regarding the propellant combustion at the Base Bleed unit, a simple approach was considered. This combustion process was modelled as a solid surface which was injecting a gas mass flow rate, normal to this surface and at a certain fixed temperature. The temperature and mass flow rate values were obtained from the propellant combustion data. The mass flow rate of combustion gases was estimated to be constant during the flight, the temperature of the propellant burning surface was estimated with static experimental combustion tests and simulations with the help of IBHVG2 code [45]. The injection of gas mass flow rate was considered to be uniform and normal to the propellant burning surface, adding an azimuthal velocity component corresponding to the contribution of the swirl movement. This surface was considered to be axisymmetric and parallel to the symmetry axis of the body.

3.3. BODY GEOMETRY AND BASE BLEED UNIT MODEL

An example of the simplified geometry of the body modelled in this work can be found in Fig. 1.

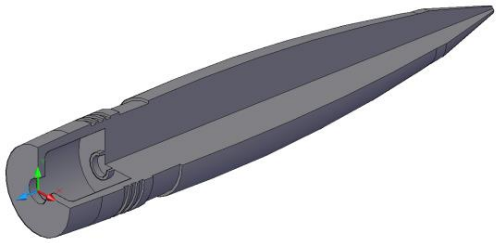

Fig. 1 Example of the body modelled. [46]

In the analysed literature, most authors studying drag reduction with Base Bleed units did not resolve the flow field within the Base Bleed cavity. However, the authors considered that the resolution of the flow field in this region was an important aspect that should be taken into account in the computations due to the fact that the flow was subsonic in the Base Bleed cavity. This resulted in a direct influence on the body wake region and thus on the drag estimation when chocked conditions were not reached at the nozzle of the Base Bleed unit. Therefore the modelling of the Base Bleed unit in these simulations accounted for the simulation of the full body shape as well as for the resolution of the Base Bleed cavity. As for the space considered in the simulations, the domain modelled extends from 5 times the body length ahead of the head fuse to 14 times the body length behind the body base surface. The diameter of the meshed domain was 3.1m, equivalent to 29.5 times the body nominal diameter. Fig. 2 shows an example of the spatial domain simulated during the computations. The figure corresponds to the grid used for the final burning point case, which only differed from the other grids in the internal Base Bleed cavity, being the external domain identical for each case simulated:

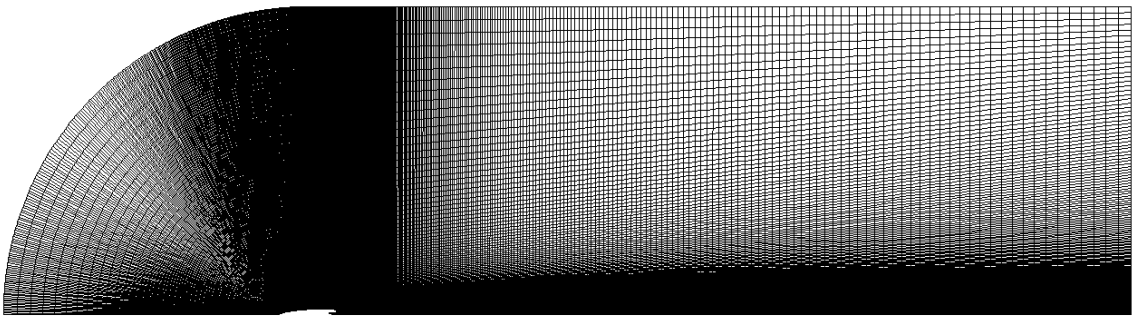

Fig. 2 Example of a grid used in the 2D computations.

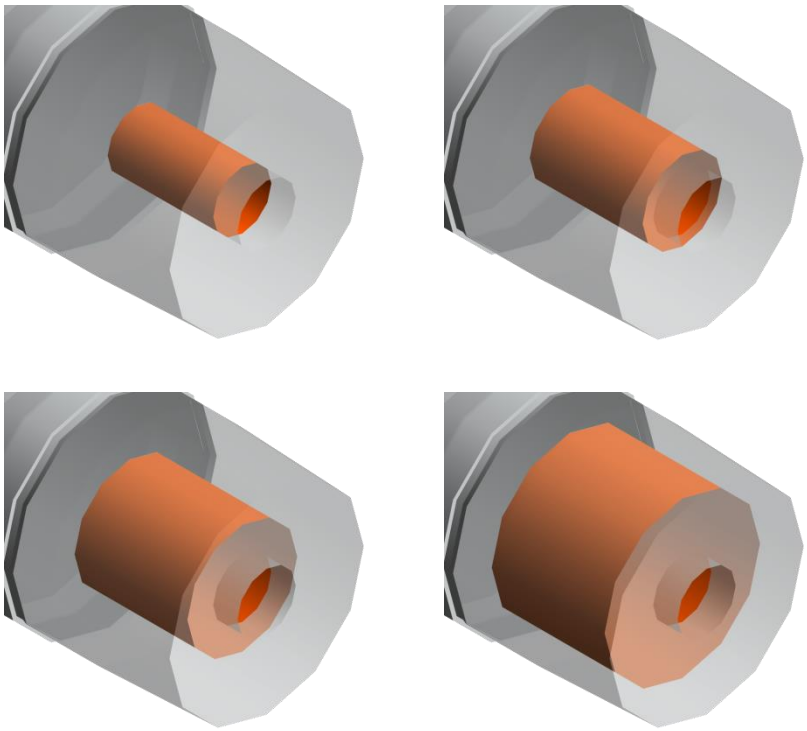

Fig. 3 Different Base Bleed propellant burning surfaces.

As previously said, the Base Bleed propellant burning surface was considered to be a solid surface with a perpendicular injection of gas mass flow at a certain temperature. The spatial configuration used for the simulation of the Base Bleed propellant burning surface is shown in Fig. 3. The top-left picture shows the case of initial flight conditions (when the Base Bleed propellant starts to burn). The bottom-right picture shows the case of final flight conditions (when the Base Bleed propellant was consumed). This last case was also the

configuration used for the cases of no active Base Bleed unit. The other pictures correspond to intermediate conditions.

In case of RANS and DES turbulence models, the final mesh used for the validation corresponds to that shown in Fig. 2. It was a structured bi-dimensional mesh with 249513 quadrangular elements and the maximum skewness factor of the mesh elements was less than 0.41. The average y^+ of the grid used had an average value of 13 for the highest Mach case studied. The meshes used in all the cases studied was the same both upstream and downstream the body and it only differed in the resolution of the domain within the base cavity, which depended on the burning point (Fig. 3). This way the influence of different parameters such as the turbulence model could be assessed with grid independence. The mesh corresponding to the start burning point had 243713 elements, being the lowest number element mesh, whereas the intermediate burning points had intermediate values between this and the consumed point meshes, having the same maximum skewness value in all cases. Due to the symmetry of the problem, both 2-dimensional (2D) axis-symmetric and 3-dimensional (3D) simulations were performed. It is worth noting that the 3D mesh was generated as a revolution of the 2D one, in order to ensure its similarity. Twelve ($N_{\Theta 12}$) and twenty four ($N_{\Theta 24}$) azimuthal revolutions of the 2-dimensional meshes were carried out, resulting meshes with up to 2994156 elements for $N_{\Theta 12}$ and 5988312 elements for the $N_{\Theta 24}$ cases. For LES turbulence modelling, finer mesh elements were needed, especially in the near wall region. Due to this reason, 3-dimensional meshes with up to 4498056 hexahedral cells in twelve azimuthal revolutions were developed for the cases with this turbulence models. Mesh dependency in each of this turbulence models was assessed. The maximums skewness values encountered in these meshes were the same as in the bi-dimensional cases. Their comparison permitted to assess the efficiency of each numerical strategy for the problem presented in this work.

3.4. SIMULATIONS OVERVIEW

Computations were performed using the general-purpose software FLUENT-ANSYS™. The whole set of equations were solved by using an implicit density based solver with a second order upwind discretization scheme, Least Squares cell based method for gradient calculations and ROE-Flux-Difference Splitting flux evaluation schemes (ROE-FDS) [47]. ROE-FDS scheme have shown to give good results when dealing with compressible flow problems. Two additional simulations were performed with pressure based (SIMPLE) solver in the 2-dimensional case to assess the influence of the solver in the results.

In spite of the stationary conditions of the problem modelled, transient simulations were performed in case of DES and LES turbulence models due to their non-stationary formulations of these models. For these cases, second order implicit transient formulation was employed. For these simulations, second order implicit time stepping method (dual-time stepping) implemented in FLUENT was used. This configuration employs a time-derivative unsteady preconditioner to provide accurate results both for pure convective processes and for acoustic processes. The time integration was performed by a second order backward scheme. Due to the stationary boundary conditions, physical time step was set to 1e-7 or lower to ensure the stability during the simulation. This way, a time marching procedure was used and main residual values were kept under 5e-3 before the following time step, with a maximum of twenty iterations per time step. The pseudo-time-step of the preconditioning scheme was determined by a CFL value of 0.15-0.25, depending on the stability of the case simulated. For RANS turbulence models, steady simulations were performed, the solution was obtained with a local time stepping with a fixed maximum CFL in 0.15-0.25 for each mesh cell.

Different convergence criteria were assumed depending on the simulation configuration. In case of stationary turbulence models, the convergence was based on the residuals values, as well as the total drag coefficient obtained. In these cases, simulations were considered to be converged when the main residuals based on continuity, velocity components and energy were stable with values under 10^{-4}. From this moment, drag coefficient was registered for, at least, five thousands iterations. When standard deviation of the registered values was under 10^{-4}, the drag coefficient of the body was obtained as the average of the registered values. In case of DES and LES turbulence models, due to the stationary boundary conditions, convergence criterion was based in the variation of global variables. In this case total drag coefficient and base pressure coefficient were chosen as control variables. At least ten thousand iterations with this maximum limited Courant number were needed to register the global parameters with a periodic behaviour. Once the simulations becomes stable in terms of the control variables monitored, the main flow-fields were sampled every iteration, averaging the results to obtain stable flow fields. In order to consider the results converged, less than 10^{-3} had to be reported in the standard deviation for the drag coefficient during two thousand iterations and 50^{-3} in the case of the area-averaged base pressure coefficient.

3.5. GRID INDEPENDENCE

In order to design the numerical model, basic best practices guidelines [48],[49] were followed. One of the key aspects in this type of models is the grid independence of the results. Grid independence was explored through the results obtained by considering several meshes.

To do so, the y^+ variable was used as reference parameter of the study. Three different 2-dimensional meshes with quadrilateral elements and different y^+ value were developed for the grid independence analysis. A comparison of the study target variable, C_D, was carried out in order to get the variability of this value with different mesh configurations. As reference case, 1.5 Mach value with Base Bleed on configuration was selected. The RANS SST k-ω, LES Smagorinsky-Lilly (LES S.L.), LES WALE and LES Dyn. k_{sgs} Eqn. were chosen to carry out the grid independence analysis. Three different meshes were used in the analysis. The y^+ values on the body wall of each grid developed are shown in Fig. 4. Left graph represents in ordinate axis the y^+ values on the body wall, being the abscissa the axial length from end to end of the body external surface. The average y^+ values of the grids analysed (obtained with LES S.L.) were: y^+= 0.54 for the finer grid labelled as "GridA", y^+= 6.5 for the medium grid labelled as "GridB" and y^+=13 for the coarser grid labelled as "GridC". As shown in the figure, LES S.L. and RANS SST k-ω were the turbulence models which reported the highest wall y^+ for the same flow conditions.

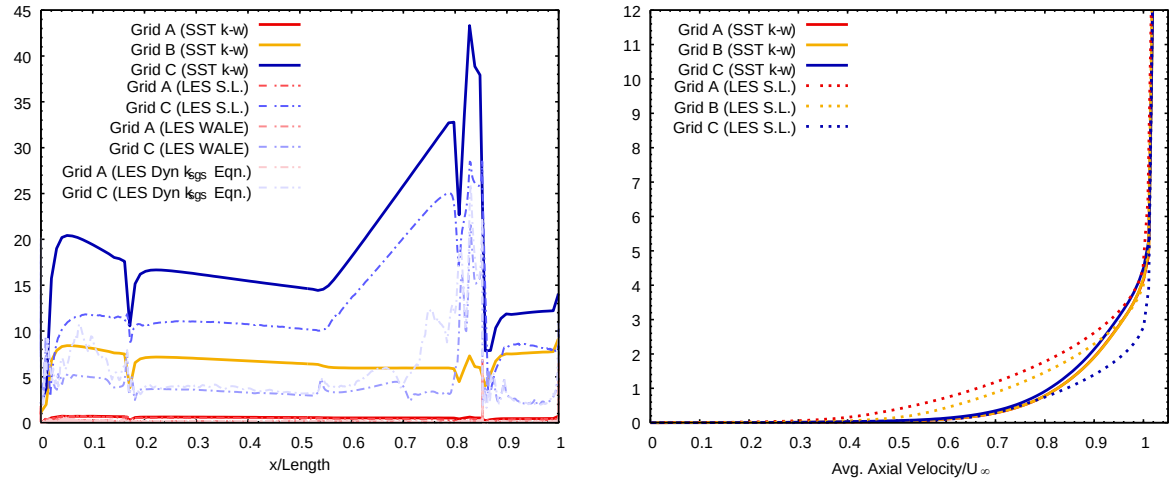

Fig. 4. (Left) y^+ values on the body surface along the axial direction. (Right) Boundary layer axial velocity profile at x/L = 0.7.

Near wall velocity profiles were, in general, very similar for the grids analysed. They only differed in certain wall locations. In Fig. 4 (Right), it is presented the near wall axial velocity profile obtained for each different

grid with RANS SST k-ω and LES Smagorinsky-Lilly at a location where the velocity profile differences can be noticed. The velocity values were obtained at a location x/L= 0.7 (i.e. 0.7 times the body length downstream the leading edge of the body). At this location, the grids had different y^+ values, reaching y^+=20 for "GridC", y^+=6 for "GridB", and y^+=0.52 in the case of "GridA". Due to the spin velocity, wall fluid velocity was not null at wall cells. Standard wall functions were considered in case of RANS and DES models, due to the near wall cell distance in the mesh considered for those models. For that reason, in case of SST k-ω turbulence model, results in Fig. 4 (Right), did not differ considerably when the initial wall spacing was slightly increased until the "GridC" case. Therefore "GridC" was the one chosen for the DES and RANS simulations presented in the following sections of this work. Fig. 4 (Right) also showed big differences between the meshes analysed in the near wall velocity profile. In case of LES with "GridC", the axial velocity reached the free stream value closer to the wall than in the case of "GridB" and "GridA". In contrast to RANS results, with LES turbulence models, there were slight differences between the velocity profiles obtained. These were due to the fact that LES with "GridB" and "GridC" had y^+>1 and wall functions were employed. On the contrary, LES with "GridA" had y^+<1 and no wall functions were imposed in this case, which means that the viscous sublayer was resolved. As a result of this analysis, "GridA" without wall functions was the final configuration used for LES results presented in the following sections of this work.

Table 1. Relative difference in C_D calculated from different grid discretization.

	"GridA"			**"GridB"**			**"GridC"**		
Turbulence Model	Normalized Pressure Drag (NPD)	Normalized Viscous Drag (NVD)	Normalized Total Drag (NTD)	Pressure Drag referenced to NPD	Viscous Drag referenced to NVD	Total Drag referenced to NTD	Pressure Drag referenced to NPD	Viscous Drag referenced to NVD	Total Drag referenced to NTD
RANS k-ω SST	1	1	1	1.02·NPD	1.02·NVD	1.02·NTD	1.02·NPD	1.14·NVD	1.03·NTD
LES S.L.	1	1	1	1.09·NPD	1.00·NVD	1.08·NTD	1.11·NPD	1.05·NVD	1.10·NTD
LES WALE	1	1	1	1.07·NPD	1.02·NVD	1.07·NTD	1.07·NPD	0.67·NVD	1.07·NTD
LES k_{sgs}-Eqn.	1	1	1	1.17·NPD	1.19·NVD	1.17·NTD	1.27·NPD	1.13·NVD	1.27·NTD

C_D values calculated are shown in the Table 1. As observed, in the case of RANS SST k-ω, C_D estimations with "GridC" differ in less than 3% from "GridA" results. This difference in the drag predicted was due to the viscous effect on body walls, whose contribution to the total drag was less than 14%. Note that, in the first case, wall functions were used whereas in the second case no wall functions were imposed. LES C_D estimations show slightly higher grid dependence, reducing the difference in the drag prediction as the grid becomes finer.

3-dimensional meshes were generated from 2-dimensional meshes. Thus, the same y+ values were expected for these meshes at the same Mach number in the 3D cases. Regarding the domain simulated (i.e. distance from the body to the boarder of the domain), Table 2 shows the results for the different grid domain sizes analysed, reporting a maximum difference of 1.6% for the different upper/down-stream domain sizes tested, ensuring that increasing the considered domain size has not a significant variation in the body drag prediction.

Regarding the simulations procedure, RANS results were employed to initialise the DES and LES simulations, being necessary to interpolate the solutions to the finer meshes in case of LES turbulence simulations.

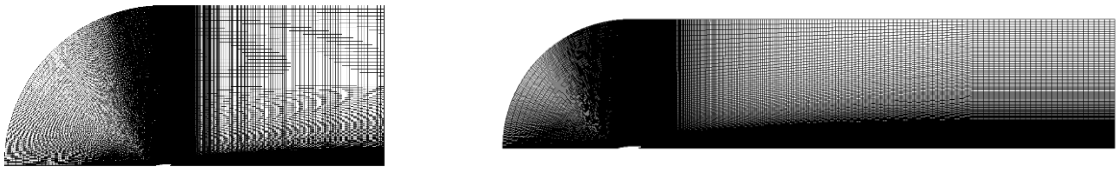

Fig. 5. Example of the different grid size domains.

Table 2. Relative difference in drag calculated from different grid size domains.

	5·L Upstream 14·L Downstream	**5·L Upstream 16·L Downstream**	**5·L Upstream 18·L Downstream**	**5·L Upstream 20·L Downstream**	**10·L Upstream 14·L Downstream**
Turbulence Model	Normalized Total Drag NTD	Total Drag referenced to NTD			
RANS k-ω SST	1	0.99·NTD	0.99·NTD	0.99·NTD	0.98·NTD

4. NUMERICAL TESTS AND RESULTS

In order to check the efficiency of the numerical model presented, the authors firstly faced the validation of the numerical simulations against experimental data. After that, the efficiency of different numerical strategies was analysed and assessed. Results were discussed in light of a benchmark between model predictions and experimental data.

4.1. EXPERIMENTAL VALIDATON

4.1.1. Experimental campaign and validation.

In order to validate the numerical model proposed, an experimental campaign was faced. Ad-hoc shooting experiments were performed with an artillery gun. Flight measurements were obtained with a meteorological data acquisition system and a Radar system model WEIBEL MFTR-2100/43. It was a Multi Frequency Trajectory Radar system based on a continuous wave Multiple Frequency Doppler Radar. It had a time resolution of 0.3ms, a velocity range that reaches 8000m/s and an instrumented range of more than 1500km [50]. The system was able to measure body flight data with a range resolution of ±0.020 m and 0.06-0.12m/s in the measurement of the velocity. Recorded data included ambient temperature, ambient pressure, wind speed at ground level as well as body position and body speed. From these data, ambient density at different altitude was obtained assuming ISA model and Flight Mach number of the body was also estimated. The lapse of time of activity of the Base Bleed unit was also measured during the experiments. Additional combustion experiments were performed at the EXPAL Propellant Laboratory with a manometric bomb to estimate the properties of the propellant grain used in the Base Bleed unit. Based on these experiments, the average gas mass flow rate generated by the Base Bleed unit was measured and the temperature of the burning front within the propellant grain was estimated to round 1855 K. The influence of this temperature in the C_D drag estimation was analysed and discussed after in this paper.

Several shots were performed during the experimental campaign, both with and without Base Bleed. Average values were obtained from the recorded data. The experimental drag coefficient values obtained were also available in [46]. The average activity of the Base Bleed unit was estimated to last up to the point of Ma = 0.995. The average values of C_D obtained from the experiments with Base Bleed active (BB on) and inactive (BB off) at different flight Mach numbers (Ma= 1.59, 1.5, 1.2, 1.05, 0.995) were used as reference values in the predictions drag coefficient. These Mach values were selected as representative of the body flight in supersonic regime (Ma=1.59, 1.5 and 1.2), as well as of the flight regime where the drag coefficient reaches maximum values due to the shock waves dynamics (Ma=1.05) and of the flight transonic regime at the end of the Base Bleed unit activity (Ma=0.995). Regarding body spin velocity, it was estimated to have an average value of the order of 2000 rad/s approximately during the flight lapse of time at Mach numbers between 1.1 and 1.5. All in all, the average uncertainty of the experimental data was estimated to be 6.01% for the experimental estimation of C_D and 0.05% for the estimation of the Mach number. This estimation was performed following the procedure

specified in [51] based on error propagation methodology with a 95% confidence (k=2). Table 3 shows the comparison of best numerical predictions with reference experimental data. Note that the estimation of the C_D relative difference was defined as:

$$C_{D\ Relative\ diference}(\%) = 100 \cdot \frac{C_{D\ Numerical} - C_{D\ Experimental}}{C_{D\ Experimental}} \qquad (8)$$

As shown, Base Bleed unit permits to reduce the body drag considerably. This reduction was also predicted with the numerical simulations. The relative difference in the C_D predictions was less than 1.1% for active Base Bleed and 1.5% (in average) for inactive Base Bleed, in both cases referring to the experimental values. These relative differences are smaller than the experimental uncertainty band of the experiments (6.01%). Note that, the best numerical prediction was obtained with different turbulent models and configuration in each flight regime. In the next section it will be faced the discussion of the prediction reached with each turbulent model and/or numerical strategy.

Table 3. Reference C_D values and best numerical predictions.

Case	Mach	C_D experimental (reference value)	C_D numerical	C_D (%) Relative difference
BB on *3D $N_{\Theta 12}$ LES WALE*	1.596	0.200	0.202	1.11
BB off *2D SST k-ω*	1.5	0.308	0.311	1.00
BB off *3D $N_{\Theta 12}$ Standard k-ω*	1.2	0.326	0.329	0.92
BB off *2D RNG k-ε*	1.05	0.308	0.309	0.28
BB off *3D $N_{\Theta 12}$ LES WALE*	0.995	0.250	0.215	-3.74

4.1.2. Prediction of drag coefficient in the case of inactive Base Bleed unit.

Under this configuration a compressible wake was developed behind the body. In addition, the average pressure within the base cavity was relatively low with respect to the rest of the flow field. This flow configuration resulted in a relatively adverse conditions from the numerical point of view. Therefore it was important to assess the real capacity of the code to predict drag coefficient in the case of this adverse flow conditions. In order to achieve this purpose, numerical predictions were benchmarked against the experimental shooting data reference values of flights with inactive Base Bleed unit. Both, 2-dimensional (2D) and 3-dimensional (3D $N_{\Theta 12}$) computations were performed with k-ε RNG, Standard and SST k-ω, Smagorinsky Lilly, WALE and Dyn. k_{sgs}

Eqn. LES models with a density based solver. Table 4 shows the comparison of the prediction reached with each numerical model with respect to the experimental reference value as a function of Mach number. The comparison was performed in relative terms in order to assess easily the capacities of each numerical strategy. These results are also showed in Fig.6. All in all, results showed a relatively good agreement for RANS, DES and LES. The average error absolute in the numerical prediction when the Base Bleed unit is not active was 9.1%. Notwithstanding, some of the models showed a better behaviour than others. For a 2D configuration, RANS RNG k-ε was found to predict efficiently C_D. For 3D configuration, Standard k-ω and LES Smagorinsky-Lilly were models that provided the smallest average prediction errors (3.75% and -3%, respectively). In light of the results, RANS turbulence models, such as Standard k-ω and RNG k-ε, with wall functions approach seemed to be an interesting approach that provided reasonable agreement (with less than 4% in the average absolute error) with relatively low computational cost. In this case, the turbulence model must predict the subsonic recirculation bubble at the wake of the body in order to recover pressure distribution at the base. These RANS turbulence models had previously showed relatively good capacities in simulating this kind of flow pattern, for example in the case of a squared cylinder in a turbulent flow [24] what confirms their ability in the base drag prediction for the BB off configuration.

Table 4. Experimental Benchmark of C_D for BB off configuration.

	CD relative Difference compared to experimental data (%)			
CASE	**Ma=1.5**	**Ma=1.2**	**Ma=1.05**	**Ma=0.995**
2D RNG k-ε	-4.37	1.47	0.28	9.20
2D SST k-ω	1.00	3.99	9.48	18.73
3D $N_{\theta l2}$ RNG k-ε	-9.97	-7.26	6.95	-5.60
3D $N_{\theta l2}$ Standard k-ω	-	0.92	3.78	6.55
3D $N_{\theta l2}$ SST k-ω	-1.53	3.61	12.01	16.84
3D $N_{\theta l2}$ LES Smagorinsky-Lilly	-13.99	-6.87	3.18	5.69
3D $N_{\theta l2}$ LES WALE	-22.81	-20.27	-7.79	-3.74
3D $N_{\theta l2}$ LES Dyn. ksgs-Eqn.	-24.91	-21.85	-20.00	-14.02

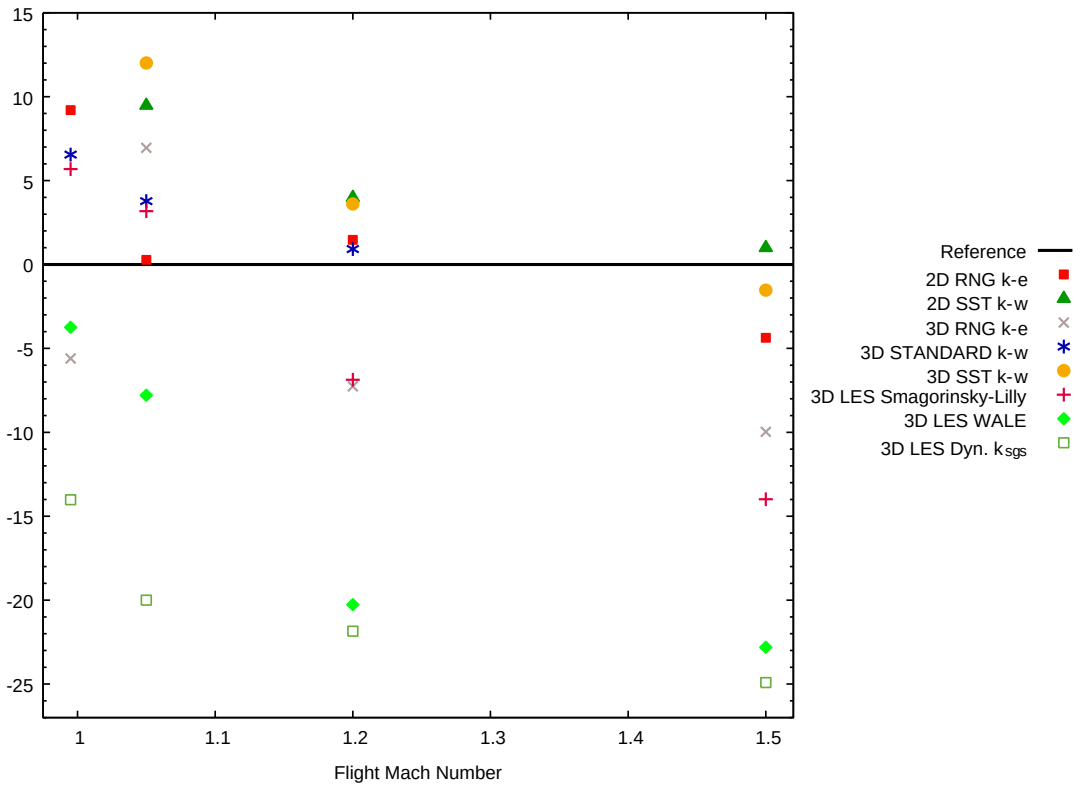

Fig.6 Experimental Benchmark of C_D for BB off configuration.

4.2.2. Prediction of drag coefficient in the case of active Base Bleed unit.

During the supersonic regime, the highly turbulent and compressible nature of the flow involving a mixing layer of a high temperature jet with a transonic wake made the BB on configuration numerically more demanding than the BB off one. In the BB on case, the gas mass flow injection detaches the main recirculation bubble from the base of the body and weakens the recompression shock at the wake. Table 5 shows the comparison of numerical predictions with experimental data for the case of Base Bleed unit (BB on). These results are also showed in Fig.7. WALE LES model was found to be the best model to estimate C_D in the case of active Base Bleed unit. C_D predictions were not very accurate in case of RANS turbulence models except for the 0.995 Mach case. For the rest of cases, the minimum error value with RANS turbulence models was 20.12%. The average error in the C_D prediction for RANS models rounded 31%. However, DES and LES modelling improved the prediction accuracy, resulting relatively good agreements in case of LES WALE and LES Dyn. ksgs Eqn. simulations. The average absolute error in the C_D prediction with Base Bleed on configuration was 4.4% in case of LES WALE calculations, and 6.9% in the case of LES Dyn. ksgs Eqn. In this configuration, RANS models sub-predict base pressure as they are not able to properly estimate the weakening of the recompression shock due to the hot gas mass injection. This might be due to the fact that they were tuned with incompressible flows and they seemed

not to be adapted to model accurately the turbulence spectra present in a high temperature jet and mixing layer such as the one presented in the case of active Base Bleed unit. In this case, the base flow generated from the unit was expanding at a relatively high temperature in a low pressure region and the modelling of turbulent mixing and thermal diffusion was a key issue to properly predict the recirculation regions and base pressure. As suggested by [1],[52],[53], RANS turbulence models seemed to over-estimate the production of turbulent kinetic energy near wake stagnation points due to the use of the Boussinesq approximation for the eddy viscosity. Contrary to RANS turbulence models, LES were able to reproduce the actual unsteady nature of the turbulence at microscale level which resulted to be a key aspect in the prediction of the turbulent mixing at the base of the body. The different behaviour of LES WALE and LES Dyn. k_{sgs} Eqn. models might be explained by the fact that the first one was specially designed to recover the right asymptotic behaviour of the effective viscosity close to solid walls (y^{+3} behaviour) but it does not use a dynamic procedure for this estimation [37],[54] whereas LES Dyn. ksgs Eqn was designed to adapt dynamically the effective viscosity in the case of isotropic turbulence–normal shock interaction problems [39]. With the BB on configuration, LES WALE predicted bigger values of effective thermal diffusion and effective viscosity than LES Dyn. ksgs Eqn at the base bleed cavity, at the nozzle and at the body base what resulted in slightly bigger velocities at the jet core for LES WALE than for LES Dyn. ksgs Eqn. Finally, it is worth to note that DES models had an intermediate behaviour between RANS and LES. The average absolute error in the C_D prediction for DES models rounded 23%.

Table 5. Experimental benchmark of C_D for BB on configuration.

	C_D relative Difference compared to experimental data (%)			
CASE	**Ma=1.5**	**Ma=1.2**	**Ma=1.05**	**Ma=0.995**
2D RNG k-ε	31.57	33.51	23.46	0.37
2D Standard k-ω	44.39	-	-	-
2D SST k-ω	43.28	55.45	47.64	25.97
3D $N_{\theta 12}$ RNG k-ε	20.12	35.34	22.33	0.30
3D $N_{\theta 12}$ Standard k-ω	40.85	40.86	29.91	13.70
3D $N_{\theta 12}$ SST k-ω	37.95	49.39	44.68	26.49
3D $N_{\theta 12}$ DES Real k-ε	17.45	26.19	9.83	-
3D $N_{\theta 12}$ DES SST k-ω	29.75	24.95	31.80	-
3D $N_{\theta 12}$ LES Smagorinsky-Lilly	21.20	40.60	39.34	10.48
3D $N_{\theta 12}$ LES WALE	-3.04	12.05	1.10	-1.53
3D $N_{\theta 12}$ LES Dyn.k_{sgs}-Eqn.	4.83	5.78	-0.92	-16.05

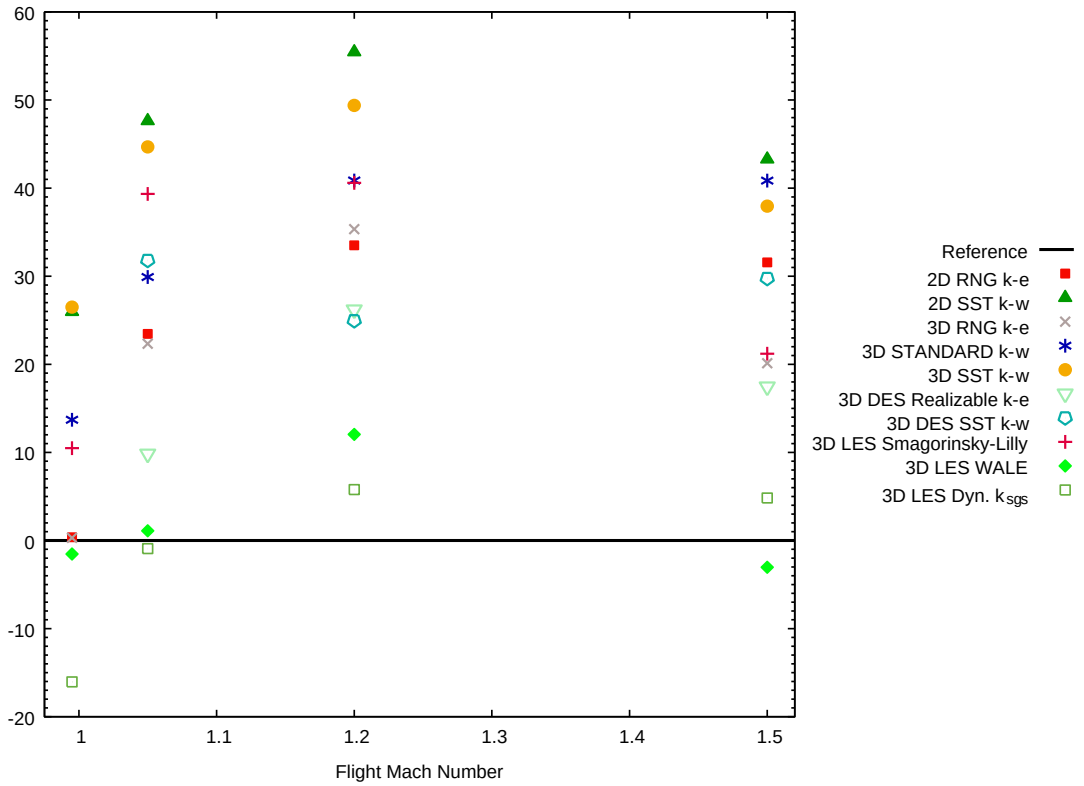

Fig.7 Experimental benchmark of C_D for BB on configuration.

4.2. ASSESMENT ON THE EFFICIENCY OF DIFFERENT NUMERICAL STRATEGIES

In this section the influence of different numerical strategies in the final results of the simulations was analysed. This analysis was be made in light of Table 6. The parameters analysed were: grid configuration (2D, 3D and number of azimuthal nodes), type of solver, and turbulence model. Additionally, Table 7 was used to study the influence of the propellant combustion model used.

Table 6. Sensitivity study: influence of different numerical strategies.

Numerical Strategy	Case	Mach	Relative difference (%)
Grid configuration BB off	-Experimental data at Ma=1.5, BB off	1.5	reference
	-Numerical2D axisymmetric, RNG k-ε		-1.01
	-Numerical 3D $N_{\Theta 12}$,RNG k-ε		-6.81
	-Numerical RNG k-ε 3D $N_{\Theta 24}$,RNG k-ε		0.17
Grid configuration BB on	-Experimental data at Ma=1.5, BB on	1.5	reference
	-Numerical 2D axisymmetric, RNG k-ε		31.57
	-Numerical 3D $N_{\Theta 12}$,RNG k-ε		20.12
	-Numerical 3D $N_{\Theta 24}$,RNG k-ε		26.69
Type of solver for 2D axisymmetric	-Experimental data at Ma=1.5, BB off	1.5	reference
	-Numerical 2D axisymmetric, RNG k-ε, Implicit-Density based solver BB off		-1.01
	-Numerical 2D axisymmetric, RNG k-ε, SIMPLE Pressure based solver BB off		-1.02
	-Experimental data at Ma=1.5, BB on	1.5	reference
	-Numerical 2D axisymmetric, RNG k-ε,Implicit Density based solver BB on		31.57
	-Numerical 2D axisymmetric, RNG k-ε, SIMPLE Pressure based solver BB on		33.24
Turbulence model for 2D axisymmetric	-Experimental data at Ma=1.5, BB on	1.5	reference
	-Numerical 2D axisymmetric, RNG k-ε		31.57
	-Numerical 2D axisymmetric, Standard k-ω		44.39
	-Numerical 2D axisymmetric, SST k-ω		43.28
Turbulence model for 3D	-Experimental data at Ma=1.5, BB on	1.5	reference
	-Numerical 3D $N_{\Theta 12}$,RNG k-ε		20.12
	-Numerical 3D $N_{\Theta 12}$, Standard k-ω		40.85
	-Numerical 3D $N_{\Theta 12}$, SST k-ω		37.95
	-Numerical 3D $N_{\Theta 12}$, DES Realizable k-ε		17.45
	-Numerical 3D $N_{\Theta 12}$, DES SST k-ω		29.75
	-Numerical 3D $N_{\Theta 12}$, LES Smagorinsky Lilly		21.20
	-Numerical 3D $N_{\Theta 12}$, LES WALE		-3.04
	-Numerical 3D $N_{\Theta 12}$, LES *Dyn.*k_{sgs}*-Eqn.*		4.83

4.2.1. Influences of grid configuration on RANS

Regarding grid configuration, the influence of the spatial domain studied in the numerical problem was assessed by comparing the C_D prediction obtained when the 2D axisymmetric problem was considered, with that obtained when the full 3D spatial domain was analysed. Two different 3D meshes with 360º of revolution were generated with 12 and 24 azimuthal elements. Fig. 8 shows an example of the type of 3D mesh used for the simulations of the body.

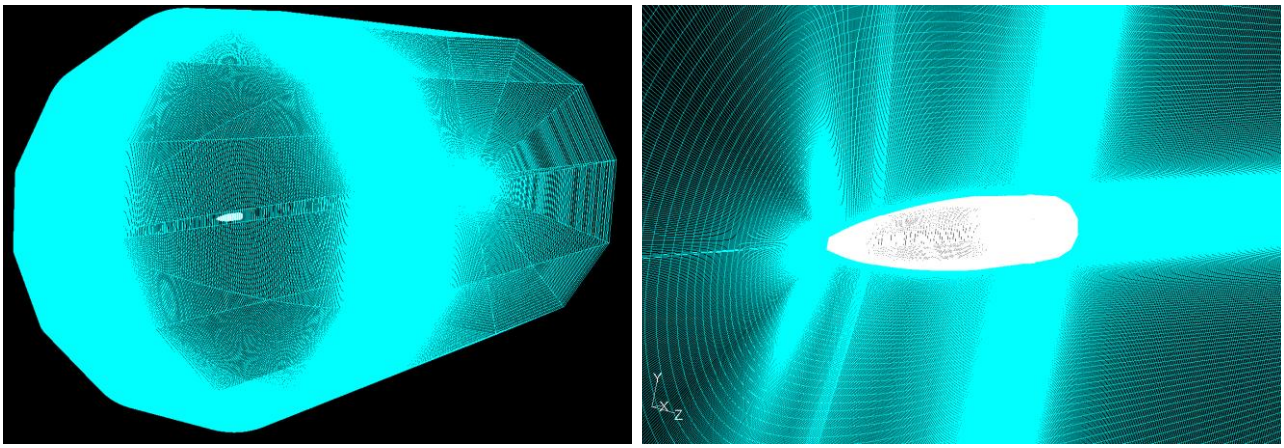

Fig. 8. Example of a 3D mesh used in the simulations.

Table 6 summarizes the main results of this comparison. In the case of grid configuration, the sensitivity study was obtained with the same solver (density based solver), turbulence model (RNG k-ε) and scheme (ROE-FDS), so that the effect of the grid configuration could be assessed. Both BB off and BB on configurations showed that C_D values calculated with 3D meshes were lower than those obtained with 2D axisymmetric cases. In case of BB off, the prediction error of RNG k-ε models decreased as the number of azimuthal nodes increased. This was due to the fact that a relatively high spatial resolution was needed in the azimuthal coordinate in order to properly describe the swirl flow close to the wall. The main penalty that had to be paid when using 3D computations was that some quality requirements of the mesh such as elements grow rate, and azimuthal resolution had to be relaxed due to the computational limitations. Therefore a compromise between mesh quality and computational cost had to be reached. In case of BB off calculations, RANS models estimated the C_D values with an average error close to 3% for 3D simulations. On the other hand, the BB on with RANS axisymmetric cases had an error of 32% whereas with the 3D configuration the average error decreased to 23% for the Ma = 1.5 case. Again, results showed that RANS is not a suitable option for the simulation of BB on configuration.

4.2.2. Solver

Both, pressure based and density based solvers were analyzed in order to assess the solver influence on the drag coefficient calculation. Pressure-based solvers employ a projection method algorithm to derive and solve a pressure equation that fulfils continuity conservation whereas density-based solvers seek to solve simultaneously mass, momentum and energy governing equation. The pressure-based solvers were originally developed for low-speed incompressible flows, while the density ones were originally developed for high speed, compressible flows. However, both solvers are currently extended to solve flow conditions beyond their original intent.

In the problem studied, there was a wide range of velocity scales within the domain. Around the body, it was developed a compressible, high speed flow. However, within the Base Bleed cavity, a flow with low speed conditions was expected. Therefore, both solvers were tested to assess their efficiency and their potential influence in the drag predictions. Results showed that both solvers obtaining similar C_D predictions and final flow field. However, from the computation and convergence point of view, results showed that the requirements needed for the cases with different solvers were different. Pressure-based solver needed from a stepping method to reach the convergence of the Mach regime desired. The method started with incompressible, non-viscous conditions and, once it was converged, it was adopted a more complex turbulent model with compressible conditions. In the case of a density based solver, stepping methods were not needed. However, this type of solver resulted to be more sensitive to mesh quality. Pressure based solver (SIMPLE algorithm) tend to calculate slightly higher C_D values than the implicit density based solver. In the case of BB off configuration with RNG k-ε turbulence model, pressure based C_D prediction differs only 0.01% from the density based solver solution. C_D prediction in case of BB on configuration with the pressure based solver was 1.27% bigger than the one predicted with the density based solver calculation.

4.2.3. Turbulence modelling

Modelling the turbulence dynamics in a transonic wake after a combustion process is a challenging issue. In this section it is discussed the ability of RANS and LES turbulence models to afford this problem in the BB on configuration. As shown in Table 6, three different RANS turbulence models were tested: RNG k-ε, Standard k-ω, and SST k-ω. DES and LES turbulence models were also compared. The comparison was made using the same flow conditions (Ma = 1.5) so that the effect of the turbulence model could be properly assessed.

Results (Table 6) showed an average error of 33% in case of 3D configuration for RANS turbulence models with a dispersion in the C_D provided of 17% depending on the turbulence model used. In the case of RANS models, the main differences in the total C_D predicted are due to the different pressure values at body walls. DES and LES improved the C_D predictions, reaching a relative difference with the reference experimental data rounding 3% for LES WALE and 4.8% for LES Dyn.k_{sgs}-Eqn. As shown, both models provided a reasonable accuracy in the C_D prediction. As expected, DES models provided an intermediate behaviour between RANS and LES models.

RANS SST k-ω BB on

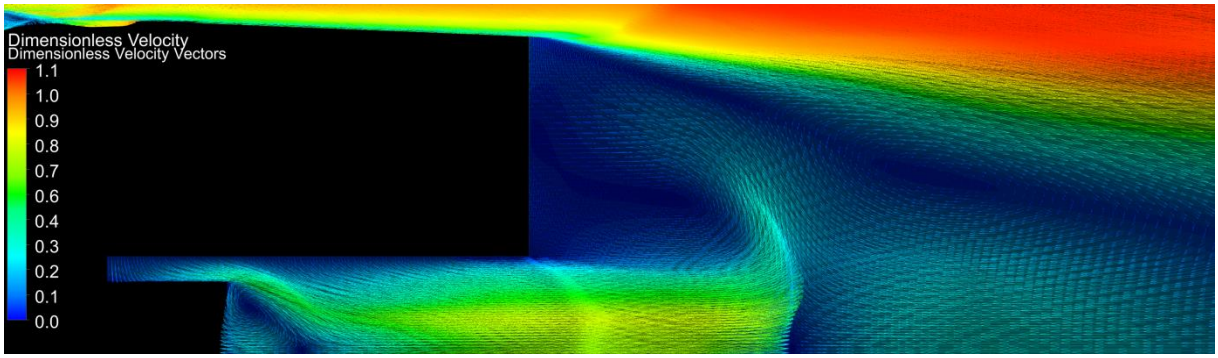

LES Smahgorinsky-Lilly BB on

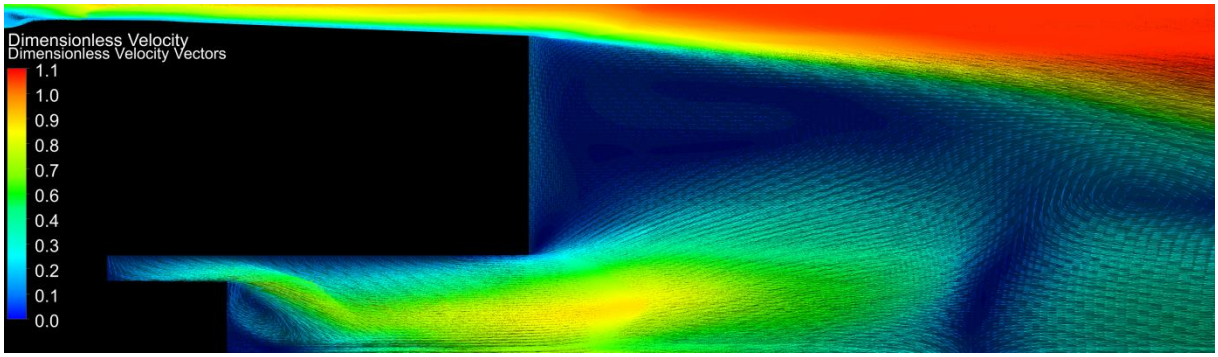

LES WALE

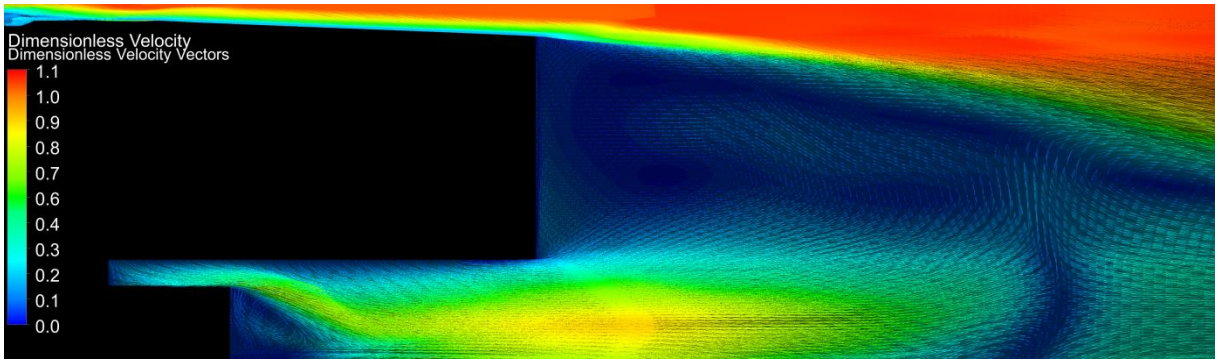

LES Dyn. k_{sgs}-Eqn.

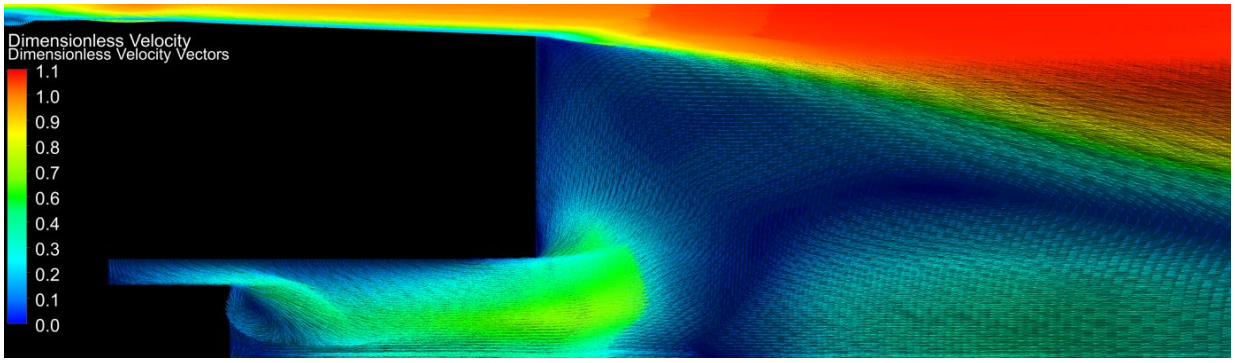

Fig. 9 Average velocity field at Ma=1.5-BB on for different turbulence models.

Fig. 9 shows the mean flow field predicted by RANS-based and LES simulations for Ma=1.5. As shown, both models simulated differently the mean flow field due to the steadiness/unsteadiness nature of the turbulence model. For example, RANS SST k-ω turbulence model predicted the smallest velocities at the nozzle exit whereas LES WALE predicted the biggest ones. In addition, the jet penetration length predicted by LES WALE is considerably bigger than the one predicted with the rest of models. Accordingly, the recirculation bubble predicted by LES WALE model was also located further downstream the base of the body than in the rest of cases. As a consequence, the recompression shock in the wake predicted with this model was weaker. In light of the experimental data available [53], this prediction is closer to the flow pattern expected in the case of BB on configuration. Thus, LES WALE seemed to provide a more realistic flow pattern within the nozzle and close to the body base.

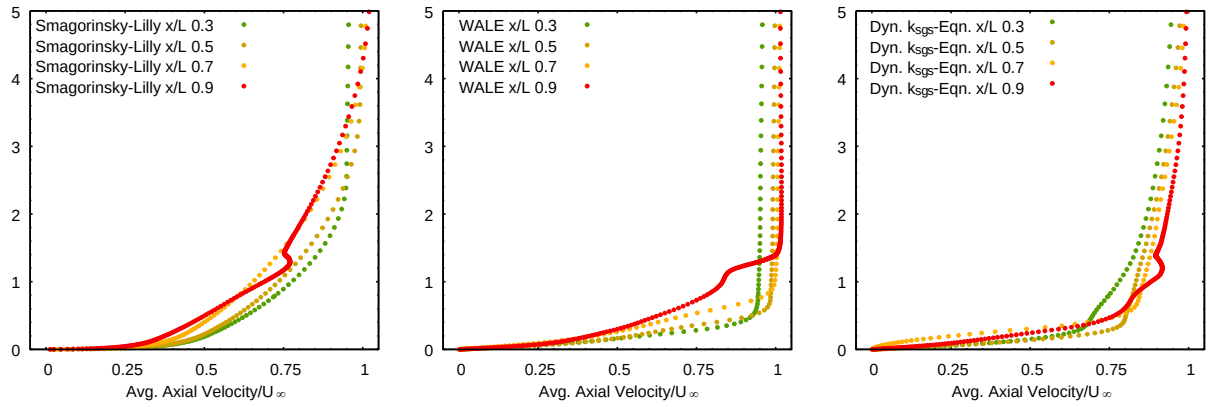

Fig. 10. Wall axial velocity profiles with different LES turbulence models.

Additional insights into the differences in the C_D prediction with LES models can be found in light of the flow field predicted close to the walls. The different near wall velocity profiles obtained with caused different values

of the drag calculated due to the viscous effect at body walls (Fig. 10). As shown, LES Dynamic k-Eqn. turbulence model provided a boundary layer detachment at body walls in the region 0.7 to 0.8 of the axial body length. Regarding friction contribution, LES Dynamic k-Eqn. turbulence model predicted a viscous drag 88.35% smaller when compared to LES Smagorinsky-Lilly results. Similarly, LES WALE model obtained a viscous drag 88.21% of the Smagorinsky-Lilly value. However, RANS turbulence models and LES Smagorinsky-Lilly predicted similar viscous drag values. These particular results were somehow expected. LES Smagorinsky-Lilly was the first LES model developed and it is known for its extradissipation in near wall regions [55] whereas WALE was designed to model correctly near wall behaviour (y^{+3}) and it is able to represent linear-to-turbulent transition [37][54]. In this last case, no dynamic procedure is used. On the contrary, the LES Dyn.k_{sgs}-Eqn. developed by [39] included a procedure to adapt dynamically SGS constants depending on flow conditions. This procedure was tested for compressible isotropic turbulence against experimental and DNS data but not specifically in the case of near wall flows. This might also explain the differences found between LES WALE and LES Dyn.k_{sgs}-Eqn. models. LES turbulence models

4.2.4. Influence of the propellant combustion model

In this section, the influence of the propellant combustion model in the numerical estimation of the drag was analysed. As previously said, the propellant combustion within the Base Bleed unit was simulated as a solid surface injecting gas at a certain temperature. Three key parameters of the model were studied: the combustion gases molecular weight, the grain burning temperature, and the average gas mass flow rate generated by the Base Bleed unit.

In order to analyse the influence of the molecular weight of the gases injected within the Base Bleed unit in the predicted drag a detailed model for the propellant combustion products was developed. It considered additional transport equations for the mass fraction of the species considered. The combustion data needed for this implementation was obtained from experimental combustion tests of the pyrotechnic grain mixture used as propellant in the Base Bleed unit and software simulations with IBHVG2 [45] .The actual composition of combustion products of a burned propellant is reach and complex. Results showed that more 70 different species are present in the process. However, a deep analysis of the data revealed that 7 species accounted for nearly 99.95% of the total mass of the gases composition (Table 7). Because of this, a simplified chemical model of the products resulting from the combustion was defined for Base Bleed propellant with a limited number of species. Up to six species were finally considered in the modelling of the combustion gases: O_2, H_2O, CO, CO_2 and N_2 within the numerical simulations of the drag predictions. They represent up to 73% of the total weight.

Table 7. Model used for the combustion gases at the Base Bleed unit.

Species	% mol.	% weight
CO_2	3.072	6.918
H_2O	12.429	11.456
N_2	6.567	9.412
CO	31.817	45.597
H_2	33.713	3.477
HCl	12.374	23.084
Total	99.94	99.944

Numerical results revealed that there is not a meaningful difference in the estimated C_D when modelling the combustion gases species compared with the use of air as Base Bleed gas. This could be explained by the relative small difference of the actual average molecular weight of the combustion gases compared to that of air at the Base Bleed cavity conditions.

Regarding the influence of the temperature of the burning gases (T) on the estimated $C_{D,}$ it was explored with a sensitivity study between 1855K and 2655K. It was found (Table 8) that variations of 43% in temperature with respect to the reference case resulted in variations of -3.2% in the C_D estimated. This means that the sensitivity of the estimated C_D with the temperature of the combustion gases rounds $d(C_D)/dT \approx -1.1 \cdot 10^{-5}$ (K^{-1}). Therefore, the influence of this parameter in the C_D prediction can be considered negligible. As for the influence of the gas mass flow rate (G) generated at the Base Bleed unit, a similar analysis (Table 8) showed that the sensitivity of the estimated C_D with G rounds $d(C_D)/dG \approx -0.56$ (s/kg). This means that variations of 50% in the estimation of the average gas mass flow rate at the Base Bleed unit results in variations of 0.005 in the predicted C_D. In short, the influence of this parameter in the C_D prediction is relatively small for the range of G expected in Base Bleed applications.

Table 8. Sensitivity study: propellant combustion model.

Parameter	Case	C_D Relative difference (%)
Influence of grain burning temperature (T) at the Base Bleed unit	Numerical 2D axisymmetric T=1855K	reference
	Numerical 2D axisymmetric T=2655K	-3.2%
Influence of the gas mass flow rate (G) at the Base Bleed unit	Numerical 2D axisymmetric Mass Flow Rate = G	reference
	Numerical 2D axisymmetric Mass Flow Rate = 0.47·G	-14.0%

5. CONCLUSIONS AND FUTURE WORK

This work analyses the ability of RANS, DES and LES numerical models to estimate drag coefficient in the case of bodies with Base Bleed unit. Results showed different level of agreement between numerical simulations and experimental data in the case of RANS, DES or LES, and highlight some key conclusions from the modelling point of view. The most important can be summarised as follows:

- The combustion within the Base Bleed unit can be modelled as a solid surface that is injecting gas at the temperature of the burning front.

- Due to the coupling between the internal Base Bleed pressure and the external body airflow pressure, the numerical simulation of the space within the Base Bleed cavity is recommended in order to predict the C_D under the flow regimes without chocked conditions at the nozzle of the Base Bleed unit.

- RANS-based models predict drag coefficient in the case of inactive Base Bleed configuration with reasonable accuracy. However, they have limitations when facing a problem involving a mixing layer of a high temperature jet with a transonic wake as in the case of active Base Bleed. In this configuration, results showed that these models are not a suitable option.

- In the case of active Base Bleed unit, Large Eddy Simulations was found to have a better prediction capacity than RANS and DES. WALE LES was found to be the best turbulence model to predict drag coefficient with an average absolute error of 4.4%.

- In the case of active Base Bleed, the use of DES models (Real k-ε, SST k-ω) is not recommended as they provide C_D average prediction errors over 23%.

- The influence of the molecular weight of the combustion gases injected within the Base Bleed unit in the drag predicted by the simulations was found to be negligible. In addition, the temperature value used for modelling the gas mass flow injected within the Base Bleed unit had very limited influence on the C_D prediction.

For future work, efforts will be oriented to employ combustion models and pressure dependent burning laws in order to obtain the gas mass flow rate of the propellant as a function of the pressure at the Base Bleed cavity.

ACKNOWLEDGEMENTS

The researchers acknowledge the support of the Spanish Ministry of Economy and Competitiveness and the European Commission (European Regional Development Fund (ERDF) / FEDER funds) throughout the INNPACTO research project “Smart Propellants” (IPT-2011-0712-020000), involving EXPAL Systems S.A. and Universidad Politécnica de Cartagena (UPCT). The researches would also acknowledge the support of CDTI (Spain) and European Commission (European Regional Development Fund (ERDF) / FEDER funds) throughout the PROBASE research project IDI-20151011.

REFERENCES

[1] J. Sahu, C.J. Nietubicz, J.L. Steger, Navier-Stokes computation of projectile base flow with and without base injection, AIAA J. 23(9) (1985) 1348-1355.

[2] J. Sahu, J.E. Danberg, Navier-Stokes computations of transonic flows with a two-equation turbulence model, AIAA J. 24(11) (1986) 1744-1751.

[3] J. Sahu, Supersonic flow over cylindrical afterbodies with base bleed, Computatoinal Mechanics 2(3) (1987), 176-184.

[4] D. Regodic, A. Jevremovi, D. Jerkovic, The prediction of axial aerodynamic coefficient reduction using Base Bleed, Aeros. Sci. & Tech. 31 (2013) 24-29.

[5] M.A. Suliman, O.K. Mahmoud, M.A. Al-Sanabawy, O.E. Abdel-Hamid, Computational investigation of base drag reduction for a projectile at different flight regimes, in: 13th Int. Conf. on Aerospace Sciences & aviation technology ASAT Conference, 2009, pp. 26-28.

[6] P. Kaurinkoski, A. Hellsten, Numerical simulation of a supersonic base bleed projectile with improved turbulence modeling. J. of Spacecraft and Rockets 35(5) (1998) 606-611.

[7] P. Kaurinkoski, Computation of the flow of thermally perfect gas past a super-sonicprojectile with Base Bleed, 1996, in: AIAA AFM Conference, 1996, pp. 725-734.

[8] F.Simons, S. Deck, P. Guillen, P. Sagaut, Reynolds-Averaged Navier–Stokes/Large-Eddy Simulations of supersonic base flow. AIAA J. 44(11) (2006) 2578-2590.

[9] R.A. Baurle, C.-J. Tam, J.R. Edwards, H.A. Hassan, Hybrid Simulation Approach for Cavity Flows: Blending, Algorithm and Boundary Treatment Issues, AIAA J. 41(8) (2003) 1463-1480.

[10] S. Kawai, K. Fujii, Computational Study of Supersonic Base Flow using Hybrid Turbulence Methodology, AIAA J. 43(6) (2005) 1265-1275.

[11] T. Mathur, J. C. Dutton, Base Bleed experiments with a cylindrical afterbody in supersonic flow, J. Spacecr. Rockets 33(1) (1995) 30-37.

[12] T. Mathur, J. C. Dutton, Velocity and turbulence measurements in a supersonic base flow with mass bleed, AIAA J. 34(6) (1996) 1153-1159.

[13] T. Mathur and J. C. Dutton, Base bleed experiments with a cylindrical afterbody in supersonic flow, J. Spacecr. Rockets 33(1), (1996) 30-37.

[14] J. L. Herrin, J. C. Dutton, Supersonic Base Flow Experiments in the Near Wake of a Cylindrical Afterbody, AIAA J. 32(1) (1994) 77-83.

[15] J. Sivasubramanian, R. Sandberg, D. Terzi, H. Fasel, Numerical investigation of flow control mechanisms for drag reduction in supersonic base-flows, in: 44th AIAA Aerospace Sciences Meeting and Exhibit, 2006, pp. 10775-10784.

[16] J.R. Shin, J.Y. Choi, DES study of base and base-bleed flows with dynamic formulation of DES constant, in: AIAA Aerospace Sciences Meeting, 2011, pp.99-110.

[17] J.R. Shin, D.R. Cho, S.H. Won, J.Y. Choi, Hybrid RANS/LES study of base bleed flows in supersonic mainstream, in: 15th AIAA Int. Space Planes and Hypersonic Systems and Technologies Conf., 2008.

[18] W. Yu, Y. Yu, B. Ni, Numerical simulation of base flow with hot Base-Bleed for two jet models. Defence Technology 10 (65) (2014) 279-284.

[19] I.P. Castro, D.D. Apsley, Flow and dispersion over topography: a comparison between numerical and laboratory data for two-dimensional flows. Atmospheric Environment 31(6) (1997) 839–850.

[20] V. Yakhot, L.M. Smith, The renormalization group, the ε-expansion and derivation of turbulence models. Journal of Scientific Computing 7(1) (1992) 35–61.

[21] L.M. Smith, W.C. Reynolds, On the Yakhot–Orszag renormalization group method for deriving turbulence statistics and models. Physics of Fluids 4 (1992) 364–390.

[22] V. Yakhot, S. A. Orszag, S. Thangam, T. B. Gatski, C. G. Speziale, Development of turbulence models for shear flows by a double expansion technique, Physics of Fluids 4(7) (1992)

[23] G. Monpean, Numerical simulation of a turbulent flow near a right-angled corner using the speziale non-linear model with RNG k-e equations, Computers & Fluids 27(7) (1998) 847-859.

[24] S. Lee, Unsteady aerodynamic force prediction on a square cylinder using k–ε turbulence models, J. Wind Eng. Ind. Aerodyn. 67-68 (1997) 79–90.

[25] T.H. Shih, J. Zhu, J. L. Lumley, A realizable Reynolds stress algebraic equation model. NASA Technical Memo. 105993 (1993)

[26] T.H. Shih, W.W. Liou, A. Shabbir, Z. Yang, J. Zhu, A New k-ε Eddy viscosity model for high reynolds number turbulent flows-Model development and validation. Computers Fluids. 24(3) (1995) 227-238.

[27] J.E. Bardina, P.G. Huang, T.J. Coakley, Turbulence Modeling Validation, Testing and Development. NASA Technical Memo. 110446 (1997)

[28] D. C. Wilcox, Formulation of the k-w Turbulence Model Revisited, AIAA J. 46(11) (2008) 2823-2838.

[29] D.C. Wilcox, Simulation of transition with a two-equation turbulence model, AIAA J. 32 (1994) 247–255.

[30] J.E. Jaramillo, C.D. Pérez-Segarra, A. Oliva, K. Claramunt, Analysis of different RANS models applied to turbulent forced convection, International Journal of Heat and Mass Transfer 50 (2007) 3749–3766.

[31] D.C. Wilcox, Turbulence Modeling for CFD, second ed., DCW Industries, La Canada, California, 2000.

[32] J. Nikuradse, Strömungsgesetze in Rauhen Rohren, vol. 361, VDI Forschungsh, 1933 (English Translation: Laws of flows in rough pipes. NACA Tech. Mem. 1292, https://ntrs.nasa.gov/archive/nasa/casi.ntrs.nasa.gov/19930093938.pdf).

[33] M.A.R. Sharif, G. Guo, Computational analysis of supersonic turbulent boundary layers over rough surfaces using the k–ω and the stress–ω models. Applied Mathematical Modelling 31(12) (2007) 2655–2667

[34] F.R. Menter, Zonal two equation kappa-omega turbulence models for aerodynamic flows, in: 24th AIAA Fluid Dynamics Conference, 1993, 93-2906.

[35] F.R. Menter, Two-equation eddy-viscosity turbulence models for engineering applications, AIAA J. 32(8) (1994) 1598-1605.

[36] F.R. Menter, M. Kuntz, R. Langtry, Ten years of industrial experience with the SST turbulence model, in: 4th International Symposium on Turbulence, Heat and Mass Transfer, 2003, pp. 625-632.

[37] F. Nicoud, F. Ducros, Subgrid-Scale Stress Modelling based on the square of the velocity gradient tensor. Flow, Turbulence and Combustion. 62(3) (1999) 183-200.

[38] W.-W. Kim, S. Menon, Application of the localized dynamic subgrid-scale model to turbulent wall-bounded flows, in 35th Aerospace Sciences Meeting, 1997.

[39] X. Chai, K. Mahesh, Dynamic k-equation model for large eddy simulations of compressible flows, J. Fluid Mech. 699 (2012) 385-413.

[40] S. Menon, W. W. Kim, High Reynolds number flow simulations using the localized dynamic subgrid-scale model, in AIAA 34th Aerospace Sciences Meeting and Exhibit. AIAA Technical Paper1996-0425, 1996.

[41] P. R. Spalart, W.H. Jou, M. Stretlets, S. R. Allmaras, Comments on the feasibility of LES for wings and on the hybrid RANS/LES approach, in: Proceedings of the 1st AFOSR International Conference on DNS/LES, 1997.

[42] M. Strelets. Detached eddy simulation of massively separated flows, in: 39th Aerospace Sciences Meeting and Exhibit, Aerospace Sciences Meetings, 2001, 2001-0879.

[43] J.R. Forsythe, K.A. Hoffmann, R.M. Cummings, K.D. Squires, Detached-Eddy Simulation with compressibility corrections applied to a supersonic axisymmetric base flow, Journal of Fluids Eng., 124(4) (2002). 911–923.

[44] F.R. Menter, Review of the shear-stress transport turbulence model experience from an industrial perspective. Int. J. Comput. Fluid Dyn. 23(4) (2009) 305-316.

[45] R.D. Anderson, K.D. Fickie, IBHVG2 – A User's Guide, BRL-TR-2829, Ballistic Research Laboratory, Aberdeen Proving Ground, MD, USA, 1987. http://www.dtic.mil/docs/citations/ADB117104

[46] R.A. Otón-Martínez, F.J.S. Velasco, J.R. García-Cascales, F. Vera-García, F.J. Ramírez-Fernández, F.J. Bullón-Sánchez, D. Fernández-Moratilla, Drag assessment on projectiles with Base Bleed unit using CFD. Numerical simulation, experimental validation and lesson learnt, in: 28th International Symposium of Ballistics, 2014.

[47] P.L. Roe, Characteristic-based schemes for the Euler equations, Ann. Rev. Fluid Mech. 18 (1986) 337–365

[48] J. Mahaffy, B. Chung, F. Dubois, F. Ducros, E. Graffard, M. Heitsch, M. Henriksson, E. Komen, F. Moretti, T. Morii, P. Muhlbauer, U. Rohde, M. Scheuerer, B.L. Smith, C. Song, T. Watanabe, G. Zigh, Best Practice Guidelines for the Use of CFD in Nuclear Reactor Safety Applications, NEA/CSNI/R(2007)5. Organisation for Economic Cooperation and Development. www.oecd-nea.org/nsd/docs/2014/csni-r2014-11.pdf

[49] F. Menter, B. Hemstrom, M. Henriksson, R. Karlsson, A. Latrobe, A. Martin, P. Muhlbauer, S.B. Mscheuerer, T. Takacs, S. Willemsen, CFD Best Practice Guidelines for CFD Code Validation for Reactor-Safety Applications. ECORA, Contract FICKS-CT-2001-00154 2002.

[50] Weibel Scientific Solvang. MFTR-2100 Medium Range TSPI & Debris Radar. MFTR-2100/40 & MFTR-2100/43Specification. Report ID CS-1017-006. Weibel Doppler Radars. Allerød Denmark, 2010. www.weibel.dk

[51] ISO NORM, Guide to expression of uncertainty in measurement. Corrected and Reprinted, ISBN 92-67-10188-9. International Organization for Standardization, Geneva, Switzerland, 1995.

[52] J. Sahu, Supersonic flow over cylindrical afterbodies with base bleed, in: 24th aerospace sciences meeting AIAA Technical Paper AIAA-1986-0487, 1986.

[53] C.J. Bourdon, J.C. Dutton, Visualization of a central bleed jet in an axisymmetric compressible base blow, Phys of Fluids, 15(2) 499-510.

[54] P. Sagaut, Large eddy simulation for incompressible flows, Springer-Verlag Berlin and Heidelberg GmbH & Co. K, 2006.

[55] H.B. Toda, K. Truffin, F. Nicoud, Is the dynamic procedure appropiate for all SGS models?, in: V European Conference on Computational Fluid Dynamics, ECCOMAS CFD 2010. J.C.F. Pereira and A. Sequeira (Editors), Lisbon, Portugal, 14-17 June 2010.

6.2 Evaluation of different models for turbulent combustion of hydrogen-air mixtures. Large Eddy Simulation of a LOVA sequence with hydrogen deflagration in ITER Vacuum Vessel

In this work, CFD codes using two different LES combustion approaches were developed and tested with the purpose of modelling unsteady premixed combustion problems in presence of a turbulent field in three dimensional confined scenarios. These two approaches have been the *Flamelet Progress Variable* (LES-FPV) and the *Thickened Flame Model* (LES-TFM). These codes were developed using C++ CFD toolbox *OpenFOAM*.

With the aim of optimize the computational cost without compromising results accuracy, some numerical strategies as the *Dynamic Adaptive Chemistry* (DAC) with a detailed kinetic mechanism for hydrogen combustion and *in-situ Adaptive Tabulation* (ISAT) methods were proposed and benchmarked, being both applicable for the LES-TFM approach because of being a finite-rate based combustion model. Moreover, in both cases, an adaptive meshing technique was used with the aim of tracking the flame front to ensure an adequate spatial resolution in this region.

An experimental validation was performed to assess the ability of the different studied approaches to predict the flame burning speed, flame acceleration, and pressure evolution for lean H_2-Air volume percent mixtures from 16 to 28% propagating within a turbulent field. The experiments presented by Goulier et al. provided combustion data in a well-characterized turbulence field inside the spherical vessel. Based on these data, simulations were carried out to assess the capabilities of the combustion models for predicting turbulent burning speeds. In order to create a turbulent field inside the vessel, models for replicating the spherical bomb with the eight impellers where developed, comparing the turbulence fields simulated by the models against those characterized in the experiments.

Results revealed that both approaches led to accurate predictions in terms of flame burning speed when compared to the experiments. When considering DAC and ISAT methods with detailed chemistry, LES-TFM model was found to be a cost-efficient solution, despite of requiring a chemical mechanism.

In addition, once the CFD codes were validated, the LES-TFM model was used to analyze two loss of vacuum accident (LOVA) sequences within ITER VV: a quiescent case (absence of breach) and a turbulent case (with the presence of a breach), in which the effect of the vessel loss of vacuum, which produces a turbulent field within the vessel as it is filled by air, is considered. Results showed that turbulence might increase the flame burning speed by a factor of up to 3.5 for the case of big breaches (0.15 m^2) but it would not affect in case of breaches of 0.02 m^2. Besides, results showed that autoignition with 2 kg of H_2 within the VV at 13.35 kPa might degenerate in detonation with average wall pressure levels around 70 kPa. This way, a key tool has been developed and validated to be applied in future analysis of ITER or other nuclear safety scenarios.

Evaluation of different models for turbulent combustion of hydrogen-air mixtures. Large Eddy Simulation of a LOVA sequence with hydrogen deflagration in ITER Vacuum Vessel.

Francisco Nicolás-Pérez[1]
Universidad Politécnica de Cartagena, Dr. Fleming s/n, 30202 Cartagena, Spain

FJS. Velasco[2]
Universidad Politécnica de Cartagena, Dr. Fleming s/n, 30202 Cartagena, Spain

José R. García-Cascales
Universidad Politécnica de Cartagena, Dr. Fleming s/n, 30202 Cartagena, Spain

Ramón A. Otón-Martínez
University Centre of Defence at the Spanish Air Force Academy, MDE-UPCT. C/Coronel López Peña s/n, 30720, San Javier, Spain

Ahmed Bentaib
Institut de Radioprotection et Sûrete Nucléaire, 31 Av. de la Division Leclerc, 92260 Fontanay-aux-Roses, France

Nabiha Chaumeix
ICARE, CNRS-INSIS, 1C Avenue de la recherche scientifique, 45071 Orléans Cedex 2, France

ABSTRACT

The modelling of premixed combustion in the presence of a turbulent field in three-dimensional (3-D) confined scenarios was studied in this work, and applied to hydrogen combustion within ITER vacuum vessel (VV). Two different combustion approaches were tested with Large Eddy Simulation: a Flamelet Progress Variable (LES-FPV) and a Thickened Flame Model (LES-TFM). For the case of LES-TFM modelling, Dynamic Adaptive Chemistry (DAC) with a detailed kinetic mechanism for hydrogen combustion and in-situ adaptive tabulation (ISAT) methods were employed. Moreover, an adaptive meshing technique was used with the aim of tracking the flame front to ensure an adequate spatial resolution in this region. Experimental validation was performed to assess the ability of the different studied approaches to predict the flame burning speed, flame acceleration, and pressure evolution for lean H_2-Air volume percent mixtures from 16 to 28% propagating within

[1] Corresponding author, present address: fnperez@lynxsimulations.com, Research engineer. Lynx Simulations,www.lynxsimulations.com, Calle del Metal 4, 30009, Murcia, Spain
[2] Corresponding author, present address: fjavier.sanchez@upct.es, Associate Professor.

a turbulent field. Results revealed that both approaches led to accurate predictions in terms of flame burning speed. When considering DAC and ISAT methods with detailed chemistry, LES-TFM model was found to be a cost-efficient solution. This model was used to analyse two loss of vacuum accident (LOVA) sequences within ITER VV. Results showed that turbulence might increase the flame burning speed by a factor of up to 3.5 for the case of big breaches (0.15 m^2) but it would not affect in case of breaches of 0.02 m^2. Besides, results showed that autoignition with 2 kg of H_2 within the VV at 13.35 kPa might degenerate in detonation with average wall pressure levels ~70 kPa.

KEYWORDS: hydrogen; premixed combustion; Large-Eddy Simulation; detailed chemistry; Thickened Flame Model; LOVA.

1. INTRODUCTION

Premixed and partially premixed turbulent combustion are highly complex processes in which turbulence, chemical reaction, and their respective interactions, are key aspects. Many accident safety studies, including those related to ITER (International Thermonuclear Experimental Reactor), require predictive modelling of turbulent combustion, which involves the coupling between turbulence and chemistry. Flame alters the turbulence characteristics of the flow, whereas turbulence also affects the flame structure and the combustion dynamics [1]. Reynolds Averaged Navier-Stokes (RANS) based combustion models have been successful in predicting gross features of combustion, but they have difficulties to predict transient phenomena, such as combustion instabilities, cycle-to-cycle variations, self-ignition, and pollutant emission [2]. In this manner, Large Eddy Simulations (LES) based combustion models are a promising alternative, demonstrating abilities that can be used to predict such flow unsteadiness. The improvements in the computational power in the last two decades have made LES an alternative to Direct Numerical Simulation (DNS) and RANS. In LES, large scale eddies, which are the most energetic, are directly resolved whereas small scales need to be modelled. LES seems to provide a semi-precise description of turbulence dynamics with an efficient computational compromise [3]. Several models are available for modelling turbulence in the sub-grid scale (SGS) with LES. In the case of reacting flows, not only the small eddies have to be modelled, but also the filtered mixing and some chemical source terms require closure modelling since the reaction zone is often not well resolved on LES grids. Thus, the characteristic length scale for the reaction processes can be below the filter length scale, especially in high Damköhler and high Reynolds numbers regime [4]. In addition, in many engineering applications, the combustion regime is in the called "thin-reaction zones" [5]. In these cases, the Karlovitz number (Ka) is above the unity, which means that the turbulent scales are smaller than the thermal flame thickness, and thus, turbulence can penetrate and alter the pre-heat zone but without affecting the thin reaction region. Chatakonda et al. [6] noted that there have been fewer validations reported for this combustion regime ($Ka > 1$).

Tracking methods applied to the flame front and simple chemistry assumptions can be employed for predicting characteristics of premixed flames without a strong presence of turbulence. On the other hand, some of the key aspects in turbulent combustion involve unsteady phenomena which are difficult to predict, as blowoff, quenching and autoignition [7],[8]. Emami et al. [9] showed that flame-vortex interaction, together with the consequent flame folding and wrinkling, are the main mechanisms for the increase in flame surface area and speed, in the slow-flame regime. In addition, during the flame acceleration, a turbulent flame might create ignition centres in nearby unreacted material, ahead of the flame front [10],[11]. In turbulent flames, the variation of the overall turbulent flame speed is the result of the interplay between turbulence, which increases flame surface continuously, and the frequent collision between embedded flame segments, which consumes the flame's surface [12]. Additionally, the flame acceleration rate can also be enhanced by external turbulence and the Darrieus-Landau flame instability [13]. Therefore, in order to obtain a proper simulation of turbulent flame physics, detailed modelling of turbulence is highly recommended. For high-Reynolds-number problems, DNS is a useful but still limited tool due to its computational cost. By contrast, LES is presented as a solution that is giving satisfactory results with reasonable accuracy [3], especially in the flamelet regime. However, no results are found in the open literature regarding the suitability of LES under the thin reaction combustion regime.

Several combustion models within the LES framework have been developed. For some models, known as Flamelet Progress Variable (LES-FPV), the burning speed is modelled from geometrical properties of the flame and by linking variables based on the physical properties of the flame front region. The LES g-equation [14],[15], and the Flame Surface density [4],[16] methods belong to this group. In addition, there is another family of methods focused on modelling the filtered reaction rates: the Finite Rate Chemistry models (LES-FRC), that include the Thickened Flame Model (LES-TFM) [17], the Partially Stirred Reactor model (LES-PaSR) [18], the Eddy Dissipation Concept (LES-EDC) [19], the Probability/Filtered Density Function (LES-PDF/FDF) [20], the LES Conditional Moment Closure (LES-CMC) [21], the Linear Eddy Models (LES-LEM) [22], or the Implicit LES (ILES), which assumes that the sub-grid domain has a homogeneous concentration and temperature [23]. A key aspect that must be considered about LES-FRC modelling is reaction kinetics. A detailed description of the chemical reactions and sub-reactions present during the combustion process is mandatory in order to properly predict the combustion dynamics and different phenomena such as induction, transition from laminar to turbulence flame, chain branching kinetics, or extinction [24],[25]. Over and above, detailed kinetic models consider endothermic initiation reactions and chain-branching reactions. The chain initiation and branching stages have well-defined times for induction zones, followed by the stage for exothermic reactions of chain recombination or termination reactions [26]. Some of these mechanisms were reported by Williams [8], Rogers et al. [27], or Marinov et al. [28]. Slack & Grillo [29]. Schultz & Shepherd [30] obtained induction times for hydrogen-air combustion experiments at atmospheric pressure, confirming the induction time increases as the ignition temperature reduces from 1100K to 900K. Experiments by Lee et al. [31],[32] on DDT in tubes filled with obstacles, led to the introduction of the characteristic regimes of flame propagation, and a better comprehension of flame structure. As for combustion at sub-atmospheric pressure conditions, Kuznetsov et al. [33] characterized the flammability limits of hydrogen-air mixtures in a spherical enclosure in the range from 2.5 to 100 kPa. Sabard et al. [34] also studied the same problem in a spherical bomb, characterizing the activation energy for initial pressures from 50 to 100 kPa. These studies at sub-atmospheric pressure are especially important in the study of ITER accident scenarios. In the case of loss of vacuum accident (LOVA) within the ITER vacuum vessel (VV), conditions might degenerate into a potential hydrogen deflagration sequence [35],

[36],[37]. The sequence might even include a dust explosion, increasing the potential impact of the accident.

As indicated, hydrogen safety is a key issue in ITER. During its operation, the in-vessel hydrogen inventory is highly dynamic and results from the balance of the fuelling rate considering the burn-up fraction and the exhaust gas rate [38]. However, in the case of an accident, part of the metallic dust of Tungsten and Beryllium in the VV might react and generate hydrogen what would increase dramatically the in-vessel H_2 inventory [39]. For example, an ex-vessel LOCA (Loss of Coolant Accident) would lead to high temperatures and failure of not-sufficiently-cooled in-vessel components, which might result in waterspill into the VV and a release of H_2 from the cryopumps. A break of the water cooling circuit of an in-vessel component might also generate a similar effect [40]. Steam may react with metallic dust on hot surfaces (over 400ºC) producing hydrogen [41]. According to Day et al. [38], the hydrogen release from the surfaces would need around six seconds to start. After that, H_2 release is assumed to be fast (around 2 kg/s) [43].

The ITER safety approach is to limit the amount of hydrogen such that the resulting pressure in case of an explosion accident is compatible with the design criteria of the VV. An administrative limit of metallic dust on hot plasma-facing surfaces is set to avoid the production of more than 5 kg hydrogen [44]. In that study, the author analyzed theoretically the potential risk and concluded that 5 kg of hydrogen uniformly mixed in the vacuum vessel with air at 1.0 bar would lead to concentrations below the flammability limit of 4 vol.%. In the last update, the limit was fixed in 4 kg of hydrogen [40]. However, in the case of air ingress into a hydrogen-containing vessel, the hydrogen concentration unavoidably passes through flammability and detonation range during its pressurization. At the beginning of the pressurization, hydrogen concentration is over the upper flammability limits, but the mixture inside the VV becomes flammable when it reaches this limit, which extends from 80% H_2 at 200-500 mbar pressures to 75% H_2 at 1000 mbar [45]. According to the theoretical estimations by Kuznetsov et al. [45], maximum adiabatic combustion pressure may exceed the design pressure of ITER VV (i.e., 2 bar) with inventories of 4 kg of H_2, when the mixture ignites at the pressure over 400 mbar. Indeed, Kuznetsov et al. [46] had performed large-scale hydrogen ignition experiments in an 8.8 m^3 vessel, as well as combustion experiences at reduced pressures, in the presence of a turbulent air jet injected into a hydrogen atmosphere. They found that for mixtures with a partial hydrogen pressure of 0.2 bars at 293 K and initial ignition pressures over 0.33 bars, final combustion pressures would reach values over 2 bars. They also showed that the required experimental ignition energies ranged 0.003-10 J. Kuznetsov et al. [33] also showed through experiments that the minimum ignition pressure was below 50 mbar for hot wire ignition, for H_2 mixtures between 4% and 45%.

Besides, it must be also considered that, even if the in-vessel average H_2 mixture is below critical values, during a LOVA, the entrained air pushes the hydrogen mass what may generate burnable clouds with local rich H_2 mixtures [36]. These cases are also of concern for ITER safety analysis [44][40].

In order to reduce the risk of explosion, it is considered the installation of mitigation solutions based on either igniters within the VV, which would ignite the mixture as soon as the lower flammability limit is reached, resulting in harmless low-pressure combustion, or a rapid injection of an inert gas into the vessel, such as nitrogen, triggered by the detection of air ingress into the vessel [47][40][41][43]. In this sense, Chuyanov and Topilski [48] review the possible penetrations in the ITER VV during a LOVA and postulated the possibility of air leakage through

one of the biggest windows, with cross section 0.02 m^2. This area was also considered in other accident studies [43][49]. Reyes et al. [49] simulated with MELCOR a large ex-vessel divertor pipe break with H_2 generation of 1.4 kg in the VV. Thanks to the actuation of the VV pressure suppression system, the maximum VV pressure might be limited to 151 kPa (below the design limit). Xiao et al. [43] considered an accident sequence with an initial temperature at the surfaces of VV, DV ports, and NBI ports of 373-470 K. They assumed an initial pressure in the VV sub-volumes of 500 Pa with an average temperature of 500 K. Under these conditions, they predicted that the nitrogen injection system would generally prevent the risk of hydrogen detonation and fast deflagration.

Considering the H_2 flammability limits discussed above and the initial conditions of the LOVA scenario, a CFD study can help to evaluate the consequences of air ingress and ignition of the reactive H_2 mixture within the VV. As indicated by Taylor et al. [40], in the last update of the licensing, a CFD study is needed with realistic assumptions, taking into account the location and dynamics of the postulated air leak, coolant leak, and hydrogen production and subsequent deflagration. This is the main objective of the present work.

For this purpose, to assess the suitability, advantages, and limitations of LES-FPV and LES-TFM models to predict hydrogen turbulent combustion dynamics in confined scenarios are analysed. Both approaches are evaluated against the experimental data reported by Goulier et al. [50][51]. Those experiments were carried out in a 95-liters spherical vessel, which is equipped with a Schlieren measurement technique to measure the flame surface evolution, as well as a Particle Image Velocimetry system to measure the velocity field within the vessel. Moreover, the vessel was equipped with fans in order to generate a controlled turbulent field where the flame propagates.

This article is organised as follows: firstly, a theory section describes in detail the conservation equations and turbulence models governing the physics for the problem; then, the numerical models and methodology are presented. Secondly, the results of the benchmark of these models against experimental data are presented, for the case of initial calm conditions within a spherical vessel (hereafter referred to as cases under “quiescent conditions”). Then, experiments including fans to generate initial turbulence are used to check the model’s ability to reproduce initial turbulent fields. Later, a section is presented where turbulent combustion experiments are modelled, and the numerical results are discussed. Finally, the article shows how one of the validated models was applied to analyse two H_2-Air combustion accident sequences inside ITER VV.

2. THEORY

2.1. GOVERNING EQUATIONS

Different combustion modelling approaches within the LES framework are used in the study presented hereinafter. On the one hand, an LES-FPV model is chosen as a flame tracking technique model. In these models, the turbulent flame speed has to be modelled as a function of the resolved and modelled interface properties. On the other hand, LES-TFM is also used. Since both modelling techniques are developed for LES, the main governing equations employed are the Favre averaged form. They are obtained by means of a density-weighted filtering procedure [52] of the dependent variables of the Navier-Stokes Equations, yielding in the mass (1), momentum (2), and energy (3) conservation equations for compressible flow.

$$\frac{\partial \bar{\rho}}{\partial t} + \nabla \cdot (\bar{\rho}\widetilde{\boldsymbol{u}}) = 0 \tag{1}$$

$$\frac{\partial (\bar{\rho}\widetilde{\boldsymbol{u}})}{\partial t} + \nabla \cdot (\bar{\rho}\widetilde{\boldsymbol{u}} \otimes \widetilde{\boldsymbol{u}}) = -\nabla \bar{p} + \nabla \cdot (\overline{\boldsymbol{S}} - \boldsymbol{B}) \tag{2}$$

$$\frac{\partial \bar{\rho}\widetilde{h_s}}{\partial t} + \nabla \cdot \left(\bar{\rho}\widetilde{\boldsymbol{u}}\widetilde{h_s}\right) = \overline{\boldsymbol{S}} \cdot \nabla \widetilde{\boldsymbol{u}} + \frac{\partial \bar{p}}{\partial t} + \nabla \bar{p} \cdot \widetilde{\boldsymbol{u}} + \nabla \cdot \left(\overline{\boldsymbol{h}} - \boldsymbol{b}_h\right) + \bar{\rho}\tilde{\sigma} - \sum_{k=1}^{NGSP} \left(\widetilde{\dot{\omega}_k} h_{f,k}^0\right) \tag{3}$$

Where the $\bar{\cdot}$ and $\tilde{\cdot}$ are the filtered and FAVRE Filtered quantities, which follow the equality of $\bar{\rho}\tilde{\phi} = \overline{\rho\phi}$. Thus, $\bar{\rho}$, $\widetilde{\boldsymbol{u}}$, $\widetilde{h_s}$, and $\bar{p}$ represent the mixture density, velocity vector, sensible enthalpy, and pressure of the gas mixture. $h_{f,k}^0$ denotes the k specie formation enthalpy and $\widetilde{\dot{\omega}_k}$ is the filtered reaction rate for this specie. $\overline{\boldsymbol{S}}$ is the viscous stress tensor, $\overline{\boldsymbol{h}}$ the heat flux vector, $\boldsymbol{B} = \bar{\rho}\left(\widetilde{\boldsymbol{u} \otimes \boldsymbol{u}} - \widetilde{\boldsymbol{u}} \otimes \widetilde{\boldsymbol{u}}\right)$ the unresolved sub-grid stress tensor, $\boldsymbol{b}_h = \bar{\rho}\left(\widetilde{\boldsymbol{u}h_s} - \widetilde{\boldsymbol{u}}\widetilde{h_s}\right)$ is the unresolved sub-grid heat flux vectors which result when applying the filtering technique to the convective terms. In this work, the mixture was assumed to be a Newtonian fluid, thus $\overline{\boldsymbol{S}} \approx 2\mu \cdot dev(\bar{S})$ and $\overline{\boldsymbol{h}} \approx D_{th}\nabla\tilde{T}$, where μ is the molecular viscosity, $dev(\bar{S})$ is the deviatoric part of the resolved rate strain tensor and D_{th} is the thermal diffusivity. Regarding the unclosed terms of these FAVRE equations, an SGS turbulence model is needed. Thus, the large-scale flow field is directly solved from the FAVRE filtered Navier-Stokes equations [52], whereas the small scale stresses were modelled. Besides, the gas phase is assumed to behave as an ideal gas with the equation of state $\bar{p} = \bar{\rho}\left(\sum_{k=1}^{NGSP} \widetilde{Y_k} \frac{R_u}{M_k}\right)\tilde{T}$.

2.1.1. The LES-FPV model

The LES-FPV model used in this work is based on the RANS model formulated by Weller [53],[54] which was adapted to LES by Tabor and Weller [4]. It was formulated using Conditional Filtering techniques to derive the different transport equations, in analogy to the conditional averaging method used for RANS. This model is eventually used as an alternative to the well-known LES g-equation model [15],[54]. The Weller LES-FPV model is constructed by solving variables that describe the geometrical properties of the surface that are linked with the flame front propagation [54]. Particularly for the two-equation formulation of this model, these variables were the combustion indicator function ($\tilde{b}$), used as a flame tracker, and the sub-grid wrinkling denoted as Ξ. These variables were used in conjunction with different approaches for estimating the stretched laminar flame speed S_L. Thus, two transport equations were formulated. The first one considers the indicator function $\tilde{b}$. It is defined as $\tilde{b} = \frac{\widetilde{\rho_u}}{\bar{\rho}}\bar{b}$, where $\overline{\rho_u}$ and $\bar{\rho}$ stands for unburnt density and mass-weighted density respectively, and $\bar{b}$ is the filtered regression variable, which is linked to the standard filtered combustion progress variable: $\bar{b} = 1 - \bar{c}$. This way, the transport equation considered in the study was [4]:

$$\frac{\partial \bar{\rho}\tilde{b}}{\partial t} + \nabla \cdot \left(\bar{\rho}\widetilde{\boldsymbol{u}}\tilde{b}\right) - \nabla \cdot \left(\bar{\rho}\widetilde{D}\nabla\tilde{b}\right) = -\overline{\rho_u} S_L \Xi \left|\nabla\tilde{b}\right| \tag{4}$$

Note that both $\bar{b} \in [0, 1]$ and $\widetilde{b} \in [0,1]$. In this case, 0 corresponds to fully unburnt and 1 to the fully burnt phase. The term $\widetilde{D}$ represents the addition of the molecular and SGS mass diffusivity

terms. Note that $\widetilde{b}$ (or $\bar{b}$) provides a measure of the grid-scale (resolved) geometry of the flame surface.

It is also necessary to model variables for the unresolved interface properties, as the sub-grid flame wrinkling factor Ξ, which represents the total sub-grid surface area divided by the smoothed surface area. In this manner, it is possible to model the sub-grid turbulent flame speed from the stretched laminar flame speed and the degree of wrinkling, by means of $S_T = \Xi \cdot S_L$. The simplified transport equation, proposed by Tabor and Weller [4] for this property is expressed as:

$$\frac{\partial \Xi}{\partial t} + \widetilde{\boldsymbol{U}_S}\,\nabla\Xi = G\Xi - R(\Xi - 1) + max[(\sigma_s - \sigma_t, 0)]\Xi \tag{5}$$

In this equation, there are terms that represent the effects of strain, propagation, and differential propagation on the sub-grid scale flame wrinkling Ξ. The differential propagation takes into account the process of flame interface distortion and cusp formation in the flame front. $\widetilde{\boldsymbol{U}_S}$ is the surface-filtered resolved velocity, σ_s and σ_t represent, respectively, the surface-filtered resolved strain rate and resolved strain rate, calculated from the rest of the variables as:

$$\begin{aligned}\sigma_s = \frac{1}{2}\left\|\nabla\widetilde{\boldsymbol{U}_I} + \widetilde{\nabla\boldsymbol{U}_I}^{T}\right\| \\ \cong \frac{\nabla\cdot\tilde{\boldsymbol{u}} - \boldsymbol{n_f}\cdot(\nabla\tilde{\boldsymbol{u}})\cdot\boldsymbol{n_f}}{\Xi} \\ + \frac{(\Xi+1)\left[\nabla\cdot(S_L\boldsymbol{n_f}) - \boldsymbol{n_f}\cdot\left(\nabla\cdot(S_L\boldsymbol{n_f})\right)\cdot\boldsymbol{n_f}\right]}{2\Xi}\end{aligned} \tag{6}$$

$$\sigma_t = \frac{1}{2}\left\|\nabla\widetilde{\boldsymbol{U}_t} + \widetilde{\nabla\boldsymbol{U}_t}^{T}\right\| \cong \nabla\cdot\left(\tilde{\boldsymbol{u}} + S_L\Xi\boldsymbol{n_f}\right) - \boldsymbol{n_f}\cdot\left(\nabla\left(\tilde{\boldsymbol{u}} + S_L\Xi\boldsymbol{n_f}\right)\right)\cdot\boldsymbol{n_f} \tag{7}$$

Where $\widetilde{\boldsymbol{U}_t}$, $\widetilde{\boldsymbol{U}_I}$, and $\boldsymbol{n_f}$ represent the overall propagation velocity, the surface filtered velocity of the flame front (interface), and a unit vector in the grid-scale interface direction (grid-scale flame propagation), respectively.

The terms $(G\Xi)$ and $(R(\Xi-1))$ in the Eq. (5) represent the generation and dissipation of sub-grid wrinkling. In this work, simple algebraic models were considered for the computation of G and R [4]. The approach was based on the turbulent flame speed correlation obtained by Gülder [55], which showed particularly good results when compared with full spectral solutions [4],[54]. Thus, the terms G and R are calculated as $G = R\frac{\Xi_{eq}-1}{\Xi_{eq}}$ and $R = \frac{0.28}{\tau_\eta}\frac{\Xi_{eq}{}^{*}}{\Xi_{eq}{}^{*}-1}$, with $\Xi_{eq} = 1 + 2\left(1-\bar{b}\right)\left(\Xi_{eq}{}^{*}-1\right)$ and $\Xi_{eq}{}^{*} = 1 + 0.62\sqrt{\frac{u'_\Delta}{S_L}}Re_\eta$. τ_η is the Kolmogorov time scale computed as $\tau_\eta = \frac{\mu_u}{\rho_u\varepsilon_\Delta}$, where the subscript "$u$" stands for the properties of the unburned gas and Re_η is the Reynolds number at Kolmogorov's scale. The sub-grid turbulence intensity was defined as $u'_\Delta = \sqrt{\frac{2}{3}k_\Delta}$ where the values of ε_Δ and k_Δ are the sub-grid scale dissipation rate and kinetic energy, being both computed depending on the turbulent SGS model employed.

In order to complete the system, these equations are solved in conjunction with the continuity (Eq. 1), momentum (Eq. 2), and energy equations (Eq. 3). In this model, two energy transport

equations are considered instead of the sensible enthalpy (Eq. 3): one for the FAVRE-filtered absolute enthalpy of the mixture, denoted as $\tilde{h}_{ma}$ and other for the FAVRE-filtered absolute enthalpy of the unburned gas $\tilde{h}_{ua}$. The mixture density is estimated as $\bar{\rho} = \overline{\rho_u}\bar{b} + \overline{\rho_c}(1-\bar{b})$. Temperatures for both phases were thus obtained, from the thermo-physical properties of the reactant mixture and combustion products. In both cases they are treated as homogeneous mixtures, and densities and molecular viscosities were obtained from these temperatures.

2.1.2. The LES-TFM model

The second combustion approach considered in this work is the Thickened Flame approach (LES-TFM) which belongs to the Finite-Rate Chemistry combustion models. The key novelty of the model consists in multiplying the thermal and mass diffusivities by a factor F, decreasing the pre-exponential factors, and thus, the reaction rates, by the same factor. This procedure results in a flame that is propagated at the same laminar flame speed ($S_L \propto \sqrt{D\dot{\omega}}$) where D denotes the laminar mass diffusivity, but with a laminar flame thickness F times increased ($\delta_L \propto \sqrt{D/\dot{\omega}}$). Thus, this modelling procedure has the advantage of eliminating the need for ad-hoc sub-models for ignition and flame-wall interactions [4]. Nevertheless, it alters the flame propagation physics, since the Damköhler number is reduced [56]. In order to overcome this disadvantage, an efficiency function, denoted as E_Δ is introduced. Thus, the set of equations employed for this model are the continuity (1), momentum (2) and energy (3) for the gas phase in their FAVRE-averaged form, as well as modified transport equations for the mass fraction of each species involved in the reaction kinetics (*NGSP*). These modified transport equations take the form:

$$\frac{\partial \bar{\rho}\widetilde{Y_k}}{\partial t} + \nabla \cdot \left(\bar{\rho}\tilde{\boldsymbol{u}}\widetilde{Y_k}\right) = \nabla \cdot \left(\bar{\rho} \cdot \left[FE_\Delta \widetilde{D} + (1-S)\cdot \widetilde{D}_{sgs}\right] \cdot \nabla \widetilde{Y_k}\right) + \frac{E_\Delta}{F}\dot{\omega}_k \qquad (8)$$

with $1 \leq k \leq NGSP - 1$. In this equation, the term $\widetilde{D}$ represents the molecular mass diffusivity, and $\widetilde{D}_{sgs}$ stands for the sub-grid scale mass diffusivity, computed as $\widetilde{D}_{sgs} = \frac{\nu_{sgs}}{Sc_t}$. It only affects the region which is not being thickened due to the TFM combustion model. It is worth to be noted that the Eq. (8) was simplified assuming the Hirschfelder and Curtiss approximation [57], that considers the mass diffusion coefficient for each of the species. The equations are simplified using the Fick's law, assuming equality of binary diffusion coefficients for all of the species [58]. S denotes a flame sensor function, which detects the flame with the aim of ensuring that the artificial thickening procedure does not affect the regions of pure mixing (non-reacting zone). In this work, the thickening factor is determined dynamically using this flame sensor as suggested by Durand and Polifke [59]: $S = 16 \cdot [c(1-\tilde{c})]^2$, with $\tilde{c} = 1 - \tilde{Y}_{H2}/Y_{H2(u)}$, being $Y_{H2(u)}$ the unburnt (fresh) H_2 mass fraction of the mixture. This flame sensor results in a local dynamic thickening factor calculated locally as $F = 1 + S(F_{max} - 1)$. The influence of varying the thickening factor (F_{max}) will be discussed later in this work.

The efficiency function (E_Δ) implemented in this work is the power-law wrinkling model proposed by Charlette et al. [60]. In this model, the power-law is a relationship of the ratio of outer (Δ) to inner (η_c) cutoff scale defined as $\Xi_\Delta = \left(1 + \frac{\Delta}{\eta_c}\right)^\beta$. In this case, the efficiency function is calculated as:

$$E_\Delta = \left(1 + min\left[\frac{\Delta}{\delta_L^0} - 1, 0\right] \cdot \Gamma_\Delta\left(\frac{\Delta}{\delta_L^0}, \frac{u'_\Delta}{S_L^0}, Re_\Delta\right)\frac{u'_\Delta}{S_L^0}\right)^\beta \quad (9)$$

The wrinkling of the function $\Gamma_\Delta\left(\frac{\Delta}{\delta_L^0}, \frac{u'_\Delta}{S_L^0}, Re_\Delta\right)$ takes the form:

$$\Gamma_\Delta\left(\frac{\Delta}{\delta_L^0}, \frac{u'_\Delta}{S_L^0}, Re_\Delta\right) = \left[\left(\left({f_u}^{-a} + {f_\Delta}^{-a}\right)^{-1/a}\right) + {f_{Re}}^{-b}\right]^{-1/b} \quad (10)$$

where $f_u = 4\left(\frac{27C_k}{110}\right)^{1/2}\left(\frac{18C_k}{55}\right)\left(\frac{u'_\Delta}{S_L^0}\right)^2$, $f_\Delta = \left[\frac{27C_k\pi^{4/3}}{110} \cdot \left(\left(\frac{\Delta}{\delta_L^0}\right)^{4/3} - 1\right)\right]^{1/2}$

and $f_{Re} = \left[\frac{9}{55}exp\left(-\frac{3}{2}C_k\pi^{4/3}{Re_\Delta}^{-1}\right)\right]^{1/2} \cdot {Re_\Delta}^{1/2}$. In these expressions,

$a = 0.6 + 0.2 \cdot exp\left[-0.1\left(\frac{u'_\Delta}{S_L^0}\right)\right] - 0.2 \cdot exp\left[-0.01\left(\frac{\Delta}{\delta_L^0}\right)\right]$ and $b = 1.4$. The Kolmogorov constant C_k was set to 1.5 [60].

The subscale turbulence intensity u'_Δ at the scale of the test filter scale Δ is calculated from the resolved velocity at Δ_{mesh} scale as $u'_\Delta = C_2{\Delta_{mesh}}^3|\nabla^2(\nabla \times \widetilde{\boldsymbol{u}})|\left(\frac{\Delta}{10*\Delta_{mesh}}\right)^{1/3}$, with a value of $C_2 = 2.0$ as proposed by Colin et al. [61]. The term $\left(\frac{\Delta}{10*\Delta_{mesh}}\right)^{1/3}$ is added to the original expression, which was designed to estimate the turbulent intensity corresponding to scales below the outer cutoff scale (Δ), omitting thus the contribution of the thermal expansion which is not related to turbulence. The filter scale turbulent Reynolds was computed as $Re_\Delta = \frac{u'_\Delta \Delta}{\nu}$.

The formulation Charlette model differs from the original formulation presented in [60] due to the replacement of $min\left[\frac{\Delta}{\delta_L^0}, 0\right]$ by $min\left[\frac{\Delta}{\delta_L^0} - 1, 0\right]$ as proposed in [62]. This is done in order to maximize the wrinkling factor Ξ_Δ by the fractal model ${\Xi_\Delta}^{max} = (\Delta/\delta_L^0)^\beta$ [63],[64]. The flame laminar flame thickness δ_L^0 was estimated for each computational cell with the relationship $\delta_L^0 \approx \frac{4 \cdot \nu}{S_L^0}$ [60]. In this work, the values obtained with this expression are compared with the laminar flame thicknesses measured from the experiments. Regarding the exponential factor (β), the constant and dynamic formulations are assessed in this work. In the case of assuming a constant value, it was set to β=0.5 according to the value proposed in [60]. In the case of the dynamic exponential factor, the formulation suggested in [60] is also considered.

2.1.3. Estimation of transport coefficients and Lewis numbers

Regarding the mass diffusion values, in the present work, Fick's law assumption is adopted, assuming the same molecular diffusivity for all the species. An effective Lewis number of the mixture is evaluated and provided in [51] for each of the H_2/Air mixtures analysed. Thus, the molecular diffusivity is calculated from the thermal diffusivity of the mixture D_{th} as $D_k = \frac{D_{th}}{Le}$, being D_{th} calculated from the conductivity and heat capacity of the mixture. The thermal conductivity was computed using the modified Eucken correlation for polyatomic gases as $\lambda = \mu C_v\left(1.32 + \frac{1.77 \cdot R_s}{C_v}\right)$, where R_s is the specific gas constant and C_v is the specific heat capacity of the mixture at constant volume. This specific heat is obtained by considering the heat capacities

of each of the mixture components. Heat capacities and specie formation enthalpies are assumed to be a function of temperature using *JANAF* polynomials. The polynomials coefficients are obtained from McBride et al.[65], and are considered to be valid for combustion modelling in a wide temperature range, being necessary to use the coefficients for all the components involved in the chemical kinetics considered in the case of the LES-TFM modelling. In the case of the LES-FPV modelling, a homogeneous mixture with only two species is considered, being reactants and products states. In such a case, coefficients for both states are obtained considering the different H_2-air mixtures studied in this work, being calculated from the coefficients for H_2, O_2 N_2, and H_2O. Finally, the molecular dynamic viscosity is calculated using Sutherland's law [66] as $\mu = A_S \frac{T^{1/2}}{(1+T_S/T)}$ with $A_S = 1.67212 \cdot 10^{-6}\ \frac{kg}{m \cdot s \cdot K^{1/2}}$ and $T_S = 170.672K$.

2.2. SGS TURBULENCE MODELLING

The SGS stresses are modelled using the one-equation eddy viscosity model (k_{sgs}-Equation), based on the Eddy viscosity assumption. Thus, the anisotropic part of the SGS stress tensor B_{ij} is approximated by relating it to the deviatoric part of the resolved rate of strain tensor $\overline{S_{ij}}$ and postulating a linear relationship between these terms as:

$$B_{ij} - \frac{1}{3} B_{kk} \delta_{ij} \approx -2 \nu_{sgs} dev(\overline{S})_{ij} \tag{11}$$

where ν_{sgs} is the SGS eddy viscosity which is calculated as:

$$\nu_{sgs} = C_k \Delta_{mesh} \sqrt{k_{sgs}} \tag{12}$$

C_k is set to the default value of 0.094 and Δ_{mesh} is the subgrid length scale (filter width) computed from the cell volume as $\Delta_{mesh} = (\Delta x \Delta y \Delta z)^{1/3}$. In this model, a transport equation for k_{sgs} is developed to overcome the deficiency of local balance assumption in algebraic eddy viscosity models. Thus, a transportation equation is derived to account for the historic effect of k_{sgs} due to production, dissipation, and diffusion as follows:

$$\frac{\partial}{\partial t}\left(\rho k_{sgs}\right) + \vec{\nabla} \cdot \left(\rho k_{sgs} \vec{u}\right) = \nabla \cdot \left(\rho \nu_{eff} \nabla k_{sgs}\right) - \rho B_{ij} : \bar{S}_{ij} - C_\varepsilon \frac{\rho {k_{sgs}}^{3/2}}{L_S} \tag{13}$$

with C_ε, set to its default constant value of 1.048.

2.3. LAMINAR FLAME SPEED AND CHEMICAL KINETICS MODELLING

In the case of the LES-FPV modelling in which no chemical kinetics are computed, values for the stretched laminar flame speed (S_L) are required. Therefore, it is necessary to calculate properly these values in order to obtain accurate turbulent flame speeds predictions. This is one of the key inputs of this combustion model.

Both unstretched laminar flame speed (S_L^0) and Markstein (L_b) lengths for each of the mixtures analysed are obtained from experiments [34]. Thus, it is possible to compute the stretched laminar flame speed locally from the surface filtered resolved strain rate σ_s, since the Markstein lengths are provided. Nevertheless, in order to take into account the strain effects on the laminar flame speed, Tabor & Weller [4] proposed to use the following equation:

$$\frac{\partial S_L}{\partial t} + \widetilde{\boldsymbol{U}_S}\,\nabla S_L = -\sigma_s S_L^{\infty}\frac{(S_L^0 - S_L)}{(S_L^0 - S_L^{\infty})} \tag{14}$$

where S_L is the estimated value of the laminar flame speed which considers the strain effects and the transport phenomenon. S_L^{∞} is obtained assuming that the laminar flame speed is in local equilibrium with the resolved strain rate σ_s, and is computed assuming linear response [4] as: $S_L^{\infty} = S_L^0 max\left(1 - \frac{\sigma_s}{\sigma_{ext}}, 0\right)$. In this equation, σ_{ext} denotes the strain rate at extinction, which is calculated from L_b by extrapolating its curve to the limit of $S_L \to 0$.

In the case of the LES-TFM simulations, a chemistry mechanism must be provided to compute reaction rates. Different detailed kinetics mechanisms are employed: the one proposed by Williams [8] with 21 reactions, the skeletal mechanism proposed by Boivin et al. [67] with 12 reactions, and the 27 reactions mechanism proposed by Marinov et al. [28]. The skeletal reaction mechanism, whose whole set of reactions is presented in [67] is a simplification of the one of Williams [8] taking into account the fact that the effect of many of the elementary reactions of the full mechanism to the reaction process is negligible. Thus, this mechanism is appropriate to describe premixed and non-premixed flames, autoignition, and detonations under conditions of practical interest [67]. Note that, as also pointed by the author, skeletal mechanisms with fewer reactions can be used for specific combustion conditions. Notwithstanding, since the experiments studied in this work consist of lean to stoichiometric mixtures, these simplifications would vary for each of the cases, and for this reason the 12 reactions have been retained in order to maintain a chemical kinetic model for the whole set of experiments.

In the case studied on ITER, it would be relevant the use of a realistic mechanism due to the non-homogeneity of the mixture, the low pressure within the VV, and the different combustion regimes in which the flame might propagate during the accident sequence. Therefore, the capability of the TFM in conjunction with detailed chemistry models is assessed.

Reaction		***A*** ***[mol/cm³]***	***β [s⁻¹]***	***E*** ***[J/mol]***
H+O₂ ↔ OH+O	k_f	$3.52\cdot10^{16}$	-0.7	71420
	k_r	$7.04\cdot10^{13}$	-0.26	600
H₂+O↔OH+H	k_f	$5.06\cdot10^{04}$	2.67	26320
	k_r	$3.03\cdot10^{04}$	2.63	20230
H₂+OH↔H₂O+H	k_f	$1.17\cdot10^{09}$	1.3	15210
	k_r	$1.28\cdot10^{10}$	1.19	78250
H+O₂+M→HO₂+M	k_∞	$4.65\cdot10^{12}$	0.44	0.0
	k_0	$5.75\cdot10^{19}$	-1.4	0.0
	T_{ROE}		$F_C = 0.5$	
HO₂+H→2OH		$7.08\cdot10^{13}$	0.0	1230
HO₂+H↔H₂+O₂	k_f	$1.66\cdot10^{13}$	0.0	3440
	k_r	$2.69\cdot10^{12}$	0.36	231860
HO₂+OH→H₂O+O₂		$2.89\cdot10^{13}$	0.0	-2800
H+OH+M↔H₂O+M	k_f	$4.00\cdot10^{22}$	-2.0	0.0
	k_r	$1.03\cdot10^{23}$	-1.75	496140
2H+M↔H₂+M	k_f	$1.30\cdot10^{18}$	-1.0	0.0
	k_r	$3.04\cdot10^{17}$	-0.65	433090
2HO₂ →H₂O₂+O₂		$3.02\cdot10^{12}$	0.0	5800
HO₂+H₂ →H₂O₂+H		$1.62\cdot10^{11}$	0.61	100140
H₂O₂+M →2OH+M	k_∞	$2.62\cdot10^{19}$	-1.39	214740
	k_0	$8.15\cdot10^{23}$	-1.9	207620

	T_{ROE}	$F_C = 0.265 \cdot e^{(-T/94K)} + 0.735 \cdot e^{(-T/1756K)} + e^{(-5182K/T)}$

Table 1. Reactions table for hydrogen-air combustion. Chemical model from Boivin et al. [67].

Note that some of the reactions involving third-body (denoted as M) had a pressure dependant behaviour, providing a low-pressure rate constant (k_0) and a high-pressure rate constant (k_∞). The Lindenmann mechanism is used to evaluate the reaction rate in these cases, in conjunction with the formula:

$$k = AT^{\beta} e^{(-E/R_c T)} \tag{15}$$

$$k = k_\infty \frac{(k_0[M]/k_\infty)}{(1 + (k_0[M]/k_\infty))} F \tag{16}$$

$$log_{10} F = \left[1 + \left[\frac{log_{10}(k_0[M]/k_\infty) + c}{n - d(log_{10}(k_0[M]/k_\infty) + c)}\right]^2\right]^{-1} log_{10} F_c \tag{17}$$

where $c = -0.4 - 0.67 \log_{10} F_C$, $n = 0.75 - 1.27 \log_{10} F_C$, and $d = 0.14$ [68]. The value of F_C is obtained for the reactions of Table 1, which need corrections.

In order to handle the detailed chemistry kinetic model presented in a more lightweight form in terms of computational time, the in situ adaptive tabulation strategy (ISAT) is used [69],[70]. ISAT is a storage retrieval method that permits to store combustion chemistry computations in a table and to use them to build approximate solutions at a later stage of computation. The algorithm reduces the number of ODE (ordinary differential equations) integrations of the chemical kinetics through tabulating and re-using the ODE solutions. This way, the overall cost of the computation is reduced. This algorithm has been successfully applied in combustion chemistry problems involving up to 50 species [71]. Under certain conditions, this technique can decrease by three orders of magnitude the computer time required to process detailed chemistry in reactive flow computations [69]. The ISAT method was also used by Emami et al. [9] for premixed H_2-air combustion with detailed kinetics and LES-TFM modelling.

3. NUMERICAL APPROACH AND METHODOLOGY

The different models for the numerical benchmark were developed under the Open-Source C++ library OpenFOAM v17.06.

A finite volume method mesh was used in which Gauss's theorem was applied for discretization together with a second-order backward time integration scheme. A second-order bounded central scheme was used for diffusion and pressure gradient terms in the governing equations. In order to diminish the numerical dissipation and dispersion, a total variation diminishing (TVD) scheme, using the Sweby flux limiter was applied for the discretization of the convective terms. Pressure momentum coupling was treated with a pressure based standard iterative procedure (PISO) algorithm. Due to the stiffness of the chemical kinetics employed, an implicit 5th order Runge-Kutta was used to solve the chemistry kinetics in conjunction with the ISAT method. The time step was set based on a maximum convective CFL value of 0.25 with a maximum time step set to $5 \cdot 10^{-6}$ s with the aim to ensure temporal convergence. Besides, the models were adapted to work with the dynamic refinement meshing process. This technique permits to reduce the time required to carry out the simulations, having more spatial resolution where the flame is presented

and reactions and discontinuities have to be appropriately captured. All calculations were performed on a shared memory parallel system with two Intel® Xeon® E5-2665 CPUs with 8 cores each and up to 64 GB of RAM.

The methodology adopted in the numerical study includes two steps:

1) First, a validation of the modelling approach is performed, by means of experiments of H_2-Air turbulent combustion in a spherical vessel reported by Goulier et al. [50],[51], both in quiescent conditions and with initial turbulence, induced by fans. The validation procedure was structured as follows: firstly, the models were benchmarked against the experimental data for the cases under quiescent conditions, analysing the influence of different constants and modelling assumptions. Then, simulations including fans inside the vessel were carried out, to reproduce the experimental turbulent field, obtained with different fan speeds. This way, it is possible to test the model's ability to reproduce the experimental turbulent fields. The turbulent velocity fields obtained in the observable region of the experiments were thus compared with the pseudo-steady state reached in the simulated results, in terms of turbulent intensity, integral length scale, mean velocity components and local isotropy level.
2) In the second stage, the turbulent combustion experiments were simulated. In those tests, the fans were operating to generate an initial turbulent field during the combustion process. The turbulent field solutions obtained from the previous step were used to model the initial turbulent field of the combustion experiments. The flame spherical radius and the flame burning speed, obtained with the different combustion models, are compared to those measured in the experiments.

4. RESULTS AND DISCUSSION

4.1. VALIDATION OF THE MODELLING APPROACH WITH SPHERICAL BOMB EXPERIMENTS

This section focuses on the advantages and limitations of the LES-FPV and the LES-TFM models with different sub-grid scale turbulence, sub-grid wrinkling and chemical approximations to predict combustion dynamics in confined scenarios. These different approaches were assessed against the experimental data reported by Goulier et al. [50],[51]. The experiments were carried out in a 95-liters spherical vessel, which was equipped with Schlieren and PIV measurement techniques to measure flame speed and flow velocity. Pressure evolution during the combustion sequence was also measured. Four different hydrogen-air mixtures were studied, varying from lean to near to stoichiometric mixtures (16, 20, 24, and 28% of molar concentration of H_2-Air). Moreover, the vessel was equipped with fans in order to generate a controlled turbulent field where the flame could propagate. Experiments with four different turbulence intensities were performed, varying the root mean square of the velocity fluctuations (u') from 0 (this first case is hereafter called field under quiescent conditions) to 2.81m/s with integral length scales from 43.9 to 53.0 mm. Thus, flame regime varied depending on the composition and the turbulent regime of each experiment, encountering flames in wrinkled, corrugated-flamelet, and thin reaction zone regimes [50]. The ignitions were performed with two tungsten electrodes mounted along a diameter of the sphere. The initial pressure and temperature were 1 bar and 293 K, respectively. More detailed information about the experimental installation and procedures can be found in [50][51].

In order to carry out the model validation, the prediction of combustion dynamics was assessed by benchmarking two experimental transient variables: flame radius and pressure evolution. Thus, the flame propagation velocity when the flame was inside the radius window was compared with the flame radius evolution predicted by the simulations. A similar criterion was followed to define the flame radius. In the experiments, a surface equivalent radius was calculated from the images based on the area of the combusted volume, whereas the numerical equivalent radius was calculated from the combusted volume V_b as $R_{eq} = (0.75 \cdot V_b/\pi)^{1/3}$. Burning speeds were calculated as $S_b = \frac{dR_{eq}}{dt}$ in analogy with the experimental data.

A snapshot of the mesh used in the numerical model is represented in Figure 1 (Left). Due to the symmetry of the problem, only an octave part sphere was simulated, considering three symmetry planes. The original structured mesh had 66250 hexahedral elements, with a characteristic length of 40 mm. The maximum cell skewness factor reported was 0.01 and the maximum aspect-ratio was 5.5. These quality indicators were kept during the mesh refinement process. The interface between the different refinement levels was fulfilled with prims connecting the nodes of the lower size cells, reducing the potential presence of spurious hanging nodes. Figure 1 (Right) shows a detail of the refinement region during a simulation with a maximum refinement level of 4. The cell selection for refinement was made based on a Schlieren-type variable: the normalized density, which permitted to capture the flame front discontinuities. A threshold value was set to establish the maximum refinement level in the flame front surface. Symmetry flame boundary conditions were imposed at the symmetry planes of the domain, and a fixed temperature of 573 K was imposed at the solid walls. Wall-modelled LES was imposed on the turbulent variables in adjacent wall regions to reduce the computational cost [72].

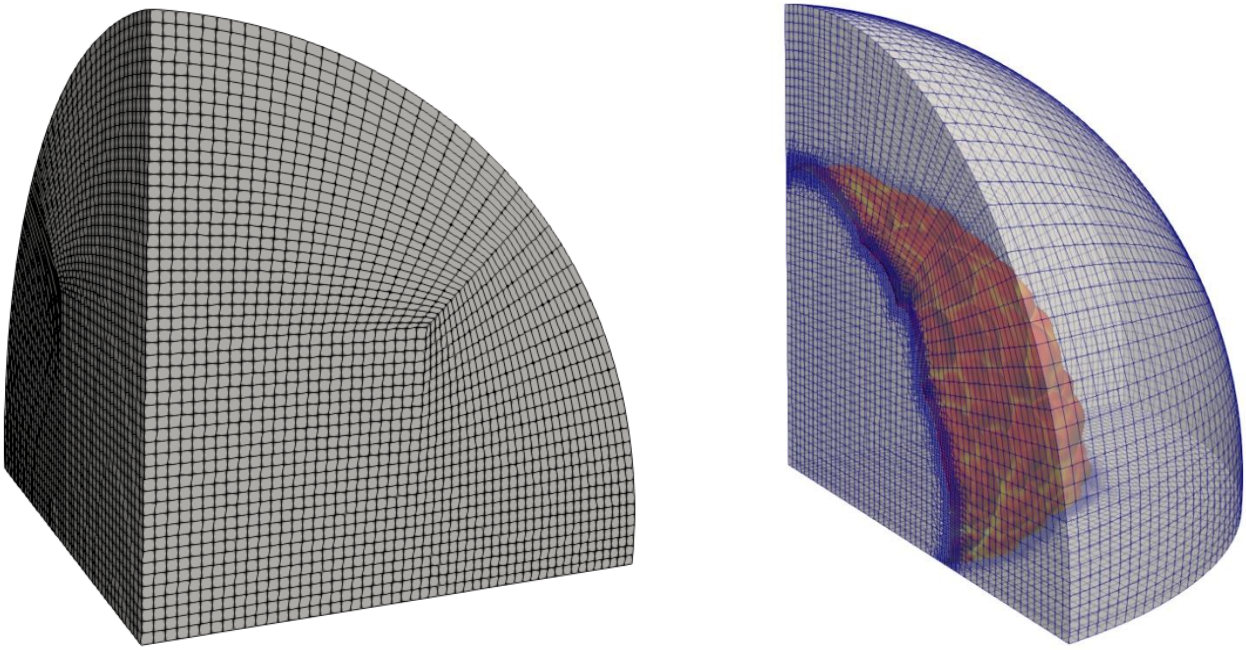

Figure 1: (Left) Initial Computational grid of spherical sector developed for the 563mm spherical bomb. (Right) Example of the dynamic mesh refinement process tracking the wrinkled flame front.

Ignition was modelled in different ways, depending on the model selected. In the case of the LES-FPV, it was based on a source term added to the regress variable equation. In the case of the LES-

TFM simulations, the ignition was modelled as a source term applied to the energy equation in the ignition region. This region was selected to be a spherical-like volume with a radius of 2.5 mm. The duration of the ignition was set to 0.1 ms, estimating in both combustion models an ignition energy of 850 kJ/m^3. This value was enough to begin with the chemical combustion process, in the case of LES-TFM simulations, and enough to create a well-defined flame surface, being able to self-propagate, for the particular turbulent burning speed modelled, in the case of LES-FPV simulations. It is worth to be noted that the ignition region was refined to the maximum refinement level set for the simulation during the ignition sequence in order to model the ignition spark in the small region, allowing smaller radius than the smaller cell size of the original mesh, and improving the original shape during the beginning of the flame propagation. After the mixture was ignited, the refinement tracked the formed flame front.

4.1.1 Numerical benchmark I: Flame propagation speed and pressure evolution prediction in a scenario without turbulence (quiescent conditions).

The two presented models were used to simulate the combustion experiments performed in a spherical vessel under initial quiescent conditions without turbulence. This scenario was denominated in previous sections as "combustion under quiescent conditions". First, the results of the grid independence analysis are presented. Then, the influence of the stretched laminar speed and the chemical kinetics on the modelling is discussed.

- **Grid independence analysis.**

A grid convergence analysis was performed to assess the influence of the spatial discretization in both used LES combustion models. Two different refinement levels (minimum cell sizes up to 2 mm and 1 mm, respectively) were analysed for a spherical domain of 1/8 of the sphere, as well as an additional "static" mesh with no refinement procedure, but with a 45º×45º solid angle spherical sector (hereafter referred to as pyramidal form). The spherical sector presented the same spatial discretization as the second step of maximum level refinement (1 mm). This static mesh was made in order to have a good spatial resolution to simulate the turbulent flame. The tests were performed for both analysed models using the 20% of H_2/Air mixture experimental test as reference case. Figure 2 shows the equivalent radius (Left), flame burning speeds (Centre) and pressure (Right) evolutions with time for the LES-FPV case using the Weller approach and a Smagorinsky sub-grid turbulence model. For the sake of comparison, the figure also includes the experimental data [50],[51]. As shown, the radius evolution with time shows a good agreement with the experimental data. Pressure evolution shows that this model had a realistic pressure prediction for the three of the meshes analysed. However, when comparing the burning velocities predicted at a certain radius (Figure 2, Center) it was found that the static mesh had less stability during the first stages of the combustion (small radius) due to the shape of the computational grid (pyramidal form). In this case, the surface modelled during the simulation with this domain was too small, the flame was artificially stretched due to the closeness of the symmetry boundaries and the turbulence is not properly modelled. This problem did not seem to appear in the 1/8 sphere domain with 1 and 2 refinement steps, which seemed to predict accurately the flame burning speeds from the ignition sequence.

The same analysis was carried out for the LES-TFM. Figure 2 shows the results obtained for the LES-TFM model using a Smagorinsky sub-grid turbulence model with the Charlette efficiency function and the 12 steps chemistry mechanism [67], with the in-situ tabulation method (ISAT). In this case, the 45º static mesh was already neglected. In this comparison, F_{MAX} was set to a

typical value of 10, ensuring a thickening factor enough to be able to handle the flame kinetics. As shown, with this F_{MAX} value, a one-step refinement seemed to be good to report a good prediction of the experimental data. However, simulations with a two-steps refinement (labelled in the figure as Ref. to 1 mm), seemed to be more stable numerically during the ignition sequence than the one-step refinement (labelled in the figure as Ref. to 2 mm).

Table 2 reports the errors obtained in the prediction of the pressure peak and time rise with the different models tested. As shown, errors in the maximum pressure prediction were below 2% in the case LES TFM models and 6.1% in the case of LES-FPV model. On the other hand, regarding the time rise LES-FPV model reported a smaller absolute relative error (<6.5%) than the LES-TFM (<10.2%)

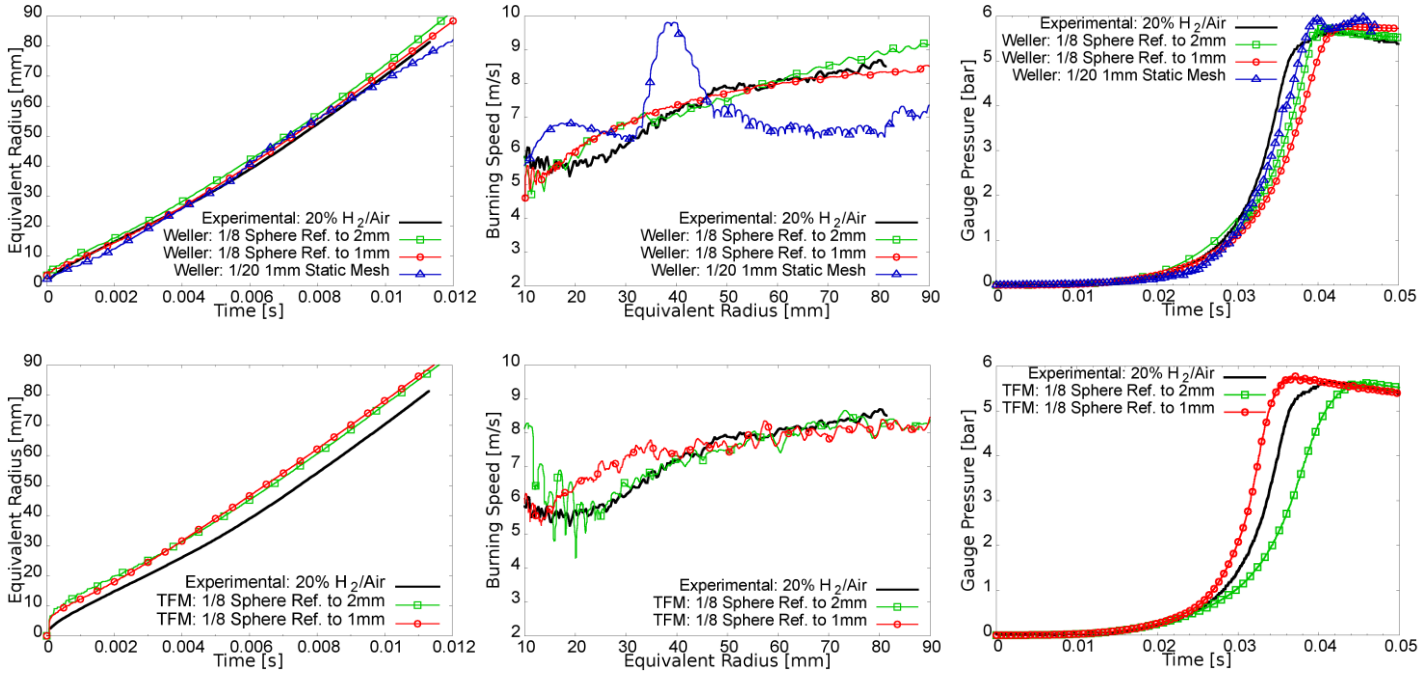

Figure 2: (Left) Equivalent flame radius versus time. (Center) Burning velocity versus flame radius. (Right) Pressure evolution versus time for LES-FPV (Weller) and LES-TFM with different spatial discretizations (20% H_2/Air).

Case ***Cell Size***	***Exp.***	***LES FPV*** ***2mm***	***LES FPV*** ***1mm***	***LES FPV*** ***45º static*** ***1mm***	***LES TFM*** ***2mm***	***LES TFM*** ***1mm***
Abs. P_{max} (bar)	6.66	6.78	6.77	7.06	6.66	6.77
Error P_{max} (%)	ref.	1.82	1.68	6.03	0.02	1.72
t_{rise} (ms)	41.30	41.01	43.53	43.96	45.19	37.10
Error t_{rise} (%)	ref.	-0.69	5.41	6.45	9.43	-10.17

Table 2: Peak pressure predictions for different spatial discretizations.

Although the grid-scale wrinkling was strictly dependant on the mesh size, the sub-grid wrinkling model seemed to predict the turbulent flame acceleration due to the lack of grid-scale corrugation.

The one-step level of refinement seemed to report accurate results but, due to stability limitations during the ignition, the mesh domain selected for the rest of the validation campaign was the 1/8 sphere with two-steps dynamic refinement. This mesh provided a good equilibrium between spatial resolution and computational cost. In addition, the dynamic refinement procedure allowed simulating the premixed combustion problem analysed with high spatial discretization in the flame surface region and preheat zone, where the turbulence flame interactions processes required small computational cells to ensure correct modelling.

- **Influence of the stretched laminar flame speed and chemical kinetics model.**

Unstretched laminar burning speeds for the different mixtures analysed were obtained from experiments by Sabard et al. [34], who also provided the laminar flame thickness from COSILAB code, with the H_2 kinetics proposed by Mével et al. [73]. A correct prediction of the laminar burning speeds and stretch effects are key aspects to ensure a correct prediction of the turbulent flame burning speed. These data were employed in order to check the performance of the different detailed chemical kinetics for H_2/Air mixtures of the cases studied. The use of the ISAT method was also analysed, estimating the reduction of the computational cost due to this method and the variation of the results when it was active. Table 3 shows the laminar flame speed and thickness computed for laminar one-dimensional (1D) steady-state flames considering 20% of H_2/Air with different chemical mechanisms and a spatial resolution of 5.6 μm, in order to ensure the correct resolution of the reaction layer. Laminar flame speed S_L^0 was calculated from the laminar burning speed S_b^0 since $S_L^0 = S_b^0 \cdot \rho_u/\rho_b$ where ρ_u and ρ_b are the burnt and unburnt gas densities. The effective Lewis number of each mixture was used for these computations. Figure 3 (Left) also shows the main physical properties obtained in the flame front region from computations.

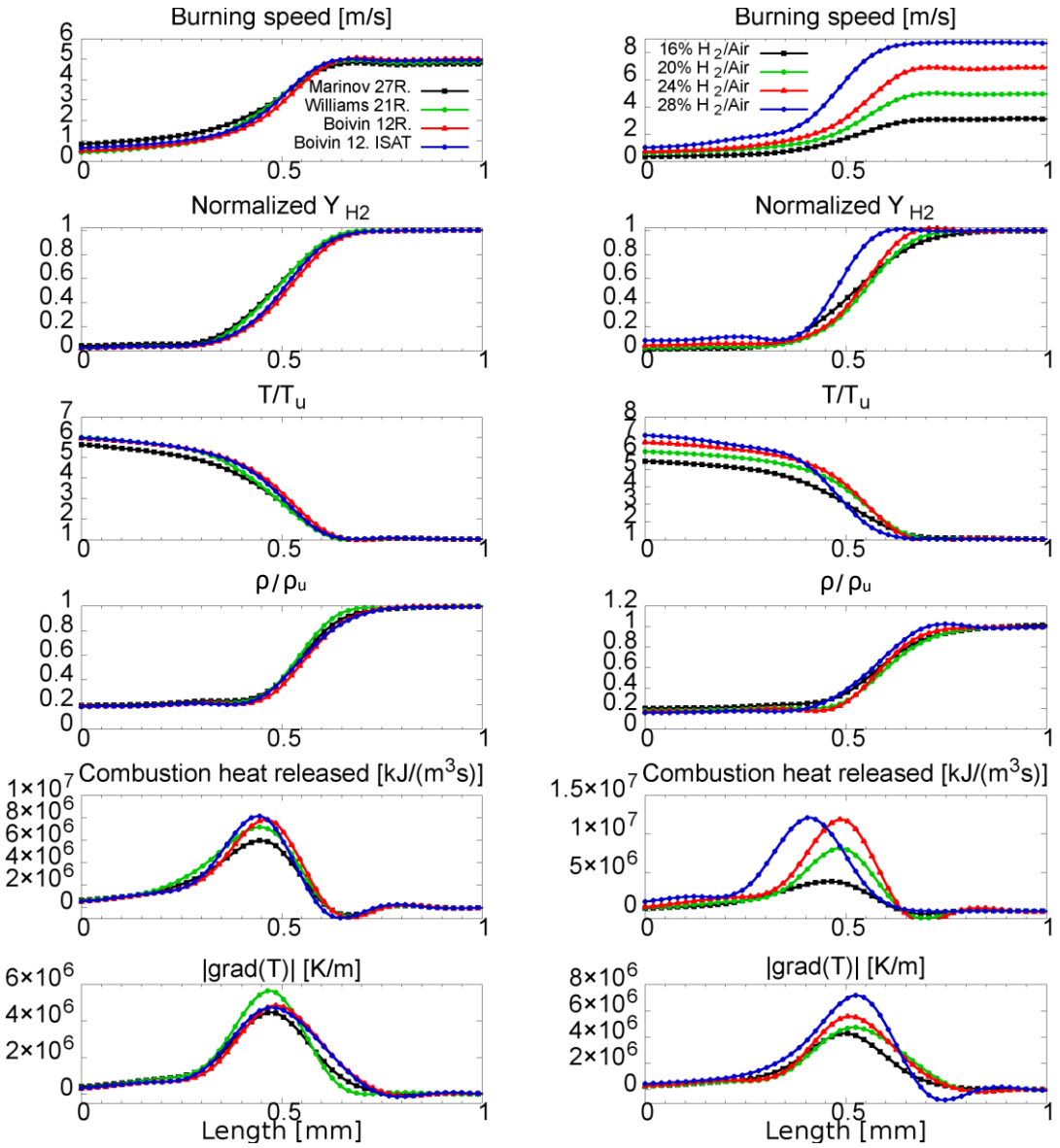

Figure 3: Main flame properties from laminar 1D flame simulations (Left) 20%H_2/Air with different chemical kinetics. (Right) Comparison for 16%, 20%, 24%, and 28% for the Boivin mechanism, with ISAT method.

Case	$S_L^0(m/s)$	$\delta_L^0(\lvert\nabla T\rvert\ based)(mm)$	Relative performance in CPU time
Experimental	0.92 =S_{Lref}	0.382 =δ_{Lref}	-
Marinov 27 R.	0.83 (=0.90·S_{Lref})	0.393 (=1.03·δ_{Lref})	6.67·P_{ref}
Williams 21 R.	0.86 (=0.94·S_{Lref})	0.311 (=0.82·δ_{Lref})	7.56·P_{ref}
Boivin 12 R.	0.87 (=0.95·S_{Lref})	0.364 (=0.95·δ_{Lref})	4.91·P_{ref}
Boivin 12 R. (ISAT)	0.87 (=0.95·S_{Lref})	0.378 (=0.99·δ_{Lref})	P_{ref}

Table 3: Laminar flame speed and thickness obtained from different detailed chemical models for 20% of H_2/Air.

Besides, some additional tests were performed at sub-atmospheric pressures to evaluate the capabilities of the model to capture the influence of the initial pressure on the laminar flame speed. For the case of combustion at 20kPa, of a mixture of 30% of H_2 in air at initial ambient temperature (290 K) the model provided a value of $S_L^0 = 1.57$ m/s with the Boivin mechanism with ISAT method whereas the experimental data of [45] and [46] provided a value of 1.7±0.1 m/s. For the case of combustion at 50kPa, the laminar flame speed for different compositions was experimentally estimated in [34] for the case of N_2/O_2=3.76 and 343 K of initial temperature. The results of the prediction are summarized in Table 4.

Case Conditions and experimental reference	**Experimental $S_L^0(m/s)$**	**Prediction of $S_L^0(m/s)$ with 1D simulation**	**Ratio $\frac{S_L^0\ experimental}{S_L^0\ prediction}$**
20 kPa, N_2/O_2=3.76, 30% H_2 in [45] and [46]	1.7±0.1	1.57	1.08
50 kPa, N_2/O_2=3.76, equivalence ratio ϕ=0.605 in [34]	1.172±0.1	1.189	0.99
50 kPa, N_2/O_2=3.76, equivalence ratio ϕ=1.025 in [34]	2.500±0.1	2.2848	1.09
50 kPa, N_2/O_2=3.76, equivalence ratio ϕ=1.581 in [34]	3.129±0.1	2.987	1.05

Table 4: Laminar flame speed obtained from different detailed chemical models for 20% of H_2/Air.

Some studies of one and two-dimensional unsteady laminar premixed flames showed a speed-up factor with ISAT method (i.e. ratio of computational time with and without ISAT method) from 4.5 to 13 [74]. In this particular case, the speedup factor obtained was 4.91 (Table 3). Due to the similar results obtained with the 12-reactions mechanism, compared to the fully detailed chemical models, this mechanism was selected in order to perform the assessment of the LES-TFM with the ISAT tabulation method against the experimental data. As shown in Table 5, one-dimensional simulations with this chemical model seemed to predict correctly the laminar flame properties for the mixtures analysed.

	16% H_2/Air	**20% H_2/Air**	**24% H_2/Air**	**28% H_2/Air**
$S_L^0(m/s)$	0.50 (=1.08·exp)	0.87 (=0.95·exp)	1.36 (=0.96·exp)	1.84 (=0.95·exp)
$\delta_L^0(\lvert\nabla T\rvert\ based)(mm)$	0.448 (=0.86·exp)	0.378 (=0.99·exp)	0.362 (=0.95·exp)	0.354 (=1.01·exp)

Table 5: Laminar flame burning speed and thickness obtained from the Boivin 12 reactions mechanism, with ISAT tabulation.

Figure 4 presents the equivalent radius, burning velocity and pressure evolution data provided by the LES-FPV and LES-TFM models when compared with the experiments for H_2/Air mixtures between 16% and 28%. As shown, both models provided a good agreement with experimental data for lean mixtures. However, in the case of the richest H_2 mixtures (24% and 28%) the LES-FPV model did not seem to predict properly the burning velocity. Tables 6 and 7 summarize the quantitative results in terms of maximum pressure and time of rising. Both models predict maximum pressure with less than 3.5% of error with the exception of the 28% H_2/Air mixture case where the LES-FPV model yielded around 7.8% of error. Regarding time rise, absolute error is less than 10.2% in all the cases with the exception of the 28% H_2/Air mixture case where the LES-FPV model provided around 20% of error.

For the considered operating conditions, the flame was initially laminar, and the equivalence ratio was smaller than 1. Results showed that the initial perturbations of the flame increased, and the flame speed was very sensitive to temperature changes. The Lewis number was, therefore, a key point in order to account for these instabilities in the simulation, as it represents the differential diffusion of heat and H_2, which was the deficient reactant.

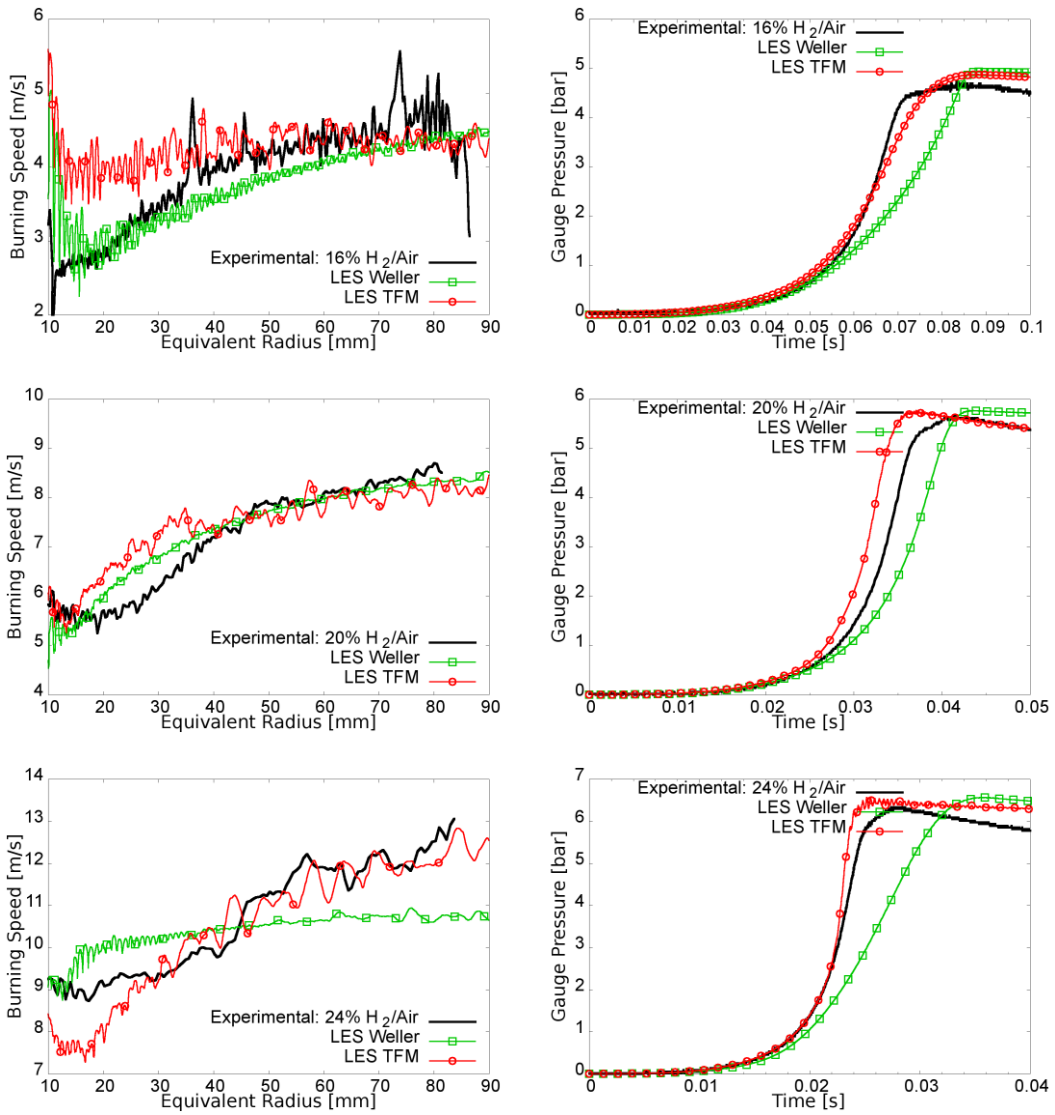

Figure 4: (Left) Burning speed (m/s) vs. equivalent radius (mm), and (Right) gauge pressure evolution with time, for LES-FPV and LES-TFM, compared to experiments.

	Exp. ***16% H_2***	***LES FPV*** ***16% H_2***	***LES TFM E_ΔCharl.*** ***16% H_2***	***Exp.*** ***20% H_2***	***LES FPV*** ***20% H_2***	***LES TFM E_ΔCharl.*** ***20% H_2***
Abs. P_{max} (bar)	5.74	5.94	5.88	6.66	6.77	6.77
Error P_{max} (%)	-	3.51	2.50	-	1.68	1.72
t_{rise} (ms)	83.30	87.49	88.15	41.30	43.53	37.10
Error t_{rise} (%)	-	5.95	5.82	-	5.41	-10.17

Table 6: Numerical errors on peak pressure and pressure rise time for mixtures 16-20% H_2.

	Exp. *24% H_2*	*LES FPV* *24% H_2*	*LES TFM E_ΔCharl.* *24% H_2*	*Exp.* *28% H_2*	*LES FPV* *28% H_2*	*LES TFM E_ΔCharl.* *28% H_2*
Abs. P_{max} (bar)	7.34	7.57	7.57	7.85	8.47	8.05
Error P_{max} (%)	-	3.15	3.15	-	7.78	2.43
t_{rise} (ms)	27.36	35.88	25.19	21.90	26.36	20.32
Error t_{rise} (%)	-	31.16	-7.92	-	20.38	-7.21

Table 7: Numerical errors on peak pressure and pressure rise time for mixtures 24-28%H_2.

4.1.2 Numerical benchmark II: Flame propagation speed and pressure evolution prediction within a turbulent field.

The experiments presented by Goulier et al. [50],[51] provided combustion data in a well-characterized turbulence field inside the spherical vessel. Based on these data, simulations were carried out to assess the capabilities of the combustion models for predicting turbulent burning speeds. In order to create a turbulent field inside the vessel, axial fans were used. The spherical bomb had eight impellers with a diameter of 130 mm each, located at the vertices of a cube inscribed in the sphere. These propelled the flow towards the sphere wall. Four different rotation speeds were tested, which generated four different turbulence fields. The rotation speeds were settled before the ignition and kept during combustion. Homogeneity and isotropy of the turbulence field generated were also analysed.

The fans were also included in simulations: a momentum source term was imposed in a circular region near the sphere wall with a thickness of $\delta = 5$ mm, in order to model the fan thrust and torque of the air mixture entering the vessel. Expressions used for evaluating the axial and

tangential volume forces have been computed in a force distribution that approximately follows the Goldstein optimum [75]. The following equations for the axial and tangential volume forces were employed:

$$f_{ax} = A_{ax} r^* \sqrt{1 - r^*} \tag{18}$$

$$f_\theta = A_\theta \frac{r^* \sqrt{1 - r^*}}{r^*(1 - r_h') + r_h'} \tag{19}$$

$$r^* = \frac{r' - r_h'}{1 - r_h'} \; with \; r' = \frac{r}{R_P} \; and \; r_h^{\text{i}} = \frac{R_H}{R_P} \tag{20}$$

The constants R_H and R_P are the internal and external radiuses respectively, where R_H was set to zero deprecating the fan axis and R_P was 0.065 m. The values of A_{ax} and A_θ were fixed from the total thrust T and torque M respectively as:

$$A_{ax} = \frac{105}{8} \frac{T}{\pi \delta R_P (3R_P + 4R_H)(R_P - R_H)} \tag{21}$$

$$A_\theta = \frac{105}{8} \frac{M}{\pi \delta R_P (3R_P + 4R_H)(R_P - R_H)} \tag{22}$$

Additionally, a fluctuation level to the total thrust and torque was added with function randomize, considering a fluctuation scale S and a fraction of the new random component to the previous time value, α, as:

$$T(t + \nabla t) = (1 - \alpha) T(t) + \alpha [\bar{T} + T'_{RMS} S (R - 0.5) \bar{T}] \tag{23}$$

$$T'_{RMS} = \frac{\sqrt{12(2S - S^2)}}{S} \tag{24}$$

R is a random value, which varies from 0 to 1 and was evaluated each time step. Values for the fluctuation scales S components were set to 10% of the mean values for torque and thrust parameters, with a factor α set to 0.5. Mean values for $\bar{T}$ and $\bar{M}$ were set in order to generate the desired turbulent field for each of the fan rotational speeds considered. An example of numerical results for the turbulent field variables is shown in Figure 5. The figure shows different characteristics of the turbulent field obtained in the simulations including the spatial 2D characterization of the mean velocity, the root mean square velocity (*Urms*), the autocorrelation of velocity components, the isotropy and the velocity probability density function *Umean/Urms*. The three first figures of the left column show the *x* velocity component properties (*U*), whereas the three first figures of the right column show the *y* velocity component properties (*V*). In the figure, RUU stands for the auto-correlation of the velocity component in the *x* direction and RVV stands for the auto-correlation of the velocity component in the *y* direction. In this case, the "Isotropy" plot represents the ratio between the root-mean-square (RMS) velocities in both directions (i.e. $Isotropy = U_{RMS}/V_{RMS}$).

The integral length scale estimated from the simulations is in the order of ~47-51mm. Goulier et al. in [50],[51] estimated a value of the integral length scale in their experiments of the spherical

bomb of the order of ~44-53 mm, what is in reasonable agreement with the estimation obtained from the simulations. The order of magnitude of the Kolmogorov scale of the problem is 0.16-0.21 mm whereas the cell size was of the order of ~5.6 mm for the problem without combustion.

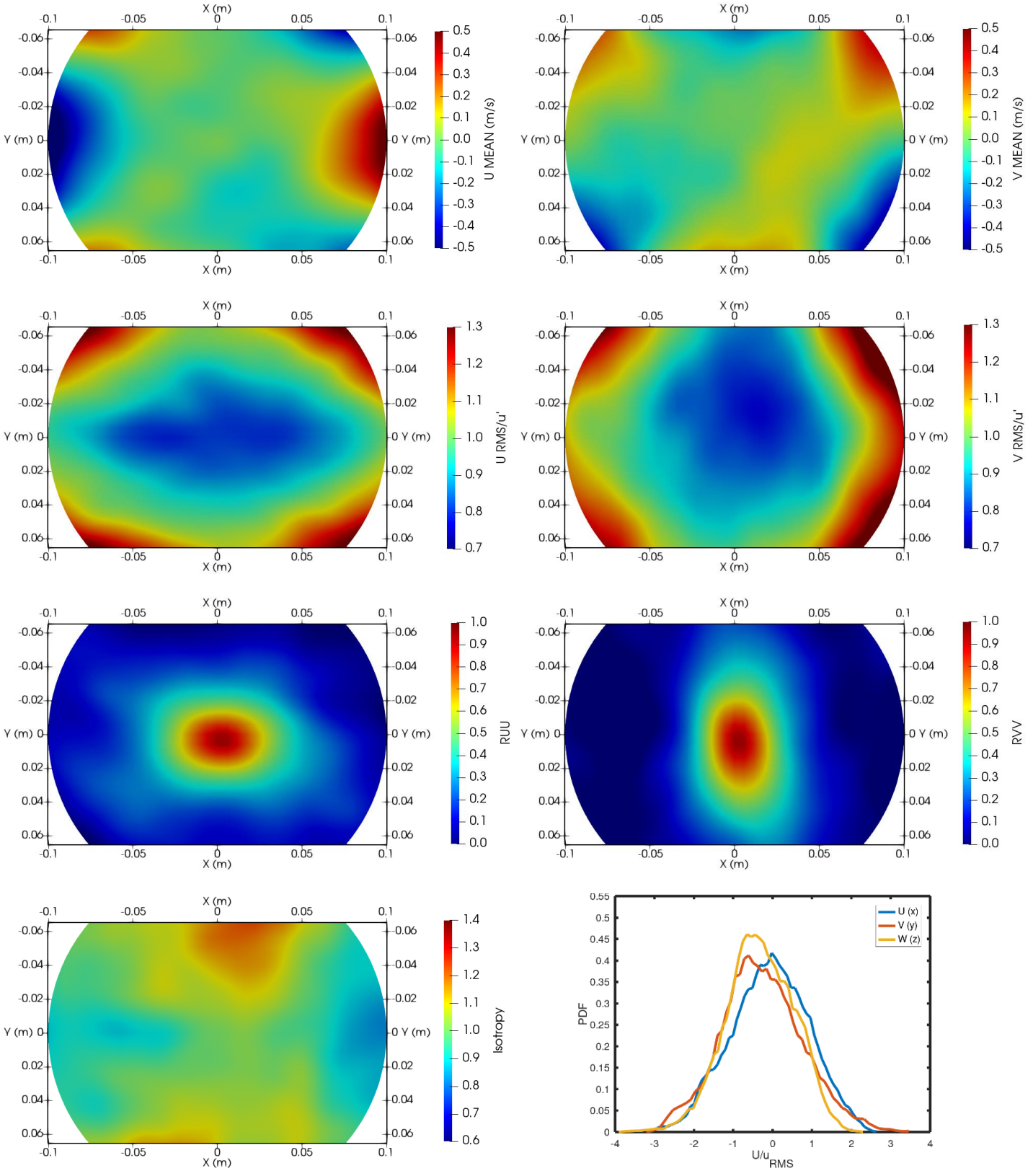

Figure 5: Main properties of the turbulent field obtained by the simulation for the experimental case of 2000 r.p.m of fan rotating speed.

After the simulations of the spherical vessel, with the eight fans working at different speeds, combustion simulations at these conditions were carried out in order to assess the behaviour of the LES-TFM and LES-FPV under the different turbulent combustion regimes. Figure 6 shows the results obtained for 16% of H_2-Air, and Figure 7 for 20% of H_2-Air, in terms of turbulent flame burning speeds versus the flame equivalent radius. As shown, the burning speed radius increases when the initial turbulence of the scenario increases. Both models captured this effect.

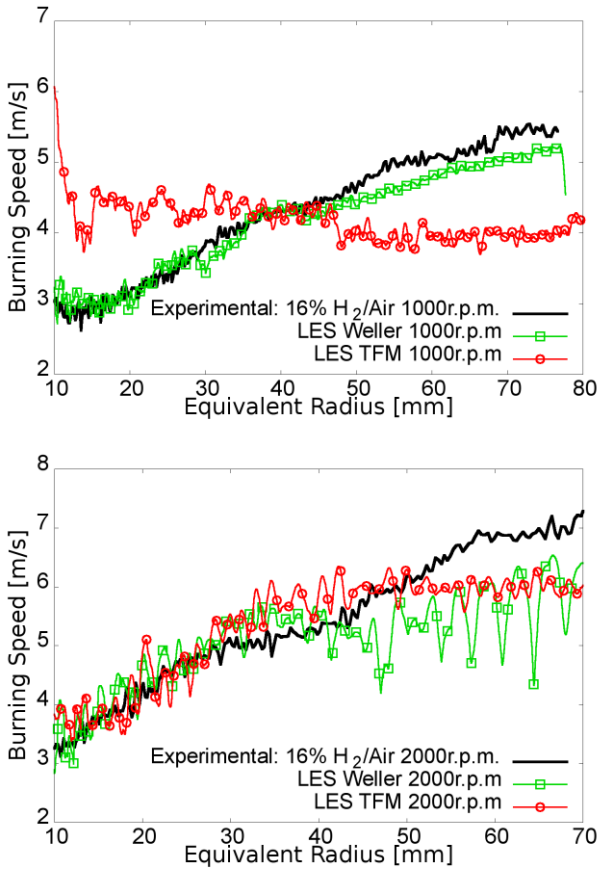

Figure 6: Turbulent burning velocity versus flame radius for LES-FPV (labelled as LES Weller) and LES-TFM models for 16% H_2/Air from 1000r.p.m. (top) to 2000 r.p.m. (bottom).

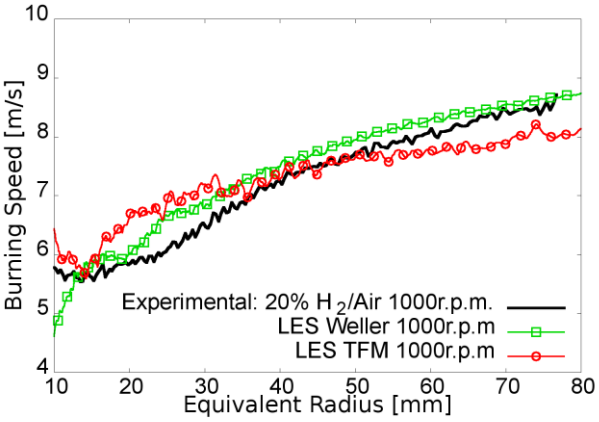

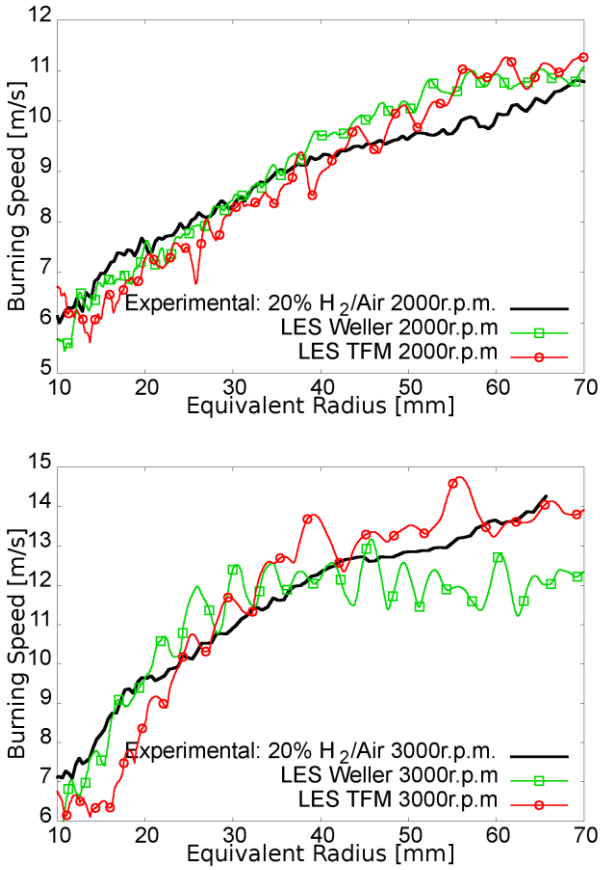

Figure 7: Turbulent burning velocity versus flame radius for LES-FPV and LES-TFM models for 20% H_2/Air from 1000r.p.m. (top) to 2000 r.p.m. (bottom).

4.2 APPLICATION OF THE MODELLING APPROACH TO LOVA ACCIDENT SEQUENCES IN ITER

In this section, the LES TFM was applied to study combustion sequences within the ITER vacuum vessel (VV). Specifically, two different LOVA sequences were considered. They are referred to as Sequence 1 and Sequence 2. Sequence 1 considered a big breach of 0.15 m^2, low H_2 content within the VV (0.584 kg), and relatively low VV pressure at the moment of the ignition (4.5 kPa). Sequence 2 considered a smaller breach (0.02 m^2), higher H_2 content within the VV (2 kg), and a higher VV pressure at the moment of the ignition (13.35 kPa). The comparison of the two sequences permitted to assess the effect of the breach size. For each sequence, two different cases were studied: a reference case with autoignition under premixed, airtight conditions (i.e. vacuum vessel without breach and with no initial turbulence), and the LOVA case with autoignition (i.e. LOVA within a VV due to a breach). In the discussion, the first case will be referred to as "Quiescent Case" and the second one as "LOVA case". Therefore, a total of four cases were simulated. In all of them, a reacting atmosphere of H_2-O_2-N_2-Ar was analysed, using a dynamic mesh, a segregated PISO solver, and the kinetic model by Williams, with ISAT. The two cases in a sequence had similar pressure and gas mixture (i.e. gas inventory) at the moment of the ignition. This way the effect of the turbulence induced by the air jet on the combustion dynamics can be assessed when the rest of the parameters remained similar. Constant temperature boundary conditions were imposed at the walls of the VV in all the cases studied.

The VV is a toroidal geometry of 1050 m^3. The whole toroid was considered in the simulations. In order to describe the sequence, we referred to (r, Θ, z) cylindrical polar coordinates, with the z-axis as the axis of symmetry of the toroid. The mesh generated for the simulation of the two sequences comprises the entire volume of the VV (i.e., $0º < Θ < 360º$). Structured meshing has been used throughout the toroid. The original mesh has a total of 448456 elements, with characteristic sizes ranging from 0.06 to 0.17 m, to which successive refinements are applied. For a domain of such dimensions, it is challenging to set an element size such that it allows resolving the flame front directly. To make sure there is an acceptable number of cells within the flame thickness, dynamic mesh refining and the flame thickening model are imposed on the flame front.

A mesh independence study has been carried out that evaluates the possible variation of combustion speed as a function of the number of mesh refining steps, given that combustion speed is usually highly influenced by element size, consequently, by the number of elements within the flame front. The selection of the refined region is done by the normalized density gradient, the S_ρ value, which detects the position of the flame front for values of density gradient ranging $0 < S_\rho < 0.95$, in a sort of numerical Schlieren (i.e. 0 for the highest density gradient). Those regions where chemical reaction takes place, have also been refined. After two refinements there are up to 14 million elements within the simulation domain.

The mesh independence study has found that the model is robust against the mesh size on the flame front, provided that dynamic refinement is done. In other words, the model makes a good adjustment of the thickening factor so that the burning rate is not affected by the original cell size. Figure 8 (top) shows the spherical equivalent radius of the flame at the first stages after the ignition, for different refining steps ("1ref": one refinement up to "4ref": four refinements). As can be seen, from the second refinement of the mesh (2ref), there is no variation of the flame radius. Figure 8 (bottom) also shows sub-grid wrinkling contours at the first moments of flame spread (at time t = 22.5 ms) for two refinements (bottom-left) and four refinements (bottom-right). The mesh resolution is higher on the right picture (4ref) than on the left (2ref). That makes the flame thinner for the case with better mesh resolution. However, the model adjusts the burning rate for both cases and, therefore, flame propagation is almost identical, and independent of the number of mesh refinement steps.

Contours in Figure 8 (bottom) also indicate that sub-grid wrinkling is more intense for the thicker mesh ("2 ref", on the left). That is consistent, since there is more turbulent mixing within each cell.

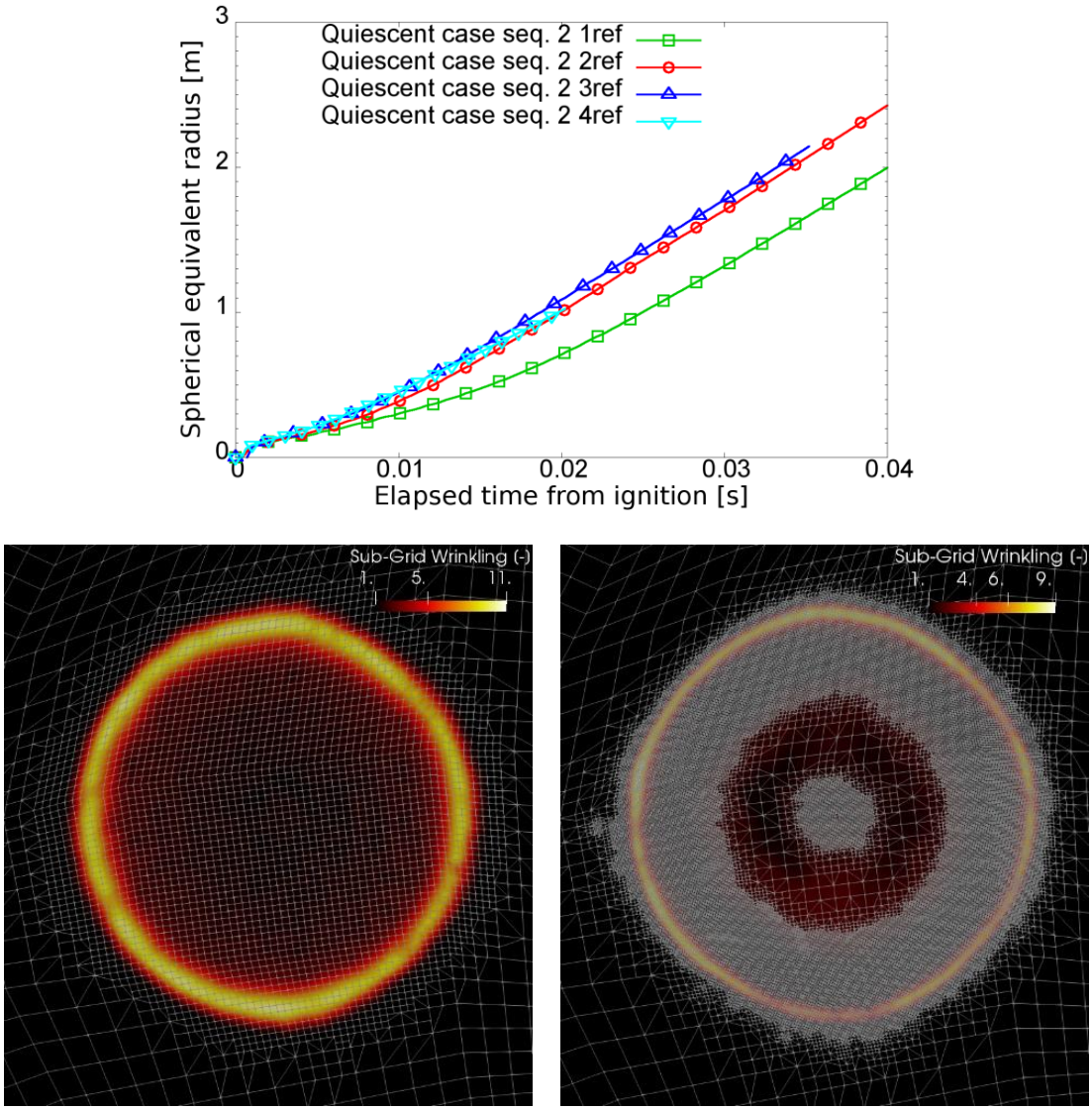

Figure 8: Independence of the flame speed against the number of mesh refining steps: spherical equivalent radius vs. time from ignition (Top); and flame front representation with two refining steps (bottom-left) and four refining steps (bottom-right).

4.2.1 Analysis of Sequence 1

As previously indicated, this sequence corresponds to a scenario with a breach of 0.15 m^2 and a pressure of 4.5kPa at the VV during the ignition. In this sequence two different combustion cases were analyzed: a reference combustion case without breach and a LOVA combustion case with the breach. Both cases were ignited with the same gas composition and pressure within the VV. This way the effect of the turbulence induced by the breach could be assessed.

In the reference combustion case called "Quiescent Case", a premixed mixture of 0.584 kg of H_2, 21.37 kg of N_2, and 5.45 kg of O_2 and 0.324 kg of Argon (Ar) was considered at the beginning of the sequence within the simulated domain. This inventory was set to be the same as the one found in the "LOVA Case of Sequence 1" (specified in the next paragraph) at the moment of the ignition. This means that both cases ignite with the same conditions (i.e. same gas mixture, temperature, and pressure) with the only difference of the existence of a breach. The mixture corresponds to an average equivalence ratio ϕ=0.84 (i.e. fuel to oxidizer ratio divided by fuel to oxidizer stoichiometric ratio). A pressure of 4.5 kPa and a gas temperature of 467 K was considered in this

case. During the simulation, a constant temperature condition of 438 K was imposed at the walls. Regarding the initiation, an autoignition process was supposed to occur in the centre of a meridional plane of Θ = 0º, as the initial conditions exceeded the flammability limits of the mixture at 4500 Pa. Initially, the isobaric ignition generated a spherical laminar flame front. Part of the flame front impacted the closest walls of the vessel at low velocity conditions (~50m/s), whereas other fraction of the flame front progressed and kept its expansion along the corridor of the toroid. During the expansion, the flame front increased progressively its speed and level of turbulent kinetic energy. Due to the symmetry of the VV, this means that two flame fronts accelerated along the two symmetric corridors of the toroid and collided with each other at the opposite side (i.e. section of Θ=180º). Because of this collision, the flame experienced a compression, and pressure levels reached 21.6 kPa. This means an overpressure level in the order of P_{max}/P_o ~ 4.8. In this case, the flame accelerated without reaching detonation conditions.

In the "LOVA Case", the simulation started with the initial entrainment of air across a wall breach of 0.15 m^2 which was located at a symmetry plane of the domain (section of Θ=180º). The initial conditions of the sequence were set, following Xiao et al. [43], as: 500 Pa, 500 K for the gas within the VV. They considered a sequence were nitrogen injectors were partially used. It this sequence it was considered an initial mixture of N_2 (3.46 kg) and H_2 (0.584 kg) within the VV at 500 Pa and 500 K and a constant temperature of 438 K was imposed at the walls. Therefore, it was considered that the nitrogen injector system partially operated, and then it failed and stopped before the beginning of the simulation. The breach generated a transonic jet due to the pressure difference between the outer ambient conditions and the vacuum conditions within the vessel (Figure 9, Top). During the sequence, chocked conditions resulted at the breach with an air entrainment rate in the VV of ~28.2 kg/s. The jet also induced a highly turbulent flow field within the vessel. Figure 9 (Bottom) shows the time-average spatial distribution of turbulence intensity (i.e. $u'/U_{local\text{-}mean}$) within the VV before the ignition and its histogram. As shown, the average level within the vessel volume before the ignition was of the order of 0.77. Nonetheless, the spatial distribution showed regions with permanent turbulence intensity values over the mean level, as for instance the jet shear layer over the breach, where a recirculation region was settled. As a consequence of the initial mass of H_2 (0.584 kg), the averaged equivalence ratio in the scenario reduced exponentially during the first 835 ms of the sequence until reaching ϕ=0.84. It is worth noting that due to the air entrainment through the breach, the H_2 was pushed and concentrated at the opposite side of the VV torus. At that moment, an ignition was artificially induced at the symmetry plane opposite to the breach (i.e., a section of Θ=0º). At the ignition, the pressure within the VV was 4.5 kPa, the average temperature was 467 K and the gas composition within the VV was a mixture of 0.584 kg of H_2, 21.37 kg of N_2, and 5.45 kg of O_2 and 0.324 kg of Ar. For comparison purposes, the ignition was generated at the same location as in the "Quiescent Case". The initial flame generated after the ignition accelerated through the corridors of the toroid interacting with the large-scale turbulence induced by the jet (Figure 9, Top). The flame front definition was based on numerical Schlieren computed as $(\nabla\rho-\nabla\rho_{min})/(\nabla\rho_{max}-\nabla\rho_{min})$. Turbulence-flame interaction enhanced transport phenomena and accelerated the flame at a higher rate than in the "Quiescent Case". As the flame expands along the corridors its acceleration rate decreases due to the increase of the O_2 enrichment of the mixture close the breach. Figure 10, shows a comparison of the spherical equivalent radius of the flame R_{eq}, burning speed and averaged pressure evolution with time. As shown, burning speed increased reaching $S_{b\ LOVA}\ /\ S_{b\ Quiescent}$ ~ 3.5, which resulted in a faster sequence when compared to the "Quiescent Case". In this sequence (with a big breach), the level of turbulence induced by the breach is high what results in a boost of the flame acceleration due to turbulence. Notwithstanding, the averaged

pressure level reached at the vessel due to combustion was similar ($P_{max}/P_o \sim 4.8$). In this case, the flame accelerated without reaching detonation conditions.

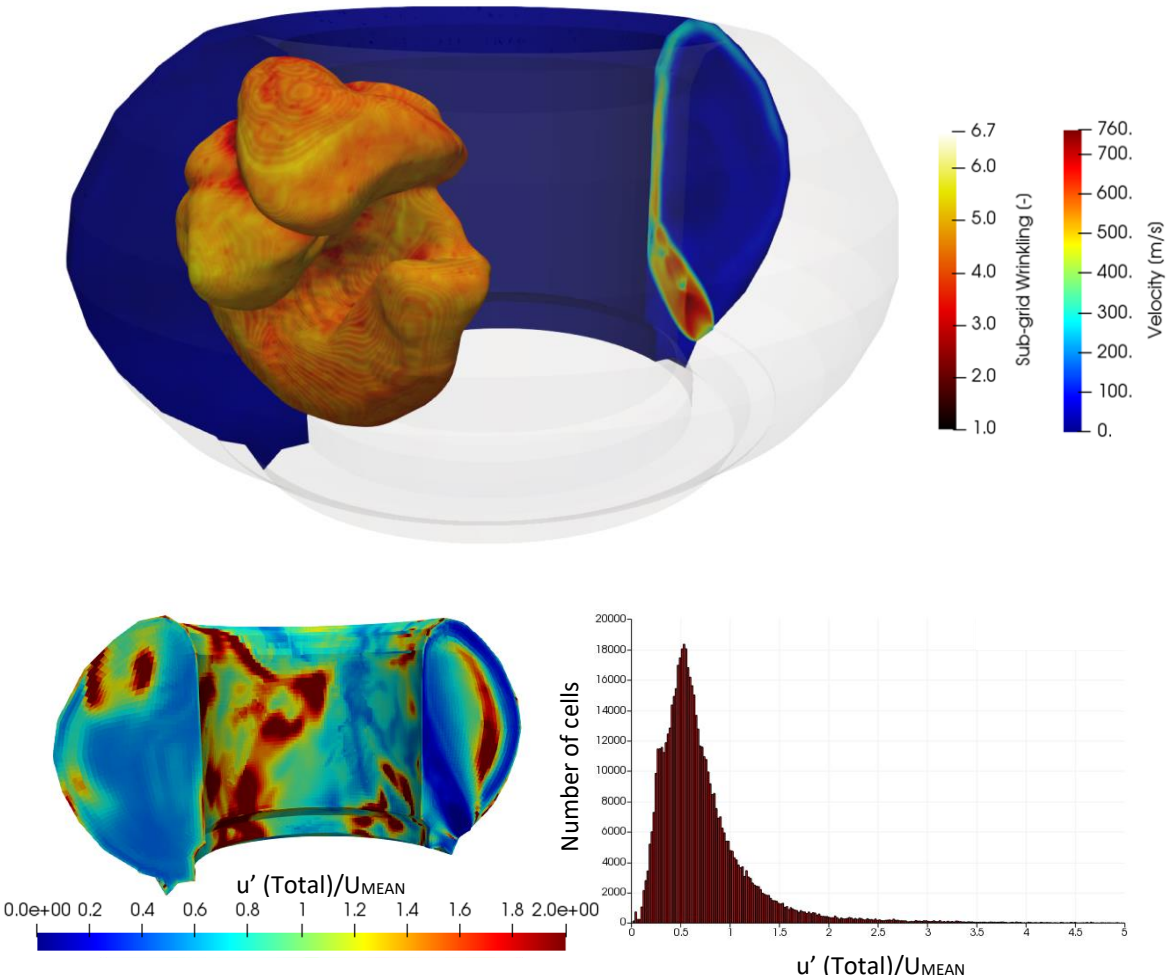

Figure 9: (Top) Jet expansion within the VV and flame front based on numerical Schlieren computed as (∇ρ-∇ρmin)/(∇ρmax-∇ρmin). (Bottom) Time-averaged turbulence intensity (u'/Ulocal-mean) within the VV before the ignition, (bottom-left) Time-averaged spatial distribution, (bottom-right) histogram.

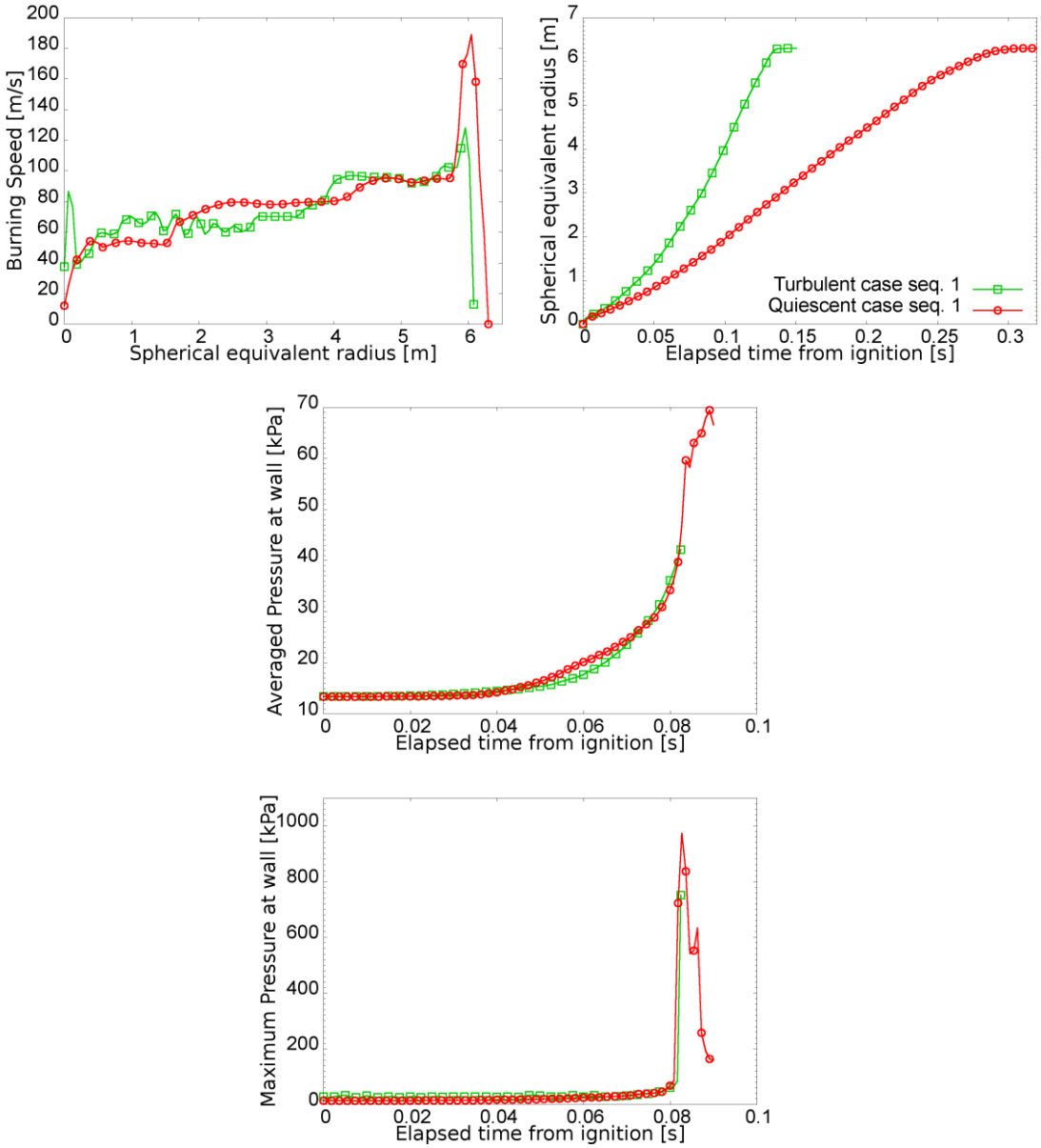

Figure 10: Dynamic evolution for Sequence 1. (Top-Left) Burning speed as a function of Spherical equivalent radius. (Top-Right) Spherical equivalent radius as a function of time elapsed from the ignition. (Bottom) Averaged pressure evolution with time elapsed from the ignition. In the legend, "Turbulent case seq. 1" corresponds to the "LOVA Case" of Sequence 1. "Quiescent case seq. 1" corresponds to the "Quiescent Case" of Sequence 1

Another interesting aspect of the results was jet-flame interaction. As the flame approached the breach, the flame front surrounded the jet generating its oscillation by thermo-diffusive and Darrieus–Landau instabilities, which also induced the wrinkling of the flame front. Figure 11 shows some snapshots of the vorticity field in the surrounding of the jet as the flame front approaches the breach. The figure shows the perturbation of the jet and the flame front during its interaction. Additionally, during the expansion of flame across the jet upper shear layer, it was found that in this region, the flame speed increased as it interacted with middle size vortex generated by the jet. All in all, results suggested that the vorticity magnitude of the middle scale eddies, located at the unburned mixture, may be a key parameter in the flame folding, the increase of the flame surface, and the subsequent flame acceleration process.

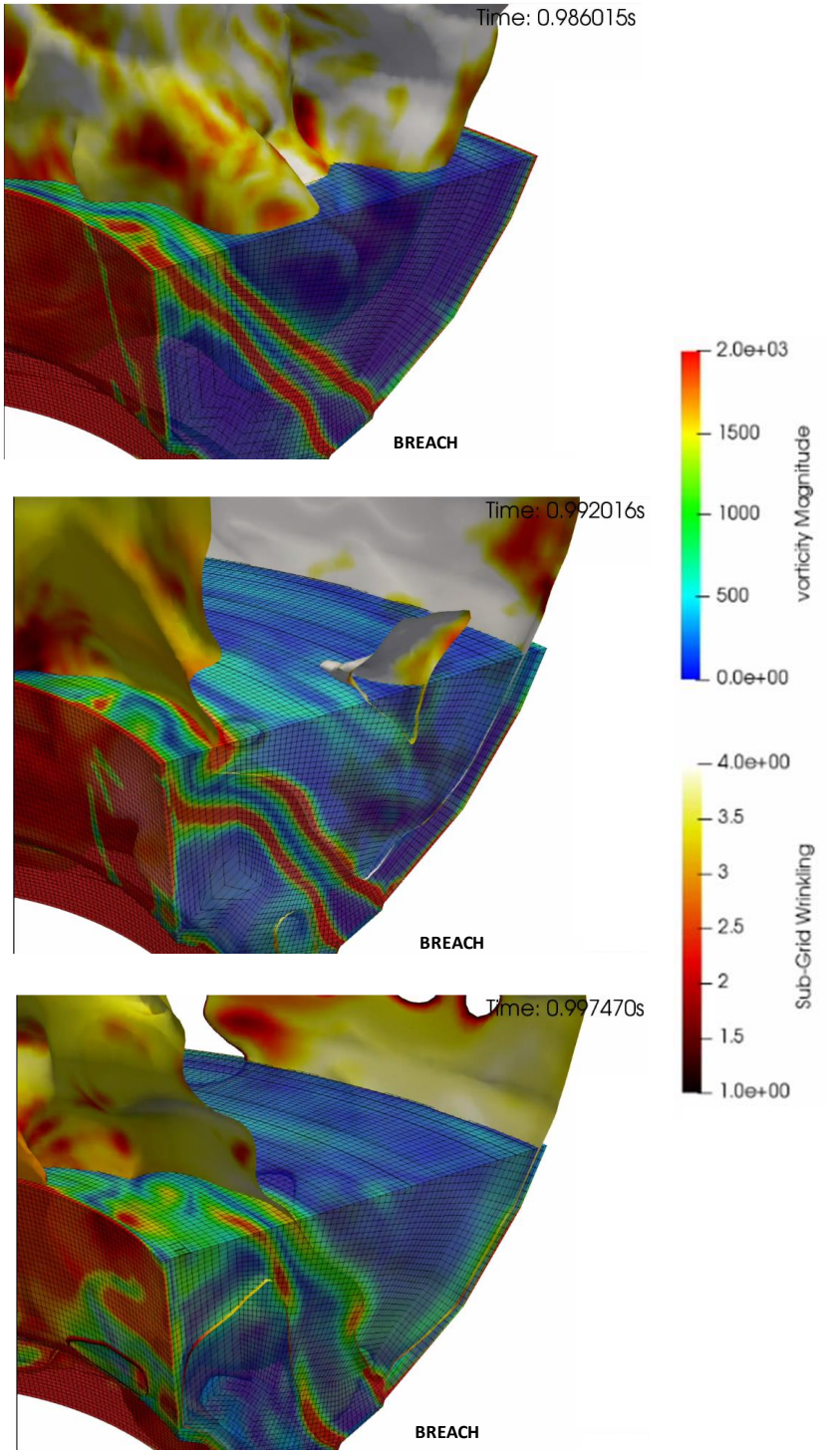

Figure 11: Time evolution of spatial vorticity field during the flame-jet interaction.

4.2.2 Analysis of Sequence 2

This sequence corresponds to a scenario with a breach of 0.02 m^2 and a pressure of 13.35 kPa at the VV during the ignition. In this sequence two different combustion cases were analyzed: a

reference combustion case without breach and a LOVA combustion case with a breach. Both cases were ignited with the same gas composition and pressure within the VV.

In the "Quiescent Case", a premixed mixture of 2 kg of H_2, 62.08 kg of N_2 and 17.27 kg of O_2 was considered at the beginning of the sequence within the simulated domain. This inventory was the same as the one found in the "LOVA Case" of Sequence 2 at the moment of the ignition. This way both simulations could be compared, and the impact of the jet induced turbulence could be assessed. The mixture corresponds to an average equivalence ratio ϕ=0.923. The ignition was supposed to occur in the centre of a meridional plane of $\Theta = 0^{o}$ at VV pressure of 13.35 kPa, gas temperature of 452 K, and a fixed wall temperature of 438 K. In this case, the combustion dynamics was similar in terms of the morphology of the flame front to the one found in the "Quiescent Case" of Scenario 1 although the flame expanded faster due to the higher initial pressure and the slightly richer H_2 composition of the mixture (what increased the S_L^o). The initial spherical laminar flame front expanded and impacted the closest walls of the vessel at velocity levels of ~150 m/s, whereas other fraction of the flame front progressed and kept its expansion along the corridor of the toroid. During the expansion, the flame front increased progressively its speed and level of turbulent kinetic energy. The two flame fronts accelerated along the two symmetric corridors of the toroid and collided with each other at the opposite side 0.08 s after the ignition (~1/3 of the time required in the "Quiescent Case" of Sequence 1). Because of this collision, the flame experienced a compression and a transition to detonation (Figure 12). Consequently, the flame reached velocity levels ~500 m/s and the pressure levels at the walls reached averaged values of 70 kPa and local peaks of ~600 kPa. This means an averaged overpressure level of the order of $P_{max}/P_o \sim 5.2$ and local peaks of $P_{max}/P_o \sim 45$ in small lapses of time. In this case, the average wall pressure at the VV was below the vessel design pressure but the local peaks reached were over it.

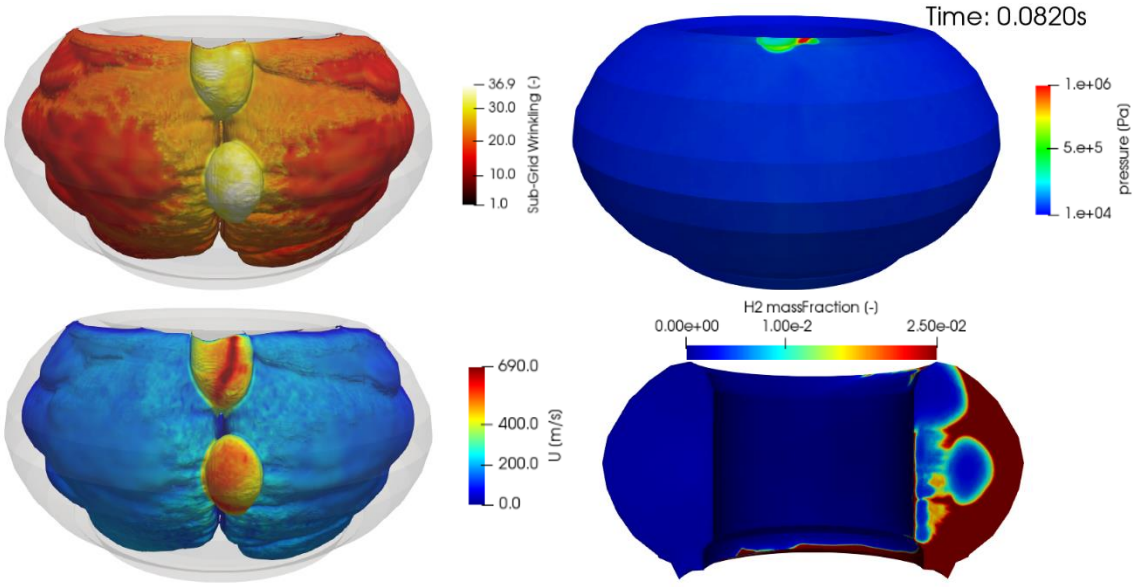

Figure 12: Quiescent Case Sequence 2. Detail of the transition to detonation when the two flame fronts collide. (Top-Left) Sub-grid wrinkling scaler field at the flame front. (Top-Right) Wall pressure. (Bottom-Left) Velocity field at the flame surface. (Bottom-Right) H_2 mass fraction.

In the "LOVA Case", the simulation started with the initial entrainment of air across a wall breach of 0.02 m^2, which was located at the same location than in the previous sequence. The initial conditions of the sequence were fixed, following Xiao et al. [43], as: 500 Pa, 500 K and 3.46 kg

of N_2 and 2 kg of H_2 within the VV. In this case, we considered that the nitrogen injection system partially operated and only part of the metal dust reacted and, as a consequence, a total inventory of 2 kg of H_2 was located in the VV at the beginning of the simulation. As the sequence starts, air ingress within the domain. During the sequence, chocked conditions resulted at the breach with an air entrainment rate lower than in Sequence 1. As a consequence of the initial mass of H_2, the averaged equivalence ratio reduced exponentially during the first 30 s of the sequence until reaching ϕ=0.923 of averaged value within the VV. Besides, it is worth noting that due to the air entrainment through the breach, the H_2 was pushed and concentrated at the opposite side of the VV torus where ϕ reached local values of ϕ =1.2 at 30 s. At that moment, the pressure within the VV was 13.5 kPa, the average temperature was 452 K and the gas inventory within the VV was, 2 kg of H_2, 62.08 kg of N_2 and 17.27 kg of O_2. The ignition was artificially induced at the symmetry plane opposite to the breach (i.e., a section of Θ=0º) at the same location as in the "Quiescent Case". The initial flame generated after the ignition accelerated through the corridors of the toroid. During the sequence, the jet momentum "pushes" the flame back what partially suppress the flame expansion and slow down its acceleration. In sequence 2 (i.e. with a small breach), the turbulence level induced by the jet at the breach is lower than in Sequence 1 and the jet turbulence cannot enhance flame acceleration as Sequence 1. Besides, in this sequence, the flame interaction with the jet is lower. The flame front is not deformed by the jet turbulence. Conversely, in Sequence 1 the flame interacts with the jet increasing the flame surface what enhances its acceleration whereas in Sequence 2 the flame surface is not increased or promoted by the jet what reduces the acceleration potential of the flame. Notwithstanding, the two flame fronts expanded along the corridors of the toroid with a dynamic and velocity level similar to the one found in the "Quiescent Case" of Sequence 2. Because of the collision, the flame experienced a compression and a transition to detonation reaching wall average values 70kPa and local peaks of ~600kPa (i.e. $P_{max}/P_o \sim 45$). The detonation is initiated relatively close to the breach and the total pressure reached close to the breach within the VV exceeds the ambient pressure and part of the gas within the VV is discharged outdoor.

Figure 13, shows a comparison of the spherical equivalent radius of the flame R_{eq}, burning speed, wall averaged pressure and wall maximum pressure evolution with time. As shown, for a breach of 0.02 m^2 the jet induced turbulence was not able to promote flame acceleration and the burning speed was similar to the quiescent case $S_{b\ LOVA}/S_{b\ Quiescent} \sim 1$. Notwithstanding, the averaged pressure level reached at the vessel wall due to combustion was similar ($P_{max}/P_o \sim 5.2$).

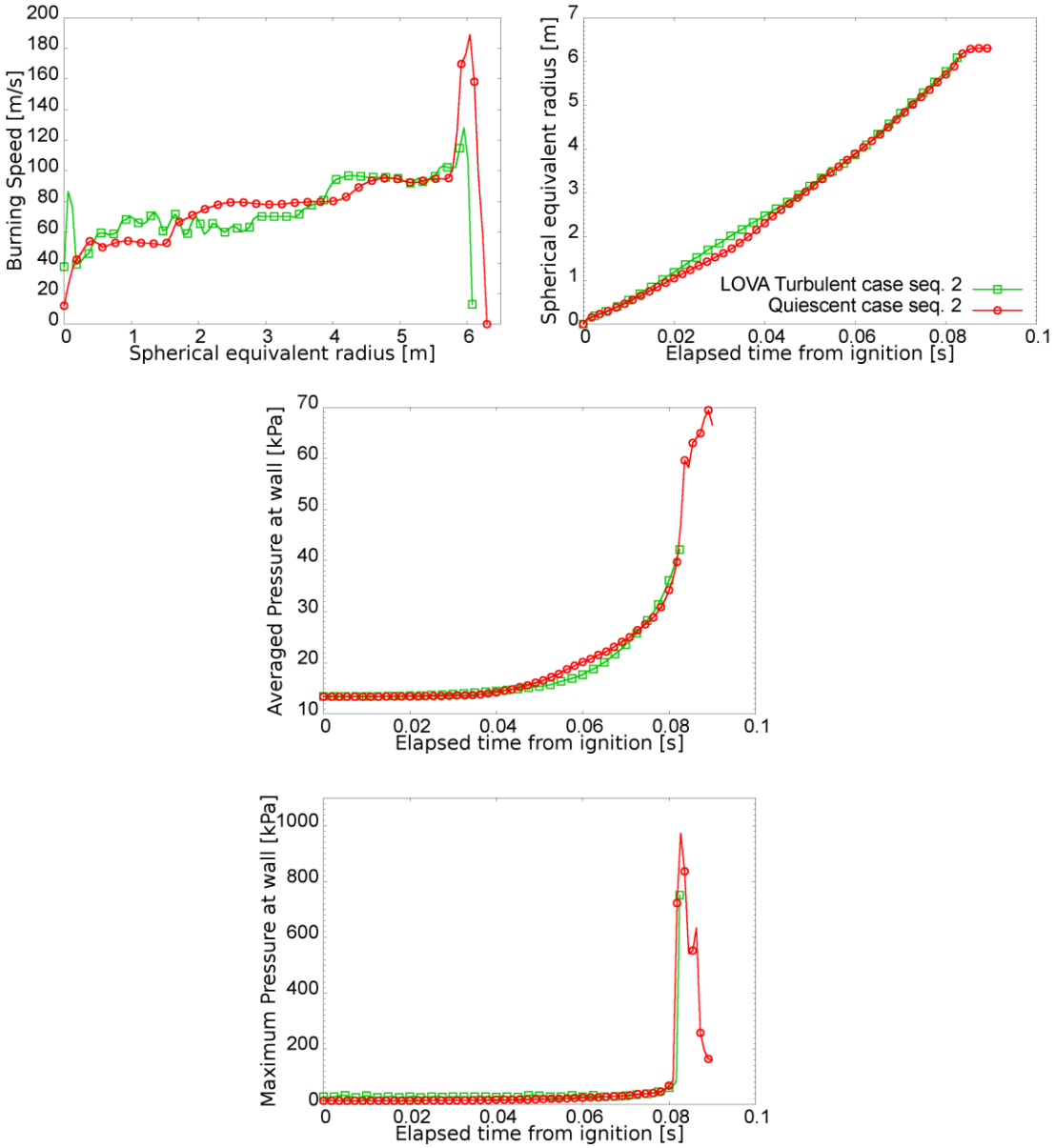

Figure 13: Dynamic evolution for Sequence 2. (Top-Left) Burning speed as a function of Spherical equivalent radius. (Top-Right) Spherical equivalent radius as a function of time elapsed from the ignition. (Middle) Averaged pressure evolution with time elapsed from the ignition. (Bottom) Maximum wall pressure evolution with time elapsed from the ignition. Bottom: In the legend, "Turbulent case seq. 2" corresponds to the "LOVA Case" of Sequence 2. "Quiescent case seq. 2" corresponds to the "Quiescent Case" of Sequence 2.

All in all, it must be remarked that, with the present model, DDT cannot be fully resolved in terms of numerical resolution. The approach predicts the flame dynamic behavior and the flame velocity evolution in such scenarios based on the thickening flame model. Thus, this sequence should be considered as a hypothetical scenario that should not be disregarded. On the contrary, this scenario should be further investigated in order to confirm the predicted results.

5. CONCLUSIONS AND FUTURE WORK

A LOVA sequence with hydrogen deflagration within ITER VV was studied. To do so, two different turbulent combustion models based on LES were proposed and benchmarked against turbulent combustion experiments in a spherical bomb. The benchmark of LES-FPV and LES-TFM models against combustion experiments under a well-characterized turbulent field showed

that this type of model, coupled with a detailed chemical kinetic scheme, behaved well for this kind of problems. The assessment also revealed that that TFM with detailed chemistry and in-situ adaptive ISAT tabulation method had a better prediction of the experimental flame speed and pressure evolution than the FPV. Results also showed that, when compared with the cases with no initial turbulence, burning speed increased drastically when the turbulence was increased, whereas the maximum combustion pressure was not affected by the turbulence and maintained almost constant.

Based on the results, the TFM model was selected to simulate two accident sequences within ITER VV. The results of the simulations showed that a breach at the wall generated a transonic jet due to the pressure difference between the outer ambient conditions and the vacuum conditions within the vessel. During the sequence, chocked conditions resulted at the breach with an air entrainment rate in the VV. In the case of a breach of 0.15 m^2 after 835 ms of the initiation of the sequence, ignition was induced at 4500 Pa with ϕ=0.84 . When this combustion sequence under LOVA conditions was compared with the combustion sequence under quiescent conditions, with airtight conditions (i.e. no breach at the walls), results showed that burning speed increased by a factor of up to 3.5, due to the flame acceleration induced by the turbulence level within the VV. That resulted in a faster sequence without detonation. Notwithstanding, the averaged pressure reached at the vessel due to the combustion was similar ($P_{max}/P_o \sim 4.5$). However, in the case of a breach of 0.02 m^2 and at ignition induced at 13.35 kPa with ϕ=0.92, the turbulence induced by the jet was not able to enhance flame acceleration and the burning speed was similar to the case of airtight conditions. This equivalence ratio and pressure level provided a deflagration to detonation transition. In this case, the average wall pressure reached at the VV was $P_{max}/P_o \sim 5.2$ whereas there were reported local peaks of ~600kPa (i.e. $P_{max}/P_o \sim 45$).

Future work will focus on the evaluation of different LOVA sequences with richer hydrogen conditions within ITER.

ACKNOWLEDGEMENTS

The authors would like to acknowledge the financial support of Institut of Radioprotection et Sûreté Nucléaire, IRSN (France), with the contract (DA 3000011012/CA32000911) IRSN SIRET: 440 546 018 00019 Code APE: 7219 Z, as well as the support of the Spanish Ministry of Economy and Competitiveness and the European Commission (European Regional Development Fund (ERDF) / FEDER funds), throughout the computational resources of SAIT-UPCT.

REFERENCES

[1] A.J. Aspden, M.S. Day, J.B. Bell, Turbulence-flame interaction in lean premixed hydrogen: Transition to the distributed burning regime, J. Fluid Mech. 680 (2011) 287-320.

[2] T. Poinsot and D. Veynante, Theoretical and numerical combustion, Ed. R. T., Edwards, Philadelphia, 2001.

[3] H. Pitsch, Large-Eddy Simulation of Turbulent Combustion, Annu. Rev. Fluid. Mech. 38 (2006) 453-482.

[4] G. Tabor, H.G. Weller, Large Eddy Simulation of Premixed Turbulent Combustion Using Ξ Flame Surface Wrinkling Model, Flow Turbul. Combustion 72 (2004) 1–28.

[5] N. Peters, Turbulent Combustion, 2nd ed.,Cambridge University Press, Cambridge, 2000.

[6] O. Chatakonda, E. R. Hawkes, M. J. Brear, J. H. Chen, E. Knudsen, H. Pitsch, Modeling of the wrinkling of premixed turbulent flames in the thin reaction zones regime for large eddy simulation. Center of turbulence Research, Proceedings of the summer Program (2010).

[7] A. L. Sánchez, F. A. Williams, Recent advances in understanding of flammability characteristics of hydrogen, Progress in Energy and Combustion Science 41 (2014) 1-55.

[8] F. A. Williams, Detailed and reduced chemistry for hydrogen autoignition, J. of Loss Prevention in the process Industries 21 (2008) 131-135.

[9] S. Emami, K. Mazaheri, A. Shamooni, Y. Mahmoudi, LES of flame acceleration and DDT in hydrogen-air mixture using artificially thickened flame approach and detailed chemical kinetics, Int. J. Hydrogen Energy 40 (2015) 7395-7498.

[10] E.S. Oran, V.N. Gamezo, Origins of the deflagration-to-detonation transition in gas-phase combustion, Combust. Flame 148 (2007) 4-47.

[11] Y.B. Zeldovich, Regime Classification of an Exothermic Reaction with Nonuniform Initial Conditions, Combust. Flame 39 (1980) 211-214.

[12] A.Y. Poludnenko, Pulsating instability and self-acceleration of fast turbulent flames, Pysh. Fluids 27 (2015) 014-106.

[13] A. Teodorczyk, P. Drobniak, A. Dabkowski, Fast turbulent deflagration and DDT of hydrogen-air mixtures in small obstructed channel. Int. J. Hydrogen Energy 34 (2009) 5887-93.

[14] P. Wang and X. S. Bai, Large eddy simulation of turbulent premixed flames using level-set G-equation, Proc. Combust. Inst. 30 (2005) 583-591.

[15] H. Pitsch, A G-equation formulation for large-eddy simulation of premixed turbulent combustion, Annu. Researh Briefs 2002, Center for Turbulence Research (2002).

[16] E.R. Hawkes and R. S. Cant., A flame surface density approach to large eddy simulation of premixed turbulent combustion, Proc. Combust. Inst. 28 (2000) 51-58.

[17] F. Charlette, C. Meneveau and D. Veynante, A power-law flame wrinkling model for LES of premixed turbulent combustion. Part I: Non-dynamic formulation and initial tests, Combust. Flame (2002) 131:159.

[18] M. Berglund, E. Fedina, C. Fureby, J. Tegnér, and V. Sabelnikov, Finite rate chemistry LES of self-ignition in a supersonic combustion ramjet. AIAA J. 48 (2010) 540. https://doi.org/10.2514/1.43746

[19] B.F. Magnussen, On the structure of turbulence and a generalised eddy dissipation concept for chemical reactions in turbulent flow, 19th AIAA Sc. Meeting, St. Louis, USA, 1981.

[20] P. Givi, Filtered density function for subgrid scale modeling of turbulent combustion. AIAA J. 44 (2006). https://doi.org/10.2514/1.15514

[21] A.Y. Klimenko, R.W. Bilger, Conditional moment closure for turbulent combustion, Prog. Energy Combust. Sci. 25 (1999) 595–687.
[22] V. Sankaran, S. Menon, Subgrid combustion modeling of 3-D premixed flames in the thin-reaction-zone regime, Proc. Combust. Inst. 30 (2005) 575–583
[23] O. Krüger, S. Terhaar, C.O. Paschereit, C. Duwig, Large Eddy Simulations of Hydrogen Oxidation at Ultra-Wet Conditions in a Model Gas Turbine Combustor Applying Detailed Chemistry, J. Eng. Gas Turbines Power 135 (2013) 021501-9.
[24] M.V. Papalexandrix, Numerical simulation of detonations in mixtures of gases and solid particles, J. Fluid Mech, 507 (2004) 95-142.
[25] M.A. Liberman, M.F. Ivanov, A.D. Kiverin, M.S. Kuznetsov, A.A. Chukalovsky, T.V. Rakhimova, Deflagration-to-detonation transistion in highly reactive combustion mixtures, Acta Astronaut 67 (2010) 683-701.
[26] M.A. Liberman, A.D. Kiverin, M.F. Ivanov, On detonation initiation by a temperature gradient for a detailed chemical reaction model. Phys. Letters A. 375 (2011) 1803-1808.
[27] R.C. Rogers, C. J. Schexnayder Jr, Chemical kinetic analysis of hydrogen-air ignition and reaction times, NASA, Langley Research Center. 1981.
[28] N.M. Marinov, C.K. Westbrook, W.J. Pitz, Detailed and global chemical kinetics model for hydrogen. In; 8th Int. Symp.on transport properties, Oct. San Francisco, Canada, 1995.
[29] M. Slack, A. Grillo, Investigation of Hydrogen-Air ignition sensitized by Nitric Oxide and Nitrogen Dioxide, Report No. CR-2896, NASA USA, 1987.
[30] E. Schultz, J. Sheperd, Validation of detailed reaction mechanisms for detonation simulation. Cal. Inst. Of Tech. Graduate Aeronautical Lab. Tech. Rep. FM 99-5 (2000) 230.
[31] J.H.S. Lee, R. Knystautas, C.K. Chan, Turbulent flame propagation in obstacle-filled tubes, Proc. Combust. Inst. 20:16 (1984) 63-72.
[32] A. Teodorczyk, J.H.S. Lee, R. Knystautas, The structure of fast turbulent flames in very rough, obstacle filled channels, Proc Combust. Inst. 23 (1990) 735-741.
[33] M. Kuznetsov, S. Kobelt, J. Grune, T. Jordan, Flammability limits and laminar flame speed of hydrogen-air mixtures at sub-atmospheric pressures, Int. J. Hydrogen Energy 37 (2012) 17580-17588.
[34] J. Sabard, N. Chaumeix, A. Bentaib, Hydrogen explosion in ITER: effect of oxygen content on flame propagation of $H_2/O_2/N_2$ mixtures, Fusion Eng. Des. 88 (2013) 2669-2673.
[35] J.R. García-Cascales, F.J.S. Velasco, R.A. Otón-Martínez, S. Espín-Tolosa, A. Bentaib, N. Meynet, A. Bleyer, Characterisation of metal combustión with DUST code, Fusion engineering and design 98-99 (2015) 2142-2146.
[36] F.J.S. Velasco, R.A. Otón-Martínez, J.R. García-Cascales, S. Espín, N. Meynet, A. Bentaib, Modelling detonation of H2-O2-N2 mixtures in presence of solid particles in 3D scenarios, Int. J. of Hydrogen Energy. 41 (2016) 17154 – 17168.
[37] A. Denkevits, S. Dorofeev, Dust explosion hazard in ITER: Explosion indices of fine graphite and tungsten dusts and their mixtures, Fusion Engineering and Design, 75 (2005) 1135–1139.
[38] C. Day, A. Antipenkov, I.-R. Cristescu, M. Dremel, G. Federici, H. Haas, V. Hauer a, A. Macka, D.K. Murdochc, M. Wykes, Hydrogen inventories in the vacuum pumping systems of ITER, Fusion Engineering and Design 81 (2006) 777–784. doi:10.1016/j.fusengdes.2005.07.020

[39] N. Taylor, D. Baker, S. Ciattaglia, P. Cortes, J. Elbez-Uzan, M. Iseli, S. Reyes, L. Rodriguez-Rodrigo, S. Rosanvallon, L. Topilski, Updated safety analysis of ITER, Fusion Engineering and Design 86 (2011) 619–622. doi:10.1016/j.fusengdes.2010.11.037

[40] N. Taylor, S. Ciattaglia, P. Cortes, M. Iseli, S. Rosanvallon, L. Topilski, ITER safety and licensing update, Fusion Engineering and Design 87 (2012) 476–481. doi:10.1016/j.fusengdes.2012.01.001

[41] F. Le Guern, S. Ciattaglia, G. Counsell, J. Kim, M. Walsh, A. Denkevitz, N. Endstrasser, H. Eixenberger, E. Gauthier, T. Jordan, L. Kammerloher, M. Kuznetsov, R. Neu, R. Redlinger, B. Reiter, V. Rohde, Z. Xu, R&D on in-vessel dust and tritium management in ITER, IEEE/NPSS 24th Symposium on Fusion Engineering, Chicago, IL, (2011) 1-5. doi: 10.1109/SOFE.2011.6052249

[42] M. Lukacs, L.G. Williams, Nuclear safety issues for fusion power plants, Fusion Engineering and Design 150 (2020) 111377. doi: 10.1016/j.fusengdes.2019.111377

[43] J. Xiao, J.R. Travis, W. Breitung, T. Jordan, Numerical analysis of hydrogen risk mitigation measures for support of ITER licensing, Fusion Engineering and Design 85 (2010) 205-214. doi:10.1016/j.fusengdes.2009.12.008

[44] M. Iseli, In-vessel hydrogen deflagration and detonation in ITER-FEAT, Fusion Engineering and Design 54 (2001) 421–430. doi: 10.1016/S0920-3796(00)00561-5

[45] M. Kuznetsov, M. Czerniak, J. Grune, T. Jordan, Effect of temperature on laminar flame velocity for Hydrogen-air mixtures at reduced pressures, International Conference on Hydrogen Safety (ICHS), Brussels, Belgium (2013).

[46] M. Kuznetsov, J. Grune, S. Kobelt, K. Sempert, T. Jordan, Experiments for the Hydrogen combustion aspects of ITER LOVA scenarios, Fusion Engineering and Design 86 (2011) 2747–2752. doi:10.1016/j.fusengdes.2011.01.050

[47] N. Taylor, P. Cortes, Lessons learnt from ITER safety & licensing for DEMO and future nuclear fusion facilities, Fusion Engineering and Design 89 (2014) 1995–2000. doi: 10.1016/j.fusengdes.2013.12.030

[48] V. Chuyanov, L. Topilski, Prevention of hydrogen and dust explosion in ITER, Fusion Engineering and Design 81 (2006) 1313-1319. doi:10.1016/j.fusengdes.2005.05.009

[49] S. Reyes, L. Topilski, N. Taylor, B.J. Merrill, L.L. Sponton, Updated Modeling of Postulated Accident Scenarios in ITER, Fusion Science and Technology 56:2 (2009) 789-793, doi: 10.13182/FST09-A9005

[50] J. Goulier, N. Chaumeix, F. Halter, N. Meynet, A. Bentaïb, Experimental study of laminar and turbulent flame speed of a spherical flame in a fan-stirred closed vessel for hydrogen safety application. Nuclear Engineering and Design 312 (2017) 214–227.

[51] J. Goulier, A. Comandini, F. Halter, N. Chaumeix, Experimental study on turbulent expanding flames of lean hydrogen/air mixtures, Proceedings of the Combustion Institute 36 (2017) 2823–2832.

[52] Favre, Statistical equations of turbulent gases, in: Problems of hydrodynamic and continuum Mechanics, SIAM, Philadelphia (1969) 231-266.

[53] H. Weller, The development of a new flame area combustion model using conditional averaging. Thermo-Fluids Section Report TF 9307, Imperial College of Science, Technology and Medicine (1993).

[54] H. Weller, S. Uslu, A. Gosman, R. Maly, R. Herweg and B. Heel, Prediction of combustion in homogeneous-charge spark-ignition Engines, International Symposium COMODIA 94 (1994) 163–169.

[55] Gülder, Ö.L., Turbulent premixed flame propagation models for different combustion regimes, Twenty-Third Symposium (International) on Combustion. The Combustion Institute, Pitts- burgh, PA (1990) 743–750.
[56] D.V.T. Poinsot, Theoretical and Numerical Combustion, third edition, 2012.
[57] J. O. Hirschfelder, C. F. Curtiss, R. B. Bird, and M. G. Mayer, Molecular theory of gases and liquids, vol. 26. Wiley New York, 1954.
[58] F. Williams, Combustion theory, second edition, Addison-Wesley Pub.,Reading, MA, Jan 1985.
[59] L. Durand, W. Polifke, ASME Turbo Expo Conf. Proc. (2007) 869–878.
[60] F. Charlette, C. Meneveau, and D. Veynante, A power-law flame wrinkling model for LES of premixed turbulent combustion. Part II: Dynamic formulation. Combust. Flame (2002) 181:197.
[61] O. Colin, F. Ducros, D. Veynante, and T. Poinsot, "A thickened flame model for large eddy simulations of turbulent premixed combustion," Physics of Fluids (1994-present) 12 (2000) 1843-1863.
[62] G. Wang, M. Boileau, D. Veynante, Implementation of a dynamic thickened flame model for large eddy simulations of turbulent premixed combustion, Combustion and Flame 158 (2011) 2199–2213.
[63] F. Gouldin, K. Bray, J. Chen, Combust. Flame 77 (1989) 241–259.
[64] O. Gulder, 23rd Symposium (International) on Combustion, The Combustion Institute, Pittsburgh, Orléans (1990) 835–842.
[65] J. B. McBride, S. Gordon, M. A. Reno, Coefficients for Calculating Thermodynamic and Transport Properties of Individual Species. NASA, 1983.
[66] W. Sutherland, The viscosity of gases and molecular force, Philosophical Magazine, S. 5, 36 (1893) 507-531.
[67] P. Boivin, C. Jiménez, A. L. Sánchez, F.A. Williams, An explicit reduced mechanism for H 2 -air combustion, Proceedings of the Combustion Institute, 2011.
[68] J. Troe, Towards a quantitative understanding of elementary combustion reactions, Proceedings of the Combustion Institute, 22 (1988) 843–862.
[69] S.B. Pope, Computationally efficient implementation of combustion chemistry using in situ adaptive tabulation, Combust. Theory Modelling 1 (1997) 41-63.
[70] L. Lu, S.B. Pope, An improved algorithm for in situ adaptive tabulation, J. Comput. Phys. 228 (2) (2009) 361–386.
[71] V. Hiremath, Z. Ren, S. B. Pope, Combined dimension reduction and tabulation strategy using ISAT–RCCE–GALI for the efficient implementation of combustion chemistry. Combustion and Flame 158 (2011) 2113–2127.
[72] C. Fureby, On LES and DES of Wall Bounded Flows, Ercoftac Bulletin No. 72, Marsh Issue, 2007.
[73] Mével, R., Lafosse, F., Chaumeix, N., Dupré, G., Paillard, C.-E., 2009. Spherical expanding flames in H2–N2O–Ar mixtures: flame speed measurements and kinetic modeling. Int. J. Hydrogen Energy 34 (21), 9007–9018.
[74] Singer MA, Pope SB, Najm HN. Modeling unsteady reacting flow with operator splitting and ISAT. Combust Flame 147 (2006) 150-62.
[75] Goldstein, S: 'On the Vortex Theory of Screw Propellers', Proceedings of the Royal Society of London. Series A, Containing Papers of a Mathematical and Physical Character, 123 (1929) 440-465

6.3 Capabilities and limitations of Large Eddy Simulation with perfectly stirred reactor assumption for engineering applications of unsteady, hydrogen combustion sequences

This work evaluates the capabilities of *Large Eddy Simulation* with *Perfectly Stirred Reactor* (PSR) assumption and detailed chemistry to predict unsteady, premixed, hydrogen combustion sequences. This approach considers that there is a homogeneous concentration and temperature in each computational cell at sub-grid level. Different sub-grid turbulence and detailed chemistry models were tested in both experimental and numerical benchmarks. This permitted to evaluate the capabilities and limitations of this modelling approach when simulating unsteady combustion sequences with low or moderate Reynolds numbers.

The model was benchmarked with hydrogen-air experimental tests and with numerical data of flame acceleration in an obstructed channel. Results permit to identify major shortcomings that should be addressed with this approach and to assess the uncertainties linked to the use of different sub-models.

Results show that this LES approach can be applied to a grid with enough resolution to resolve flame thickness and wrinkling patterns. In this case, no sub-grid scale combustion modelling is needed. However, spatial resolution was found to be critical. The unstretched laminar flame speed predicted with this type of models with meshes $\delta_L^0/\Delta x \sim 1$ provide errors of ~18%. Furthermore, numerical diffusion might play an important role in the predicted flame speed. To overcome this issue, dynamic mesh refinement with flame tracking techniques have been developed and tested, improving the results, and reducing the computational cost required. Thus, the computational resources needed to reach the required level of flame resolution of this modelling approach increases as the flame expands and the flow increases its Reynolds number due to flame wrinkling and the effective increase of the flame surface. This LES approach coupled with detailed chemistry and in-situ adaptive tabulation (ISAT) method is an accurate and cost-affordable strategy to simulate the initial stages (i.e., post-ignition and flame acceleration) of premixed combustion problems, with low or moderate Reynolds numbers with reasonable accuracy, if a certain level of grid refinement is reached ($\delta_L^0/\Delta x \geq 8$). An important effect of the sub-grid models is found, which points out the uncertainty linked with its election, especially in the case of grids that do not provide enough flame resolution.

As for the prediction of the combustion products, the models predicted, with an error smaller than 6%, the final species composition. PISO scheme and Williams' chemical model provided the smallest deviations from experimental data. Results also showed that this LES approach was able to account for the cellular flame pattern at the post-ignition phase, and provided results which were qualitatively similar to the experimental ones. Besides, this approach is also able to predict flame acceleration in an obstructed channel if the required level of flame resolution is met. These results permit to postulate this LES approach for experiments interpretation and dynamic studies of the early stage of a flame expansion.

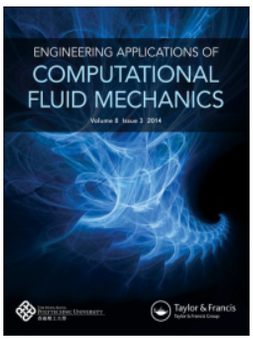

Taylor & Francis
Taylor & Francis Group

Engineering Applications of Computational Fluid Mechanics

ISSN: (Print) (Online) Journal homepage: https://www.tandfonline.com/loi/tcfm20

Capabilities and limitations of Large Eddy Simulation with perfectly stirred reactor assumption for engineering applications of unsteady, hydrogen combustion sequences

F. Nicolás-Pérez, F. J. S. Velasco, R. A. Otón-Martínez, J. R. García-Cascales, A. Bentaib & N. Chaumeix

To cite this article: F. Nicolás-Pérez, F. J. S. Velasco, R. A. Otón-Martínez, J. R. García-Cascales, A. Bentaib & N. Chaumeix (2021) Capabilities and limitations of Large Eddy Simulation with perfectly stirred reactor assumption for engineering applications of unsteady, hydrogen combustion sequences, Engineering Applications of Computational Fluid Mechanics, 15:1, 1452-1472, DOI: 10.1080/19942060.2021.1974092

To link to this article: https://doi.org/10.1080/19942060.2021.1974092

Published online: 30 Sep 2021.

ENGINEERING APPLICATIONS OF COMPUTATIONAL FLUID MECHANICS
2021, VOL. 15, NO. 1, 1452–1472
https://doi.org/10.1080/19942060.2021.1974092

Taylor & Francis
Taylor & Francis Group

Capabilities and limitations of Large Eddy Simulation with perfectly stirred reactor assumption for engineering applications of unsteady, hydrogen combustion sequences

F. Nicolás-Pérez[a*], F. J. S. Velasco [a], R. A. Otón-Martínez [b], J. R. García-Cascales [a], A. Bentaib [c] and N. Chaumeix [d]

[a]Fluids and Thermal Engineering, Technical University of Cartagena, Cartagena, Spain; [b]University Centre of Defence at the Spanish Air Force Academy, MDE-UPCT, Murcia, Spain; [c]Institut de Radioprotection et Sûrete Nucléaire, Fontanay-aux-Roses, France; [d]ICARE, CNRS-INSIS, Orléans, France

ABSTRACT

This work evaluates the capabilities of Large Eddy Simulation with perfectly stirred reactor (PSR) assumption and detailed chemistry to predict unsteady, premixed, hydrogen combustion sequences. The model was benchmarked with hydrogen-air experimental tests and with numerical data of flame acceleration in an obstructed channel. Results permit to identify major shortcomings that should be addressed with this approach and to assess the uncertainties linked to the use of different sub-models. Spatial resolution was found to be critical and limits the applications of this approach due to the increase of the computational costs with the flame surface. While the influence of the detailed kinetic chemical scheme used was low, the impact of the sub-grid turbulence model used was high. Results showed that simulations provided good agreement with the experimental data when a minimum spatial resolution of 1/8 of the laminar flame thickness was imposed. This threshold permits to simulate with good results the early stages of the combustion sequence (ignition and initial flame acceleration) but limits the model applications when the flame surface increases. In-situ Adaptive Tabulation (ISAT) was an effective strategy to overcome the limitations and partially reduce the computational cost when detailed chemistry models are used together with PSR-LES.

ARTICLE HISTORY
Received 14 January 2021
Accepted 23 August 2021

KEYWORDS
Perfectly stirred reactor; implicit LES; fast combustion; unsteady

1. Introduction

Chemical industry (Hoi et al., 2007), nuclear power plants (Garcia-Cascales et al., 2014; Karata et al., 2012; OECD, 2000; Sathiah et al., 2012), propulsion (Roy et al., 2004; Smirnov et al., 1999) are some of the fields where experts are especially concerned about safe combustion, accident prevention or hydrodynamics prediction. Benchmarks and real case studies of applications of computational fluid dynamics (CFD) models are key exercises to improve the knowledge in these fields (Issakhov et al., 2020; Kim & Kim, 2019; Pedersen & Rüther, 2019; Soto-Meca et al., 2016; Xiang et al., 2020). These strategies and others where CFD models are coupled with artificial techniques (Mosavi et al., 2019; Park et al., 2020; Shamshirband et al., 2020) are contributing to enhance the efficiency of the computations in these fields. Mosavi et al. (2019) showed how machine learning can help CFD in the prediction of hydrodynamic parameters on two-phase flow of a bubble column reactor with lower computational costs. Shamshirband et al. (2020) proposed a combination of an artificial intelligence optimization algorithm and CFD for modeling chemical-reactor hydrodynamics. Pedersen and Rüther (2019) used a case study to validate a hybrid CFD model and reduce the uncertainty in the prediction of peak flood discharges in rivers. In their study, the authors built both, a lab-scale model and a mesh grid from the same stereolithographic file of a gauging station located in a river in Norway and validated the simulations with the experimental data obtained from the lab-scale model. Issakhov et al. (2020) studied the chemical reaction of combustion sub-products emitted from a thermal power plant located in Kazakhstan and its dispersion in the nearby of the plant with CFD. They used two benchmarks to validate their CFD model before they applied it to the actual case of the study. Xiang et al. (2020) applied different finite-rate combustion models to tran-

CONTACT F. J. S. Velasco fjavier.sanchez@upct.es.

*Currently at Lynx Simulations, Spain.

sonic combustion test cases and compared the results with reference experimental combustors. This comparison permitted to evaluate their capabilities when modeling turbulence-chemistry interactions in transonic combustors. In H_2 accident prevention, Kim and Kim (2019) developed a CFD model for predicting H_2 detonation accidents in nuclear power plants. They used a Euler approach with a 7-step chemical-kinetics scheme that validated both theoretical transonic tests and lab-scale detonation experiments with good results. After the validation, they applied the model to the containment of a nuclear power plant and evaluated the wall overpressure levels that could be reached if a detonation took place. They found that an inventory of 20% of H_2 in the containment would generate overpressure levels of the order of $\sim$2 MPa if a detonation sequence happened.

Nowadays, accurate modeling of H_2 combustion on accident sequences in confined scenarios is difficult due to computational costs and the limited ad-hoc experiments available to validate the models. When it comes to validation, turbulence and chemistry are key topics (Xiang et al., 2020). Modeling of these processes together is highly desirable in many high-Reynolds-number problems, to obtain realistic predictions from the numerical results. Large-Eddy Simulations (LES) seems to be a cost-effective method to reach this goal when analyzing H_2 combustion dynamics in accident sequences. A realistic description of this type of combustion sequences requires the model to take into account several important flow mechanisms. Flow instability and wall interaction are key aspects of gas combustion dynamics playing an important role in flame acceleration or quenching. The non-linearity of the advection process leads to instabilities making the flow unsteady and three dimensional (3D). These instabilities, linked with the vortex dynamics, are some of the dominant flow mechanisms leading to the combustion dynamics. During acceleration, interactions between the flame front and the reflections of pressure perturbations in walls and obstacles might enhance heat release rate and vorticity generation due to Richtmyer-Meshkov instability (Ciccarelli et al., 2010; Meshkov, 1969). Several investigations (Ciccarelli et al., 2010), showed that stretching of the flame front due to the interaction with a non-uniform velocity field is one of the main causes of the flame acceleration. Therefore, to obtain a proper prediction of a combustion sequence, correct modeling of turbulence is essential. For problems with high Reynolds number, Direct Numerical Simulation (DNS) is a useful but demanding approach in terms of computational cost. On the contrary, LES is an option that provides results with reasonable accuracy for turbulent combustion (Pitsch, 2006). Another significant aspect that must be considered is the reaction kinetics. Some of the finite-rate combustion approaches which can be found within the LES framework are: the Implicit LES (ILES) (Duwig et al., 2011; Duwig & Dunn, 2013; Duwig & Ludiciani, 2014; Fureby, 2007; Grinstein & Kailasanath, 1995; Krüger et al., 2013), the Thickened Flame Models / Artificially Thickened Flame models (TFM / ATF) (Colin et al., 2000), the Partially Stirred Reactor (PaSR) models (Berglund et al., 2010) or the combustion modeling based on the Eddy Dissipation Concept (EDC) (Giacomazzi et al., 2004). It is also worth citing other models such as the LES Conditional Moment Closure (CMC), that uses conditionally averaged species equations (Navarro-Martinez et al., 2005), the Linear Eddy Model (LEM) which is based on solving 1D problems with high resolution meshes to obtain data required to model the sub-grid variables involved in LES of a 3D problem (Sankaran & Menon, 2005) or Probability/Filtered Density Function (PDF/FDF) models (Raman & Pitsch, 2007). The ILES, sometimes called 'monotonically integrated' LES (or MILES), considers that each computational cell has a homogeneous concentration and temperature at sub-grid level. In other words, it considers a perfectly stirred reactor situation within the sub-grid domain (PSR-LES). Thus, the validity of this model depends on the intensity of the sub-grid mixing for the combustion regime considered (Fureby, 2007; Duwig et al., 2011). Previous studies showed ILES was able to predict the burning flame speed of reactive flows which had intense small-scale turbulence (Duwig & Dunn, 2013; Duwig & Ludiciani, 2014; Grinstein & Kailasanath, 1995; Krüger et al., 2013). This is the case for distributed combustion regime (Duwig et al., 2011). For the corrugated flamelet regime, to neglect sub-grid scale contributions of the reaction modeling can be a good strategy when the resolution of the grid applied in LES is enough to resolve flame wrinkling patterns (Fiorina et al., 2015). However, it has limitations if the LES grid resolution is not enough. In practice, this strategy can predict the reaction rate relatively well if the heat loses or the stratification weaken the combustion reaction (what results in the thickening of the flame) or if the flame regime falls within the distributed reaction zone or close to it (Dodoulas & Navarro-Martinez, 2013; Duwig et al., 2012; Grinstein & Kailasanath, 1995). Out of that range, this approach may have limitations that must be identified. In the case of steady/frozen combustion conditions, Fiorina et al. (2015) compared this LES approach with others for a gas burner. In that work, they used a Smagorinski sub-grid scale turbulence model. The authors indicated that the selection of the chemical kinetics scheme also influences the reliability of this approach, as the reaction intermediaries that have shorter characteristic length scales may require finer meshes. They also showed that, in the case of stratified flame conditions,

compared to other models, implicit LES exhibited the shortest downstream flame expansion. In that region, the authors found that the grid was not fine enough to capture the wrinkling and thickness of the flame. As a consequence, the under resolution within the flame and the lack of a sub-grid scale flame wrinkling model underestimated the release of heat through the flame front. This resulted in a underprediction of the burning velocity of the flame and its expansion. Nonetheless, under those steady flow conditions, the PSR-LES was able to predict the average flame position in the region of laminar or quasi-transitional flow at the burner base (Fiorina et al., 2015).

As previously commented, PSR-LES model increases its computational requirements as a flame increases its surface, wrinkling and/or it transitions to turbulent regime. These processes eventually result an exponential increase of the computational demands that makes it challenging to fulfill. In this work, it is investigated whether there exists a minimum, flame grid-resolution, criterion that should be imposed in the model in order to fulfill the quality requirements needed to rely on the simulation results. Besides, it is analyzed whether a chemical integration strategy like ISAT could help effectively to overcome this limitation and to reduce the computational demand of this LES approach.

To the author's knowledge, there is a lack of studies in the open literature where the capabilities and drawbacks of the PSR-LES approach are critically assessed to predict unsteady burning speed, and time evolution of other global variables, for example, during the initial stages of transient combustion sequences. Accordingly, this work seeks to evaluate the capabilities and the limitations of implicit LES without sub-grid scale combustion modeling (PSR-LES), coupled with detailed chemical kinetic schemes, to predict global variables of the combustion process. Moreover, it seeks to evaluate the performance of this approach at the initial stage of the combustion sequence (i.e. in the post-ignition, and in the flame acceleration phases, where the flow regime has a low or moderate Reynolds number). This assessment is performed by benchmarking the numerical simulations against combustion experiments performed with hydrogen-air mixtures in a spherical bomb by Sabard et al. (2013), and Goulier, Comandini, et al. (2017). Through this evaluation, the work also seeks to assess the impact of different sub-grid scale models, numerical schemes and chemical kinetic models, when applied in reactive flows in confined scenarios. Besides, numerical data of flame acceleration in an obstructed channel obtained with a different, contrasted, LES approach (i.e. the Artificially Thickened Flame (ATF) sub-grid combustion model), is also used to benchmark this approach.

In section 2, the physical models formulated for the problem studied are presented. These include conservation equations for the gas mixture, condition-dependent heat capacities, and the modeling of turbulence and chemistry with different sub-grid scale models, and chemical kinetics. Secondly, the numerical models are described. In section 3, the model is compared with the results of several experiments carried out in a spherical bomb, and with numerical data of flame acceleration in an obstructed channel. These data were used to identify and discuss the capabilities and drawbacks of this approach in section 4. Finally, in the last section, the conclusions and future work are outlined.

2. Materials and methods: the mathematical model

2.1. Governing equations

The model relies on the multicomponent transport equations of momentum, species mass fractions, and energy, and is closed with an equation of state. The approach used in this work is based on the modeling of turbulence by Large Eddy Simulation. Thus, the governing equations are presented in the Favre-averaged form (Chen et al., 1991) for the conservation of mass, momentum and energy (Equations 1–3) for compressible flow, as well as the transport equations for the species involved in the combustion process (Equation 4):

$$\text{Continuity:} \frac{\partial \bar{\rho}}{\partial t} + \nabla \cdot (\bar{\rho}\tilde{\boldsymbol{u}}) = 0 \tag{1}$$

$$\text{Momentum}: \frac{\partial (\bar{\rho}\tilde{\boldsymbol{u}})}{\partial t} + \nabla \cdot (\bar{\rho}\tilde{\boldsymbol{u}} \otimes \tilde{\boldsymbol{u}}) = -\nabla \bar{p} + \nabla \cdot (\bar{\boldsymbol{S}} - \boldsymbol{B}) \tag{2}$$

$$\text{Energy}: \frac{\partial \bar{\rho}\widetilde{h_s}}{\partial t} + \nabla \cdot (\bar{\rho}\tilde{\boldsymbol{u}}\widetilde{h_s}) = \bar{\boldsymbol{S}} \cdot \nabla \tilde{\boldsymbol{u}} + \frac{\partial \bar{p}}{\partial t} + \nabla \bar{p} \cdot \tilde{\boldsymbol{u}} + \nabla \cdot (\bar{\boldsymbol{h}} - \boldsymbol{b_h}) + \bar{\rho}\tilde{\sigma} - \sum_{k=1}^{N} (\widetilde{\dot{\omega}_k} h^0_{f,k}) \tag{3}$$

$$\text{Mass Fraction of species}: \frac{\partial \bar{\rho}\widetilde{Y_k}}{\partial t} + \nabla \cdot (\bar{\rho}\tilde{\boldsymbol{u}}\widetilde{Y_k}) = \nabla \cdot (\overline{\boldsymbol{J}_i^k Y_k} - \bar{\rho}(\widetilde{\boldsymbol{u}Y_k} - \tilde{\boldsymbol{u}}\widetilde{Y_k})) + \widetilde{\dot{\omega}_k} \quad \text{with} \times k = 1, \ldots, \text{NS} - 1 \tag{4}$$

where NS is the number of gas species, the $\bar{\cdot}$ and $\tilde{\cdot}$ are, respectively, the Favre Filtered quantities, which fulfill the property: $\bar{\rho}\tilde{\phi} = \overline{\rho\phi}$. Thus, $\bar{\rho}$, and $\tilde{\boldsymbol{u}}$, represents the density of the mixture and the velocity vector, whereas $\widetilde{h_s}$ and $\bar{p}$ stands for the sensible enthalpy and the gas pressure. $h^0_{f,k}$ is the formation enthalpy, and $\widetilde{\dot{\omega}_k}$ denotes the filtered reaction rate for the k-th species. The viscous stress

tensor is denoted by $\bar{\mathbf{S}}$, whereas the heat flux vector is $\bar{\boldsymbol{h}}$ and $\boldsymbol{B} = \bar{\rho}(\widetilde{\boldsymbol{u} \otimes \boldsymbol{u}} - \tilde{\boldsymbol{u}} \otimes \tilde{\boldsymbol{u}})$ is the tensor of unresolved sub-grid stress. $\boldsymbol{b}_h = \bar{\rho}(\widetilde{\boldsymbol{u}h_s} - \tilde{\boldsymbol{u}}\widetilde{h_s})$ is the vector of unresolved sub-grid heat flux that results when Favre filtering is applied to the convective terms. Besides, it is assumed that $\bar{\mathbf{S}} \approx 2\mu \cdot dev(\bar{S})$ and $\bar{\boldsymbol{h}} \approx D_{th}\nabla\tilde{T}$. Note that μ is the viscosity and the deviatoric part of the resolved rate strain tensor is denoted by $dev(\bar{S})$, and D_{th} is the thermal diffusivity. Besides, a sub-grid LES model was employed for the unclosed terms for the filtered equations of the momentum and energy conservation.

Regarding the transport of species (Equation 4), the term $\boldsymbol{J}_i^k$ is the i-th component of the laminar diffusive flux of species k. This term can be simplified by assuming the approximation of Hirschfelder et al. (1954), and by using Fick's law, and assuming that the corresponding binary diffusion coefficients are equal (Williams, 1985). That yields: $\nabla \cdot (\bar{\rho}\tilde{D}\nabla\widetilde{Y_k})$. This Favre form of the species equation has two unclosed terms which have to be modeled: the unresolved scalar transport term is commonly modeled in LES as $\widetilde{\boldsymbol{u}Y_k} - \tilde{\boldsymbol{u}}\widetilde{Y_k} = -\tilde{D}_{sgs}\nabla\widetilde{Y_k}$, with $\tilde{D}_{sgs} = \frac{\nu_{sgs}}{Sc_t}$, where ν_{sgs} is the sub-grid scale turbulent viscosity, and the Sc_t is the turbulent or sub-grid scale Schmidt number. The second unclosed term of Equation (4) is the filtered chemical source term $\widetilde{\dot{\omega}_k}$.

Regarding the laminar and sub-grid scale mass diffusion coefficients, in this work the same value of this coefficient is considered for all the species. The values adopted for each H_2-air mixture simulated are obtained from the estimations of the effective Lewis, calculated from the combustion experiments performed with similar H_2-air mixtures by Goulier, Comandini, et al. (2017). The Sutherland law is used to estimate the dynamic viscosity (Sutherland, 1893) as $\mu = A_S\frac{T^{1/2}}{(1+T_S/T)}$, with $A_S = 1.67212 \cdot 10^{-6}\frac{\text{kg}}{\text{m}\cdot\text{s}\cdot\text{K}^{1/2}}$, and $T_S = 170.672\text{K}$.

In this model, it is considered the ideal gas approach and thus, $\bar{p} = \bar{\rho}\left(\sum_{k=1}^{NGSP}\widetilde{Y}_k\frac{R_u}{M_k}\right)\tilde{T}$. The heat capacities for each component are considered to be functions of temperature (McBride et al., 1993). The specific enthalpy of the gas mixture can be calculated from these values as: $\widetilde{h_s} = \sum_{k=1}^{NGSP}\widetilde{Y}_k\int_{T_{ref}}^{T} c_{p,k}(\tilde{T})d\tilde{T}$.

As shown, a model for the sub-grid scale terms as well as a combustion model is needed for the closure of the system.

2.2. Sub-grid scale turbulence models

In the present study, the included sub-grid scale terms are modeled with four different sub-grid LES models to assess the influence of this closure issue. The first of these models, by Smagorinsky-Lilly (Lilly, 1991), relies on the Eddy viscosity assumption and it considers the anisotropic part of the sub-grid scale stress tensor B_{ij} can be related to the resolved rate of the strain tensor $\overline{S_{ij}}$, following:

$$B_{ij} - \frac{1}{3}B_{kk}\delta_{ij} \approx -2\nu_{sgs}dev(\overline{S_{ij}}) \tag{5}$$

where ν_{sgs} is the sub-grid scale eddy viscosity. This magnitude is modeled as:

$$\nu_{sgs} = C_k L_S\sqrt{k_{sgs}} \tag{6}$$

C_k is equal to 0.094, and L_S is the sub-grid length scale (filter width). For the LES models considered, L_S was computed by using the van-Driest damping function, to correct the ν_{sgs} behavior in the limit $y \to 0$, where y denotes the distance to the closest wall. This correction is needed for the Smagorinsky model. Thus, the filter width can be computed as $L_S = \min(f, \Delta_V)$ (Wallin & Johansson, 2000), where $\Delta_V = V^{1/3}$ is an estimation of the local grid scale which is calculated from the cell volume V, and f is:

$$f = \frac{\kappa \cdot y}{C_\Delta}\left(1 - e^{\left(\frac{y}{y^* A^+}\right)}\right) \tag{7}$$

where κ is the *von-Kàrman* constant, set to a value of 0.46;y^* is calculated as $y^* = \frac{\nu}{(\nu+\nu_{sgs})}|\nabla_n\bar{u}|$, with ∇_n denoting the gradient in the normal wall direction. A^+ is set to 26.

The sub-grid scale kinetic energy k_{sgs} can be defined as $k_{sgs} = \frac{1}{2}B_{kk} = \frac{1}{2}(\overline{u_k u_k} - \bar{u}_k\bar{u}_k)$, and for this model, it is computed taking into account the balance between the sub-grid scale energy production and dissipation. For compressible flow, k_{sgs}, results in:

$$k_{sgs} = \left(\frac{-\frac{2}{3}tr(\bar{S}) + \sqrt{\left(\frac{2}{3}tr(\bar{S})\right)^2 + 8C_\varepsilon C_k(dev(\bar{S}) : \bar{S})}}{\frac{2C_\varepsilon}{L_S}}\right)^2 \tag{8}$$

where C_ε is set to 1.048, and: represents the double inner product.

The second model considered is Wall-Adapting Local Eddy viscosity (WALE) (Nicoud & Ducros, 1999). This model also relies on the Eddy viscosity assumption. It was specially tuned to provide the expected asymptotic behavior of wall-bounded flows (y^{+3}). In this model, the sub-grid scale eddy viscosity is computed by Equation (6), with the default constants. The difference remains in the calculation of the sub-grid scale kinetic energy, k_{sgs},

which is obtained from:

$$k_{sgs} = \left(\frac{{C_w}^2 L_S}{C_k}\right)^2 \frac{\left(S^d_{ij} S^d_{ij}\right)^3}{\left(\left(\bar{S}_{ij}\bar{S}_{ij}\right)^{5/2} + \left(S^d_{ij} S^d_{ij}\right)^{5/4}\right)^2} \quad (9)$$

where C_w value was set to its default value of 0.325, $\bar{S}_{ij} = \frac{1}{2}\left(\frac{\partial \bar{u}_i}{\partial x_j} + \frac{\partial \bar{u}_j}{\partial x_i}\right)$ and S^d_{ij} is the traceless symmetric part of the square of the velocity gradient tensor, calculated by $S^d_{ij} = \frac{1}{2}\left(\frac{\partial \bar{u}_k}{\partial x_i}\frac{\partial \bar{u}_j}{\partial x_k} + \frac{\partial \bar{u}_k}{\partial x_j}\frac{\partial \bar{u}_i}{\partial x_k}\right) - \frac{1}{3}\delta_{ij}\frac{\partial \bar{u}_k}{\partial x_l}\frac{\partial \bar{u}_l}{\partial x_k}$.

Finally, both static (Yoshizawa & Horiuti, 1985) and dynamic k_{sgs}-Equation (Chai & Mahesh, 2012) models adapted for compressible flows were tested. In this case, the model considers an additional transport equation which is derived formally for compressible flows. Both models are also based on the Eddy viscosity assumption, and Eq. 6 is used for the sub-grid scale eddy viscosity calculation, with the same default value for C_k. In these models, a transport equation for k_{sgs} is also considered:

$$\frac{\partial}{\partial t}(\bar{\rho} k_{sgs}) + \nabla \cdot (\bar{\rho} k_{sgs} \tilde{\boldsymbol{u}}) = \nabla \cdot (\bar{\rho} \nu_{eff} \nabla k_{sgs}) - \bar{\rho} B_{ij} : \bar{S}_{ij} - C_\varepsilon \frac{\bar{\rho} {k_{sgs}}^{3/2}}{L_S} \quad (10)$$

with a constant value $C_\varepsilon = 1.048$. In the case of the dynamic version of this model, constants are determined dynamically to adjust to the local flow conditions. For that purpose, additional explicit filtering (a Gaussian anisotropic filter) is considered at SGS level. Thus, C_w and C_ε are evaluated dynamically by filtering the velocity field.

2.3. Combustion and chemical kinetics modeling

As previously commented, not only a sub-grid scale model is needed, but also a combustion scheme must be employed, also, for the closure of the system. Since a finite rate chemical model is incorporated into LES modeling, it is required a suitable reaction mechanism for the filtered reaction rates, $\widetilde{\dot{\omega}_k}$, which implies an additional modeling issue. The reaction rates are commonly nonlinear functions which depend on temperature and concentration of species.

The adopted approach relies on the hypothesis of perfectly stirred reaction (i.e. $\widetilde{\dot{\omega}_k} = \dot{\omega}_k(\widetilde{Y}_j, \tilde{T})$). It is worth to highlight here that this assumption is valid for laminar flow simulations, as well as DNS (Duwig & Ludiciani, 2014; Krüger et al., 2013). The validity of this assumption depends on two factors: (i) the grid resolution, and (ii) the intensity of the sub-grid mixing. First, if the grid resolution was capable to adequately resolve the reacting layer (close to DNS mesh), then the assumption of $\widetilde{\dot{\omega}_k} = \dot{\omega}_k(\widetilde{Y}_j, \tilde{T})$ would be valid. Notwithstanding, even using a typical LES-grid (coarser than DNS grids), it may approximate the reaction rate with good results, as indicates Fureby (2007), Duwig et al. (2011), Duwig and Dunn (2013). Regarding the second factor, the validity of the model would depend on the intensity of the sub-grid mixing, since high mixing intensity ensures that a perfectly stirred reactor can reasonably represent the physics under the LES-grid cells, with quite homogeneous sub-grid concentrations and temperature. Consequently, this work aims to evaluate the capabilities and limitations of LES with detailed chemical kinetic schemes, and without the use of additional sub-grid scale combustion modeling. The influence of the mesh size and validity of this approach applied for the cases studied will be discussed in section 3.

Regarding the chemical kinetic model, the models considered in this work are that of Williams (2008) and that of Marinov et al. (1995). The reactive species considered are: H_2, H, O_2, O, OH, H_2O, H_2O_2, and HO_2. N_2 and Ar are assumed to be non-reacting gases. For Williams, the set of reactions considered are those presented in Table 1.

In the case of reactions that involve a third body (M) with a pressure-dependent behavior, the scheme provides a constant for the case of low pressure rate (k_0) and a constant for the case of high pressure rate (k_∞). The Lindenmann mechanism and the formula of Troe (1988)

Table 1. Scheme for H_2 autoignition detailed chemistry (Williams, 2008).

Subreaction		A (mol/cm^3)	β (s^{-1})	E (J/mol)
$H + O_2 = OH + O$		$3.52{\cdot}10^{16}$	−0.7	71,400
$H_2 + O = OH + H$		$5.06{\cdot}10^{4}$	2.7	26,300
$H_2 + OH = H_2O + H$		$1.17{\cdot}10^{9}$	1.3	15,200
$H_2O + O = OH + OH$		$7.60{\cdot}10^{0}$	3.8	53,400
$H + H + M = H_2 + M$		$1.30{\cdot}10^{18}$	−1.0	0.0
$H + OH + M = H_2O + M$		$4.00{\cdot}10^{22}$	−2.0	0.0
$O + O + M = O_2 + M$		$6.17{\cdot}10^{15}$	−0.5	0.0
$H + O + M = OH + M$		$4.71{\cdot}10^{18}$	−1.0	0.0
$O + OH + M = HO_2 + M$		$8.00{\cdot}10^{15}$	0.0	0.0
$H + O_2 + M = HO_2 + M$	k_∞	$4.65{\cdot}10^{12}$	0.4	0.0
	k_0	$5.75{\cdot}10^{19}$	−1.4	0.0
	T_{ROE}	$F_C = 0.5$		
$HO_2 + H = OH + OH$		$7.08{\cdot}10^{13}$	0.0	1200
$HO_2 + H = H_2 + O_2$		$1.66{\cdot}10^{13}$	0.0	3400
$HO_2 + H = H_2O + O$		$3.10{\cdot}10^{13}$	0.0	7200
$HO_2 + O = OH + O_2$		$2.00{\cdot}10^{13}$	0.0	0.0
$HO_2 + OH = H_2O + O_2$		$2.89{\cdot}10^{13}$	0.0	−2100
$OH + OH + M = H_2O_2 + M$	k_∞	$7.40{\cdot}10^{13}$	−0.4	0.0
	k_0	$2.30{\cdot}10^{18}$	−0.9	−7100
	T_{ROE}	$F_C = 0.265{\cdot}e^{(-T/94K)} + 0.735{\cdot}e^{(-T/1756K)} + e^{(-5182K/T)}$		
$HO_2 + HO_2 = H_2O_2 + O_2$		$3.02{\cdot}10^{12}$	0.0	5800
$H_2O_2 + H = HO_2 + H_2$		$4.79{\cdot}10^{13}$	0.0	33,300
$H_2O_2 + H = H_2O + OH$		$1.00{\cdot}10^{13}$	0.0	15,000
$H_2O_2 + OH = H_2O + HO_2$		$7.08{\cdot}10^{12}$	0.0	6000
$H_2O_2 + O = HO_2 + OH$		$9.63{\cdot}10^{6}$	2.0	2000

were used in these cases:

$$k = AT^{\beta} e^{(-E/R_c \tilde{T})} \tag{11}$$

$$k = k_{\infty} \frac{(k_0[M]/k_{\infty})}{(1 + (k_0[M]/k_{\infty}))} F \tag{12}$$

$$\log_{10} F = \left[1 + \left[\frac{\log_{10}(k_0[M]/k_{\infty}) + c}{n - d(\log_{10}(k_0[M]/k_{\infty}) + c)} \right]^2 \right]^{-1} \times \log_{10} F_c \tag{13}$$

where $c = -0.4 - 0.67\log_{10} F_C$, $n = 0.75 - 1.27\log_{10} F_C$, and $d = 0.14$. A detailed description of the procedure, as well as third body Chaperon efficiencies, can be found in Williams (2008). Note that all the reactions in Table 1 are reversible. The reverse reaction rates were calculated considering chemical equilibrium from the forward rates (McBride & Gordon, 1996).

In this work, an in situ adaptive tabulation strategy (ISAT) (Lu & Pope, 1997, 2009) is tested with the PSR-LES and the detailed kinetic models in order to evaluate the potential reduction achieved in the computational costs. ISAT permits to store chemistry calculations of the ordinary differential equations (ODE) in tables and to retrieve them when needed to avoid repeated calculations, reducing the computational cost (Hiremath et al., 2011; Pope, 1997).

2.4. Numerical approach

The CFD code used in the present work is based on the OpenFOAM v5 toolbox. Different finite-volume solvers and integration strategies were tested to assess their capabilities on this kind of combustion problems. Both, segregated and coupled computational methods were used. In the case of segregated simulations, the pressure-velocity coupling is done using PISO (Pressure Implicit with Splitting of Operator) scheme (Issa, 1986). A second-order central differencing is used for the reconstruction of convective fluxes. The convective terms in the scalar equations are solved using a second-order Total Variation Diminishing scheme (TVD). To solve the discretized equations, a solver based on preconditioned bi-conjugate gradient, and multi-grid methods are used to speed-up the pressure-velocity coupling steps.

Regarding coupled solvers, the hybrid schemes AUSMup (Liou, 2006) and AUSM+ (Liou, 1996) and a flux-difference splitting scheme proposed by Rusanov (1962) were tested with different primitive reconstruction schemes, that is, a first-order unbounded upwind scheme, and second-order schemes with different TVD limited weighting factors, such as Barth-Jespersen (BJ) (Barth & Jespersen, 1989), van Albada (VA), van-Leer (VL), and van-Leer's MUSCL (Toro, 1997).

A backward scheme of second order was used for the integration of time variable for both kinds of solvers. The equations were solved sequentially using explicit combustion source terms (Otón-Martínez et al., 2015). The variable time stepping was evaluated with a maximum Courant-Fredrich-Levy (CFL) number of 0.35, resulting in time steps of around $3{\cdot}10^{-7}$ s. Regarding the chemical source terms, a 4th order Rosenbrock ODE solver, with an absolute tolerance convergence criteria of 10^{-10} was used to integrate the chemical reactions, when required by the ISAT tabulation method. This ODE solver was tested for the ignition of a H_2/air mixture with the GRI-Mech 3.0 mechanism and showed high stability during the system integration (Stone & Bisetti, 2014).

Additionally, a four-stage Runge–Kutta scheme was also used for the fluxes integration in case of coupled solvers. Even though, a higher number of operations per time step were needed due to the intermediate evaluation of the fluxes with the new primitive values, this scheme permitted to set a higher CFL number without the presence of instabilities in the simulation results (Otón-Martínez et al., 2015).

A local grid refinement strategy was used to progressively increase the resolution in the combustion region. The refinement was based on the local normalized density gradient. This procedure permitted to achieve an appropriate spatial resolution in the preheat, reacting and oxidation layer zones, acting as a flame sensor which tracked the flame surface during its propagation and adapting the mesh to its shape. This led to an affordable computational domain, with slightly coarser meshes in the burnt and unburnt regions, where a high spatial resolution is not needed. During the ignition sequence, a refinement was also carried out increasing the resolution upstream the flame surface. This procedure seemed to be a proper strategy for the premixed combustion cases faced in this work.

3. Results and discussion

3.1. Validation of the CFD model

The present model was validated by simulating the experiments performed by Sabard and his co-workers and described in Sabard et al. (2013), Sabard (2013), Sabard et al. (2012) and Velasco et al. (2016).

These experiments were performed in a spherical bomb with different mixtures of H_2–O_2–N_2. The experimental set-up and the test procedure can be found in (Sabard, 2013; Sabard et al., 2013). The bomb is a stainless-steel sphere of 125 mm of internal radius, instrumented with wall pressure sensors with a measurement range of 0–1 MPa and a measurement uncertainty

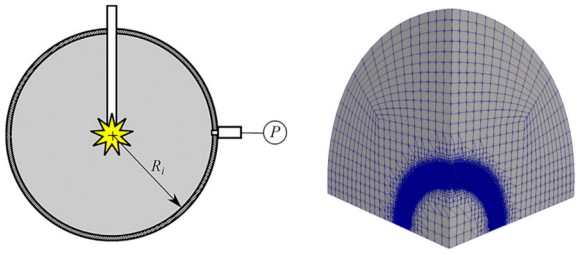

Figure 1. (Left) Simplified geometry of the spherical bomb estimated for the modeling of this test and (Right) detail of the computational grid with a refinement strategy near the flame front.

lower than 2%. In this work two different tests were selected for the model validation:

Experiment 1 (H-EXP1) with 20% in volume of H_2 and a ratio of N_2/O_2 3.76.

Experiment 2 (H-EXP2) with 20% in volume of H_2 and a ratio of N_2/O_2 2.33.

In those experiments, a pressure of 1 bar and a temperature of 298 K was set within the gas mixture after the gas feeling. The uncertainty in the setting of the composition of the gas mixture within the sphere was below 0.3%. Afterwards, the combustion sequence was initiated by the ignition of the mixture with an electric spark. During the experiments, it was also measured the molar composition of the combustion products in the gas phase, with a gas chromatographic diagnosis system HP 5890 Serie II (Agilent, 1994). The uncertainty of the measurements was estimated to be less than 0.5% of the mole percentage of the mixture (Sabard, 2013).

In order to validate the CFD model, simulation of the combustion sequence with different physical models was benchmarked against the time evolution of experimental variables, such as pressure, with the predictions provided from numerical simulations. The mesh used for simulation is represented in Figure 1 (Right).

As for the modeling of the ignition sequence, in the case of spark type, it is a common practice to follow the approach described by Liberman et al. (2011). It considers that the beginning of the initiation sequence can be modeled as an isobaric, quasi-instantaneous, heating process, that affects a very small volume of the domain (i.e. the ignition volume). In this work, different enthalpies and radius of ignition were tested (all for spherical volumes). An increase of the gas enthalpy within the ignition volume, corresponding to an energy spark around 800 kJ/m^{3,} was enough to make progress the laminar autoignition sequence.

3.1.1. Influence of the spatial discretization strategy

In order to evaluate the influence of the spatial grid resolution on the model results, it was performed an analysis of the influence of the grid size on the flame front and the reacting layer. Table 2 summarizes the results of the convergence analysis compared with experimental data from Goulier, Comandini, et al. (2017), for similar H_2/Air composition and conditions than in the H-EXP1 case. These values were calculated from the flame properties obtained for the different 3D computational grids tested with no sub-grid modeling (hereafter called laminar case). Results showed that the unstretched laminar flame speed predicted with these models with meshes $\delta_L^0/\Delta x \sim 1$ provided errors below 18%. However, when a mesh with $\delta_L^0/\Delta x = 8$ was used, the errors in the prediction of the unstretched laminar flame speed were smaller than 1%.

At the initial stage of the propagation, the fundamental unstretched laminar flame speed (S_L^0) was calculated from the spatial flame velocity (denoted as burning speed, V_L^0), and the expansion ratio at null strain (ρ_u/ρ_b), as $S_L^0 = \frac{\rho_b}{\rho_u} V_L^0$ (Giannakopoulos et al., 2015). This way, the effect of the different discretizations on obtaining a good prediction of the laminar flame with the detailed chemical kinetics was assessed. This analysis was performed using the 21-reactions model proposed by Williams in conjunction with the ISAT procedure. As shown in Table 2, coarse grids were not able to predict neither the unstretched laminar flame speed S_L^0 (cases 1, 2, and 4), nor the laminar flame thickness based on thermal gradient $\delta_L^0 = (T_b - T_u)/\max|\nabla T|$ (cases 1–6). It was needed a $\delta_L^0/\Delta x > 6$ grid to obtain a realistic laminar flame (case 7).

Table 2. Grid convergence analysis.

Case	S_L^0(m/s)	δ_L^0(|∇T|based)(mm)
Experimental Goulier, Chaumeix, et al. (2017)	0.92 m/s (S_{Lref})	0.382 mm (δ_{Lref})
CASE 1 (30° × 30°, $\delta_L^0/\Delta x = 0.5$ static mesh)	1.18 m/s (1.28·S_{Lref})	1.734 mm (4.54·δ_{Lref})
CASE 2 (30° × 30°, $\delta_L^0/\Delta x = 1$ static mesh)	1.09 m/s (1.18·S_{Lref})	1.165 mm (3.05·δ_{Lref})
CASE 3 (30° × 30°, $\delta_L^0/\Delta x = 4$ static mesh)	0.961 m/s (1.04·S_{Lref})	1.090 mm (2.85·δ_{Lref})
CASE 4 (1/8 Sphere, $\delta_L^0/\Delta x = 0.5$ dynamic mesh)	1.03 m/s (1.11·S_{Lref})	2.049 mm (5.36·δ_{Lref})
CASE 5 (1/8 Sphere, $\delta_L^0/\Delta x = 1$ dynamic mesh)	0.981 m/s (1.06·S_{Lref})	1.117 mm (2.93·δ_{Lref})
CASE 6 (1/8 Sphere, $\delta_L^0/\Delta x = 4$ dynamic mesh)	0.951 m/s (1.03·S_{Lref})	0.769 mm (2.01·δ_{Lref})
CASE 7 (1/8 Sphere, $\delta_L^0/\Delta x = 8$ dynamic mesh)	0.911 m/s (0.99·S_{Lref})	0.394 mm (1.03·δ_{Lref})

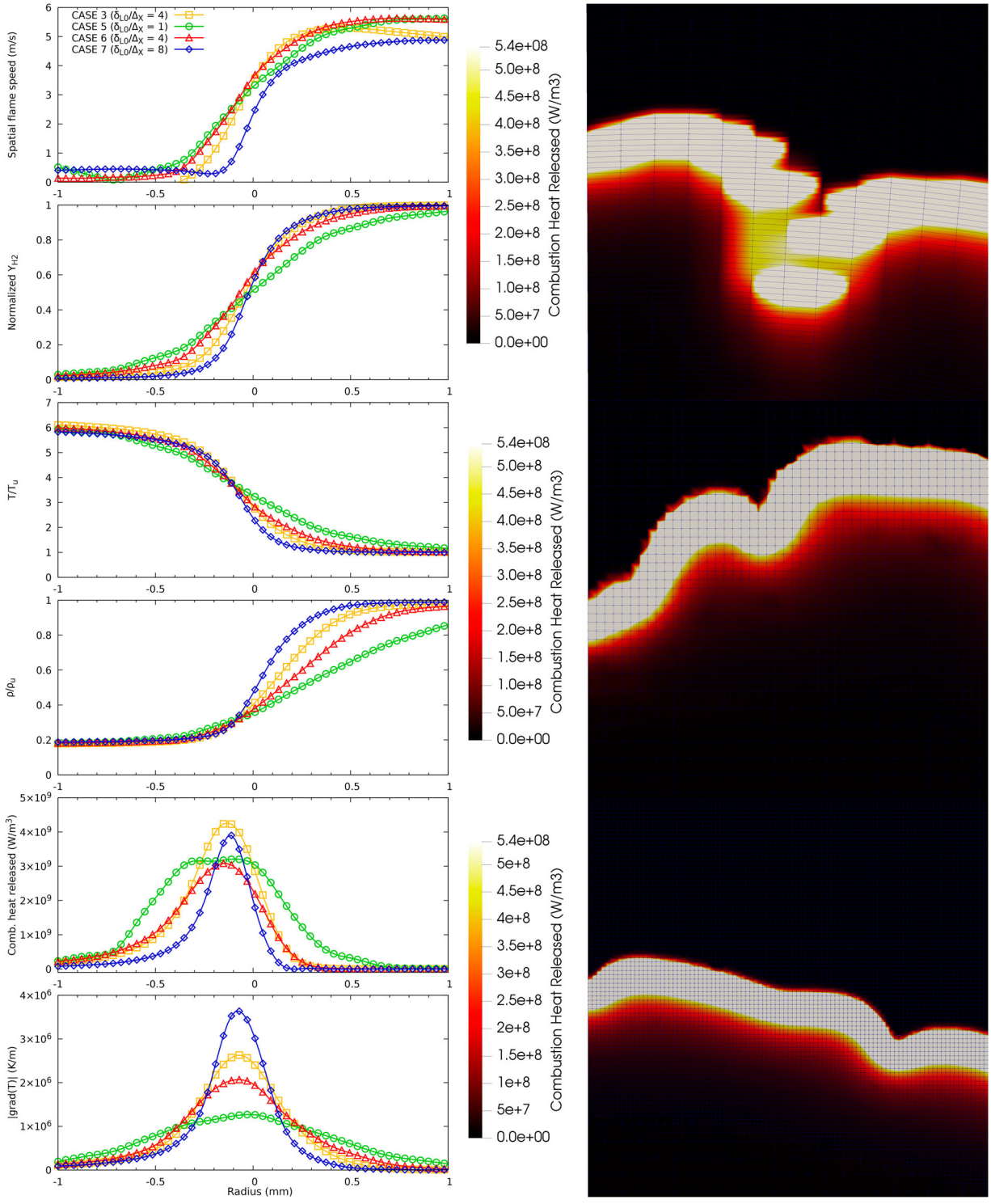

Figure 2. (Left) Distribution of main physical properties vs. distance from the center ('Radius'), 2 ms after the ignition sequence (laminar cases). (Right) Details of different grids and refinement levels used for the resolution of the combustion region at 4 ms (flame surface with cells), with k_{sgs} model, CASE 4 (Top), CASE 6 (Center), and CASE 7 (Bottom).

Figure 2 (Left) shows the distribution of the main flame physical properties obtained in the laminar cases, plotted along a radius line, after 2 ms from the beginning of the sequence (flame spherical equivalent radius of 15 mm). Figure 2 (Right) represents three snapshots with different grids used for the resolution of the combustion region: 30° × 30° (case 4), and a 90° × 90° (cases 6, and 7). These cases were simulated using the k_{sgs} model and the 21-reactions model proposed by Williams and ISAT strategy. As shown, at the moment of the snapshot,

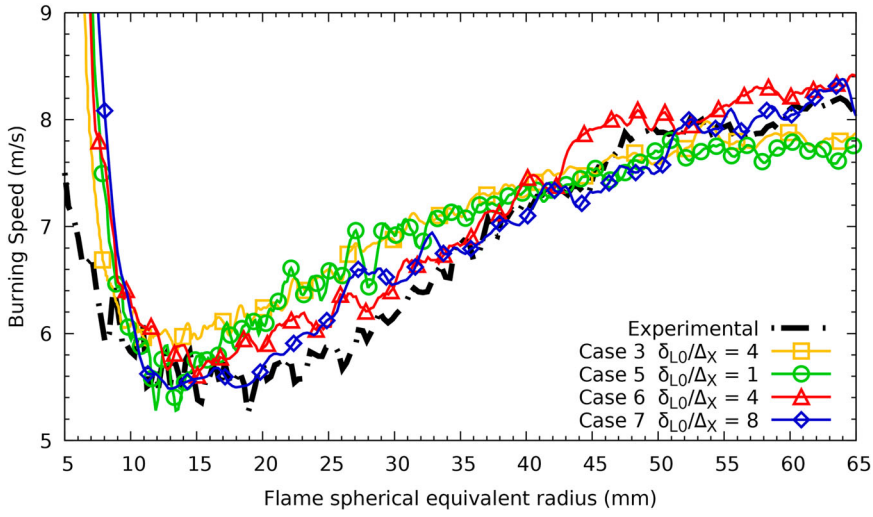

Figure 3. Flame burning speed versus spherical equivalent radius for different meshes.

when the spherical equivalent radius was approximately 26 mm, the flame surface was not completely spherical.

Regarding the performance of the meshing strategy, the grids of a spherical sector have the benefit of a smaller computational domain, and consequently, fewer cells for a given resolution. On other hand, with this kind of meshes, the cells aspect-ratio increased with the distance to the domain center, which is not recommended (Figure 2 Top-right). This might eventually break artificially the continuity of the flame, and might result in unphysical flame shape for low grid resolution (Case 4). However, with adequate grid resolution within the region with dynamic refinement, this potential problem disappeared. Therefore, Case 7 was the most appropriate to properly simulate the flame expansion (Figure 2 Bottom-right). On the other hand, results also showed that, in the case of considering a static mesh, the number of elements required to resolve the flame was higher than the one needed with the dynamic strategy. Due to this reason, to achieve that spatial resolution with affordable meshes, it was decided to use the dynamic mesh refinement process.

Figure 3 shows the numerical results of burning speed, defined as $\frac{dr_{eq}}{dt}$, where r_{eq} is the spherical equivalent radius, computed as $r_{eq} = \left(\frac{3}{4} \cdot V_{burnt}/\pi\right)^{1/3}$, with V_{burnt} the total volume of the burnt region. Results show that, despite the difference in the flame thickness provided by meshes with $\delta_L^0/\Delta x = 4$ (cases 3 and 6), it is possible to achieve a reasonably good prediction, in terms of burning speed, for the model considered. It is worth mentioning the similarities in the burning speed obtained especially in cases 6 and 7, which predict the flame burning speed properly with LES and detailed chemistry.

Results in Figure 3 suggest that the model proposed is able to predict the burning speed at the beginning of the combustion sequence (i.e. initiation and initial flame acceleration), when the Reynolds number is low. Regarding the validity of the LES approach, it was confirmed to be directly related to the mesh resolution (filter size Δ), as well as to the intensity of the sub-grid mixing. In order to assess the validity of this assumption for the different computational grids, the regime diagram proposed by Pitsch (2006) was employed. This diagram was designed for premixed combustion in LES using the filter size Δ as the length scale and the subfilter velocity fluctuations u'_Δ as the velocity scale. This takes into account not only physical properties of the combustion regime, but also modeling parameters, since the effect of the filter size is included. The parameters relevant in this diagram are the sub-grid Reynolds (Re), sub-grid Damköhler (Da) and the Karlovitz (Ka) numbers, defined as (Pitsch, 2006):

$$Re = \frac{\mathrm{u}'}{s_L l_F} \tag{14}$$

$$Da = \frac{s_L}{\mathrm{u}' l_F} \tag{15}$$

$$Ka = \sqrt{\frac{\mathrm{u}'^3 l_F}{s_L{}^3}} \tag{16}$$

Figure 4 shows the evolution of these parameters obtained for cases 3, 5, 6 and 7. These values were sampled over the flame surface and averaged in each time step. Using the relationship Δ/δ_L and the Ka values obtained during the complete combustion sequence, one may obtain the zone regions of each case within the regime diagram, as shown in Figure 5.

The validity of the perfectly stirred reactor hypothesis can be addressed by the level of the sub-grid mixing intensity at the given length scale Δ. In order to fulfill this hypothesis, the sub-grid mixing effects must act faster

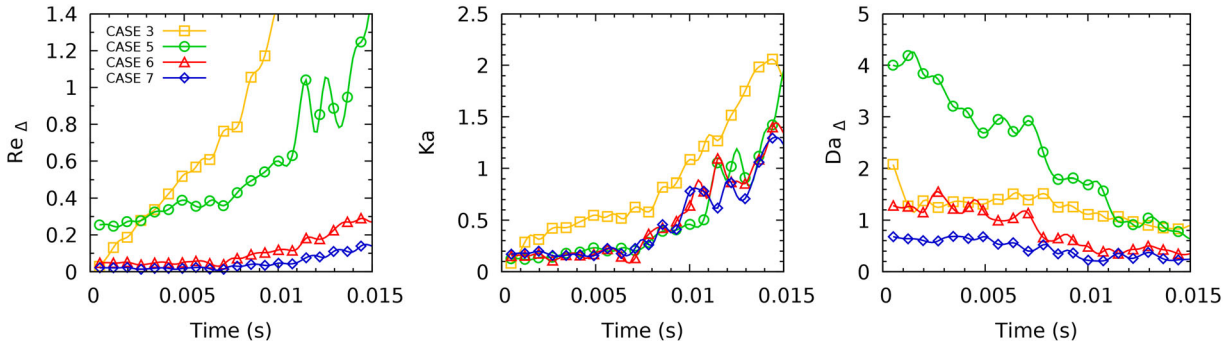

Figure 4. Evolution of nondimensional modeling parameters for different computational grids. (Left) $\boldsymbol{Re}_\Delta$ (Center) Karlovitz and (Right) $\boldsymbol{Da}_\Delta$

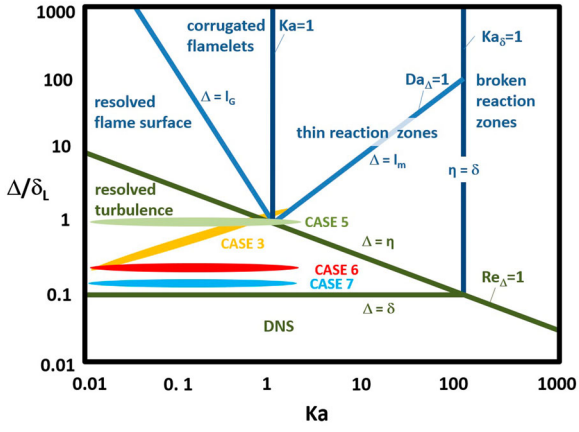

Figure 5. Regime diagram proposed by Pitsch (2006) with the points obtained for cases 3, 5, 6, and 7.

than any chemical reaction. This implies that the sub-grid structure characteristic time scale $\tau_\Delta \sim \Delta/u'_\Delta$ must be smaller than the chemical time scale $\tau_c \sim \delta_L/S_L$. This leads to $Da < 1$ as a requirement for the validity of the perfectly stirred reactor assumption in the cases where the flow conditions are not laminar, or the mesh resolution is far from the grids required for DNS. As shown in Figure 4 (Right), when the mesh size is smaller, and consequently Δ decreases, Da values also decreases.

The combustion experiments used in the present work (Goulier, Comandini, et al., 2017; Sabard et al., 2013), were carried out in initial calm conditions (i.e. with no flow velocity within the scenario) where low Re_Δ and Ka_Δ values are expected. That means that a small filter size would be needed to ensure well-stirred sub-grid concentrations and temperatures. This is only achieved in case 7, according to the Da values reported in Figure 4. In addition, the low Ka values reported (especially for the cases 5, 6, and 7) indicate that the sub-grid modeling does not alter the flame structure, being the chemical region in laminar conditions, where the perfectly stirred reactor assumption is valid. As shown in Figure 4 (Left), the sub-grid turbulent intensity increases with the propagation of the flame, due to the flow velocity fluctuations induced by the propagation of the flame front. As a consequence, the Karlovitz values increase, reducing the Da values in the reacting zone. This relaxes the mesh cell size requirement, which permits case 6 to fulfill the $Da < 1$ criterium, *at* $t = 6$ ms. As shown in Figure 5, all points in simulations fall within the region of resolved turbulence for the cases 6 and 7, which may indicate that, in practice, the turbulence-chemistry interactions may be well simulated at grid-scale level. In fact, the burning speeds predicted in the four cases represented in Figure 5 were quite accurate, as shown in Figure 3.

In this section, the validity of the model at the initial stages of the combustion sequence was assessed. For the simulations presented in the next sections, case 7 with dynamic mesh refinement is the selected strategy.

3.1.2. Influence of the sub-grid scale turbulence model

In order to analyze the influence of the LES model used, the experimental data previously commented (Sabard et al., 2012; Sabard et al., 2013) is used. The influence of the sub-grid scale turbulence model used will be assessed, based on the experimental benchmark H-EXP1. For these conditions, Figure 6 (Left) shows pressure evolution as a function of time. The figure also includes the experimental data recorded at the wall of the sphere during the experiment. Different LES sub-grid scale models are applied, together with the chemical model by Williams and ISAT tabulation: Smagorinsky-Lilly, WALE, k_{sgs}-equation, and Dynamic Anisotropic k_{sgs}-equation. These models provide different results in the prediction of the pressure history at the wall of the sphere (Figure 6 (Left)). k_{sgs}-equation model provides the best prediction compared to the experimental data. The Smagorinsky-Lilly model shows less stable behavior, when the flame front is close to the wall. With this model, the flame accelerates at a higher rate, getting the

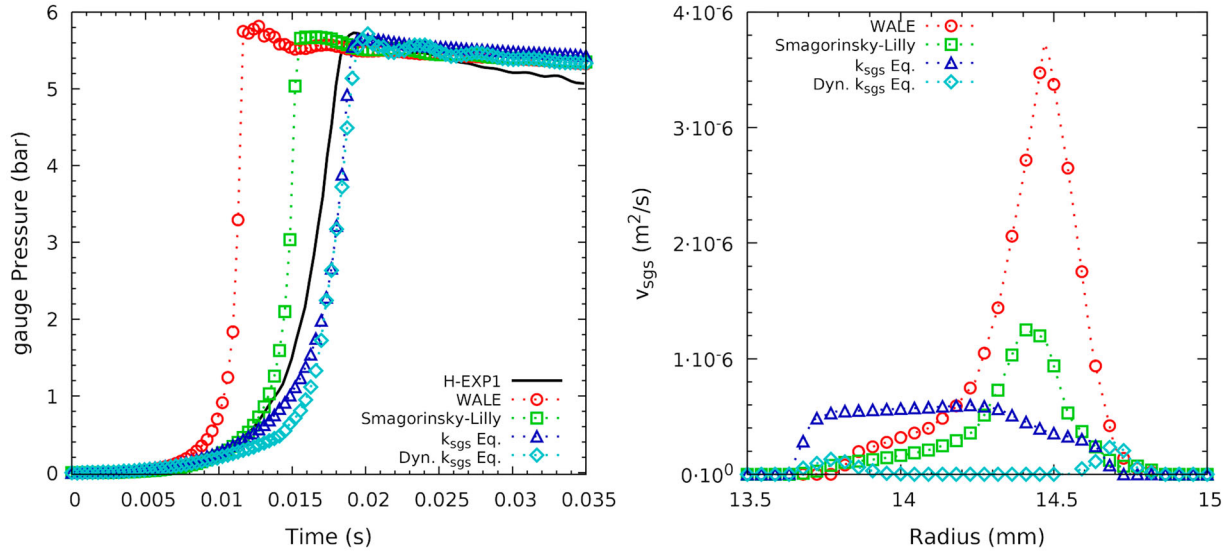

Figure 6. (Left) Influence of the LES modeling on the pressure evolution at sphere wall (H-EXP1 conditions). (Right) Different kinematic sub-grid scale viscosity values obtained in the frame front region with the tested LES models ($t = 2{\cdot}10^{-3}$s H-EXP1 conditions).

wall faster than in the case of the k_{sgs}-equation model. As shown, the WALE model also overestimates the flame acceleration. The reasons behind this dissimilar behavior partially rely on the different estimation of the transport phenomena (sub-grid scale viscous term, ν_{sgs}) provided by each model. Figure 6 (Right) permits to illustrate this point. The figure presents the spatial distribution of the sub-grid viscous term provided by the four different models in the flame front region. The ν_{sgs} obtained by the dynamic k_{sgs}-equation model is negligible compared to the one obtained with the other sub-grid scale models within the flame front, whereas it is not null in front and behind the flame front region at $2{\cdot}10^{-3}$ s of simulated time. Regarding the non-dynamic sub-grid models, the k_{sgs}-equation model estimated the smallest value for the sub-grid scale viscous term ν_{sgs} in the region of the flame front, although it reported higher values downstream flame front. On the other hand, WALE and Smagorinsky-Lilly models predicted higher values of the subgrid diffusive terms. These differences might also be explained by their different properties. WALE was tuned to predict the y^{+3} profile of the effective viscosity close to walls, under non-reacting flow conditions. However, the k_{sgs}-equation models are able to overcome the deficiency of local balance assumption between the sub-grid scale energy production and dissipation adopted in algebraic eddy viscosity models as the Smagorinsky-Lilly and WALE (Nicoud & Ducros, 1999). On the other hand, WALE and Smagorinsky-Lilly models were originally tuned against experimental data in incompressible conditions (Nicoud & Ducros, 1999), whereas k_{sgs}-equation models were designed for compressible flow conditions.

When comparing both versions of the k_{sgs}-equation model, the main difference is the 'non-dynamic' one (here denoted simply as k_{sgs}-equation model) slightly underestimates the pressure rise near the wall, upstream the flame front (in the time lapse rounding 15 ms). As a result, it overestimates the deflagration factor near the wall, which is proportional to $\mathrm{d}P/\mathrm{d}t$. All in all, Figure 6 shows an important effect of the sub-grid models what points out the uncertainty linked with its election. The differences found among the models might be due to the fact that sub-grid scale models are developed, case by case, based on operators originally designed to behave more 'accurately' when facing certain canonical problems such as homogeneous isotropic turbulent flow, pure shear flows, pure rotating flows or wall flows in turbulent channels. Some examples of this challenging developing process can be found in the works of Sankaran and Menon (2005), Lilly (1991), Wallin and Johansson (2000), Nicoud and Ducros (1999) and Yoshizawa and Horiuti (1985). Overall, in the case of unsteady combustion problems, such as the one presented here, it is of paramount importance to benchmark LES against experimental data to ensure reliable results.

3.1.3. Influence of the chemical kinetics model

A comparison of the pressure evolution at the sphere predicted with two different chemical kinetic models is shown in Figure 7. These two are detailed chemical combustion models: the one by Williams (2008), and the one by Marinov et al. (1995). In both cases, ISAT tabulation was used to reduce the computational cost of the integration of these detailed models. The figure includes the experimental pressure recorded at the wall of the sphere

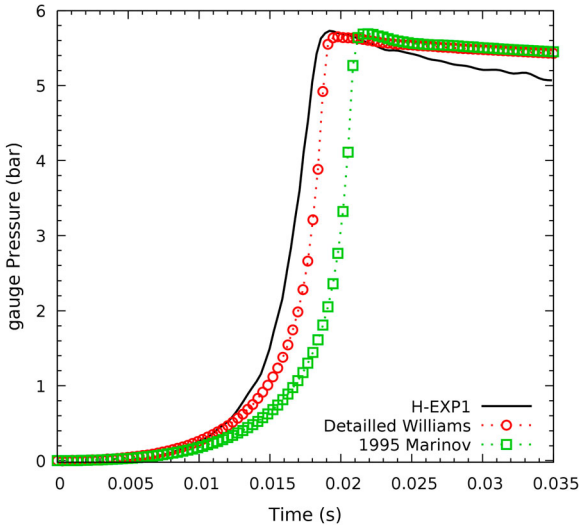

Figure 7. Influence of hydrogen combustion modeling on the pressure evolution at sphere wall (H-EXP1 conditions).

during H-EXP-1. As shown, both detailed combustion models predict with reasonable accuracy the wall pressure evolution with time, with a slight delay in pressure rise for both models. Nonetheless, the model by Williams gives more accurate results. Altogether, the comparison permits to estimate the uncertainty linked to the use of different detailed chemical kinetic models. As shown, results were less sensitive to the detailed kinetic model than to the LES sub-grid scale model.

3.1.4. Cellular flames pattern

In the configuration studied in this work, the flame is initially laminar. During the initial stages of the flame expansion, the flame thickness is enough to permit this LES approach to resolve with a reasonable agreement the reacting flow phenomena. Under these lean H_2/O_2 conditions, thermodiffusive instabilities should occur leading to the formation of cellular flames. As previously said, the model considers an effective Lewis number equal for all species, and smaller than unity. Its value can be obtained from experiments (Goulier, Comandini, et al., 2017). Under these conditions, the simulation performed with detailed chemistry models, and with enough mesh resolution to resolve the flame front, should account for these instabilities, and the strain effects of the flame should be taken into account intrinsically with the model used. Figure 8 shows a comparison of the flame pattern observed in the experiments of Goulier, Comandini, et al. (2017), and the simulated pattern obtained for the same conditions. The numerical flame surface is represented as an isosurface based on a variable which represents a numerical Schlieren (based on the normalized density gradient). As shown in Figure 8, the numerical

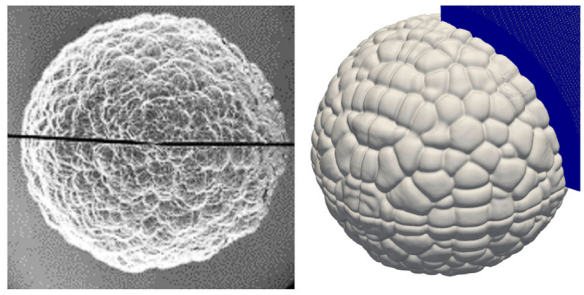

Figure 8. Experimental flame with 60 mm of equivalent radius from Goulier, Comandini, et al. (2017) (Left), and numerical results of the present work (Right), representing the flame pattern for 20% molar fraction of H_2/air at 60 mm of equivalent radius.

approach is able to account for this flame pattern, and provides results qualitatively similar to the experimental ones. Also, the critical radius at which the cellular cell pattern appears is predicted to be around 20 mm for an H_2-Air mixture of 20%, which is in agreement with the experimental measurements of Goulier, Comandini, et al. (2017).

3.1.5. Experimental benchmark and assessment of numerical schemes

In this section, the numerical schemes presented in Section 2.4 are analyzed by benchmarking against experimental data. Tables 3 and 4 show numerical predictions in terms of maximum wall pressure and sequence time, for the different numerical schemes considered. Regarding the estimation of maximum combustion pressure (P_{max}), the use of the different approaches entails less than 4% of error, except for Rusanov's scheme. As for the prediction of the combustion time (t_{rise}), PISO, AUSMup and AUSM+ showed better prediction capacities. This is somehow expected, as the Rusanov scheme is known to be very diffusive, and it is not accurate for low Mach flow conditions, whereas AUSM is very efficient in transonic conditions (Prá et al., 2010; Velasco et al., 2016), and its variations (AUSM+, and AUSMup) are also adequate for a wide range of Mach values (Liou, 1996, 2006).

Regarding the prediction of the unsteady behavior of the sequence, Figures 9 and 11 show the wall pressure evolution predicted by the different schemes. In general, most of the numerical approaches capture the evolution, although with different precision. Flux difference splitting schemes (FDS), as Rusanov's, show a too diffusive behavior. Figure 10 permits to support this point. In this figure, it is represented the radial distribution of the net mass flux in each cell in the surroundings of the flame front. As shown, Rusanov scheme predicts a

Table 3. Model predictions of maximum pressure and pressure rise time. H-EXP1.

H-EXP1	Experimental	PISO	AUSMup (Barth-Jespersen)	AUSM+ (Barth-Jespersen)	RUSANOV (Barth-Jespersen)	
P_{max} (bar)	5.72	5.68	5.74	5.74	7.14	
Error P_{max} (%)	Ref.	0.67	0.31	0.37	24.84	
t_{rise} (ms)	19.20	19.74	19.49	18.44	5.12	
Error t_{rise} (%)	Ref.	2.81	1.51	−3.96	−73.33	
H-EXP1	AUSMup (Van-Leer)	AUSMup (Van-Leer) (Runge Kutta)	AUSMup (MUSCL)	AUSMup (Van-Albada)	AUSMup (Upwind)	AUSM+ (Van-Leer)
P_{max} (bar)	5.67	5.66	5.72	5.65	5.65	5.65
Error P_{max} (%)	−0.86	−1.14	0.077	−1.15	−1.22	−1.20
t_{rise} (ms)	21.66	20.15	16.54	21.66	16.15	20.26
Error t_{rise} (%)	12.81	4.95	−13.85	12.81	−15.89	5.52

Table 4. Model predictions of maximum pressure and pressure rise time (H-EXP2).

H-EXP2	Experimental	PISO	AUSMup (Barth-Jespersen)	AUSM+ (Barth-Jespersen)	AUSMup (Van-Leer)	AUSMup (Van-Leer) (Runge Kutta)	AUSM+ (Van-Leer)
P_{max} (bar)	5.585	5.663	5.712	5.694	5.638	5.62	5.616
Error P_{max} (%)	Ref.	1.41	2.28	1.94	0.94	0.65	0.55
t_{rise} (ms)	16.20	16.98	16.13	15.3	18.98	17.12	17.88
Error t_{rise} (%)	Ref.	1.28	−6.22	−11.05	10.35	−0.47	3.95

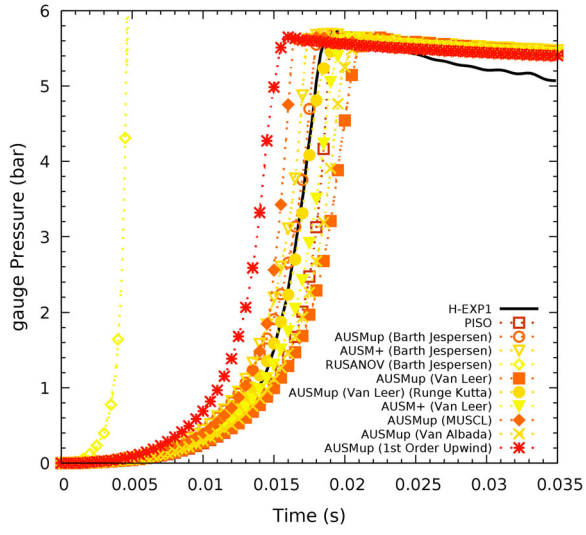

Figure 9. Influence of the numerical scheme. Time evolution of gauge pressure at the sphere wall (H-EXP1 conditions).

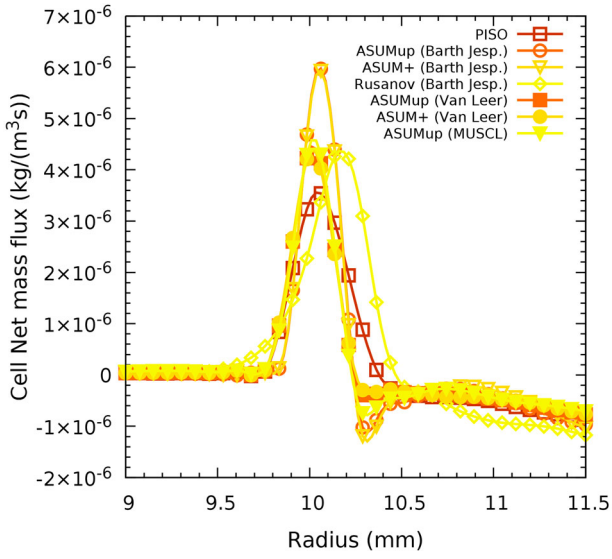

Figure 10. Cell net mass fluxes in the flame front region at 10^{-3} s after initiation sequence (H-EXP1 conditions).

wider spatial region of positive cell net mass flux, compared to the AUSM-type schemes for the same primitive spatial interpolation scheme used in the cell-to-face reconstruction. As a result, the flame thickness numerically obtained with this scheme is also larger (Figure 11, Right), what increases the heat released due to combustion, and provides a non-realistic burning speed. As a result, the scheme does not provide a realistic dynamic of the combustion sequence.

On the other hand, a coupled solver with flux vector splitting (FVS) schemes, such as AUSMup and AUSM+ can provide better results under the conditions of the experiment. In this case, AUSMup flux-schemes, with the Bath-Jespersen slope limiter, provide the best results, not only in maximum pressure at the wall but also in the rising time predicted. These schemes are less diffusive and do not introduce artificial numerical transport of the conserved variables, resulting in a thinner flame front with a more accurate combustion heat release. PISO segregated solver shows stability and robustness under the subsonic conditions of the experiments. It also provides a reasonable agreement on the dynamic evolution of wall pressure at the late stage of the sequence.

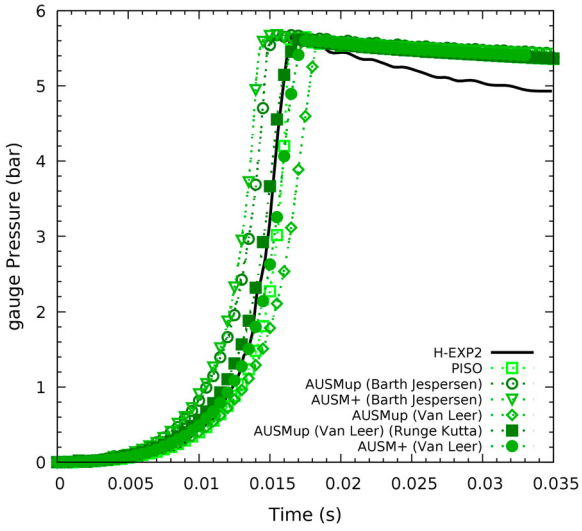

Figure 11. Numerical and experimental results of gauge pressure at the sphere wall (H-EXP2 conditions).

As shown in Figure 11, the effect of increasing the oxygen fraction in the gas mixture (as defined for H-EXP2) is well captured by the numerical models, although different time evolutions are predicted, with errors between −0.4% and 11% in terms of rising time (t_{rise}), and between 0.5% and 1.4% in terms of peak pressure (P_{max}), as summarized in Table 4. PISO and AUSMup (Van-Leer, Runge–Kutta) are the schemes that provide the smallest prediction errors. AUSMup (Van-Leer, Runge–Kutta) scheme gives the best prediction of pressure evolution during the period when dP/dt reached maximum values (i.e. during the intermediate lapse of time of the sequence, $11 < t < 17$ ms), whereas PISO scheme yields a better prediction at low-pressure conditions (i.e. during the initial stage of the sequence $t < 11$ ms). All in all, PISO and AUSMup (Van-Leer, Runge–Kutta) provide the smallest averaged errors for both experiments.

Concerning the benchmark for the combustion products, Table 5 presents a comparison of the experimental data and the model predictions with different schemes and Williams chemical model. As shown, the models can predict the final composition, with errors smaller than 6%. PISO, with Williams' chemical model, provides the smallest deviations from experimental data. Similar results are obtained with the same scheme and Marinov's chemical model, although with slightly bigger errors.

3.2. Flame acceleration in an obstructed channel

In order to assess the capability of this combustion modeling strategy to predict flame acceleration phenomena of H_2-Air mixtures, simulations in an obstructed channel were carried out. The results presented in this section show the capabilities of ILES for this purpose, with different modeling procedures, taking into account its behavior under flame-vortex interactions. The simulation conditions are set to reach the turbulent combustion regime

Table 5. Benchmark of the combustion products with Williams (2008) and Marinov et al. (1995) chemistry models.

H-EXP1 (% mol)	EXPERIMENTAL	PISO (Williams ch.)	AUSMup BJ (Williams ch.)	AUSM+ BJ (Williams ch.)	AUSMup VL (Williams ch.)	PISO (Marinov ch.)
$\%H_2$	0.00	0.05	0.22	0.22	0.17	0.08
%H	0.00	0.01	0.22	0.05	0.04	0.01
$\%O_2$	7.65 ± 0.50	7.46	7.21	7.21	7.31	7.41
%O	0.00	0.04	0.17	0.17	0.14	0.06
%OH	0.00	0.40	1.14	1.14	0.98	0.58
$\%HO_2$	0.00	0.00	0.00	0.00	0.00	0.00
$\%H_2O_2$	0.00	0.00	0.00	0.00	0.00	0.00
$\%H_2O$	22.59 ± 0.50	21.93	22.72	22.62	21.45	21.80
$\%N_2$	69.76 ± 0.50	70.11	68.47	68.58	69.91	70.06
Error (%)						
$\%O_2$	–	2.50	5.73	5.71	4.44	3.13
$\%H_2O$	–	2.90	−0.60	−0.13	5.04	3.50
$\%N_2$	–	−0.50	1.85	1.69	−0.22	−0.43
H-EXP2 (% mol)	EXPERIMENTAL	PISO (Williams ch.)	AUSMup BJ (Williams ch.)	AUSM+ BJ (Williams ch.)	AUSMup VL (Williams ch.)	
$\%H_2$	0.00	0.03	0.01	0.01	0.01	
%H	0.00	0.01	0.00	0.00	0.00	
$\%O_2$	14.68 ± 0.50	15.44	15.42	15.44	15.50	
%O	0.00	0.05	0.02	0.02	0.02	
%OH	0.00	0.44	0.25	0.25	0.25	
$\%HO_2$	0.00	0.00	0.00	0.00	0.00	
$\%H_2O_2$	0.00	0.00	0.00	0.00	0.00	
$\%H_2O$	22.82 ± 0.50	21.93	22.28	22.23	22.07	
$\%N_2$	62.5 ± 0.50	62.10	62.02	62.05	62.15	
Error (%)						
$\%O_2$	–	−5.16	−5.04	−5.19	−5.62	
$\%H_2O$	–	3.90	2.37	2.59	3.29	
$\%N_2$	–	0.64	0.78	0.73	0.56	

during the sequence. That allows us to extend the evaluation of this modeling approach as a potential global strategy that might permit to simulate a complete combustion sequence, from the initial stages (laminar) to the fully turbulent combustion regime.

A 2D channel, 4 cm wide and 64 cm long, with a blockage ratio of 0.5 is considered for this study. It is filled in with rectangular obstacles of width $d/16$, and length $d/4$, being d the channel width. The obstacles are equally spaced along the channel. The distance between two consecutive obstacles is set to d. The first obstacle is placed at a longitudinal distance of $d/2$ from the ignition side. Simulations on a similar channel were carried out by Gamezo et al. (2007) for a stoichiometric H_2-Air mixture, and initial conditions of 1 atm and 293 K. These conditions result in flame laminar properties of $S_L^0 = 2.98$ m/s and $\delta_L^0 = 0.35$mm, as reported by Gamezo et al. (2007).These computations were performed with a Godunov-type solver with no turbulence, in conjunction with a one-step Arrhenius kinetic model. A more recent study was performed by Emami et al. (2015) using a PISO solver with the 27-steps Marinov's chemical mechanism, ISAT tabulation, and the k_{sgs} modeling, as performed in this work, but with the difference of using an Artificially Thickened Flame (ATF) for the modeling of the sub-grid scale combustion effects. In that case, cell sizes of 0.125 and 0.0625 mm were employed. More detailed information about the channel geometry and physical properties of the flame can be found in Gamezo et al. (2007).

In the present work, computational domains with a discretization of 0.0875 mm ($\delta_L^0/\Delta x = 4$) and 0.04375 mm ($\delta_L^0/\Delta x = 8$) are used, to keep a similar grid resolution to that analyzed in the deflagration validation in section 3.1.1. Also, the PISO algorithm and an ignition volume with 5 mm of radius are considered. The same algorithm and ignition volume were used by Emami et al. (2015). No-slip boundary conditions are imposed at the wall surfaces. The channel is opened at its end, where a wave-transmissive boundary condition is imposed. A symmetry plane is imposed at the horizontal midplane of the channel (upper horizontal boundary in Figure 13) so that the computational domain considered is half of the channel. In order to perform the LES simulations on the 2D domain correctly, a structured mesh with a uniform cell size is considered, where the cell size (Δx) is the third cell dimension (i.e. 3D domain with an extrusion length of Δx in the third spatial direction, not resolving velocities and gradients in this direction). This way, the filter size for the LES sub-grid scale modelization is properly calculated from the cell volume. Besides, an effective Lewis of unity is considered. This is approximately the value reported by Goulier, Chaumeix, et al. (2017), for a stoichiometric H2-Air mixture under similar conditions.

Three different simulations are presented: two of them with the 21-step chemical mechanism by Williams, one with $\delta_L^0/\Delta x = 4$ (CASE A) and another with $\delta_L^0/\Delta x = 8$ (CASE B); finally, a third one with $\delta_L^0/\Delta x = 8$ and the 27-step chemical mechanism by Marinov (CASE C), to assess the influence of the chemical mechanism in the computations. Note that ISAT method is used. This strategy was also adopted by Emami et al. (2015).

Figure 12 shows a comparison of the results predicted with the present approach against the numerical prediction by Emami et al. (2015) and Gamezo et al. (2007). The images at the top illustrate the flame tip speed versus the flame position and time, whereas the images at the bottom represent the dimensionless flame surface area versus flame position, as well as the combustion heat released versus the flame position. Note that the ordinate axes include both the position of the obstacles and the flame. The flame position was computed as the largest distance of the flame surface from the ignition point, whereas the flame surface was defined as the isosurface where $Y_{H2} = 0.5 \cdot Y_{H2}^0$. Here, Y_{H2}^0 denotes the initial H_2 mass fraction of the premixed mixture within the channel. As shown, the present ILES approach can describe the flame acceleration mechanism in good agreement with the approaches used by Emami et al. and Gamezo et al. It is worth to be noted that the results of Figure 12 (Top-left) were shifted by 0.65 ms for a better comparison of the results by Emami et al. (2015) against those by Gamezo et al. (2007). Emami et al. attributed this time difference to the different chemical induction times obtained with the one-step mechanism used by Gazemo et al. compared to the detailed Marinov's mechanism used by Emami et al. This induction time was reported by the authors to be a few times smaller for a one-step mechanism, when compared to real induction times (Liberman et al., 2010).

Concerning the results of the present work, they were also shifted by 0.65 ms for CASE C (Marinov's mechanism) but only 0.5 ms for CASE B (Williams' mechanism). This shifting revealed that, during the initial stage of the propagation, where the flame is laminar, the chemical mechanism and the modelization of the heat capacities of the mixture are key aspects to predict accurately the burning flame speed. Note that the values reported by Emami et al. with an ATF combustion modeling and those reported in this work were shifted by the same value when considering the same reaction mechanism. This confirmed the agreement of the present approach with the one of Emami et al. [61]. In addition, the comparison of CASE A and B show that the grid-independent solution found for the initial stage of the flame acceleration (Figure 12 Top-Left) is lost at a later stage of flame acceleration, when the coarse mesh (CASE A) is not

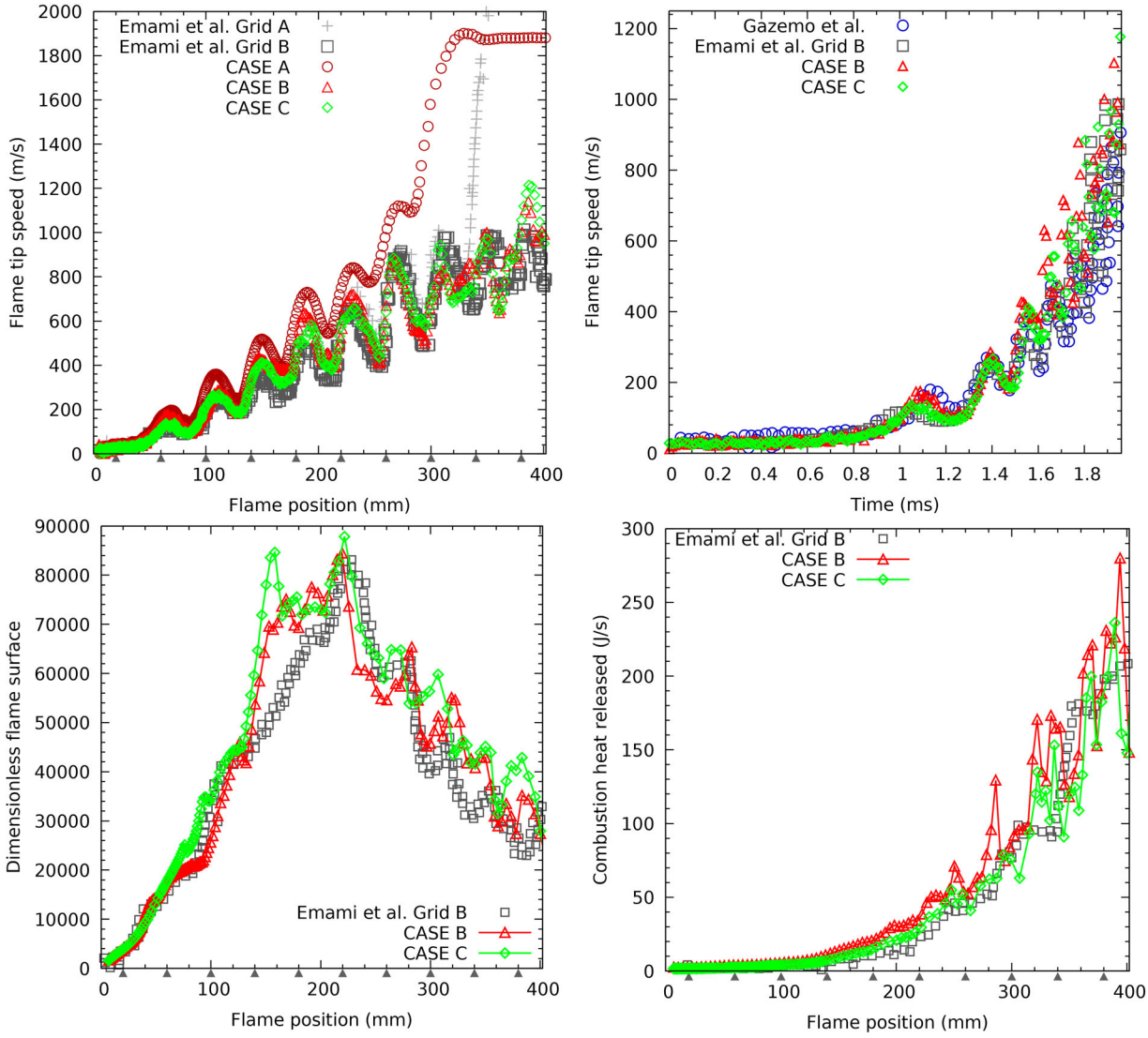

Figure 12. Comparison of the results predicted in the present work against the numerical prediction by Emami et al. (2015) and Gamezo et al. (2007). Top-left: Flame tip speed versus flame position. Top-right: Flame tip speed versus simulated time. Bottom-left: Dimensionless flame surface area versus flame position. Bottom-right: Flame heat released versus flame position.

able to follow the tendency of the refined one (CASE B). Notwithstanding, CASE B ($\frac{\delta_L^0}{\Delta x} = 8$) provides a reasonably good prediction of the numerical results in Gamezo et al. (2007) and Emami et al. (2015), for a turbulent flow regime with medium-high Reynolds numbers.

Figures 13 and 14 show some 2D snapshots of the sequence and permit to get some insights into the acceleration mechanism. Figure 13 shows the vorticity field with colourized flame front during the flame acceleration between obstacles 1 and 6 (CASE B), whereas Figure 14 shows a numerical Schlieren with the flame front colourized by H_2 reaction rate during the sequence. In these figures, the flame front is represented as an isovolume with H_2 mass fraction values between 0.5 and 23%.

As shown in Figures 12–14, the flame progressively accelerates as it surpasses the subsequent obstacles. At the initial stage, this acceleration is promoted by the increase of the effective flame surface area during the flame expansion (Figure 12 Top-Left). As the flame front surpasses an obstacle, the vortex shedding process increases the effective area of the flame (Figure 13). Once the flame surface area reaches its maximum value (Figure 12 Bottom-Left and Figure 13, obstacles 4-6), the promotion of the flame acceleration is mainly sustained by the combustion heat released, increased with the turbulence enhancement (Figure 14). Figures 13 and 14 also permit to show the interaction of the vortex and flame front during the flame acceleration. As the flame accelerates, the compressibility effects become significant, and the vortex structures induce the deformation of the flame front, increasing not only turbulence features but also local precursors of 'hot-spots'. The presence of the obstacles also promotes

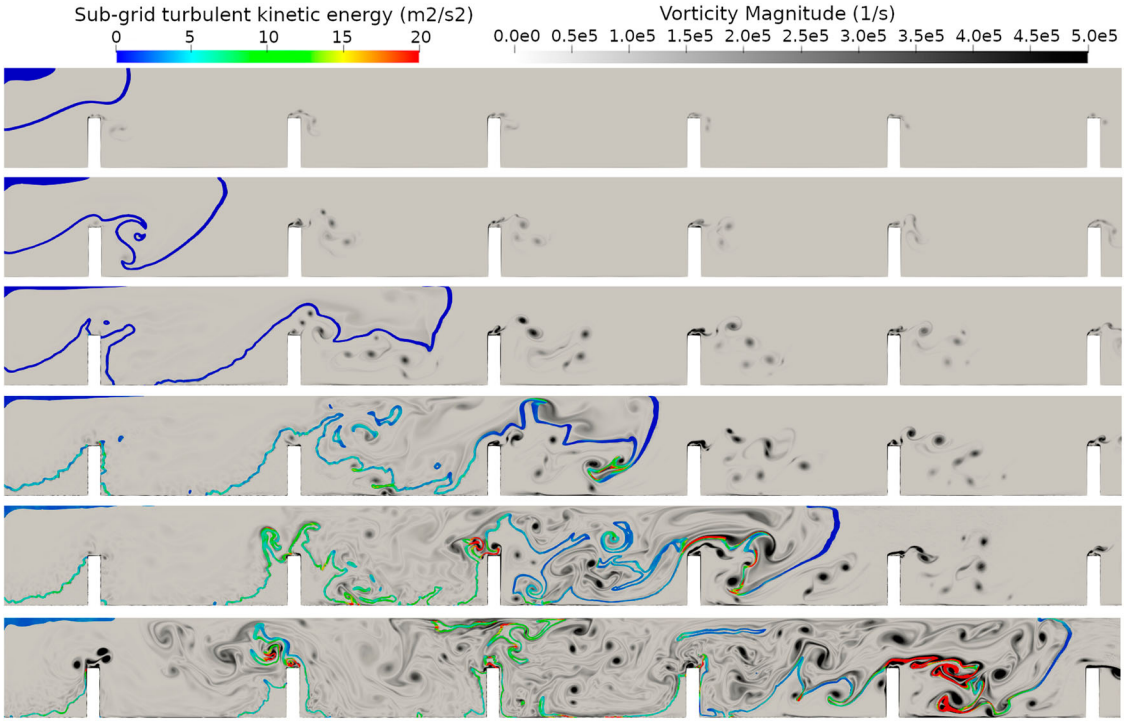

Figure 13. Vorticity field with the flame front colourized by sub-grid turbulent intensity during the flame acceleration sequence between obstacles 1 and 6 (CASE B). From top to bottom: 0.9, 1.4, 1.8, 2.0, 2.1 and 2.2 ms of simulated time.

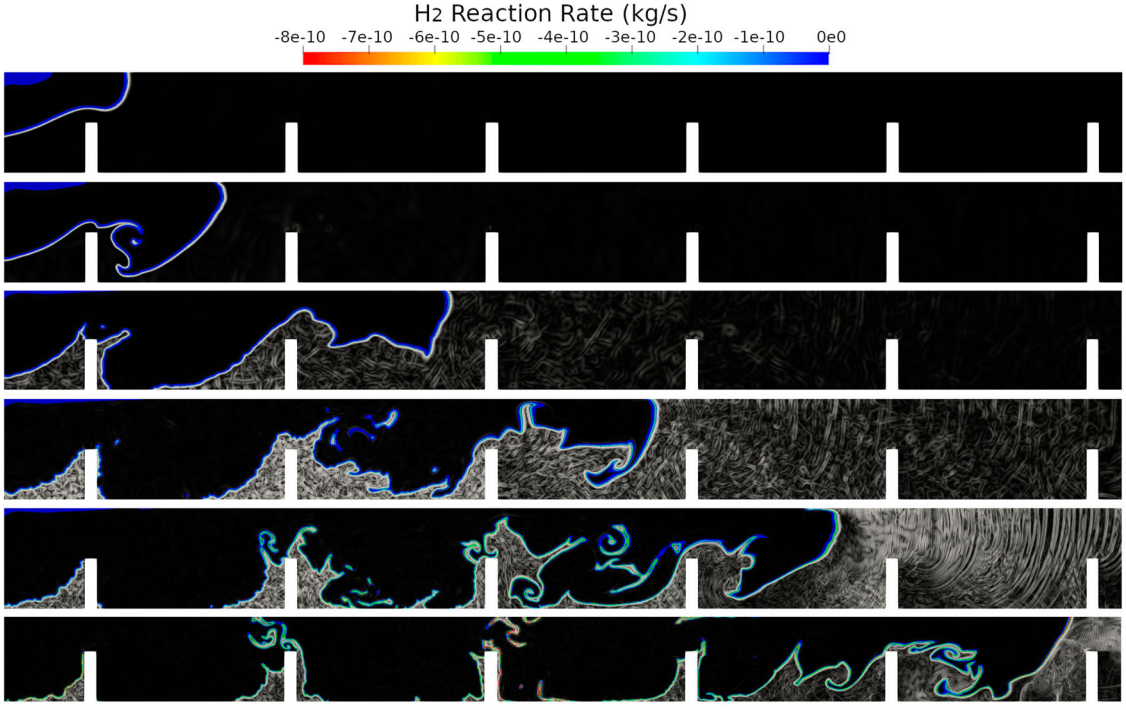

Figure 14. Numerical Schlieren with the flame front colourized by H_2 reaction rate during the flame acceleration sequence between obstacles 1 and 6 (CASE B). From top to bottom: 0.9, 1.4, 1.8, 2.0, 2.1 and 2.2 ms of simulated time.

the reflection of the local density gradient waves, which also distort the flame front, increasing its area and promoting the transition of the flame combustion regime.

4. Major limitations and needs of the model

The benchmarks performed permit to identify several shortcomings of this LES approach, that should be

considered and addressed. These can be summarized as follows:

- Results show that the unstretched laminar flame speed predicted with this type of models with meshes $\delta_L^0/\Delta x \sim 1$, provide errors of $\sim$18%. In this case, the numerical diffusion (i.e. numerical errors) might play an important role in the predicted flame speed.
- There is an important effect of the sub-grid models, which points out the uncertainty linked with its election, especially in the case of grids that do not provide enough flame resolution.
- In practice, the present LES approach can be only used in the initial stages of unsteady combustion sequences, due to computational cost, as the grid conditions required in the absence of sub-grid combustion modeling are difficult to satisfy when the flame surface increases.
- This study has pointed out some uncertainties and grid resolution requirements that must be controlled rigorously, to provide reliable results. Therefore, the present LES approach is not recommended or, at least, should be used with great care, if applied to critical applications. In those applications, other LES approaches, such as TFM / ATF (Nicolás-Pérez et al., 2020), would permit to relax those criteria.

The analysis of these limitations has highlighted major requirements or needs that must be fulfilled to use this LES approach under unsteady sequences. Among them, the grid resolution criterium was found to be critical. For the specific conditions of the cases considered in this work, at least $\delta_L^0/\Delta x \sim 8$, and $Da < 1$ should be respected. However, these criteria should be checked for other types of configurations.

5. Conclusions and future work

In this study, the capabilities and limitations of LES coupled with the PSR hypothesis were evaluated to simulate the initial stages of H_2-air combustion experiments. This approach considers that there is a homogeneous concentration and temperature in each computational cell at sub-grid level. Different sub-grid turbulence and detailed chemistry models were tested in both experimental and numerical benchmarks. This permitted to evaluate the capabilities and limitations of this modeling approach when simulating unsteady combustion sequences with low or moderate Reynolds numbers. The study showed this LES approach can be applied to a grid with enough resolution to resolve flame thickness and wrinkling patterns. In this case, no sub-grid scale combustion modeling is needed. However, the model has important limitations that must be considered:

- Spatial resolution was found to be critical. The unstretched laminar flame speed predicted with this type of models with meshes $\delta_L^0/\Delta x \sim 1$ provide errors of $\sim$18%. Furthermore, numerical diffusion might play an important role in the predicted flame speed.
- There is an important effect of the sub-grid models, which points out the uncertainty linked with its election, especially in the case of grids that do not provide enough flame resolution.
- The computational resources needed to reach the required level of flame resolution of this modeling approach increases as the flame expands and the flow increases its Reynolds number due to flame wrinkling and the effective increase of the flame surface.

As for the suggested improvements, results also showed this LES approach coupled with detailed chemistry and ISAT method was an affordable strategy to simulate the initial stages (i.e. post-ignition and flame acceleration) of premixed combustion problems, with low or moderate Reynolds numbers with reasonable accuracy, if a certain level of grid refinement was reached ($\delta_L^0/\Delta x \geq 8$).

Besides, the benchmarks highlighted other significant specifics:

- The impact of sub-grid turbulence models was found to be high whereas the influence of the detailed kinetic scheme used was lower. Therefore, it is recommended to benchmark the sub-grid model used against experimental results.
- Regarding the prediction of the unsteady behavior of the sequence, AUSMup, AUSM+, and PISO schemes showed reasonable agreement with experimental data. Flux difference splitting (FDS) schemes as Rusanov scheme showed not accurate performance at low Mach regime. AUSMup flux-schemes with the Bath-Jespersen slope limiter provided the best results ($<$ 4% of error), not only in rising time but also in maximum wall pressure predicted.
- As for the prediction of the combustion products, the models predicted, with an error smaller than 6%, the final species composition. PISO scheme and Williams' chemical model provided the smallest deviations from experimental data.

Finally, the results also showed that this LES approach was able to account for the cellular flame pattern at the post-ignition phase, and provided results which were qualitatively similar to the experimental ones. Besides,

this approach is also able to predict flame acceleration in an obstructed channel if the required level of flame resolution is met. These results permit to postulate this LES approach for experiments interpretation and dynamic studies of the early stage of a flame expansion.

The study also permits to identify research needs that should be addressed to improve the reliability of this LES approach. In this sense, the future direction of this work will focus on the extension of the benchmark of this LES approach with others based on reference experimental or numerical data to assess its limitations in different key combustion problems. Additional efforts should be also devoted to the development of combustion and subgrid turbulence models or strategies with lower computational costs which could be applied to the simulation of transient combustion sequences.

Disclosure statement

No potential conflict of interest was reported by the author(s).

Funding

This work was performed with the support of Institut of Radioprotection et Sûreté Nucléaire of France [DA 3000011012/CA32000911] IRSN SIRET: 440 546 018 00019 Code APE: 7219 Z and with resources of Servicio de Apoyo a la Investigación Tecnologlócia of UPCT which was supported by the Spanish Ministry of Economy and Competitiveness and the European Commission (European Regional Development Fund ERDF) [UPCA13-2E-2352].

ORCID

F. J. S. Velasco http://orcid.org/0000-0002-9311-794X
R. A. Otón-Martínez http://orcid.org/0000-0003-2123-9785
J. R. García-Cascales http://orcid.org/0000-0002-6369-9563
A. Bentaib http://orcid.org/0000-0002-9540-5515
N. Chaumeix http://orcid.org/0000-0002-4042-8218

References

Agilent Corp. (1994). *Agilent chemical analysis group 5890 gas chromatograph*. 5890 Series II. http://www.agilent.com/cs/library/support/documents/a15282.pdf.

Barth, T. J., & Jespersen, D. C. (1989). The design and application of upwind schemes on unstructured meshes. *AIAA Journal*, 0366. https://doi.org/10.2514/6.1989-366

Berglund, M., Fedina, E., Tegnér, J., Fureby, C., & Sabelnikov, V. (2010). Finite rate chemistry LES of self-ignition in a supersonic combustion ramjet. *AIAA Journal*, *48*(3), 540. https://doi.org/10.2514/1.43746

Chai, X., & Mahesh, K. (2012). Dynamic k-equation model for Large Eddy Simulations of compressible flows. *Journal of Fluid Mechanics*, *699*, 385–413. https://doi.org/10.1017/jfm.2012.115

Chen, C., Riley, J. J., & McMurtry, P. A. (1991). A study of Favre averaging in turbulent flows with chemical reaction. *Combustion and Flame*, *87*(3–4), 257–277. https://doi.org/10.1016/0010-2180(91)90112-O

Ciccarelli, G., Johansen, C. T., & Parravani, M. (2010). The role of shock-flame interactions on flame acceleration in an obstacle laden channel. *Combustion and Flame*, *157*(11), 2125–2136. https://doi.org/10.1016/j.combustflame.2010.05.003

Colin, O., Ducros, F., Veynante, D., & Poinsot, T. (2000). A thickened flame model for Large Eddy Simulations of turbulent premixed combustion. *Physics of Fluids*, *12*(7), 1843–1863. https://doi.org/10.1063/1.870436

Dodoulas, I. A., & Navarro-Martinez, S. (2013). Large Eddy Simulation of premixed turbulent flames using the probability density function approach. *Flow, Turbulence and Combustion*, *90*(3), 645–678. https://doi.org/10.1007/s10494-013-9446-z

Duwig, C., Ducruix, S., & Veynante, D. (2012). Studying the stabilization dynamics of swirling partially premixed flames by proper orthogonal decomposition. *Journal of Engineering for Gas Turbines and Power*, *134*(10), 101501. https://doi.org/10.1115/1.4007013

Duwig, C., & Dunn, M. J. (2013). Large Eddy Simulation of a premixed jet flame stabilized by a vitiated co-flow: Evaluation of auto-ignition tabulated chemistry. *Combustion and Flame*, *160*(12), 2879–2895. https://doi.org/10.1016/j.combustflame.2013.06.011

Duwig, C., & Ludiciani, P. (2014). Large Eddy Simulation of turbulent combustion in a stagnation point reverse flow combustor using detailed chemistry. *Fuel*, *123*, 256–273. https://doi.org/10.1016/j.fuel.2014.01.072

Duwig, C., Nogenmyr, K. J., Chan, C. K., & Dunn, M. J. (2011). Large Eddy Simulations of a piloted lean premix jet flame using finite-rate chemistry. *Combustion Theory and Modelling*, *15*(4), 537–568. https://doi.org/10.1080/13647830.2010.548531

Emami, S., Mazaheri, K., Shamooni, A., & Mahmoudi, Y. (2015). LES of flame acceleration and DDT in hydrogen-air mixture using artificially thickened flame approach and detailed chemical kinetics. *International Journal of Hydrogen Energy*, *40*(23), 7395–7408. https://doi.org/10.1016/j.ijhydene.2015.03.165

Fiorina, B., Mercier, R., Kuenne, G., Ketelheun, A., Avdic, A., Janicka, J., Geyer, D., Dreizler, A., Alenius, E., Duwig, C., Trisjono, P., Kleinheinz, K., Kang, S., Pitsch, H., Proch, F., Cavallo Marincola, F., & Kempf, A. (2015). Challenging modeling strategies for LES of non-adiabatic turbulent stratified combustion. *Combustion and Flame*, *162*(11), 4264–4282. https://doi.org/10.1016/j.combustflame.2015.07.036

Fureby, C. (2007). *Comparison of flamelet and finite rate chemistry LES for premixed turbulent combustion*. 45th AIAA Aerospace Sciences Meeting and Exhibit Reno, Nevada. https://doi.org/10.2514/6.2007-1413

Gamezo, V. N., Ogawa, T., & Oran, E. S. (2007). Numerical simulations of flame propagation and DDT in obstructed channels filled with hydrogen–air mixture. *Proceedings of the Combustion Institute*, *31*(2), 2463–2471. https://doi.org/10.1016/j.proci.2006.07.220

García-Cascales, J. R., Otón-Martínez, R. A., Velasco, F. J. S., Vera-García, F., Bentaib, A., & Meynet, N. (2014). Advances in the characterisation of reactive gas and solid mixtures

under low pressure conditions. *Computers & Fluids*, *101*, 64–87. https://doi.org/10.1016/j.compfluid.2014.05.017

Giacomazzi, E., Battaglia, V., & Bruno, C. (2004). The coupling of turbulence and chemistry in a premixed bluff-body flame as studied by LES. *Combustion and Flame*, *134*(4), 320–335. https://doi.org/10.1016/j.combustflame.2004.06.004

Giannakopoulos, G. K., Matalon, M., Frouzakis, C. E., & Tomboulides, A. G. (2015). The curvature Markstein length and the definition of flame displacement speed for stationary spherical flames. *Proceedings of the Combustion Institute*, *35*(1), 737–743. https://doi.org/10.1016/j.proci.2014.07.049

Goulier, J., Chaumeix, N., Halter, F., Meynet, N., & Bentaïb, A. (2017). Experimental study of laminar and turbulent flame speed of a spherical flame in a fan-stirred closed vessel for hydrogen safety application. *Nuclear Engineering and Design*, *312*, 214–227. https://doi.org/10.1016/j.nucengdes.2016.07.007

Goulier, J., Comandini, A., Halter, F., & Chaumeix, N. (2017). Experimental study on turbulent expanding flames of lean hydrogen/air mixtures. *Proceedings of the Combustion Institute*, *36*(2), 2823–2832. https://doi.org/10.1016/j.proci.2016.06.074

Grinstein, F. F., & Kailasanath, K. (1995). Three dimensional numerical simulations of unsteady reactive square jets. *Combustion and Flame*, *101*(1–2), 2–10. https://doi.org/10.1016/0010-2180(94)00095-A

Hiremath, V., Ren, Z., & Pope, S. B. (2011). Combined dimension reduction and tabulation strategy using ISAT-RCCE-GALI for the efficient implementation of combustion chemistry. *Combustion and Flame*, *158*(11), 2113–2127. https://doi.org/10.1016/j.combustflame.2011.04.010

Hirschfelder, J. O., Curtiss, C. F., Bird, R. B., & Mayer, M. G. (1954). *Molecular theory of gases and liquids* (Vol. 26). Wiley.

Hoi, D. N., Ju, Y., & Lee, J. H. S. (2007). Assessment of detonation hazards in high-pressure hydrogen storage from chemical sensitivity analysis. *International Journal of Hydrogen Energy*, *32*, 93–99. https://doi.org/10.1016/j.ijhydene.2006.03.012

Issa, R. I. (1986). Solution of the implicit discretized fluid flow equations by operator splitting. *Journal of Computational Physics*, *62*(1), 40–65. https://doi.org/10.1016/0021-9991(86)90099-9

Issakhov, A., Alimbek, A., & Issakhov, A. (2020). A numerical study for the assessment of air pollutant dispersion with chemical reactions from a thermal power plant. *Engineering Applications of Computational Fluid Mechanics*, *14*(1), 1035–1061. https://doi.org/10.1080/19942060.2020.1800515

Karata, G., Ota, M., Terada, H., Chino, M., & Nagai, H. (2012). Atmospheric discharge and dispersion of radionuclides during the Fukushima Dai-Ichi nuclear power plant accident. Part I: Source term estimation and local-scale atmospheric dispersion in early phase of the accident. *Journal of Environmental Radioactivity*, *109*, 103–113. https://doi.org/10.1016/j.jenvrad.2012.02.006

Kim, D., & Kim, J. (2019). Numerical method to simulate detonative combustion of hydrogen-air mixture in a containment. *Engineering Applications of Computational Fluid Mechanics*, *13*(1), 938–953. https://doi.org/10.1080/19942060.2019.1660219

Krüger, O., Terhaar, S., Paschereit, C. O., & Duwig, C. (2013). Large Eddy Simulations of hydrogen oxidation at ultra-wet conditions in a model gas turbine combustor applying detailed chemistry. *Journal of Engineering for Gas Turbines and Power*, *135*(2), 021501-9. https://doi.org/10.1115/1.4007718

Liberman, M. A., Ivanov, M. F., Kiverin, A. D., Kuznetsov, M. S., Chukalovsky, A. A., & Rakhimova, T. V. (2010). Deflagration-to-detonation transition in highly reactive combustible mixtures. *Acta Astronautica*, *67*(7–8), 688–701. https://doi.org/10.1016/j.actaastro.2010.05.024

Liberman, M. A., Kiverin, A. D., & Ivanov, M. F. (2011). On detonation initiation by a temperature gradient for a detailed chemical reaction model. *Physics Letters A*, *375*(17), 1803–1808. https://doi.org/10.1016/j.physleta.2011.03.026

Lilly, D. K. (1991). A proposed modification of the germano subgrid-scale closure method. *Physics of Fluids A: Fluid Dynamics*, *4*(3), 633. https://doi.org/10.1063/1.858280

Liou, M. S. (1996). A sequel to AUSM: AUSM+. *Journal of Computational Physics*, *129*(2), 364–382. https://doi.org/10.1006/jcph.1996.0256

Liou, M. S. (2006). A sequel to AUSM, part II: AUSM+-up for all speeds. *Journal of Computational Physics*, *214*(1), 137–170. https://doi.org/10.1016/j.jcp.2005.09.020

Lu, L., & Pope, S. B. (2009). An improved algorithm for in situ adaptive tabulation. *Journal of Computational Physics*, *228*(2), 361–386. https://doi.org/10.1016/j.jcp.2008.09.015

Marinov, N. M., Westbrook, C. K., & Pitz, W. J. (1995, October). *Detailed and global chemical kinetics model for hydrogen*. 8th International Symposium on Transport Properties, San Francisco, CA, USA. https://digital.library.unt.edu/ark:/67531/metadc794810/

McBride, B. J., & Gordon, S. (1996). *Computer program for calculation of complex chemical equilibrium compositions and application* (Report No. 1311 NASA).

McBride, B. J., Sanford, G., & Reno, M. A. (1993). *Coefficients for calculating thermodynamic and transport properties of individual species* (NASA Technical Report).

Meshkov, E. E. (1969). Instability of the interface of two gases accelerated by a shock wave. *Fluid Dynamics*, *4*(5), 101–104. https://doi.org/10.1007/BF01015969

Mosavi, A., Shamshirband, S., Salwana, E., Chau, K.-W., & Tah, J. H. M. (2019). Prediction of multi-inputs bubble column reactor using a novel hybrid model of computational fluid dynamics and machine learning. *Engineering Applications of Computational Fluid Mechanics*, *13*(1), 482–492. https://doi.org/10.1080/19942060.2019.1613448

Navarro-Martinez, S., Kronenburg, A., & Di Mare, F. (2005). Conditional moment closure for Large Eddy Simulations. *Flow, Turbulence and Combustion*, *75*(1–4), 245–274. https://doi.org/10.1007/s10494-005-8580-7

Nicolás-Pérez, F., Velasco, F. J. S., García-Cascales, J. R., Otón-Martínez, R. A., Bentaib, A., & Chaumeix, N. (2020). Evaluation of different models for turbulent combustion of hydrogen-air mixtures. Large Eddy Simulation of a LOVA sequence with hydrogen deflagration in ITER vacuum vessel. *Fusion Engineering and Design*, *161*, Article 111901. https://doi.org/10.1016/j.fusengdes.2020.111901

Nicoud, F., & Ducros, F. (1999). Sub-grid scale stress modelling based on the square of the velocity gradient tensor. *Flow, Turbulence and Combustion*, *62*(3), 183–200. https://doi.org/10.1023/A:1009995426001

OECD. (2000). *State-of-the art report, nuclear safety flame acceleration and deflagration-to-detonation transition in nuclear safety*. NEA/CSNI/R.

Otón-Martínez, R. A., Monreal-González, G., García-Cascales, J. R., Vera-García, F., Velasco, F. J. S., & Ramírez-Fernández, F. J. (2015). An approach formulated in terms of conserved variables for the characterisation of propellant combustion in internal ballistics. *International Journal for Numerical Methods in Fluids*, *79*(8), 394–415. https://doi.org/10.1002/fld.4056

Park, D., Cha, J., Kim, M., & Sang Go, J. (2020). Multi-objective optimization and comparison of surrogate models for separation performances of cyclone separator based on CFD, RSM, GMDH-neural network, back propagation-ANN and genetic algorithm. *Engineering Applications of Computational Fluid Mechanics*, *14*(1), 180–201. https://doi.org/10.1080/19942060.2019.1691054

Pedersen, Ø, & Rüther, N. (2019). CFD modeling as part of a hybrid modeling case study for a gauging station with challenging hydraulics. *Engineering Applications of Computational Fluid Mechanics*, *13*(1), 265–278. https://doi.org/10.1080/19942060.2019.1581661

Pitsch, H. (2006). Large-Eddy Simulation of turbulent combustion. *Annual Review of Fluid Mechanics*, *38*(1), 453–482. https://doi.org/10.1146/annurev.fluid.38.050304.092133

Pope, S. B. (1997). Computationally efficient implementation of combustion chemistry using in situ adaptive tabulation. *Combustion Theory and Modelling*, *1*(1), 41–63. https://doi.org/10.1080/713665229

Prá, C. L. D., Velasco, F. J. S., & Herranz, L. E. (2010). Simulation of a gas jet entering the secondary side of a steam generator during a SGTR sequence: Validation of a FLUENT 6.2 model. *Nuclear Engineering and Design*, *240*(9), 2206–2214. https://doi.org/10.1016/j.nucengdes.2009.11.021

Raman, S., & Pitsch, H. (2007). A consistent LES/filtered-density function formulation for the simulation of turbulent flames with detailed chemistry. *Proceedings of the Combustion Institute*, *31*(2), 1711–1719. https://doi.org/10.1016/j.proci.2006.07.152

Roy, G. D., Frolov, S. M., Borisov, A. A., & Netzer, D. W. (2004). Pulse detonation propulsion: Challenges, current status and future perspective. *Progress in Energy and Combustion Science*, *30*(6), 545–672. https://doi.org/10.1016/j.pecs.2004.05.001

Rusanov, V. V. (1962). The calculation of the interaction of non-stationary shock waves and obstacles. *Journal of Computational Mathematics and Mathematical Physics*, *1*(2), 304–320. https://doi.org/10.1016/0041-5553(62)90062-9

Sabard, J. (2013). *Etude de l'explosion de mélanges diphasiques: hydrogène et poussières* [PhD thesis, Université d'Orléans]. http://www.theses.fr/2013ORLE2022

Sabard, J., Chaumeix, N., & Bentaib, A. (2013). Hydrogen explosion in ITER: Effect of oxygen content on flame propagation of $H_2/O_2/N_2$ mixtures. *Fusion Engineering and Design*, *88*(9–10), 2669–2673. https://doi.org/10.1016/j.fusengdes.2013.02.128

Sabard, J., Goulier, J., Chaumeix, N., Mevel, R., Studer, E., & Bentaib, A. (2012, 22-27 July). *Determination of explosion combustion parameters of $H_2/O_2/N_2$ mixtures*. International Symposium on Hazard, Prevention, and Mitigation of Industrial Explosions, Cracov, Poland.

Sankaran, V., & Menon, S. (2005). Subgrid combustion modeling of 3-D premixed flames in the thin-reaction-zone regime. *Proceedings of the Combustion Institute*, *30*(1), 575–583. https://doi.org/10.1016/j.proci.2004.08.023

Sathiah, P., Komena, E., & Roekaerts, D. (2012). The role of CFD combustion modeling in hydrogen safety management part I: Validation based on small scale experiments. *Nuclear Engineering and Design*, *248*, 93–107. https://doi.org/10.1016/j.nucengdes.2012.03.047

Shamshirband, S., Babanezhad, M., Mosavi, A., Nabipour, N., Hajnal, E., Nadai, L., & Chau, K.-W. (2020). Prediction of flow characteristics in the bubble column reactor by the artificial pheromone-based communication of biological ants. *Engineering Applications of Computational Fluid Mechanics*, *14*(1), 367–378. https://doi.org/10.1080/19942060.2020.1715842

Smirnov, N. N., Nikintin, V. F., Boichenco, A. P., Tyurnikov, M. V., & Baskakov, V. V. (1999). Deflagration-to-detonation transition in gases and its application to pulsed detonation devices. Gaseous and heterogeneous detonations: Science to applications. In G. D. Roy, S. M. Frolov, K. Kailasaath, & N. Smirnov (Eds.), *Gaseous and heterogeneous detonations* (pp. 65–94). ENAS Publishers.

Soto-Meca, A., Serna, J., & Velasco, F. J. S. (2016). Heat and mass transfer enhancement in a double diffusive mixed convection lid cavity under pulsating flow. *Computers and Chemical Engineering*, *94*, 128–140. https://doi.org/10.1016/j.compchemeng.2016.06.018

Stone, C. P., & Bisetti, F. (2014). Comparison of ODE solvers for chemical kinetics and reactive CFD applications. *AIAA SciTech*, 0822. https://doi.org/10.2514/6.2014-0822

Sutherland, W. (1893). The viscosity of gases and molecular force. *Philosophical Magazine*, *36*(223), 507–531. https://doi.org/10.1080/14786449308620508

Toro, E. (1997). *Riemann solvers and numerical methods for fluid dynamics, a practical introduction*. Springer-Verlag.

Troe, J. (1988). Towards a quantitative understanding of elementary combustion reactions. *Proceedings of the Combustion Institute*, *22*(1), 843–862. https://doi.org/10.1016/S0082-0784(89)80094-3

Velasco, F. J. S., Otón-Martínez, R. A., García-Cascales, J. R., Espín, S., Meynet, N., & Bentaib, A. (2016). Modelling detonation of H_2-O_2-N_2 mixtures in presence of solid particles in 3D scenarios. *International Journal of Hydrogen Energy*, *41*(38), 17154–17168. https://doi.org/10.1016/j.ijhydene.2016.06.096

Wallin, S., & Johansson, A. (2000). An explicit algebraic Reynolds stress model for incompressible and compressible turbulent flows. *Journal of Fluid Mechanics*, *403*, 89–132. https://doi.org/10.1017/S0022112099007004

Williams, F. (1985). *Combustion theory* (2nd ed.). Addison-Wesley.

Williams, F. A. (2008). Detailed and reduced chemistry for hydrogen autoignition. *Journal of Loss Prevention in the Process Industries*, *21*(2), 131–135. https://doi.org/10.1016/j.jlp.2007.06.002

Xiang, Z., Yang, S., Xie, S., Li, J., & Ren, H. (2020). Turbulence–chemistry interaction models with finite-rate chemistry and compressibility correction for simulation of supersonic turbulent combustion. *Engineering Applications of Computational Fluid Mechanics*, *14*(1), 1546–1561. https://doi.org/10.1080/19942060.2020.1842248

Yoshizawa, A., & Horiuti, K. (1985). A statistically-derived sub-grid scale kinetic energy model for the Large-Eddy Simulation of turbulent flows. *Journal of the Physical Society of Japan*, *54*(8), 2834–2839. https://doi.org/10.1143/JPSJ.54.2834

6.4 Mathematical modelling of turbulent combustion of two-phase mixtures of gas and solid particles with a Eulerian-Eulerian approach

The numerical modelling of turbulent combustion of H_2-air mixtures with solid graphite particles is a challenging and key issue in many different fields, including industrial combustors, pollutant emissions, solid propellants or accident prediction and mitigation. In this last field, prediction of particle behavior with and without combustion is a key topic in nuclear power plants as well as in fusion reactors such as the *International Thermonuclear Experimental Reactor* (ITER). In this case, the presence of particles might influence the combustion dynamics during a potential accident. Therefore, it is of outmost importance to properly predict the effects of this type of turbulent combustion sequences in presence of solid particles.

Among the technological applications of this combustion scenario it can be cited the ITER "old design" where graphite blanket walls were considered, nuclear safety sequences in presence of H_2, CO and CO_2 and the design of energetic materials for rocket propulsion systems or drag reductions units. In order to be able to include in the computations the effects of this solid graphite particles, an extension of the *Thickened Flame Model* developed for *Large Eddy Simulation* (LES-TFM) for being applicable to multiphase flows have been carried out. This study presents a Eulerian–Eulerian model based on the resolution of the Navier–Stokes equations via LES coupled with a system of *Ordinary Differential Equations* (ODEs) of the detailed chemical kinetics to simulate the combustion of mixtures of gases and particles.

The developed model was applied to predict the transient evolution of turbulent combustion sequences of mixtures of hydrogen, air and graphite particles under low concentration (i.e. highly diluted) conditions. When applied to simulate lab-scale combustion experiments, the results showed a good agreement between experimental and numerical data using a detailed chemical kinetic model. Moreover, the model was able to predict some key experimental tendencies and revealed that the presence of a low concentration of graphite particles (~96 g/m^3) in the scenario influenced the hydrogen combustion dynamics for mixtures of 20% (in volume) of hydrogen in air. Under these conditions, pressure levels reached at the walls of the sphere were increased and the combustion time was shortened. The results also showed the viability of using this kind of a model for obtaining global combustion parameters such as wall pressure evolution with time.

mathematics

MDPI

Article

Mathematical Modelling of Turbulent Combustion of Two-Phase Mixtures of Gas and Solid Particles with a Eulerian–Eulerian Approach: The Case of Hydrogen Combustion in the Presence of Graphite Particles

Francisco Nicolás-Pérez [1], F.J.S. Velasco [2,*], Ramón A. Otón-Martínez [3], José R. García-Cascales [2], Ahmed Bentaib [4] and Nabiha Chaumeix [5]

[1] Lynx Simulations S.L., C/Del Metal 4, 30009 Murcia, Spain; fnperez@lynxsimulations.com
[2] Department of Fluids and Thermal Engineering, Universidad Politécnica de Cartagena, Dr. Fleming s/n, 30202 Cartagena, Spain; jr.garcia@upct.es
[3] Department of Engineering and Applied Techniques, University Centre of Defense at the Spanish Air Force Academy, C/López Peña s/n, 30720 San Javier, Spain; ramon.oton@cud.upct.es
[4] Institut de Radioprotection et Sûrete Nucléaire, 31 Av. de la Division Leclerc, 92260 Fontanay-aux-Roses, France; ahmed.bentaib@irsn.fr
[5] INSIS, CNRS, 1C Avenue de la Recherche Scientifique, 45071 Orléans, France; chaumeix@cnrs-orleans.fr
* Correspondence: fjavier.sanchez@upct.es; Tel.: +34-968-325306

check for updates

Citation: Nicolás-Pérez, F.; Velasco, F.; Otón-Martínez, R.A.; García-Cascales, J.R.; Bentaib, A.; Chaumeix, N. Mathematical Modelling of Turbulent Combustion of Two-Phase Mixtures of Gas and Solid Particles with a Eulerian–Eulerian Approach: The Case of Hydrogen Combustion in the Presence of Graphite Particles. *Mathematics* **2021**, *9*, 2017. https://doi.org/10.3390/math9172017

Academic Editors: Theodore E. Simos and Charampos Tsitouras

Received: 14 July 2021
Accepted: 13 August 2021
Published: 24 August 2021

Abstract: The numerical modelling of turbulent combustion of H_2–air mixtures with solid graphite particles is a challenging and key issue in many industrial problems including nuclear safety. This study presents a Eulerian–Eulerian model based on the resolution of the Navier–Stokes equations via large eddy simulation (LES) coupled with a system of ordinary differential equations (ODEs) of the detailed chemical kinetics to simulate the combustion of mixtures of gases and particles. The model was applied to predict the transient evolution of turbulent combustion sequences of mixtures of hydrogen, air and graphite particles under low concentration conditions. When applied to simulate lab-scale combustion experiments, the results showed a good agreement between experimental and numerical data using a detailed chemical kinetic model. Moreover, the model was able to predict some key experimental tendencies and revealed that the presence of a low concentration of graphite particles (~96 g/m^3) in the scenario influenced the hydrogen combustion dynamics for mixtures of 20% (in volume) of hydrogen in air. Under these conditions, pressure levels reached at the walls of the sphere were increased and the combustion time was shortened. The results also showed the viability of using this kind of a model for obtaining global combustion parameters such as wall pressure evolution with time.

Keywords: turbulent combustion; LES; two-phase flow

1. Introduction

Combustion of gas and particles mixtures is an issue of major interest in many different fields, including industrial combustors [1–3], pollutant emissions [4–6], solid propellants [7–9] or accident prediction and mitigation [10,11]. In this last field, prediction of particle behaviour with and without combustion is a key topic in nuclear power plants [12,13] as well as in fusion reactors such as the International Thermonuclear Experimental Reactor (ITER) [14,15]. In this case, the presence of particles might influence the combustion dynamics during a potential accident [16,17]. Therefore, it is of outmost importance to properly predict the effects of this type of turbulent combustion sequences in presence of solid particles.

Mathematical modelling of turbulent combustion requires a proper description of two key aspects: chemistry and turbulence. Large eddy simulation (LES) is a mathematical

approach that provides a compromise between efficiency in terms of computational costs and detailed physical description of turbulence dynamics [18]. Several models are available for modelling turbulence at the subgrid scale (SGS) with LES. The Smagorinsky–Lilly [19] was the first one. It was developed for flows with homogeneous turbulence conditions. The wall-adapting local eddy model [20] is a common choice in the case of incompressible wall flows whereas the dynamic k_{sgs} equation model has been shown to behave relatively well in compressible flow conditions [21–23]. Regarding chemistry, it is important to use detailed kinetic models in order to predict several mechanisms such as ignition or quenching [24]. This is critical not only in the case of hydrogen combustion [25], but also in the case of other mixtures such as hydrogen and carbon. However, in this case, the number of detailed chemistry models available is still limited. Saxena and Williams [26] proposed a chemical kinetic mechanism for the combustion of hydrogen and carbon monoxide with 13 species and 30 reactions. They showed good results in their testing. Gibeling and Buggein [27] also developed a simplified model for the oxidation mechanism of carbon monoxide in the presence of hydrogen and oxygen. It considered nine species and 12 reactions and was used in propellant applications with satisfactory results. Zhuo et al. [28] also used a chemical kinetic model with eight species and 12 reactions for modelling carbon monoxide oxidation in the presence of hydrogen for propellant applications. In the case of mixtures of gases and particles, Bournot et al. [29] simulated a reactive two-phase flow with aluminium particles for base bleed applications. In this case, the chemistry model was very simple and only considered three species for the gas phase and two species for the particle phase. The turbulent nature of the flow was modelled in a statistical way. The results permitted to identify the global flow regimes of the problem. As for carbon particles, Chelliah et al. [30,31] studied the influence of particle porosity on the combustion of graphite particles in the presence of hydrogen under quasi-steady burning conditions. They relied on the chemical kinetic models proposed by Bradley [32] for nonporous graphite particles and by Yetter et al. [33] for CO–H_2O–O_2. A total of five reactions were considered for the solid carbon phase and 28 for the gas phase. A total of 13 species were considered in the problem. They confirmed the suitability of this kind of kinetic models with a comparison against experimental data. As for the modelling of particle behaviour in a turbulent gas flow, results of direct numerical simulations (DNS) for canonical problems permitted to give credit to less demanding numerical models such as LES. The Eulerian treatment when solving the governing continuum equations for averaged quantities of both phases is still limited with LES and DNS. There are just a few articles that have been devoted to the implementation of the Eulerian two-fluid approach in the framework of DNS or LES [34,35]. Yeh and Lei [36] used LES to investigate the motion of particles in isotropic and homogeneous shear flows. The generated particle-statistics by neglecting the subgrid scale (SGS) effects on particles showed that LES can successfully predict second-order statistics of particle motion. Similar results were obtained by other researchers [37–40].

As previously said, in the case of a combustion sequence within a dust-laden atmosphere in an industrial environment, a mining environment [10] or an accident scenario at a fission nuclear power plant [11] or the ITER fusion reactor [17], the presence of graphite particles might influence a potential hydrogen deflagration [41]. The sequence might degenerate into a dust explosion which might increase the accident impact [17]. Therefore, it is of major importance to properly predict the effects of this type of combustion sequences [41]. Previous works have assessed the effectiveness of LES models to predict the dynamics of premixed turbulent combustion of H_2–air mixtures [23]. In this work, we present a two-phase reacting model based on a Eulerian–Eulerian approach for both the gas and the solid phases. The model includes LES turbulence modelling and detailed kinetic schemes for the combustion chemistry of both the gas and the solid phases. These two approaches are not usually used in two-phase flow models that consider a Eulerian approach of both the gas and the solid phases. We explore the application of this model to a combustion two-phase flow problem with graphite particles in the presence of a premixed H_2–O_2–N_2 atmosphere. As commented above, this scenario is prototypical of several key

industrial and safety problems. Specifically, we focus on the case of sequences in closed three-dimensional (3D) H_2 scenarios and investigate the effect of the presence of a low concentration of graphite dust particles in the combustion sequence. The comparison of combustion experiments from the literature with the numerical simulations permits to face the validation of the mathematical model proposed and evaluate its prediction capabilities. The article is structured as follows: firstly, the physical model and the numerical method used are presented. Later, the model is validated against ad-hoc experimental results obtained in a spherical bomb and the results obtained are discussed. Finally, some conclusions are drawn.

2. Mathematical Equations of the Model

2.1. A Two-Phase Flow Model for Mixtures of Gases and Solid Particles

The two-phase model used in this work relies on the hypothesis of highly diluted mixtures of gas and solid particles and considers a Eulerian–Eulerian approximation of the mass, momentum and energy conservation equations for both the gas phase and the solid phase. The system of equations also includes those corresponding to the concentration of the species of each phase. The gas phase is considered to be an ideal gas initially composed of a mixture of hydrogen and air (i.e., oxygen, nitrogen and argon). The solid phase was initially considered to be a monodisperse distribution of graphite (i.e., carbon, C) particles of 35 micrometres in diameter (Sauter median diameter) and particle density of 2160 kg/m^3. During the combustion process, these species may react and generate additional species that will be detailed in the Combustion Model section.

In this case, the system of conservation equations averaged with the FAVRE approach (filtered local volume average of the equations) [42] was as follows:

$$\begin{array}{l}
\frac{\partial \rho_g}{\partial t} + \vec{\nabla}\cdot\left(\rho_g \vec{u}_g\right) = \Gamma \\
\frac{\partial}{\partial t}\left(\rho_g \vec{u}_g\right) + \vec{\nabla}\cdot\left(\rho_g \vec{u}_g \otimes \vec{u}_g + p\bar{I}\right) = \vec{\nabla}\cdot\bar{\tau} - \vec{F}_d + \Gamma \vec{u}_{\mathrm{p}} \\
\frac{\partial}{\partial t}\left(\rho_g E_g\right) + \vec{\nabla}\cdot\left(\rho_g \vec{u}_g H_g - \vec{\nabla}\cdot\left[\bar{\bar{\tau}}\cdot\vec{u}\right] + \vec{\nabla}\cdot\vec{q}\right) = -\vec{F}_d\cdot\vec{u}_g - \dot{Q}_g + \Gamma E_p + \frac{E_\Delta}{F}\dot{Q}_{g,c} \\
\frac{\partial\left(\rho_g Y_{g,k}\right)}{\partial t} + \nabla\cdot\left(\rho_g Y_{g,k}\vec{u}_g\right) = S\nabla\cdot\left(F E_\Delta \rho_g D \nabla Y_{g,k}\right) + (1-S)\nabla\cdot\left(\rho_g\left(D + D_{sgs}\right)\nabla Y_{g,k}\right) + \frac{E_\Delta}{F}\dot{\omega}_{g,k} \\
\text{with } k = 1, \ldots, \mathrm{NGSP} - 1 \\
\frac{\partial \sigma}{\partial t} + \vec{\nabla}\cdot\left(\sigma \vec{u}_p\right) = -\Gamma \\
\frac{\partial}{\partial t}\left(\sigma \vec{u}_p\right) + \vec{\nabla}\cdot\left(\sigma \vec{u}_p \otimes \vec{u}_p\right) = \vec{F}_d - \Gamma \vec{u}_{\mathrm{p}} \\
\frac{\partial}{\partial t}\left(\sigma E_p\right) + \vec{\nabla}\cdot\left(\sigma \vec{u}_p E_p\right) = \vec{F}_d \vec{u}_p + \dot{Q}_g - \Gamma E_{\mathrm{p}} + \frac{E_\Delta}{F}\dot{Q}_{p,c} \\
\frac{\partial}{\partial t}\left(\sigma Y_{p,k}\right) + \vec{\nabla}\cdot\left(\sigma Y_{p,k}\vec{u}_p\right) = \dot{\omega}_{p,k} \quad k = 1, \ldots, NSSP - 1
\end{array} \tag{1}$$

with

$$\Gamma = \frac{E_\Delta}{F}\sum_{k=1}^{NPSP}\dot{\omega}_{p,\mathrm{k}} = -\frac{E_\Delta}{F}\sum_{k=1}^{NGSP}\dot{\omega}_{g,\mathrm{k}} \tag{2}$$

where the gas mixture is formed by NGSP gases and the solid mixture is formed by NPSP solids. The subscript g indicates variables relating to the gas phase, while the subscript p refers to the solid phase; ρ_g is the average gas density, $\vec{u}_m$ is the velocity of phase m (i.e., gas phase "g" or solid particle phase "p"), $Y_{m,k}$ represents the mass fraction of species k from phase m.

The hypothesis of a highly diluted mixture implies that void fraction (α) could be assumed to be near unity ($\alpha \approx 1$). Therefore, the concentration of particles is defined by $\sigma = \rho_g(1-\alpha)$. E_m and H_m indicate, respectively, the total internal energy and the total enthalpy of phase m (where "m" can be solid phase "p" or gas phase "g"). Mass fractions

are defined so that if $NGSP$ is the number of components of the gas mixture and $NSSP$ is the number of solid species, the following relations are fulfilled:

$$\sum_{k=1}^{NGSP} Y_{g,\mathrm{k}} = 1; \quad \sum_{k=1}^{NSSP} Y_{p,k} = 1 \tag{3}$$

Note that $\overline{\overline{\tau}}$ represents the stress tensor and includes the turbulent (subgrid) stress terms, $\vec{q}$ is the heat flux vector, Y_k is the mass fraction of species k, $\dot{\omega}_k$ is the reaction rate of the k species and D_k is the diffusion term of species k. Note that the expression of the species conservation equations includes the terms of the thickened flame model (TFM) used for modelling the turbulent combustion mechanism. These terms are explained in detail in the Combustion Model section of this work. Similarly, the energy conservation equation of the gas phase also includes the corresponding terms of the TFM in the transport terms (i.e., $\vec{\nabla}\cdot[\overline{\overline{\tau}}\cdot\vec{u}] + \vec{\nabla}\cdot\vec{q}$) in order to properly account for the heat and diffusion process in the turbulent combustion model.

$\dot{Q}_c$ is the heat released per unit of volume and time due to the chemical reactions, which is defined as follows:

$$\dot{Q}_{g,c} = \sum_{k=1}^{NGSP} \dot{\omega}_{g,\mathrm{k}}\cdot\Delta H_{fg,\mathrm{k}}; \quad \dot{Q}_{p,c} = \sum_{k=1}^{NSSP} \Delta H_{p,\mathrm{k}}. \tag{4}$$

where $\Delta H_{fm,\mathrm{k}}$ is the formation heat of species k.

In the model, the pressure effect on the solid phase is negligible and, therefore, solid particles can be considered to be incompressible. The gas–particle interaction was taken into account through source terms in the mass, momentum and energy equations. $\vec{F}_d$ is the gas–particle drag force, $\dot{Q}_g$ is the interfacial heat transfer rate, Γ stands for the total mass exchange between phases, $\dot{\omega}_{m,k}$—for the species reaction rates. In the present approach, particle size was considered to be constant. This means that the model does not consider the change of particle diameter during the combustion process.

The equation of the state considered for the gas phase was as follows:

$$\mathrm{p} = \rho\left(\sum_{\mathrm{k}=1}^{NGSP} Y_\mathrm{k}\frac{R_\mathrm{u}}{M_\mathrm{k}}\right)\mathrm{T} \tag{5}$$

where p denotes gas pressure, T—the gas temperature, R_u—the universal constant, M_k—the specific molar mass of the species k. Specific heats are temperature-dependent following the database by McBride et al. [43] and dynamic viscosity was considered to be temperature-dependent through Sutherland's formula [44]:

$$\mu = A_S\frac{T^{1/2}}{(1+T_S/T)} \tag{6}$$

Closure Equations for the Interphase Transport

The momentum exchange between the gas phase and the solid phase was taken into account by considering the drag force acting on a particle:

$$\vec{F}_d = \frac{1}{2}\rho_g C_d A\left|\vec{u}_g - \vec{u}_p\right|\left(\vec{u}_g - \vec{u}_p\right) \tag{7}$$

where C_d is the drag coefficient which is a function of the particle Reynolds number $\mathrm{Re_p}$ and A are the representative area of the particle [45]. Considering that the number of particles is σ/m_p, where m_p is the mass of a particle, and assuming spherical particles [46], the previous equation can be expressed as follows:

$$\vec{F}_d = \frac{3\sigma}{4d_p\rho_p}\rho_g C_d \left|\vec{u}_g - \vec{u}_p\right|\left(\vec{u}_g - \vec{u}_p\right) \quad (8)$$

The expression adopted in this work for the drag coefficient C_d is the one proposed by Otterman and Levine [47] and used by Miura and Glass [48] in their work:

$$C_d = 0.48 + 28\mathrm{Re_p}^{-0.85} \quad (9)$$

where the Reynolds number for particles $Re_p = \frac{\rho_g d_p \left|\vec{u}_g - \vec{u}_p\right|}{\mu_g}$. The rate of the heat transferred from the gas to a particle at its surface, $\dot{Q}_g$, is as follows:

$$\dot{Q}_g = -\frac{\sigma}{m_p}\pi d_p \mu_g c_{pg} \mathrm{Pr}^{-1}(T_g - T_p)\mathrm{Nu} \quad (10)$$

where the Nusselt number (Nu) can be calculated as follows:

$$\mathrm{Nu} = 2 + 0.6\mathrm{Pr}^{\frac{1}{3}}\mathrm{Re}^{\frac{1}{2}} \quad (11)$$

where Re is the gas Reynolds number, Pr—Prandtl number. This equation is valid for Re $\leq$ 50,000 according to Crowe et al. [45]. It was originally proposed by Knudsen and Katz [49] and has been used by different authors [47,48].

2.2. Model of the Chemical Kinetics

In order to evaluate precisely the rates of the chemical reactions present in the problem, a system of 33 ordinary differential equations (ODE) is considered and numerically solved to calculate the concentration of the different species at each timestep. In this work, the detailed chemical kinetics model used by Chelliah [30,31] was considered to describe the combustion of H_2 and solid carbon (C) in the presence of air. It was based on the chemical kinetic models proposed by Bradley [32] for nonporous graphite particles and Yetter et al. [33] for CO–H_2O–O_2. The model considered the following reactive species: C, CO, CO_2, HCO, H_2, H, O_2, O, OH, H_2O, H_2O_2 and HO_2. In accordance with the chemical kinetic models of Chelliah [30,31] and Yetter et al. [33] that were adopted in this work, it has been considered that atmospheric N_2 and Ar are nonreacting species that do not intervene in any of the reactions and do not undergo any oxidation process. This was done to maintain the integrity of the chemical models, without making any modifications that could alter their validity.

A total of five reactions were considered for the solid carbon phase (Table 1). Two different mechanisms were tested in this study. One considered semiglobal heterogeneous surface reactions for nonporous graphite particles (Table 1a). The other considered semiglobal heterogeneous surface reactions for porous graphite particles (Table 1b). The mechanisms assumed that the primary product was CO and that each rate w < s independent of the others. The first assumption is known to be reasonable for high-temperature oxidation of graphite (i.e., temperature at the particle surface over 800 K) [50]. Note that in Table 1a, the rate $\dot{s_i}$ is expressed in terms of $k_i = A_i T^{\alpha i} \exp(-E_i/RT)$, the partial pressure P_j is in Pa, T—in degrees Kelvin, whereas in Table 1b, the rate $\dot{s_i}$ is expressed in terms of $\dot{s_i} = W_i\, c_i\, B_i T^{\alpha i} \exp(-E_i/RT)$ in kg/m^2/s. In this formula, $B_i T^{\alpha i}$ is in m/s, T—in degrees Kelvin. The gas phase homogeneous reaction mechanism of CO oxidation in the presence of H_2O considered here is the one proposed by Yetter et al. [33]. It consists of 12 species in 28 elementary reactions (Table 2). The rate constants for this mechanism were validated for a wide range of temperatures, pressures and reactant concentrations using shock tubes and flow reactor measurements. Following Yetter et al. [33], for high-temperature oxidation of CO, the non-Arrhenius rates recommended for reaction steps 4 and 22 were implemented.

Table 1. (**a**) Heterogenous rate constants for nonporous graphite oxidation (from Chelliah [30]). (**b**) Heterogenous rate constants for porous graphite oxidation (from Chelliah [30]). Here, $\dot{s}_i = W_i c_i B_i T^{\alpha_i} \exp(-E_i/RT)$ in kg/m^2/s.

(a)

Reaction	i	A_i [(1)]	α_i	E_i (J/kmol)	$\dot{s_i}$ (kg/m^2/s)
C+OH→CO+H	1	3.56×10^{-3}	−0.5	0.0	$\dot{s_1} = k_1 P_{OH}$
C+O→CO	2	6.56×10^{-3}	−0.5	0.0	$\dot{s_2} = k_2 P_O$
C+H_2O→CO+H_2	3	4.74	0.0	2.878592×10^8	$\dot{s_3} = k_3 P_{H_2O}^{0.5}$
C+CO_2→2CO	4	8.88×10^{-2}	0.0	2.849304×10^8	$\dot{s_4} = k_4 P_{CO_2}^{0.5}$
C+(1/2)O_2→CO	5	2.37×10^{-2}	0.0	1.255200×10^8	$\dot{s_5} = \left\{ \frac{k_5 Y \cdot P_{O_2}}{1+k_6 P_{O_2}} + k_7 P_{O_2}(1-Y) \right\}$
	6	2.10×10^{-4}	0.0	-1.715440×10^7	
	7	5.28×10^{-4}	0.0	6.359680×10^7	where $Y = \left[1 + \frac{k_8}{k_7 P_{O_2}}\right]^{-1}$
	8	1.79×10^2	0.0	4.058480×10^8	

(b)

Reaction	i	B_i [(1)]	α_i	E_i (J/kmol)
C+OH→CO+H	9	1.65	0.5	0.0
C+O→CO	10	3.41	0.5	0.0
C+H_2O→CO+H_2	11	6.00×10^7	0.0	2.690312×10^8
C+CO_2→2CO	12	6.0×10^7	0.0	2.690312×10^8
2C+O_2→2CO	13	2.2×10^6	0.0	1.799120×10^8

(a) [(1)] The values of A_i are in SI units: partial pressures are in Pa, $\dot{s}_i$ is in kg/(m^2·s); α_i is dimensionless. **(b)** [(1)] Units of $B_i \cdot T^{\alpha_i}$ are s/m, and α_i is dimensionless.

For the species k, the total mass reaction rate $\dot{\omega}_k$ was defined as the contribution of all reactions:

$$\dot{\omega_k} = \sum_{i=1}^{NR} \dot{\omega_{k,i}} \delta_{k,i} \tag{12}$$

where NR is the number of reactions. The Kronecker delta $\delta_{k,i}$ permits to take into account the reaction rate if species k was involved in reaction i. Finally, the heat released by the chemical reactions was modelled by the term $\dot{Q}$, which included the contributions of all the reactions. It was defined as follows:

$$\dot{Q} = -\sum_{i=1}^{NGSP} \dot{\omega_i} H_{fm,i} \tag{13}$$

where $\Delta H_{fm,i}$ is the heat of formation of species i.

2.3. A Detailed Turbulence Model

In order to describe the turbulence phenomena during the combustion in a realistic way in the model, LES approach was considered in this work. LES models make use of the filtered local volume-averaged conservation equations (FAVRE approach) [42] to solve the flow field, being the small-scale stresses solved with a subgrid-scale model [20] due to the low dependence of these scales on the geometry. In particular, the LES dynamic subgrid-scale kinetic energy model (LES k_{sgs} Eqn.) was used [21] in this work. This model was specially designed for compressible flows. In this model, the subgrid turbulent kinetic energy (k_{sgs}) is defined as followed:

$$k_{sgs} = \frac{1}{2}(\overline{u_k u_k} - \overline{u}_k \overline{u}_k) \tag{14}$$

It is calculated making use of the transport equation:

$$\rho \frac{\partial \bar{k}_{sgs}}{\partial t} + \rho \frac{\partial \overline{u}_j \bar{k}_{sgs}}{\partial x_j} = -\tau_{ij} \frac{\partial \overline{u}_i}{\partial x_j} - C_\varepsilon \rho \frac{{k_{sgs}}^{3/2}}{\Delta_f} + \frac{\partial}{\partial x_j}\left(\frac{\mu_t}{\sigma_k} \frac{\partial k_{sgs}}{\partial x_j}\right) \tag{15}$$

The subgrid-scale eddy viscosity is modelled as follows:

$$\mu_t = C_k \rho {k_{sgs}}^{1/2} V^{1/3} \tag{16}$$

where C_k is a constant and $V^{1/3}$ is the local grid scale calculated from the cell volume V in each cell as $V = (\Delta x \Delta y \Delta z)$ for inhomogeneous grids. The subgrid-scale turbulent stress tensor is calculated as follows:

$$\tau_{ij} - \frac{2}{3} k_{sgs} \delta_{ij} = -2 C_k {k_{sgs}}^{1/2} V^{1/3} \, dev\left(\overline{S_{ij}}\right) \tag{17}$$

where $dev\left(\overline{S_{ij}}\right)$ is the deviatoric component of the rate-of-strain tensor for the resolved scales. This way, the model relates the subgrid-scale stresses τ_{ij} to the large-scale strain-rate tensor $\overline{S_{ij}}$. This LES model showed good results when dealing with compressible flows [22] and gas reacting flows [18].

Table 2. Homogeneous rate constants of the $CO/H_2O/O_2$ reaction mechanism (from Chelliah, Chelliah et al. and Yetter et al. [30,31,33]) in the form $k_i = B_i T^{\alpha_i} \exp(-E_i/RT)$. Units are J, kmol, cm and K.

Step	Reaction	B_i [b]	α_i [b]	E_i (J/kmol)
1	$H + O_2 = OH + O$	1.91×10^{14}	0.0	68,784,960
2	$H_2 + O = OH + H$	5.13×10^{4}	2.67	26,317,360
3	$H_2 + OH = H_2O + H$	2.14×10^{8}	1.51	14,351,120
4	$OH + OH = O + H_2O$	$k = 5.46 \times 10^{11}$	x	exp (0.00149·T)
5	$H_2 + M = H + H + M$ [a]	4.57×10^{19}	−1.4	436,725,920
6	$O + O + M = O_2 + M$ [a]	6.17×10^{15}	−0.5	0
7	$H + O + M = OH + M$ [a]	4.68×10^{18}	−1.0	0
8	$H + OH + M = H_2O + M$ [a]	2.24×10^{22}	−2.0	0
9	$H + O_2 + M = HO_2 + M$ [a]	4.76×10^{19}	−1.42	0
10	$HO_2 + H = H_2 + O_2$	6.61×10^{13}	0.0	8,911,920
11	$HO_2 + H = OH + OH$	17.0×10^{14}	0.0	3,640,080
12	$HO_2 + O = OH + O_2$	1.74×10^{13}	0.0	−1,673,600
13	$HO_2 + OH = H_2O + O_2$	1.45×10^{16}	−1.0	0
14	$HO_2 + HO_2 = H_2O_2 + O_2$	3.02×10^{12}	0.0	5,815,760
15	$H_2O_2 + M = OH + OH + M$ [a]	1.20×10^{17}	0.0	190,372,000
16	$H_2O_2 + H = H_2O + OH$	1.00×10^{13}	0.0	15,020,560
17	$H_2O_2 + H = HO_2 + H_2$	4.79×10^{13}	0.0	33,262,800
18	$H_2O_2 + O = HO_2 + OH$	9.55×10^{6}	2.0	16,610,480
19	$H_2O_2 + OH = H_2O + HO_2$	7.08×10^{12}	0.0	5,983,120
20	$CO + O + M = CO_2 + M$ [a]	2.51×10^{13}	0.0	−18,995,360
21	$CO + O_2 = CO_2 + H$	2.51×10^{12}	0.0	199,534,960
22	$CO + OH = CO_2 + O$	$K = 6.75 \times 10^{10}$	x	exp(0.000907·T)
23	$CO + HO_2 = CO_2 + OH$	6.03×10^{13}	0.0	96,022,800
24	$HCO + M = CO + H + M$ [a]	1.86×10^{17}	−1.0	71,128,000
25	$HCO + H = CO + H_2$	7.24×10^{13}	0.0	0
26	$HCO + O = CO + OH$	3.02×10^{13}	0.0	0
27	$HCO + OH = CO + H_2O$	3.02×10^{13}	0.0	0
28	$HCO + O_2 = CO + HO_2$	4.17×10^{12}	0.0	0

[a] The third-body efficiencies are H_2: 2.5, H_2O: 12.0, CO_2: 3.8, CO: 1.9. [b] Units of $B_i \cdot T^{\alpha_i}$ are s/cm, and α_i is dimensionless.

2.4. The Turbulent Combustion Model

The modelling of the combustion mechanism under the turbulent regime is a challenging physical problem that usually requires high computational costs as it must solve different time and spatial scales of a turbulent flame. In this work, the model chosen for modelling the turbulent combustion was the artificially thickened flame model (TFM). This model introduces an F factor in the energy and species equations of the gas phase

that affects the thermal and molecular diffusivities (see Equation (1)). On the one hand, the F factor multiplies the pre-exponential factor of the kinetic equations; this permits to decrease the reaction rates by that factor. On the other hand, it increases the molecular diffusivity by the same factor. As the laminar flame speed is proportional to both magnitudes ($S_u \propto \sqrt{D\dot{\omega}}$), the model provides a flame which propagates at the same speed. Besides, the modelled flame is F times thicker as the laminar flame thickness is a function of $\left(\delta_L^0 \propto \sqrt{D/\dot{\omega}}\right)$. This way, the computational requirements of the mathematical model are relaxed, and less demanding grid sizes are required [51]. However, this approach modifies the physics of flame propagation since the Damköhler number is reduce [52]. This drawback is solved by taking into account the efficiency function E_Δ that takes into account the actual wrinkling of a turbulent flame by introducing subgrid wrinkling of the modelled flame. In this study, we used the efficiency function proposed by Charlette [53,54]. This function was calculated as follows:

$$E_\Delta = \left(1 + min\left[\frac{\Delta}{\delta_L^0} - 1,\ 0\right] \cdot \Gamma_\Delta\left(\frac{\Delta}{\delta_L^0}, \frac{u'_\Delta}{S_L^0}, Re_\Delta\right) \frac{u'_\Delta}{S_L^0}\right)^\beta \tag{18}$$

where $\Gamma_\Delta\left(\frac{\Delta}{\delta_L^0}, \frac{u'_\Delta}{S_L^0}, Re_\Delta\right)$ is a function of the turbulent intensity u'_Δ at the scale of the test filter scale Δ, the subgrid-scale turbulent Reynolds Re_Δ and the laminar flame thickness δ_L^0. The subgrid-scale turbulence intensity u'_Δ was obtained from the obtained velocity resolved at the Δ_{mesh} scale as $u'_\Delta = C_2 {\Delta_{mesh}}^3 \left|\nabla^2(\nabla \times \widetilde{\boldsymbol{u}})\right| \left(\frac{\Delta}{10 * \Delta_{mesh}}\right)^{1/3}$, with $C_2 = 2$. The Reynolds number at the subgrid scale was estimated as follows: $Re_\Delta = \frac{u'_\Delta \Delta}{\nu}$. The flame laminar flame thickness at each cell was estimated following Charlette [53] procedure with the relationship $\delta_L^0 \approx \frac{4 \cdot \nu}{S_L^0}$. Regarding the exponential factor, in this work, we used the fixed value of $\beta = 0.5$ proposed by Charlette [53].

3. Numerical Methods

The finite volume approach was used to numerically solve the system of equations. After testing different numerical integration strategies, the numerical procedure that provided the best results was selected for the validation of the model. The numerical schemes chosen were AUSMup-HLLC Low Mach [55–57], Godunov Scheme for the gas phase and a flux-difference splitting scheme (Rusanov) [58] for the particle phase, both with a Van-Leer [59] TVD scheme. Time integration was performed with the classical four-stage Runge–Kutta scheme for the fluxes, inter-phase, turbulent and chemistry source terms. Thus, the fluxes and source terms involved in each transport equation were evaluated in multiple substeps per each fluid-convection timestep. Primitive variables were then reevaluated from the intermediate conservative variables evaluated for each Runge–Kutta slope evaluation substep. Fluxes, diffusive terms and source terms were then recalculated from the corresponding intermediate primitive values. Although a higher number of operations per timestep is needed, this scheme permitted to set a higher CFL number with a more stable fluid flow behavior during the simulation, avoiding the presence of numerical instabilities that might be encountered in the simulation results [7].

A second-order linear Gauss scheme was considered for spatial discretization, including gradient, divergence and Laplacian calculations. This numerical strategy was previously tested for hydrogen premixed turbulent combustion problems with good results [23]. Regarding the solid phase, a Rusanov scheme [58] was used to evaluate the convective fluxes in the conservation equations of the solid phase. This approach was previously validated for gas–particle combustion problems [7,8,14,16,17].

The integration of the ODE equation corresponding to chemistry source terms was a stiff problem difficult to solve in a cost-efficient way. After testing different strategies, an in situ adaptive tabulation method (ISAT) with ODE(SEULEX) integration [60,61] was used to solve the system of equations of the chemical kinetics of the gas phase and to estimate the

reaction rate of the k^{th} species in the i^{th} reaction ($\dot{\omega}_{k,i}$). ISAT is a method originally proposed for turbulent reacting flow simulations [60]. This method aims to approximate non-linear system solutions by means of a set of linear regressions of independent variables from a lookup tabulated database constructed dynamically with previous solutions (storage and retrieval method). Thus, it permits to reduce the number of ODE integrations for the chemistry set of ODE equations, being in the problem analyzed in this work one of the most computation-demanding tasks per integrated timestep. It has been reported that using this technique allows, under certain conditions, decreasing by three orders of magnitude the computer time required to compute the detailed chemistry in reacting flow computations [60]. This algorithm has been successfully applied in combustion chemistry problems involving up to 50 species [62] and was also used for premixed H_2–air combustion with detailed kinetics and LES–TFM modelling, similar approaches to the presented in this work [23,63]. A relative tolerance of 10^{-4} was set as the threshold for retraining the tabulated dataset. It is worth mentioning that this method is being extended to the applications other than the initially intended, especially for real-time predictive control [64] as an alternative to neural networks since it presents some advantages, e.g., it does not need training data before use.

The SEULEX ODE integration consists of a semi-explicit multistep method based on numerical extrapolation. An absolute tolerance 10^{-9} has been set, limiting to 1000 the maximum number of iterations per chemical gas integration.

Regarding the particle phase, a first-order implicit Euler scheme was used to integrate the chemistry equations with good results. Reaction rates for each timestep were evaluated using a sub-timestep (chemical timestep) in which each reaction rate for a given species and reaction is updated by the previous sub-timestep species concentrations. The temperatures used for evaluating the reaction rates were also updated from the last sub-timestep. An initial timestep of 10^{-12} s was set, thus avoiding numerical fluctuations and divergences that may lead to nonphysical results.

4. Results and Discussion

In the previous section, a two-phase flow model for turbulent combustion of gas and particles mixtures was presented. The use of LES, TFM and detailed kinetic schemes was explored as a way to take into account a realistic description of turbulence, flame wrinkling and reaction mechanisms in the turbulent combustion process. In order to validate the present model and evaluate its prediction capabilities, the experimental results from combustion tests presented by Sabard and Sabard et al. [65,66] were used as a reference benchmark. These experiments were performed at CNRS Orleans (France) and assessed the combustion of gas mixtures of H_2–O_2–N_2 and graphite (carbon) particles in a spherical bomb. The experimental facility consists of a spherical bomb with the internal radius of 125 mm equipped with different instrumentation including piezo-resistive wall pressure sensors, a Schlieren system, an electrical (spark) ignition system as well as a laser-induced ignition system (Figure 1). A detailed description of the experimental setup and methodology can be found in the works by Sabard and Sabard et al. [65–67]. During the experiments, different concentrations of C, H_2 and O_2 were introduced in the spherical bomb. The uncertainty in the volumetric composition of the gas mixture was below 0.3%, whereas the wall pressure measurements obtained had an experimental uncertainty smaller than 2%. The ignition of the mixture was generated with an electric spark between two electrodes. The initial pressure and temperature within the sphere were 1 bar and 298 K, respectively. The experimental conditions of the tests were as follows:

- Experiment 1 (C-EXP1): N_2/O_2 3.76 and 20% H_2. Graphite powder concentration C(solid) = 94.1 g/m^3;
- Experiment 2 (C-EXP2): N_2/O_2 2.33 and 20% H_2. Graphite powder concentration C(solid) = 96.6 g/m^3.

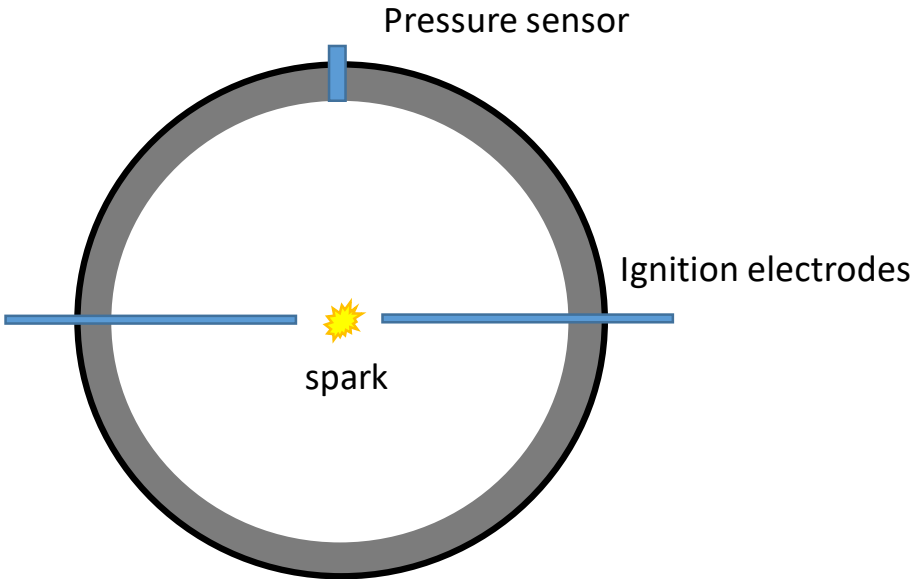

Figure 1. Sketch of the spherical bomb ignition system and a wall pressure sensor.

These experiments were simulated with the model presented in the previous section. The numerical domain defined for the simulations consists of an eighth part of a sphere with the radius of 125 mm. Thus, three different symmetry planes were considered. A grid sensitivity study was performed in order to check the potential influence of the spatial discretization simulated on the results. The results showed that there was a small influence of discretization in the radial direction when the mesh size was under 125 μm (i.e., 1000 radial elements). Independency of the opening angle was also assessed, reporting less than 0.3% in the variation of the maximum pressure and less than 0.115 ms differences in the rising time between the meshes with different angles. The final mesh size of 125 microns was used. Finer meshes had no influence on the chemistry mechanism and fluid fields. Regarding the initiation, it was assumed that an autoignition of the mixture which affected a small sphere with the radius of 2.5 mm initiated the sequence. This initiation was modelled as an addition of energy of 850 kJ/m^3 applied to the ignition volume in 0.1 ms. This quantity of energy was enough to initiate a laminar flame in the domain.

The results of the experimental benchmark of the two-phase model are presented in Figure 2. The figure shows a comparison of the model prediction of pressure evolution at the wall of the spherical bomb with time with the experimental data obtained in Experiment 1 and Experiment 2. For the sake of comparison, an experiment performed without particles (called in the figure H-EXP2) was also included [66,67]. Its conditions were similar to Experiment 2 except for the presence of particles.

As shown, the two-phase approach proposed with LES and a detailed chemistry kinetic model was able to predict with good results the pressure evolution with time including the fast pressure rise found at the wall between 10 and 20 ms. As indicated in Table 3, the model permitted to predict the maximum wall pressure (P_{max}) and the time lapsed to reach the maximum pressure (t_{rise}) with the relative error of 3.3% and 20.8%, respectively, for Experiment 1 and 7.8% (in P_{max}) and 18.2% (in t_{rise}) for Experiment 2. Taking into account the uncertainties linked with the ignition process (which are of the milliseconds order), the prediction of the time locus of the maximum pressure by the model could be considered satisfactory.

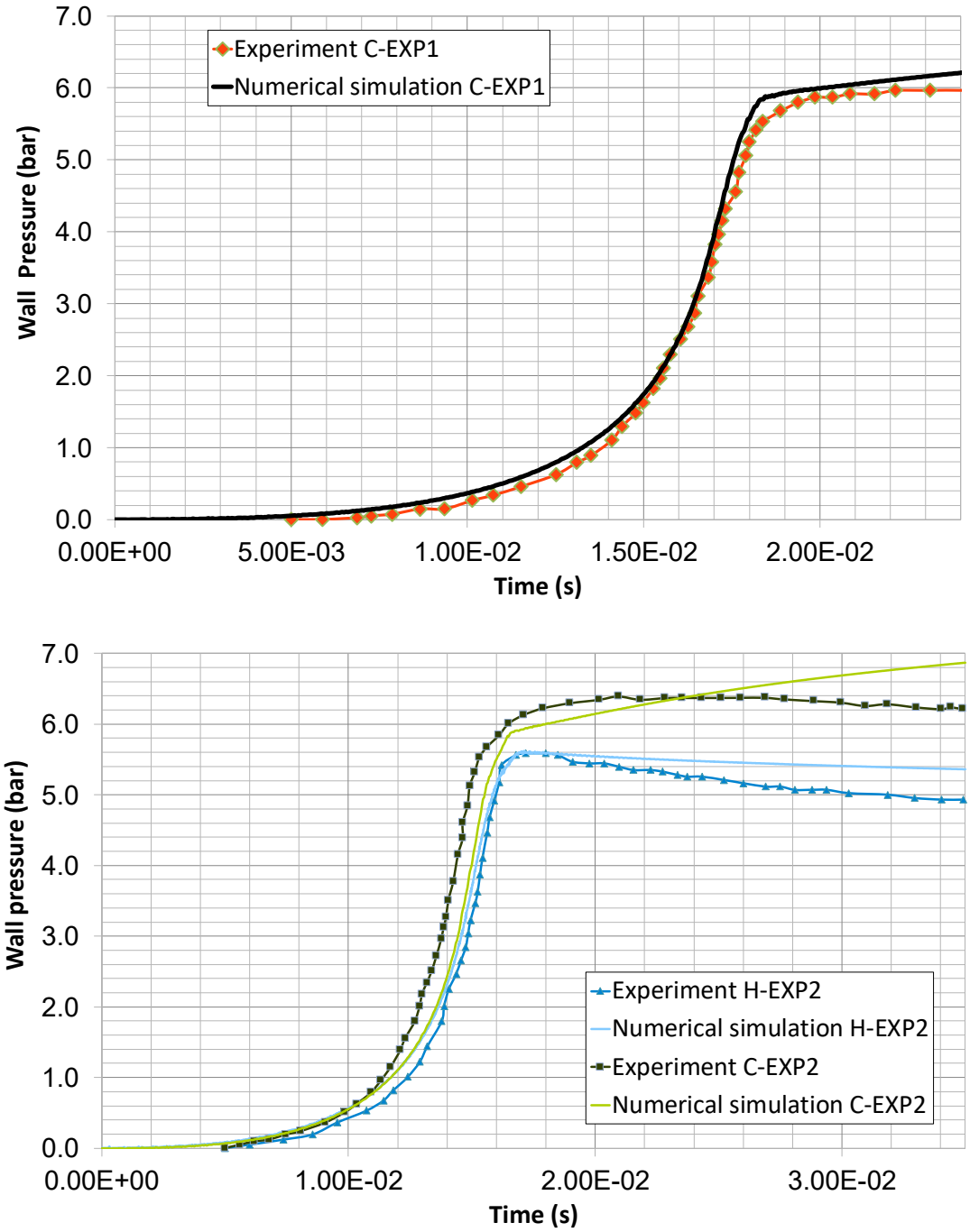

Figure 2. Wall pressure evolution as a function of time. Comparison of numerical and experimental results for Experiment 1 (C-EXP1) (**up**) and Experiment 2 (C-EXP2) (**down**). "Wall pressure" represents relative pressure with respect to the atmospheric pressure.

Table 3. Comparison of the two-phase model prediction with experimental data. Prediction of the peak pressure and time of pressure rise.

Experiment 1	Experimental	Two-phase Model	Experiment 2	Experimental	Two-phase Model
P_{max} (bar)	6.0	6.2	P_{max} (bar)	6.4	6.9
Error, P_{max} (%)	-	3.3	Error, P_{max} (%)	-	7.8
t_{rise} (ms)	24.0	19.0	t_{rise} (ms)	20.9	17.1
Error, t_{rise} (%)	-	20.8	Error, t_{rise} (%)	-	18.2

The model's capacity to predict particle concentration effect on the combustion sequence can also be assessed by taking into account C-EXP2 and H-EXP2. As shown in Figure 2 (down), the model was able to predict the reduction of the maximum wall pressure when the particle concentration was reduced to zero. The model also showed a slight time displacement of the curve when the particle concentration was reduced. This displacement resulted in the increase of the combustion time but with approximately the same dP/dt. This experimental tendency was also well-captured by the model qualitatively. However, the experimental increase of the combustion time was larger than the one predicted by the model.

In general terms, Figure 2 shows a good agreement of the model with the experimental data. The main deviations between the simulations and the experiments are related to the final stage of the combustion process (i.e., for $t > 20$ ms) when the pressure level reached is maintained. These deviations can be related to the uncertainty found in the chemical model at high temperatures and to the influence of the graphite particle size. Therefore, the range of applicability of this model can be set on the basis of the conditions used in the validation, that is, H_2 concentration in the air of 20% for mixtures of N_2/O_2 between 2.33 and 3.76 at the initial ambient pressure and temperature, graphite particle size of the order of 35 microns and particle concentration between 0 and 97 g/m^3.

As for the prediction of the combustion products, Table 4 shows a comparison of the concentration of CO percentage in the combustion products estimated by this model and the one experimentally measured in the test C-EXP1 and C-EXP2 [66,67]. The table also includes the numerical prediction estimated with the Cosilab software for the same tests [66]. The results also permitted to compare the effect of different modelling approaches in the oxidation mechanism considered in the solid phase (porous vs. nonporous approximation). As shown, the mathematical model presented in this study provided better predictions of the CO composition in the combustion products than the Cosilab software in the case of both porous and nonporous modelling approaches. The table shows a good estimation of the porous model proposed, with deviations of less than 1.5% in the prediction of the volumetric percentage of CO in the combustion products and less than 0.1% in the case of the nonporous approach, whereas Cosilab provided a minimum deviation of 11%. The porous model provided results slightly closer to the experiments than the nonporous model in the prediction of gas combustion products. The comparison of the simulation results with both kinetic models (porous and nonporous) and its comparison with the experimental data of C-EXP1 and C-EXP2 also highlighted that the actual particle porosity was an important factor to predict transient subproducts of the combustion sequence. In fact, the consideration of the porous or the nonporous chemical kinetics model resulted in differences in the reaction rates of two order of magnitude. For example, in the case of the reactions $C + 0.5\ O_2 \rightarrow CO$ and $C + CO_2 \rightarrow 2\ CO$, there were found differences of the order of 100 between both models. This was somehow expected as the particle porosity is directly linked to the actual effective particle surface which is directly linked to the reaction rates of the solid phase (Table 1). However, the actual particle porosity in industrial and safety problems commented upon above is usually unknown and must be considered from the practical point of view as an uncertainty factor of the model. All in all, it has to be remarked that regarding the prediction of P_{max} and t_{rise} both, the porous and nonporous chemical kinetics models presented the similar behaviour without remarkable quantitative differences in the dynamic evolution of wall pressure with time.

As for the applications of this model, it can be used to evaluate the efficiency of different strategies for tuning the products of the H_2–graphite combustion process to the desired conditions depending on the context.

In the nuclear safety context, a reduction of the combustion velocity and/or a quenching of the combustion process would be desirable. In this case, the strategy was to reduce the concentration of H_2 and/or O_2 in the scenario by promoting catalytic recombination that would reduce the probabilities of the deflagration-to-detonation transition. Under these circumstances, passive autocatalytic recombiners (PARs) are used to promote the

reaction $H_2 + O_2 \rightarrow H_2O$. In this case, there are undesirable subproducts in the H_2–graphite combustion whose concentration should be reduced to the minimum possible in order to avoid the poisoning of the catalyser. Specifically, because of the large sticking coefficient of CO compared to the other adsorbed species within a PAR and its high activation energy for desorption, the presence of CO in the mixture would poison the catalytic surface; this would prevent the desired recombination reaction in the PAR from occurring [68]. Besides, the lean limit concentration of hydrogen combustion decreases as the CO concentration increases and the flammable region widens for H_2–CO mixtures. Thus, CO is an undesirable by-product in the overall reaction [69]. Thus, in the safety context, the present model could be a useful tool to evaluate by means of numerical simulation the efficiency of different strategies used to mitigate the potential hazard during an accident sequence. For example, it can be applied in the prediction of accident sequences in ITER or in containment buildings of nuclear power plants, to adjust the parameters of mitigation systems such as N_2 injectors or passive autocatalytic recombiners.

In the industrial context, this numerical model can be applied in syngas combustors to evaluate potential strategies to reduce the concentration of H_2, CO and solid C at the exit of the combustor. For example, the development of IGCC technologies, involving gas-turbine combustion of syngas, derived, for instance, from air or O_2 gasification of pulverized coal, has recently promoted interest in studies of CO/H_2 combustion. In this case, this numerical model can be used to improve the efficiency of these combustors by predicting quenching, flame acceleration and/or spatial regions where the combustion process is inefficient and might lead to an increase in undesirable by-products.

Table 4. Comparison of the prediction of species concentration (%mol) in combustion gas products. Numerical prediction, experiments and the present model.

Experiment and Combustion Product Considered	COSILAB Numerical Prediction of the Combustion Products Considered (%mol) [66]	Experimental Measurements of the Combustion Products (%mol) [66]	Present Study: Two-Phase Model with the Porous Approach; (%mol) Prediction in Combustion Products	Present Study: Two-Phase Model with the Nonporous Approach; (%mol) Prediction in Combustion Products
Experiment 1, CO	15.44%	0%	0.22%	<0.0001%
Experiment 2, CO	11.57%	0%	1.46%	-
Experiment 1, H_2O	10.76%	22.26%	20.77%	21.98%
Experiment 2, H_2O	16.49%	22.29%	19.26%	-
Experiment 1, CO_2	3.16%	4.34%	3.48%	0.012%
Experiment 2, CO_2	8.23%	6.08%	5.26%	-

5. Conclusions

In this work, we presented a numerical model for describing the turbulent combustion of two-phase flow mixtures of gas and particles. Specifically, we analysed the influence of the presence of solid carbon particles in the turbulent combustion of an H_2–air atmosphere. A two-phase model was proposed to describe this reacting flow with LES and detailed chemistry. The model proposed was benchmarked against experimental combustion data obtained in a spherical bomb. The results highlighted some significant specifics:

- In case of highly diluted mixtures of H_2–air and graphite particles, the benchmarked results showed that LES with a detailed chemistry model were found to be an appropriate engineering approach for analysing premixed turbulent combustion of graphite–H_2 mixtures.
- The validation against the experimental data show that the two-phase approach used in the present model based on the Eulerian–Eulerian approach seems to be accurate enough to afford this type of combustion sequences with highly diluted mixtures.
- Under the conditions studied, the model captured well the key tendencies linked to the presence of carbon particles of the microns order. In this sense, the model was able to predict that the presence of a low concentration of carbon particles (of the order of

96 g/m^3) accelerated the combustion sequence, obtaining smaller combustion times than in the absence of particles and larger maximum wall pressure levels (of the order of 15%).

- Classical graphite and hydrogen detailed oxidation mechanisms [30,31,33] coupled with a Eulerian–Eulerian model provided good results in the prediction of combustion products under turbulent combustion conditions. Regarding graphite combustion, the porous oxidation model provided results closer to the experiments than the non-porous model.

Future work will face the extension of this model to other metal particles such as tungsten and to engineering applications of hydrogen turbulent combustion sequences.

Author Contributions: Literature survey, F.J.S.V. and R.A.O.-M.; Model development, F.N.-P. and J.R.G.-C.; Numerical schemes, F.N.-P.; Programming and code development, F.N.-P. and J.R.G.-C.; Two-phase flow modelling, Experiments A.B., and N.C.; J.R.G.-C., R.A.O.-M. and F.J.S.V.; Analysis of the results and writing, R.A.O.-M. and F.J.S.V.; Analysis of the results and discussion, R.A.O.-M.; Revision of the results, F.J.S.V. All authors have read and agreed to the published version of the manuscript.

Funding: This research was funded by IRSN of France through contract DA 3000011012/CA32000911.

Institutional Review Board Statement: Not applicable.

Informed Consent Statement: Not applicable.

Data Availability Statement: The data presented in this study could be available on request from the corresponding author.

Acknowledgments: The authors would like to acknowledge the SAIT service of UPCT for their support.

Conflicts of Interest: The authors declare no conflict of interest. The funders had no role in the design of the study; in the collection, analyses, or interpretation of data; in the writing of the manuscript, or in the decision to publish the results.

Nomenclature

A	Representative area of a particle.
C_d	Drag coefficient of particles.
C_k	Proportional constant of the turbulent model.
$c_{p,m}$	Specific heat capacity of phase m.
d_p	Mean diameter of particles.
D_k	Diffusion coefficient of species k.
E_i	Activation energy for reaction i.
E_g	Total energy of the gas phase.
E_p	Total energy of the solid phase.
E_Δ	Efficiency function accounting for turbulent flame wrinkling.
F	Factor decreasing the reaction rate for the TFM.
$\vec{F}_d$	Drag force over particles.
H_g	Enthalpy of gas.
$\bar{\bar{I}}$	All-ones vector.
k_i	Kinetic coefficient of reaction i.
k_{sgs}	Turbulent kinetic energy at the subgrid scale.
m_p	Mass of a particle.
Nu	Nusselt number.
p	Pressure.
P_j	Partial pressure of reagent j.
Pr	Prandtl number.
$\vec{\mathrm{q}}$	Heat flux vector.
Q_g	Interphase heat transfer rate.

$\dot{Q}_{g,c}$	Heat released to the gas phase by chemical reactions.
$\dot{Q}_{p,c}$	Heat released to the solid phase by chemical reactions.
Re_p	Reynolds number based on particle diameter d_p.
$\dot{s}_i$	Mass reaction rate of reaction i.
$\overline{S_{ij}}$	Large-scale strain-rate tensor.
S_u	Laminar flame speed.
t	Time.
$\widetilde{\boldsymbol{u}}$	Grid-scale or FAVRE-filtered velocity.
$\vec{u}_g$	Velocity vector of the gas phase.
$\vec{u}_p$	Velocity vector of the solid phase.
u'_δ	Turbulent.
V	Cell volume defined as $V = (\delta x \delta y \delta z)$.
$Y_{m,k}$	Mass fraction of species k in phase m.
Greek Letters	
α	Void fraction.
α_i	Temperature exponent in reaction i.
Γ	Combustion mass source term.
δ_L^0	Laminar flame thickness.
$\Delta H_{fm,k}$	Formation enthalpy of species k in phase m.
μ	Viscosity.
μ_t	Eddy viscosity.
ρ_g	Density of the gas phase.
ρ_p	Density of the solid phase.
σ	Concentration of particles.
$\overline{\tau}$	Friction stress tensor.
τ_{ij}	Subgrid-scale turbulent stress tensor component i,j.
$\dot{\omega}_{m,k}$	Mass reaction rate for species k in phase m.

References

1. Farid, M.M.; Jeong, H.J.; Kim, K.H.; Lee, J.; Kim, D.; Hwang, J. Numerical investigation of particle transport hydrodynamics and coal combustion in an industrialscale circulating fluidized bed combustor: Effects of coal feeder positions and coal feeding rates. *Fuel* **2017**, *192*, 187–200. [CrossRef]
2. Adamczyk, W.P.; Weçel, G.; Klajny, M.; Kozołub, P.; Klimanek, A.; Białecki, R.A. Modeling of particle transport and combustion phenomena in a large-scale circulating fluidized bed boiler using a hybrid Euler-Lagrange approach. *Particuology* **2014**, *16*, 29–40. [CrossRef]
3. Alattab, K.A.; Zainal, Z.A. Syngas production and combustion characteristics in a biomass fixed bed gasifier with cyclone combustor. *Appl. Therm. Eng.* **2017**, *113*, 714–721. [CrossRef]
4. Yang, B.; Wang, L.; Ning, L.; Zeng, K. Effects of pilot injection timing on the combustion noise and particle emissions of a diesel/natural gas dualfuel engine at low load. *Appl. Therm. Eng.* **2016**, *102*, 822–828. [CrossRef]
5. Goix, S.; Lévêque, T.; Xiong, T.; Schreck, E.; Baeza-Squiban, A.; Geret, F.; Uzug, G.; Austruy, A.; Dumat, C. Environmental and health impacts of fine and ultrafine metallic particles: Assessment of threat scores. *Environ. Res.* **2014**, *133*, 185–194. [CrossRef] [PubMed]
6. Benajes, J.; García, A.; Monsalve-Serrano, J.; Boronat, V. Gaseous emissions and particle size distribution of dualmode dualfuel dieselgasoline concept from low to full load. *Appl. Therm. Eng.* **2017**, *120*, 138–149. [CrossRef]
7. Otón-Martínez, R.A.; Monreal-González, G.; García-Cascales, J.R.; Vera-García, F.; Velasco, F.J.S.; Ramírez-Fernández, F.J. An approach formulated in terms of conserved variables for the characterisation of propellant combus-tion in internal ballistics. *Int. J. Numer. Meth. Fluids* **2015**, *79*, 394–415. [CrossRef]
8. Monreal-González, G.; Otón-Martínez, R.A.; Velasco, F.J.S.; García-Cascáles, J.R.; Ramírez-Fernández, F.J. One-Dimensional Modelling of Internal Ballistics. *J. Energetic Mater.* **2017**, *35*, 397–420. [CrossRef]
9. Kuo, K.K.; Summerfield, M. *Fundamentals of Solid-Propellant Combustion*, 90th ed.; American Institute of Aeronautics and Astronautics: New York, NY, USA, 1984.
10. Hamdan, M.; Qubbaj, A. Inhibition effect of inert compounds on oil shale dust explosion. *Appl. Therm. Eng.* **1998**, *18*, 221–229. [CrossRef]
11. Peng, W.; Chen, T.; Sun, Q.; Wang, J.; Yu, S. Preliminary experiment design of graphite dust emission measurement under accident conditions for HTGR. *Nucl. Eng. Des.* **2017**, *316*, 218–227. [CrossRef]

12. Herranz, L.; Del Prá, C.L.; Velasco, F.S. Preliminary steps toward assessing aerosol retention in the break stage of a dry steam generator during severe accident SGTR sequences. *Nucl. Eng. Des.* **2008**, *238*, 1392–1399. [CrossRef]
13. Raimond, E.; Clément, B.; Denis, J.; Guigueno, Y.; Vola, D. Use of Phébus FP and other FP programs for atmospheric radioactive release assessment in case of a severe accident in a PWR (deterministic and probabilistic approaches developed at IRSN). *Ann. Nucl. Energy* **2013**, *61*, 190–198. [CrossRef]
14. García-Cascales, J.R.; Otón-Martínez, R.A.; Sánchez-Velasco, F.J.; Vera-García, F.; Bentaiby, A.; Meynet, N. Advances in the characterisation of reactive gas and solid mixtures under low pressure conditions. *Comput. Fluids* **2014**, *101*, 64–87. [CrossRef]
15. Topilski, L.; Reyes, S. *Accident Analysis Report—Vol. iii: Hypothetical Event Analysis*; Technical Report ITER-D-2E2XAMv4.1, ITER Project; France, 2009.
16. García-Cascales, J.R.; Velasco, F.J.S.; Otón-Martínez, R.A.; Espín-Tolosa, S.; Bentaib, A.; Meynet, N.; Bleyer, A. Characterisation of metal combustion with DUST code. *Fusion Eng. Des.* **2015**, *98–99*, 2142–2146. [CrossRef]
17. Velasco, F.J.S.; Otón-Martínez, R.A.; García-Cascales, J.R.; Espín, S.; Meynet, N.; Bentaib, A. Modelling detonation of H2-O2-N2 mixtures in presence of solid particles in 3D scenarios. *Int. J. Hydrog. Energy* **2016**, *41*, 17154–17168. [CrossRef]
18. Pitsch, H. Large-eddy simulation of turbulent combustion. *Annu. Rev. Fluid Mech.* **2006**, *38*, 453–482. [CrossRef]
19. Lilly, D.K. A proposed modification of the Germano subgrid-scale closure method. *Phys. Fluids A Fluid Dyn.* **1992**, *4*, 633–635. [CrossRef]
20. Nicoud, F.; Ducros, F. Subgrid-Scale Stress Modelling Based on the Square of the Velocity Gradient Tensor. *Flow Turbul. Combust.* **1999**, *62*, 183–200. [CrossRef]
21. Chai, X.; Mahesh, K. Dynamic k-equation model for large eddy simulations of compressible flows. *J. Fluid Mech.* **2012**, *699*, 385–413. [CrossRef]
22. Nicolás-Pérez, F.; Velasco, F.J.S.; García-Cascales, J.R.; Otón-Martínez, R.A.; López-Belchí, A.; Moratilla, D.; Rey, F.; Laso, A. On the accuracy of RANS, DES and LES turbulence models for predicting drag reduction with Base Bleed technology. *Aerospace Sci. Technol.* **2017**, *67*, 126–140. [CrossRef]
23. Emami, S.; Mazaheri, K.; Shamooni, A.; Mahmoudi, Y. LES of flame acceleration and DDT in hydrogen–air mixture using artificially thickened flame approach and detailed chemical kinetics. *Int. J. Hydrog. Energy* **2015**, *40*, 7395–7408. [CrossRef]
24. Sánchez, A.L.; Williams, F.A. Recent advances in understanding of flammability characteristics of hydrogen. *Prog. Energy Combust. Sci.* **2014**, *41*, 1–55. [CrossRef]
25. Williams, F.A. Detailed and reduced chemistry for hydrogen autoignition. *J. Loss Prev. Process. Ind.* **2008**, *21*, 131–135. [CrossRef]
26. Saxena, P.; Williams, F.A. Testing a small detailed chemical-kinetic mechanism for the combustion of hydrogen and carbon monoxide. *Combust. Flame* **2006**, *145*, 316–323. [CrossRef]
27. Gibeling, H.; Buggeln, R. *Reacting Flow Models for Navier-Stokes Analysis of Projectile Base Combustión*; AIAA Paper No. 91-2077; AIAA: Reston, VA, USA, 1991.
28. Zhuo, C.; Feng, F.; Wu, X.; Liu, Q.; Ma, H. Numerical simulation of the muzzle flows with base bleed projectile based on dynamic overlapped grids. *Comput. Fluids* **2014**, *105*, 307–320. [CrossRef]
29. Bournot, H.; Daniel, E.; Cayzac, R. Improvements of the base bleed effect using reactive particles. *Int. J. Therm. Sci.* **2006**, *45*, 1052–1065. [CrossRef]
30. Chelliah, H. The influence of heterogeneous kinetics and thermal radiation on the oxidation of graphite particles. *Combust. Flame* **1996**, *104*, 81–94. [CrossRef]
31. Chelliah, H.K.; Makino, A.; Kato, I.; Araki, N.; Law, C.K. Modeling of graphite oxidation in a stagnation-point flow field using detailed homogeneous and semiglobal heterogeneous mechanisms with comparisons to experiments. *Combust. Flame* **1996**, *104*, 469–480. [CrossRef]
32. Bradley, D.; Dixon-Lewis, G.; Habik, S.E.; Mushi, E.M.J. *Twentieth Symposium (International) on Combustion*; The Combustion Institute: Pittsburgh, PA, USA, 1984; pp. 931–940.
33. Yetter, R.A.; Dryer, F.L.; Rabitz, H. A Comprehensive Reaction Mechanism For Carbon Monoxide/Hydrogen/Oxygen Kinetics. *Combust. Sci. Technol.* **1991**, *79*, 97–128. [CrossRef]
34. Druzhinin, O.A.; Elghobashi, S. On the decay rate of isotropic turbulence laden with micropaticles. *Phys. Fluids* **1999**, *11*, 602–610. [CrossRef]
35. Shotorban, B.; Balachandar, S. A Eulerian model for large-eddy simulation of concentration of particles with small Stokes numbers. *Phys. Fluids* **2007**, *19*, 118107. [CrossRef]
36. Yeh, F.; Lei, U. On the motion of small particles in a homogeneous isotropic turbulent flow. *Phys. Fluids A Fluid Dyn.* **1991**, *3*, 2571–2586. [CrossRef]
37. Simonin, O.; Deutsch, E.; Minier, J.P. Eulerian prediction of the fluid/particle correlated motion in turbulent two-phase flows. *Flow Turbul. Combust.* **1993**, *51*, 275–283. [CrossRef]
38. Wang, Q.; Squires, K. Large eddy simulation of particle-laden turbulent channel flow. *Phys. Fluids* **1996**, *8*, 1207–1223. [CrossRef]
39. Boivin, M.; Simonin, O.; Squires, K. On the prediction of gas–solid flows with two-way coupling using large eddy simulation. *Phys. Fluids* **2000**, *12*, 2080. [CrossRef]
40. Apte, S.; Mahesh, K.; Moin, P.; Oefelein, J. Largeeddy simulation of swirling particle-laden flows in a coaxialjet combustor. *Int. J. Multiphase Flow* **2003**, *29*, 1311–1331. [CrossRef]

41. Denkevits, A.; Dorofeev, S. Dust explosion hazard in ITER: Explosion indices of fine graphite and tungsten dusts and their mixtures. *Fusion Eng. Des.* **2005**, *75–79*, 1135–1139. [CrossRef]
42. Favre, A. Statistical equations of turbulent gases. In *Problems of Hydrodynamic and Continuum Mechanics*; SIAM: Philadelphia, PA, USA, 1969; pp. 231–266.
43. McBride, B.J.; Gordon, S.; Reno, M.A. *Coefficients for Calculating Thermodynamic and Transport Properties of Individual Species*; NASA: Washington, DC, USA, 1983.
44. Lii, W.S. The viscosity of gases and molecular force. *Lond. Edinb. Dublin Philos. Mag. J. Sci.* **1893**, *36*, 507–531. [CrossRef]
45. Crowe, C.T.; Schwarzkopf, J.D.; Sommerfeld, M.; Tsuji, Y. *Multiphase Flows with Droplets and Particles*; CRC Press: Boca Raton, FL, USA, 2011.
46. García-Cascales, J.R.; Vera-García, F.; Zueco-Jordán, J.; Bentaïb, A.; Meynet, N.; Vendel, J.; Perrault, D. Development of a IRSN code for dust mobilisation problems in ITER. *Fusion Eng. Des.* **2010**, *85*, 2274–2281. [CrossRef]
47. Otterman, B.; Levine, A.S. Analysis of Gas-Solid Particle Flows in Shock Tubes. *AIAA J.* **1974**, *12*, 579–580. [CrossRef]
48. Miura, H.; Glass, I.I. On dusty-gas shock tube. *Proc. R. Soc. Lond.* **1982**, *382*, 373–388.
49. Knudsen, J.G.; Katz, D.L.; Street, R.E. Fluid Dynamics and Heat Transfer. *Phys. Today* **1959**, *12*, 40–44. [CrossRef]
50. Laurendeau, N.M. Heterogeneous kinetics of coal char gasification and combustión. *Prog. Energy Combust. Sci.* **1978**, *4*, 221–270. [CrossRef]
51. Tabor, G.; Weller, H.G. Large Eddy Simulation of Premixed Turbulent Combustion Using Ξ Flame Surface Wrinkling Model. *Flow Turbul. Combust.* **2004**, *72*, 1–28. [CrossRef]
52. Poinsot, D.V.T. *Theoretical and Numerical Combustion*, 3rd ed.; RT Edwards, Inc.: West Bundaberg, Australia, 2012.
53. Charlette, F.; Meneveau, C.; Veynante, D. A power-law flame wrinkling model for LES of premixed turbulent combustion Part I: Non-dynamic formulation and initial tests. *Combust. Flame* **2002**, *131*, 159–180. [CrossRef]
54. Wang, G.; Boileau, M.; Veynante, D. Implementation of a dynamic thickened flame model for large eddy simulations of turbulent premixed combustion. *Combust. Flame* **2011**, *158*, 2199–2213. [CrossRef]
55. Liou, M.-S. A sequel to AUSM, Part II: AUSM+-up for all speeds. *J. Comput. Phys.* **2006**, *214*, 137–170. [CrossRef]
56. Liou, M.-S. A Sequel to AUSM: AUSM+. *J. Comput. Phys.* **1996**, *129*, 364–382. [CrossRef]
57. Koop, A.H. Numerical Simulation of Unsteady Three Dimensional Sheet Cavitation. Ph.D. Thesis, University of Twente, Enschede, The Netherlands, 2009. [CrossRef]
58. Rusanov, V. Calculation of interaction of non-steady shock waves with obstacles. *J. Comput. Math. Phys.* **1962**, *1*, 267–279.
59. Toro, E.F. *Riemann Solvers and Numerical Methods for Fluid Dynamics*; Springer: Berlin, Germany, 1997.
60. Pope, S. Computationally efficient implementation of combustion chemistry using in situ adaptive tabulation. *Combust. Theory Model.* **1997**, *1*, 41–63. [CrossRef]
61. Lu, L.; Pope, S.B. An improved algorithm for in situ adaptive tabulation. *J. Comput. Phys.* **2009**, *228*, 361–386. [CrossRef]
62. Hiremath, V.; Ren, Z.; Pope, S.B. Combined dimension reduction and tabulation strategy using ISAT–RCCE–GALI for the efficient implementation of combustion chemistry. *Combust. Flame* **2011**, *158*, 2113–2127. [CrossRef]
63. Nicolás-Pérez, F.; Velasco, F.J.S.; García-Cascales, J.R.; Otón-Martínez, R.A.; Bentaib, A.; Chaumeix, N. Evaluation of dif-ferent models for turbulent combustion of hydrogen-air mixtures. Large Eddy Simulation of a LOVA sequence with hy-drogen deflagration in ITER Vacuum Vessel. *Fusion Eng. Des.* **2020**, *161*, 111901. [CrossRef]
64. Hedengren, J.D.; Edgar, T.F. In Situ Adaptive Tabulation for Real-Time Control. *Ind. Eng. Chem. Res.* **2005**, *44*, 2716–2724. [CrossRef]
65. Sabard, J.; Chaumeix, N.; Bentaib, A. Hydrogen explosion in ITER: Effect of oxygen content on flame propagation of H2/O2/N2 mixtures. *Fusion Eng. Des.* **2013**, *88*, 2669–2673. [CrossRef]
66. Sabard, J. Etude de L'explosion de Mélanges Diphasiques: Hydrogène et Poussières. Ph.D. Thesis, Université d'Orléans, Orléans, France, 2013; pp. 185–221.
67. Sabard, J.; Goulier, J.; Chaumeix, N.; Mevel, R.; Studer, E.; Bentaib, A. Determination of explosion combustion parameters of H2/O2/N2 mixtures. In Proceedings of the International Symposium on Hazard, Prevention and Mitigation of Industrial Explosions (ISHPMIE), Cracov, Poland, 22–27 July 2012.
68. Jiménez, M.A.; Martín-Valdepeñas, J.M.; Martín-Fuertes, F.; Fernández, J.A. A detailed chemistry model for transient hy-drogen and carbon monoxide catalytic recombination on parallel flat Pt surfaces implemented in an integral code. *Nucl. Eng. Des.* **2007**, *237*, 460–472. [CrossRef]
69. Nuclear Energy Agency, Committee on the Safety of Nuclear Installations. *Carbon Monoxide—Hydrogen Combustion Characteritics in Containment Conditions*; Final Report, NEA/CSNI/R(2000)10; Nuclear Energy Agency: Paris, France, 2000.

7 Conclusions

The following conclusions and findings are presented in this section.

On the one hand, regarding the work related to CFD modelling for analysis of slender bodies flight with *Base bleed* units, results showed different level of agreement between numerical simulations and experimental data in the case of RANS, DES or LES, and highlight some key conclusions from the modelling point of view. The most important can be summarized as follows:

- The combustion within the *Base Bleed* unit can be modelled as a solid surface that is injecting gas at the temperature of the burning front.
- Due to the coupling between the internal *Base Bleed* pressure and the external body airflow pressure, the numerical simulation of the space within the *Base Bleed* cavity is recommended in order to predict the drag coefficient under the flow regimes without chocked conditions at the nozzle of the *Base Bleed* unit.
- Active *Base Bleed* wake region flow has a stronger dependency on how the turbulence is modelled than for inactive *Base Bleed* configuration. Flow field in the wake region varies significantly. Different predicted main recirculation bubble location and shape, as well as the mean velocities of the secondary recirculation zone depends on turbulence modelling.
- RANS-based models predict drag coefficient in the case of inactive *Base Bleed* configuration with reasonable accuracy. However, they have limitations when facing a problem involving a mixing layer of a high temperature jet with a transonic wake as in the case of active *Base Bleed*. In this configuration, results showed that these models are not a suitable option.
- In the case of active *Base Bleed* unit, *Large Eddy Simulations* was found to have a better prediction capacity than RANS and DES. WALE LES was found to be the best turbulence model to predict drag coefficient with an average absolute error of 4.4%.
- In the case of active *Base Bleed*, the use of DES models (Real k-ε, SST k-ω) is not recommended as they provide C_D average prediction errors over 23%.
- The influence of the molecular weight of the combustion gases injected within the *Base Bleed* unit in the drag predicted by the simulations was found to be negligible. In addition, the temperature value used for modelling the gas mass flow injected within the *Base Bleed* unit had very limited influence on the C_D prediction.

Regarding future work in this line, it is worth to remark some key points obtained from the last phase of the PhD thesis where H_2-CO-air post-combustion process was included:

- LES-PSR combustion model and with both chemical kinetic mechanisms (12Step and 30Step) report similar results for local (flow-field) and integral (drag, weighted

averaged pressure) values. Williams H_2-CO 30Step mechanism[24] seems to predict higher temperatures and base pressures than the reduced 12Step mechanism. With this approach the relative error of C_D prediction with respect to experimental data is reduced to -2.87%.

- Jet-flow pattern changes significantly when considering combustion due to the volumetric effects. This produces increases the base pressure values due to the volumetric effects created by the higher temperature gases prediction. Moreover, flow field obtained when modelling post-combustion has a *Base Bleed* jet which penetrates a longer distance, separating the low-pressure regions (main recirculation bubble, first stagnation point) from the base surface. *Base Bleed* gases jet has a more stable behavior with less turbulent kinetic energy.
- RANS v2-f for 2D axil-symmetric approach is presented as a reduced computational cost alternative to 3D LES simulations with reasonable accuracy for both *Base Bleed* inactive and active configurations. In the case of active *Base Bleed*, including post-combustion effects using a steady combustion model, RANS *Eddy Dissipation Concept* (EDC) and Williams H_2-CO 30Step[24] has been tested with results similar to the more demanding 3D LES computations. With this approach the relative error of C_D prediction with respect to experimental data is reduced to -7.8%.

On the other hand, conclusions regarding the work carried out for *Large Eddy Simulations* for hydrogen combustion modelling are exposed below:

- The benchmark of LES-FPV and LES-TFM models against combustion experiments under a well-characterized turbulent field within a spherical bomb showed that this type of model, coupled with a detailed chemical kinetic scheme, behaved well for this kind of problems. The assessment also revealed that TFM with detailed chemistry and in-situ adaptive ISAT tabulation method had a better prediction of the experimental flame speed and pressure evolution than the FPV. Results also showed that, when compared with the cases with no initial turbulence, burning speed increased drastically when the turbulence was increased, whereas the maximum combustion pressure was not affected by the turbulence and maintained almost constant.
- Based on the validation results, TFM model was selected to simulate two accident sequences within ITER VV. The results of the simulations showed that a breach at the wall generated a transonic jet due to the pressure difference between the outer ambient conditions and the vacuum conditions within the vessel.
- During the sequence, chocked conditions resulted at the breach with an air entrainment rate in the VV. In the case of a breach of 0.15 m^2 after 835 ms of the initiation of the sequence, ignition was induced at 4500 Pa with ϕ=0.84. When this combustion sequence under LOVA conditions was compared with the combustion sequence under quiescent conditions, with airtight conditions (i.e. no breach at the

walls), results showed that burning speed increased by a factor of up to 3.5, due to the flame acceleration induced by the turbulence level within the VV that resulted in a faster sequence without detonation. Notwithstanding, the averaged pressure reached at the vessel due to the combustion was similar ($P_{max}/P_0 \sim 4.5$). However, in the case of a breach of 0.02 m^2 and at ignition induced at 13.35 kPa with ϕ=0.92, the turbulence induced by the jet was not able to enhance flame acceleration and the burning speed was similar to the case of airtight conditions. This equivalence ratio and pressure level provided a deflagration to detonation transition. In this case, the average wall pressure reached at the VV was $P_{max}/P_0 \sim 5.2$ whereas there were reported local peaks of ~600kPa (i.e. $P_{max}/P_0 \sim 45$).

Additionally to the LES-FPV and LES-TFM models, the capabilities and limitations of LES coupled with the PSR hypothesis were evaluated to simulate the initial stages of H_2-air combustion experiments. The main conclusions regarding this LES-PSR modelling research are:

- The study showed this LES approach can be applied to a grid with enough resolution to resolve flame thickness and wrinkling patterns. In this case, no sub-grid scale combustion modelling is needed. However, the model has important limitations that must be considered:
- Spatial resolution was found to be critical. The unstretched laminar flame speed predicted with this type of models with meshes $\delta_L^0/\Delta x \sim 1$ provide errors of ~18%. Furthermore, numerical diffusion might play an important role in the predicted flame speed.
- There is an important effect of the sub-grid models, which points out the uncertainty linked with its election, especially in the case of grids that do not provide enough flame resolution.
- The computational resources needed to reach the required level of flame resolution of this modelling approach increases as the flame expands and the flow increases its Reynolds number due to flame wrinkling and the effective increase of the flame surface.
- As for the suggested improvements, results also showed this LES approach coupled with detailed chemistry and ISAT method was an affordable strategy to simulate the initial stages (i.e., post-ignition and flame acceleration) of premixed combustion problems, with low or moderate Reynolds numbers with reasonable accuracy, if a certain level of grid refinement was reached ($\delta_L^0/\Delta x \geq 8$).
- The impact of sub-grid turbulence models was found to be high whereas the influence of the detailed kinetic scheme used was lower. Therefore, it is recommended to benchmark the sub-grid model used against experimental results.
- Regarding the prediction of the unsteady behaviour of the sequence, AUSMup, AUSM+, and PISO schemes showed reasonable agreement with experimental data.

Flux Difference Splitting (FDS) schemes as Rusanov scheme showed not accurate performance at low Mach regime. AUSMup flux-schemes with the Bath-Jespersen slope limiter provided the best results (<4% of error), not only in rising time but also in maximum wall pressure predicted.

- As for the prediction of the combustion products, the models predicted, with an error smaller than 6%, the final species composition. PISO scheme and Williams' chemical model provided the smallest deviations from experimental data.
- Results also showed that this LES approach was able to account for the cellular flame pattern at the post-ignition phase, and provided results which were qualitatively similar to the experimental ones.
- Besides, this approach is also able to predict flame acceleration in an obstructed channel if the required level of flame resolution is met. These results permit to postulate this LES approach for experiments interpretation and dynamic studies of the early stage of a flame expansion.

Finally, a two-phase model has been derived from the LES-TFM previously validated. This model was proposed to describe this reacting flow with LES and detailed chemistry. The model proposed was benchmarked against experimental combustion data obtained in a spherical bomb. The following conclusions are worth to be remarked:

- In case of highly diluted mixtures of H2–air and graphite particles, the benchmarked results showed that LES with a detailed chemistry model were found to be an appropriate engineering approach for analyzing premixed turbulent combustion of graphite-H_2 mixtures.
- The validation against the experimental data show that the two-phase approach used in the present model based on the Eulerian–Eulerian approach seems to be accurate enough to afford this type of combustion sequences with highly diluted mixtures.
- Under the conditions studied, the model captured well the key tendencies linked to the presence of carbon particles of the microns order. In this sense, the model was able to predict that the presence of a low concentration of carbon particles (of the order of 96 g/m^3) accelerated the combustion sequence, obtaining smaller combustion times than in the absence of particles and larger maximum wall pressure levels (of the order of 15%).
- Classical graphite and hydrogen detailed oxidation mechanisms[25-27] coupled with a Eulerian–Eulerian model provided good results in the prediction of combustion products under turbulent combustion conditions. Regarding graphite combustion, the porous oxidation model provided results closer to the experiments than the non-porous mode.

8 References

1. T. Poinsot and D. Veynante, Theoretical and numerical combustion, Ed. R. T., Edwards, Philadelphia, 2001
2. R. Benay, P. Servel, Two-equation turbulence model: Application to a supersonic base flow, AIAA Journal 39 (2001)
3. J. Sahu, C.J. Nietubicz, J.L. Steger, Navier-Stokes computation of projectile base flow with and without base injection, AIAA J. 23(9) (1985) 1348-1355.
4. J. Sahu, J.E. Danberg, Navier-Stokes computations of transonic flows with a two-equation turbulence model, AIAA J. 24(11) (1986) 1744-1751.
5. J. Sahu, Supersonic flow over cylindrical afterbodies with base bleed, Computatoinal Mechanics 2(3) (1987), 176-184.
6. P. Kaurinkoski, A. Hellsten, Numerical simulation of supersonic base bleed projectile with improved turbulence modelling, Journal of Spacecraft and Rockets 35 (5) (1998) 606–611.
7. P. Kaurinkoski, Computation of the flow of thermally perfect gas past a super-sonicprojectile with Base Bleed, 1996, in: AIAA AFM Conference, 1996, pp. 725-734.
8. F. Nicolás-Pérez, F.J.S. Velasco, J.R. García-Cascales, R.A. Otón-Martínez, A. López-Belchí, D. Moratilla, F. Rey, A. Laso, On the accuracy of RANS, DES and LES turbulence models for predicting drag reduction with Base Bleed technology, Aerospace Science and Technology 67 (2017) 126-140
9. Xiang, Z., Yang, S., Xie, S., Li, J., & Ren, H., Turbulence–chemistry interaction models with finite-rate chemistry and compressibility correction for simulation of supersonic turbulent combustion, Engineering Applications of Computational Fluid Mechanics, 14:1, (2020) 1546-1561.
10. Ciccarelli, G., Johansen, C.T., Parravani, M., The role of shock-flame interactions on flame acceleration in an obstacle laden channel. Combust. Flame 157, (2010) 2125-36.
11. Meshkov, E. E., Instability of the Interface of Two Gases Accelerated by a Shock Wave, Soviet Fluid Dynamics. 4, (1969) 101-104.
12. Pitsch, H., Large-Eddy Simulation of Turbulent Combustion. Annu. Rev. Fluid. Mech. 38, (2006) 453-482.
13. Duwig, C., Ducruix, S., Veynante, D., Studying the Stabilization Dynamics of Swirling Partially Premixed Flames by Proper Orthogonal Decomposition, J. Eng.GasTurbines Power 134 (2012) 101501.
14. Duwig, C., Dunn, M. J., Large Eddy Simulation of a premixed jet flame stabilized by a vitiated co-flow: Evaluation of auto-ignition tabulated chemistry. Combust. Flame 160 (2013) 2879-2895.

15. Duwig, C., Ludiciani, P., 2014. Large Eddy Simulation of turbulent combustion in a stagnation point reverse flow combustor using detailed chemistry. Fuel. 123, 256-273.
16. Fureby, C., Comparison of Flamelet and Finite Rate Chemistry LES for Premixed Turbulent Combustion, 45th AIAA Aerospace Sciences Meeting and Exhibit Reno, Nevada 2007.
17. Grinstein, F.F., Kailasanath, K., Three dimensional numerical simulations of unsteady reactive square jets. Combust. Flame. 101, (1995) 2-10.
18. Krüger, O., Terhaar, S., Paschereit, C.O., Duwig, C., Large Eddy Simulations of Hydrogen Oxidation at Ultra-Wet Conditions in a Model Gas Turbine Combustor Applying Detailed Chemistry. J. Eng. Gas Turbines Power. 135, (2013) 021501-9.
19. Colin, O., Ducros, F., Veynante, D., & Poinsot, T., A thickened flame model for Large Eddy Simulations of turbulent premixed combustion. Physics of Fluids, 12(7), (2000) 1843–1863.
20. Berglund, M., Fedina, E., Tegnér, J., Fureby, C., Sabelnikov, V., Finite rate chemistry LES of self-ignition in a supersonic combustion ramjet, AIAA J. 48 (2010) 540.
21. Giacomazzi, E., Battaglia, V., Bruno, C., The coupling of turbulence and chemistry in a premixed bluff-body flame as studied by LES. Combust. Flame 134, (2004) 320-335.
22. Navarro-Martinez, S., Kronenburg, A., Di Mare, F., Conditional Moment Closure for Large Eddy Simulations. Flow, Turbulence and Combustion. 75, (2005) 245-274.
23. Sankaran, V., Menon, S., Subgrid combustion modeling of 3-D premixed flames in the thin-reaction-zone regime. Proc. Combust. Inst. 30, (2005) 575-583.
24. Priyank Saxena, Forman A. Williams. Testing a small detailed chemical-kinetic mechanism for the combustion of hydrogen and carbon monoxide. Center of Energy Research, Department of Mechanical and Aerospace Engineering, University of California, San Diego, La Jolla, CA 92093, USA. (2005) 318.
25. Chelliah, H. The influence of heterogeneous kinetics and thermal radiation on the oxidation of graphite particles. Combust. Flame, 104, (1996) 81–94.
26. Chelliah, H.K., Makino, A., Kato, I., Araki, N., Law, C.K., Modeling of graphite oxidation in a stagnation-point flow field using detailed homogeneous and semiglobal heterogeneous mechanisms with comparisons to experiments. Combust. Flame 104 (1996), 469–480.
27. Yetter, R.A., Dryer, F.L., Rabitz, H. A, Comprehensive Reaction Mechanism For Carbon Monoxide/Hydrogen/Oxygen Kinetics. Combust. Sci. Technol. 79, (1991) 97–128.

Appendix

Article 1.- F. Nicolás-Pérez, F.J.S. Velasco, J.R. García-Cascales, R.A. Otón-Martínez, A. López-Belchí, D. Moratilla, F. Rey, A. Laso, On the accuracy of RANS, DES and LES turbulence models for predicting drag reduction with Base Bleed technology, Aerospace Science and Technology, Volume 67, 2017, Pages 126-140, ISSN 1270-9638, https://doi.org/10.1016/j.ast.2017.03.031

2020 JOURNAL IMPACT FACTOR
5.107
View calculation

JOURNAL IMPACT FACTOR WITHOUT SELF CITATIONS
2.932
View calculation

Journal Impact Factor contributing items Export

Journal Impact Factor Trend 2020 Export

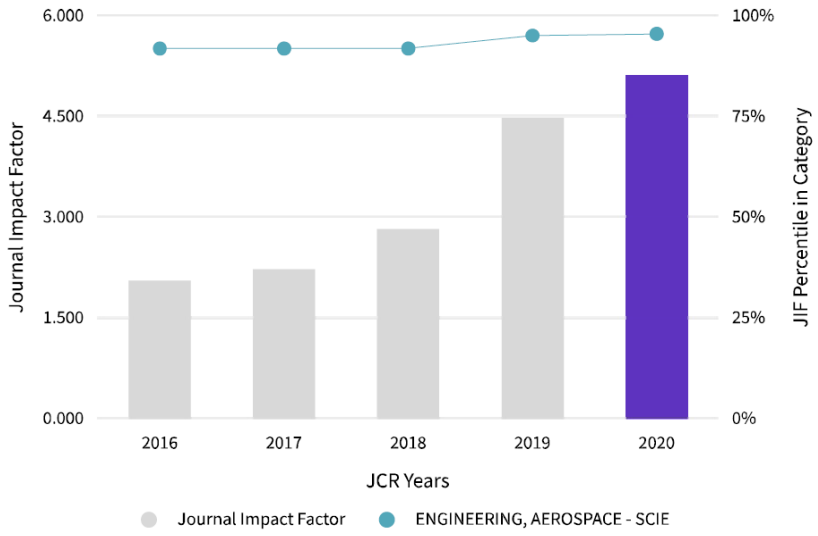

Rank by Journal Impact Factor

Journals within a category are sorted in descending order by Journal Impact Factor (JIF) resulting in the Category Ranking below. A separate rank is shown for each category in which the journal is listed in JCR. Data for the most recent year is presented at the top of the list, with other years shown in reverse chronological order. Learn more

EDITION
Science Citation Index Expanded (SCIE)

CATEGORY
ENGINEERING, AEROSPACE
2/34

JCR YEAR	JIF RANK	JIF QUARTILE	JIF PERCENTILE
2020	2/34	Q1	95.59
2019	2/31	Q1	95.16
2018	3/31	Q1	91.94
2017	3/31	Q1	91.94
2016	3/31	Q1	91.94

EDITION
Science Citation Index Expanded (SCIE)

CATEGORY
AEROSPACE ENGINEERING & TECHNOLOGY
n/a

JCR YEAR	JIF RANK	JIF QUARTILE	JIF PERCENTILE
2020	n/a	n/a	n/a
2019	n/a	n/a	n/a
2018	n/a	n/a	n/a
2017	n/a	n/a	n/a

Article 2.- F. Nicolás-Pérez, F.J.S. Velasco, José R. García-Cascales, Ramón A. Otón-Martínez, Ahmed Bentaib, Nabiha Chaumeix, Evaluation of different models for turbulent combustion of hydrogen-air mixtures. Large Eddy Simulation of a LOVA sequence with hydrogen deflagration in ITER Vacuum Vessel, Fusion Engineering and Design, Volume 161, 2020, 111901, ISSN 0920-3796, https://doi.org/10.1016/j.fusengdes.2020.111901

2020 JOURNAL IMPACT FACTOR
1.453
View calculation

JOURNAL IMPACT FACTOR WITHOUT SELF CITATIONS
0.914
View calculation

Journal Impact Factor contributing items Export

Journal Impact Factor Trend 2020 Export

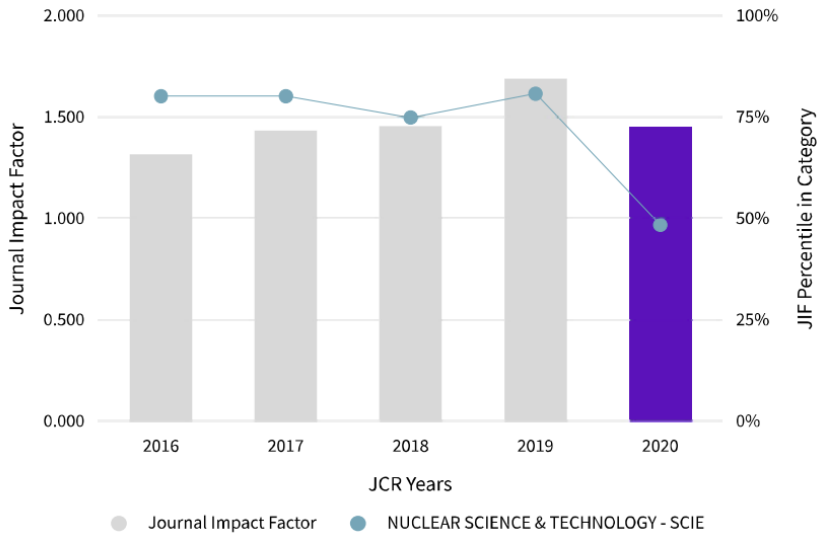

Rank by Journal Impact Factor

Journals within a category are sorted in descending order by Journal Impact Factor (JIF) resulting in the Category Ranking below. A separate rank is shown for each category in which the journal is listed in JCR. Data for the most recent year is presented at the top of the list, with other years shown in reverse chronological order. Learn more

EDITION
Science Citation Index Expanded (SCIE)

CATEGORY
NUCLEAR SCIENCE & TECHNOLOGY
18/34

JCR YEAR	JIF RANK	JIF QUARTILE	JIF PERCENTILE
2020	18/34	Q3	48.53
2019	7/34	Q1	80.88
2018	9/34	Q2	75.00
2017	7/33	Q1	80.30
2016	7/33	Q1	80.30

Article 3.- F. Nicolás-Pérez, F.J.S. Velasco, Ramón A. Otón-Martínez, José R. García-Cascales, Ahmed Bentaib and Nabiha Chaumeix, Capabilities and limitations of Large Eddy Simulation with perfectly stirred reactor assumption for engineering applications of unsteady, hydrogen combustion sequences, Engineering Applications of Computational Fluid Mechanics (TCFM) 2021 https://doi.org/10.1080/19942060.2021.1974092

2020 JOURNAL IMPACT FACTOR
8.391
View calculation

JOURNAL IMPACT FACTOR WITHOUT SELF CITATIONS
6.105
View calculation

Journal Impact Factor contributing items Export

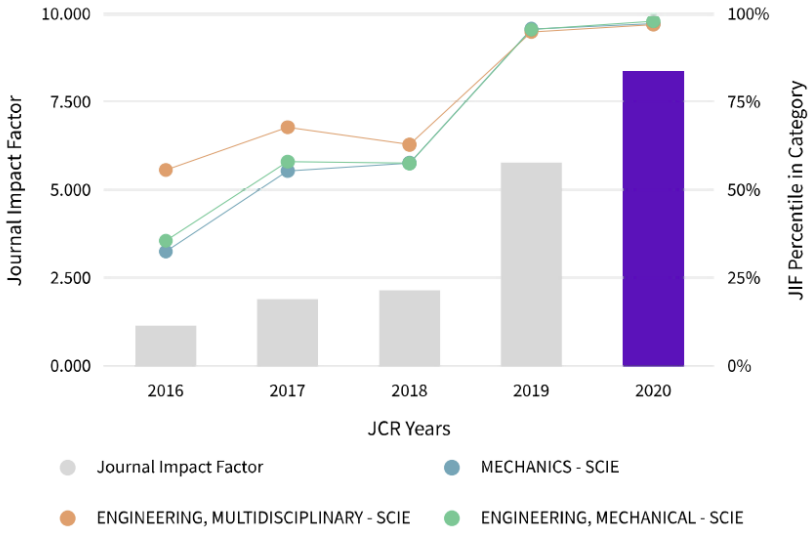

Rank by Journal Impact Factor

Journals within a category are sorted in descending order by Journal Impact Factor (JIF) resulting in the Category Ranking below. A separate rank is shown for each category in which the journal is listed in JCR. Data for the most recent year is presented at the top of the list, with other years shown in reverse chronological order. Learn more

EDITION
Science Citation Index Expanded (SCIE)

CATEGORY
ENGINEERING, MECHANICAL
3/133

JCR YEAR	JIF RANK	JIF QUARTILE	JIF PERCENTILE
2020	3/133	Q1	98.12
2019	6/130	Q1	95.77
2018	55/129	Q2	57.75
2017	54/128	Q2	58.20
2016	84/130	Q3	35.77

EDITION
Science Citation Index Expanded (SCIE)

CATEGORY
ENGINEERING, MULTIDISCIPLINARY
3/90

JCR YEAR	JIF RANK	JIF QUARTILE	JIF PERCENTILE
2020	3/90	Q1	97.22
2019	5/91	Q1	95.05
2018	33/88	Q2	63.07
2017	28/86	Q2	68.02
2016	38/85	Q2	55.88

Article 4.- F. Nicolás-Pérez, F.J.S. Velasco, Ramón A. Otón-Martínez, José R. García-Cascales, Ahmed Bentaib and Nabiha Chaumeix, Mathematical Modelling of Turbulent Combustion of Two-Phase Mixtures of Gas and Solid Particles with a Eulerian–Eulerian Approach: The Case of Hydrogen Combustion in the Presence of Graphite Particles, Mathematics 2021, 9(17), 2017; https://doi.org/10.3390/math9172017

2020 JOURNAL IMPACT FACTOR
2.258
View calculation

JOURNAL IMPACT FACTOR WITHOUT SELF CITATIONS
1.835
View calculation

Journal Impact Factor contributing items Export

Journal Impact Factor Trend 2020 Export

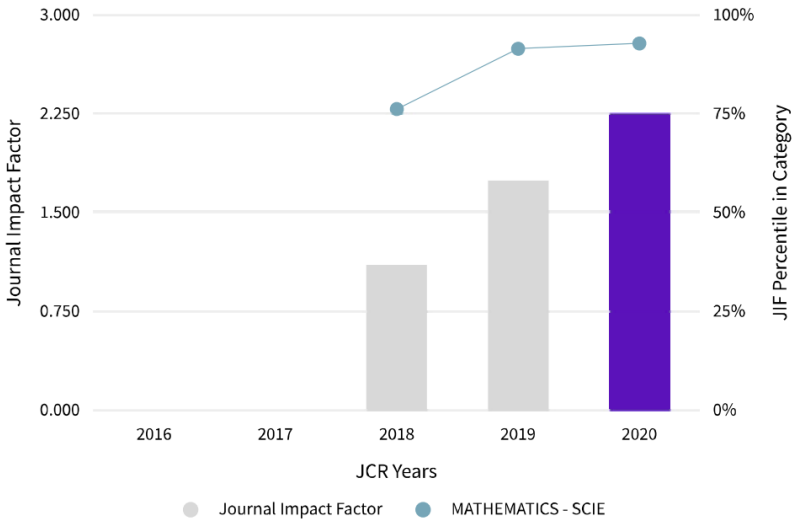

Rank by Journal Impact Factor

Journals within a category are sorted in descending order by Journal Impact Factor (JIF) resulting in the Category Ranking below. A separate rank is shown for each category in which the journal is listed in JCR. Data for the most recent year is presented at the top of the list, with other years shown in reverse chronological order. Learn more

EDITION
Science Citation Index Expanded (SCIE)

CATEGORY
MATHEMATICS
24/330

JCR YEAR	JIF RANK	JIF QUARTILE	JIF PERCENTILE
2020	24/330	Q1	92.88
2019	28/325	Q1	91.54
2018	75/314	Q1	76.27